

D4.25: Results of codes validation with wave tank tests

Editor: Nicolai F. Heilskov

With the contribution of:

J. Azcona, H. Bredmose, F. Borisade, N.F. Heilskov, Y. Kim, L. Klein, C. Koch, F. Lemmer, T. Lutz, A. Manjock, L. Mauser, D. Manolas, A. Pegalajar-Jurado, A. Robertson, J. Jonkman, F. Wendt, F. Vittori and S. Voutsinas

Agreement n.:	308974
Duration	November 2012 – October 2017
Co-ordinator:	Mr Peter Hjuler Jensen



The research leading to these results has received funding from the European Community's Seventh Framework Programme FP7-ENERGY-2012-1-2STAGE under grant agreement No. 308974 (INN WIND.EU).nn

Document information

Document Name:	Results of codes validation with wave tank
Confidentiality Class:	PU
Deliverable Number:	D4.25
Edited By:	Nicolai F. Heilskov (DHI)
Contributing Authors:	J. Azcona, H. Bredmose, F. Borisade, N. F. Heilskov, Y. Kim, L. Klein, C. Koch, F. Lemmer, T. Lutz, A. Manjock, L. Mauser, D. Manolas, A. Pegalajar-Jurado, A. Robertson, J. Jonkman, F. Wendt, F. Vittori and S. Voutsinas
Review:	J. Azcona (CENER)
Date:	18 October 2016
WP:	WP4: Offshore Foundations and Support Structures
Task:	Task 4.2: Verification and validation of design methods for floating structures

TABLE OF CONTENTS

TABLE OF CONTENTS	3
1 INTRODUCTION.....	6
1.1 OPASS dynamic mooring lines simulator [CENER].....	6
1.2 High fidelity non-linear, viscid hydrodynamic CFD model [DHI].....	7
1.3 High fidelity CFD Simulations using FLOWer [USTUTT- IAG]	8
1.4 FLEX5 aero-hydro-elastic model [DTU]	8
1.5 FAST aero-hydro-elastic model [NREL, CENER].....	8
1.6 Simplified Low-Order Wind Turbine Model (SLOW) [USTUTT-SWE].....	9
1.7 Coupled multibody model for floating offshore wind turbines (SIMPACK) [USTUTT-SWE]	12
1.8 Coupled multibody model for floating offshore wind turbines (hGAST) [NTUA].....	14
1.9 BLADED aero-hydro-elastic model [GL-RC].....	20
1.10 REFERENCES.....	23
2 SEMISUBMERSIBLE VALIDATION TEST CASES.....	25
2.1 Introduction	25
2.2 Load cases database.....	26
2.3 Validation based on the Froude-Scaled rotor model	26
Scaled model properties	26
Description of the test cases	27
Static mooring displacement (LC96).....	27
Free Decay (LC32).....	30
Regular wave only (LC52)	33
Irregular wave only (LC12)	36
Wind only cases (LC142-145)	38
Wind and Regular Wave (LC65).....	41
Wind and Irregular Wave (LC 166)	44
Survival Load Case (LC162).....	46
Conclusions of the validation based on the model with Froude-Scaled rotor	48
2.4 Ducted Fan Tests	49
Description of the numerical models	49
Scaled floating wind turbine model.....	50
Description of the test cases	53
Free decay test	54
Constant wind and no waves.....	55
Constant wind and regular waves	56
Free decay tests under constant wind	61

Constant wind and irregular waves	63
Turbulent wind and irregular waves	67
Software in the Loop (SiL) performance	71
Conclusions of the validation based in the model with SiL and a ducted fan force actuator.....	73
2.5 Aerodynamic High-Fidelity Simulations.....	74
Blade surface smoothing and 1/3 model simulations.....	74
Modelling of the jet flow.....	80
Simulation of the full turbine in uniform inflow and test environment	82
Simulation of the turbine with prescribed motion	87
Conclusion of the aerodynamic high-fidelity model validation	89
2.6 Conclusions on the semisubmersible test campaign	90
2.7 Acknowledgements.....	91
2.8 REFERENCES.....	92
3 TLP VALIDATION TEST CASES	95
3.1 Introduction	95
3.2 The test campaign	95
Floater concept and rotor.....	96
Model specifications	96
Wave basin and wave generation.....	98
Instrumentation and sensors.....	98
3.3 Test cases.....	98
3.4 Analysis specifications and tuning strategy.....	100
3.5 Validation and Model Comparison	101
Data processing.....	101
Steady thrust curve	102
Decay tests in water	103
Response to regular waves.....	104
Response to irregular waves.....	107
Response to irregular waves and wind	112
Response to focused waves	116
3.6 Additional simulations with simulation code BLADED	121
3.7 Conclusions	129
Further research and development.....	130
3.8 REFERENCES.....	131
4 VALIDATION OF THE DYNAMIC MOORING LINE CODE OPASS	132
4.1 Description of the numerical model.....	132
4.2 Description of the experimental tests.....	132
4.3 Parameters of the computational model.....	136

4.4	Comparison of computational and experimental results	137
	Static cases.....	137
	Dynamic cases: tension at the fairlead.....	138
	Dynamic cases: motion of the chain	142
4.5	Conclusions	146
4.6	REFERENCES.....	148
5	CONCLUSIONS.....	149

1 INTRODUCTION

This document reports the validation of the numerical prediction codes of different partners by comparison of computational simulations with the results from water tank tests. The report builds on top of INN WIND.EU delivery 4.21 and 4.24 (Azcona et al., 2014; 2016), and is a result of tight collaboration between the 4.25 authors. The motivation for the development of accurate prediction tools can be found in report 4.21. The present document will include a description of the main features of the codes and the development status at the moment when the simulations were performed.

Two different concepts of a floating wind turbine are the objects for validation. The first one is a semi-submersible concept and the second one is a TLP (Tension Leg Platform) concept. A TLP is a column foundation characterized by achieving stability by virtue of excess buoyancy and tensioned mooring lines, so-called tendons. A semi-submersible foundation is characterized by providing restoring moment to the floater through a combination of ballast and buoyancy stabilization.

The scaled models that were tested in this campaign, represent

- 1) a 10MW wind turbine with a semi-submersible floating substructure, where the rotor was represented by a Froude-scaled wind turbine model, built at Politecnico di Milano or a real-time controlled ducted fan built by CENER, respectively and
- 2) a Froude-scaled model of the DTU/INN WIND.EU 10MW wind turbine installed on a TLP floating substructure built by DTU (D4.24, INN WIND.EU: Azcona et al., 2016).

The numerical results and their comparison with the prior experimental measurements are presented and discussed. For each chapter, first the experimental model test details are given, which are then followed by a code-to-code and the code-to-experiment comparisons.

The report consists of three main chapters. The present chapter 1 introduces the numerical models subject to validation. In chapter 2 the numerical models are validated against model tests of a semi-submersible concept of a floating wind turbine, whereas chapter 3 validates the numerical models against measurements of a floating wind turbine mounted on a TLP foundation. Chapter 4 focuses on the mooring system and measurements from the semi-submersible concept are used in the validation. Each chapter ends with a specific conclusion and outlook. At the end of the report a main conclusion is provided as drawn from all three chapters.

Before diving into the validations, we will begin with a short introduction of the numerical codes that have been tested - with special focus on updates of the codes when the validation was performed. For detailed model descriptions of previous described models in INN WIND.EU report D4.21, we refer to Azcona et al. (2014).

Note that the contribution from DNV-GL is absent. DNV-GL plan to include their part at a later point in time and update all affected chapters in this report accordingly.

1.1 OPASS dynamic mooring lines simulator [CENER]

The code OPASS (Offshore Platform Anchorage System Simulator) is a tool developed by CENER for the simulation of the mooring line dynamics. The tool has been coupled with FAST v6, but can be also used as a stand-alone simulator. The coupled FAST-OPASS tool has been validated in Chapter 2 and the OPASS tool as a stand-alone code is validated in Chapter 4.

OPASS is based in Finite Element Method and takes into account the line inertia, the hydrodynamic tangential and normal drag, the added mass, the structural damping and the seabed-line contact and also the friction in the longitudinal and normal directions.

The OPASS code has been described in detail in the INN WIND.EU deliverable 4.21. Since the publication of this deliverable, some improvements have been introduced in the OPASS code. The code is now able to model lines composed of different segments with different materials and can also include buoys at a certain position. Nevertheless none of these improvements were applicable to the test data from this validation.

1.2 High fidelity non-linear, viscid hydrodynamic CFD model [DHI]

Accurately predicting hydrodynamic motion response of floating offshore wind turbine is key in view optimization of performance and energy harvesting. Inertial forces is part but damping is the governing mechanism for floating structure motion response. In some situations, non-linear viscous effects may play a significant part on the response and stability. This is particular likely in situations where the wind turbine foundation is excited by extreme wave conditions, strong currents, wave run-up, wave overtopping and drag dominated wave interaction (large KC number). In the case of large KC-number (Keulegan-Carpenter number), vortex shedding can induce roll motion of the floating wind turbine. A CFD¹ model accounts not only for influence of wave making damping, but for eddy making damping and nonlinear viscosity damping. The absence of viscosity in potential theory codes not only alters fluid damping but also, to some extent, the added-inertia characteristics. The shortfall of viscous effects in codes based on potential flow theory is often compensated by introducing an external empirical viscosity term in the body equations of motion. However, this demands a calibration of the floater damping in term of drag coefficient. CFD decay simulations of the floater has the potential of complimenting aero-hydro-elastic models by providing the needed damping calibration. No calibration is needed for a floating CFD model.

The open source code library OpenFOAM® (Weller et al., 1998) based on the finite volume method was used to build the CFD model of the floating wind turbine. Details on the CFD model for floater simulation and analysis of CFD modelling of floating wind turbine can be found in Heilskov and Petersen (2016). The code includes a solver for the Navier-Stokes equations for two immiscible and incompressible fluids air and water. It captures the air-water interface using a variation of the Volume-of-Fluid (VOF) method (Berberovic et al., 2009). Accurately predicting the wave kinematics in the top part of the waves is of particular importance if the draft of the floating wind turbine (e.g. a TLP) is relatively small compared to depth. For this, a wave making² boundary and outlet boundary based on an active absorption approach is applied (Higuera et al., 2013). The governing methodologies in CFD needed for accurately capturing hydrodynamic impact on the floating wind turbine lie in not only in the surface capturing algorithm but also in the two-way coupling between the body motion algorithm and the hydrodynamic solver of the Navier-Stokes equation. The latter involves not only the coupling between the Navier-Stokes equation and the 6-DOF (Six Degrees of Freedom) rigid body motion solver, but also a “re-meshing” technique is needed to follow the movement of the floating structure. The floating structure is handled by a dynamic movable mesh algorithm that redistribute mesh points inside the fluid domain at each time step to using a Laplace smoothing equation to ensure the mesh quality (Jasak, 2009; Jasak and Tukovic, 2010). A fluid-structure interaction (FSI) problem as wave hydrodynamics of a floating wind turbine, is a characterized by strong coupling between the fluid and the rigid body motion. The standard FSI implementation in OpenFOAM® 2.3 suffer from stability sensitivity due to its weak coupling algorithm between the rigid body motion and the hydrodynamics. A strong coupling has therefore been implemented in OpenFOAM by constructing a partitioned scheme using an iteration technique combined with predictor-corrector scheme for solving the governing equations for the body motion. The partitioned scheme is constructed in such way that flow-induced forces on body, tension in tendons, body motion/position and grid update are transferred several times in an iterative manner within every time step. The four mooring lines are modeled defining pairs of attachment point and anchor point combined with properties of a massless

¹ Computational Fluid Dynamics

² Even though the wave field is synthesized from linear theory at the wave generator wall, its propagation through the computational domain is governed by the full non-linear Navier-Stokes equations.

spring definition. For further CFD model detailed on boundary conditions, turbulence model, etc., we refer to report D4.21 (Azcona et al., 2014) and Heilskov and Petersen (2016).

1.3 High fidelity CFD Simulations using FLOWer [USTUTT–IAG]

FLOWer is a compressible finite volume code. It solves the RANS equations on structured grids and has been developed by German Aerospace Center (DLR) (Kroll et al., 2000). Originally developed for aircraft purposes, it has been extended for rotating blade simulations. In this study the second order central differencing scheme JST is used for spatial discretization while an implicit dual time stepping scheme is used for discretization in time. For convergence acceleration a multigrid algorithm has been applied. In this study the Menter SST model is used for turbulence modelling.

At the Institute of Aerodynamics and Gas Dynamics FLOWer has been applied for wind turbine simulations for several years and is extended continuously specifically for wind turbine simulation requirements. The applications range from wake turbine interaction (Weihsing et al., 2014) to aeroacoustics (Lutz et al., 2015).

1.4 FLEX5 aero-hydro-elastic model [DTU]

The TLP wind turbine is implemented in the aero-hydro-elastic tool FLEX5 (Øye, 1996 and Ramachandran, 2013). The aerodynamics is modelled using unsteady Blade Element Momentum (BEM) theory and no control strategy is active in the tests, hence the rotor speed and blade pitch are constant within a given simulation. The hydrodynamic forcing is computed with the Morison equation, where the added mass and drag coefficients are first selected based on Reynolds and Keulegan-Carpenter numbers and later calibrated. The added mass matrix is taken as constant at the zero-frequency limit. The model does not include the option of additional linear hydrodynamic damping, hence the only source of damping below the waterline comes from the drag Morison term. The wave kinematics are computed with linear wave theory up to sea water level, and no stretching is applied since the hydrodynamic loads are inertia-dominated and therefore no significant effect of stretching is expected. This approach corresponds to the model labeled in this report as FLEX5 v1. For focused waves, non-linear second-order wave kinematics are used as input for FLEX5, and the label FLEX5 v2 is used in this report to refer to such model. The mooring lines are represented with four quasi-static, massless springs. Extensive FLEX5 results are reported in (Pegalajar-Jurado, 2015) and (Pegalajar-Jurado et al, 2016 (a) and 2016 (b)).

1.5 FAST aero-hydro-elastic model [NREL, CENER]

FAST, developed by the National Renewable Energy Laboratory (NREL) through U.S. Department of Energy support, is an open-source multiphysics tool practical to the engineering design of wind turbines, including both fixed-bottom and floating offshore wind turbines. For land-based wind turbine simulations, FAST has modules for wind inflow (InflowWind); aerodynamics (AeroDyn); control and electrical-drive dynamics (ServoDyn); and blade, drivetrain, nacelle, and tower structural dynamics (ElastoDyn). A new structural-dynamics module (BeamDyn) enables the modeling of advanced aeroelastically tailored blades. Additional FAST modules support offshore multimember substructures (SubDyn), hydrodynamics (HydroDyn), mooring statics and dynamics (MAP++, MoorDyn, FEAMooring), and sea-ice dynamics (IceFloe, IceDyn).

AeroDyn models the rotor wake/induction using quasi-steady Blade-Element/Momentum (BEM) theory, with corrections for high induction, hub- and tip-loss, and skewed wake. The blade airfoil aerodynamics can be steady or unsteady, the latter accounting for flow hysteresis via the Beddoes-Leishman model, including unsteady attached flow, trailing-edge flow separation, dynamic stall, and flow reattachment. AeroDyn also includes models for the influence of the tower

on the wind local to the blade and wind loads on the tower. HydroDyn provides multiple approaches for calculating the hydrodynamic loads on a structure: a potential-flow theory solution (1st or 2nd-order), a strip-theory solution, or a hybrid combination of the two. HydroDyn can either read in measured wave signals or generate waves analytically for finite depth using first-order (linear Airy) or first- plus second-order wave theory with the option to include directional spreading. In future versions, wave stretching will also be available.

For the validation against data for the semi-submersible in Chapter 2, FAST 6 has been used. In this version, member-level viscous damping was not available, but was implemented manually by CENER. A new FAST 8 version has been released, including nonlinear hydrodynamics, but version 6 has been used in Chapter 2, because CENER's modules had not been coupled to version 8 yet.

Version 8 of FAST was used to model the TLP wind turbine using a strip-theory-only approach for the hydrodynamic loads. This FAST model has similar features to the aforementioned FLEX5 model for the TLP wind turbine, with the following differences: the FAST model includes the capability of introducing linear hydrodynamic damping, in addition to the damping introduced by the Morison drag term; and the mooring lines in FAST are modelled using MoorDyn, which includes gravitational and buoyancy forces on the tendons, as well as mooring dynamics such as mass inertia, and Morison hydrodynamic forces. A second version of the FAST TLP model was used to simulate a subset of the TLP test cases using second-order wave kinematics, hence in Chapter 3 the FAST version of the TLP wind turbine with linear wave kinematics will be referred to as FAST v1, and the FAST model with second-order wave kinematics will be labeled FAST v2. No stretching was applied in any of the two FAST models for the TLP wind turbine.

1.6 Simplified Low-Order Wind Turbine Model (SLOW) [USTUTT-SWE]

As additional model in this report the simplified SLOW model is shown. It is useful to understand the main system dynamics with a very low computational effort. It is commonly used for conceptual and controller design.

The model developed at the University of Stuttgart is a reduced-order model, integrated in Matlab/Simulink with a modular structure and symbolic equations of motion. The work on the model started in 2012 with the objective of standalone symbolic equations (the whole right-hand side of the ordinary differential equation is not set up step by step as numeric values but is available in the program code directly in terms of symbolic variables). This has first the advantage of computational speed but it is also straightforward to implement the equations in other environments like real-time systems for model-based control. The nonlinear symbolic equations can be linearized for linear system analysis. The tool started with Newton-Euler equations for rigid bodies linked by spring-damper elements and Morison Equation for hydrodynamics, quasi-static mooring lines and "actuator-point aerodynamics", see (Sandner, Schlipf, Matha, Seifried, & Cheng, Reduced Nonlinear Model of a Spar-Mounted Floating Wind Turbine, 2012). It has been improved compared to INN WIND.EU D4.24, (Azcona, et al., 2014) to account for flexible bodies and is coupled to the AeroDyn-BEM model by NREL. It has been applied for fast design load calculations (Matha, Sandner, & Schlipf, 2014), as internal model for linear and nonlinear model-predictive control (Lemmer, Raach, Schlipf, & Cheng, 2015), (Schlipf, Sandner, Raach, Matha, & Cheng, 2013) and for controller design of floating wind turbines in (Sandner, Schlipf, Matha, & Cheng, Integrated Optimization Of Floating Wind Turbine Systems, 2014). The latter is an important driver for the present work: With the wave excitation "disturbance" transfer function the dynamics from the input wave height to the system output, like e.g. tower bending is known and can be incorporated the design of the controller for optimal disturbance attenuation.

More details on the validation of the SLOW model with the experiments described here can be found in (Mayer, 2016).

The different submodels will be shortly introduced for the reader to understand the basic assumptions in the next sections.

Figure 1 shows a sketch of the reduced-order structural model. It is a multibody model, which is based on the assumption of a large rigid-body reference motion together with small elastic deformations. If no flexible bodies are involved the rigid-body system consists of point-mass bodies coupled with spring-damper elements. The equations of motion consist of Newton's second law for translational motion and Euler's law for rotational motion for each of the different bodies and thus, no conservation of energy is applied as in Lagrange's principle, but the momentum equations are set up directly.

An input file for setting up the equations of motion includes the position vector to the center of mass of each body in inertial coordinates and the angular velocity vector based on the generalized coordinates. Also the point mass properties as mass and inertia tensor are necessary. In this work the equations of motion have been set up for five DOFs in 2D: Four rigid DOFs as platform surge x_p , platform heave z_p , platform pitch β_p and the rotor speed Ω and the elastic tower fore-aft deformation x_t .

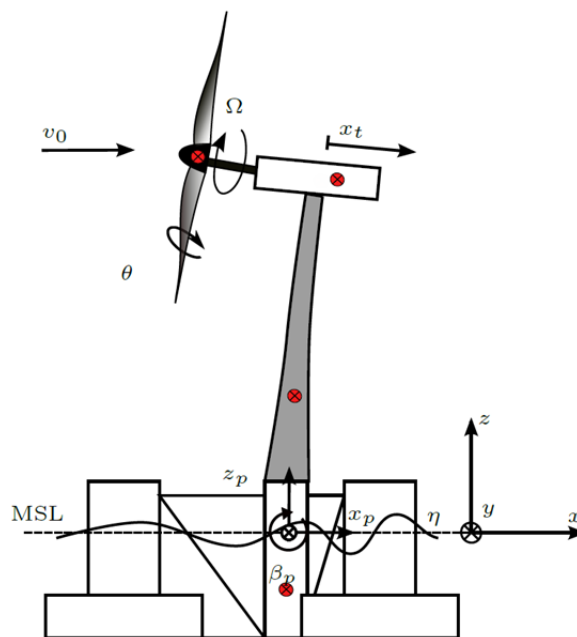


Figure 1 - SLOW model topology.

The aerodynamic forces are approximated here using the global rotor power- and thrust coefficients. These are previously calculated with a BEM model for the operating range of blade-pitch angles and tip-speed ratios (TSR). Wind shear and azimuth-dependencies as well as any dynamic effects (dynamic inflow, dynamic stall) are not accounted for. Nonetheless, the model is beneficial for this validation exercise as it can represent the basic dynamic properties like the steady states. Detailed models can then be used for an analysis of advanced load effects after the basic properties are confirmed. This has been done within USTUTT before the CFD calculations presented later in this report were done.

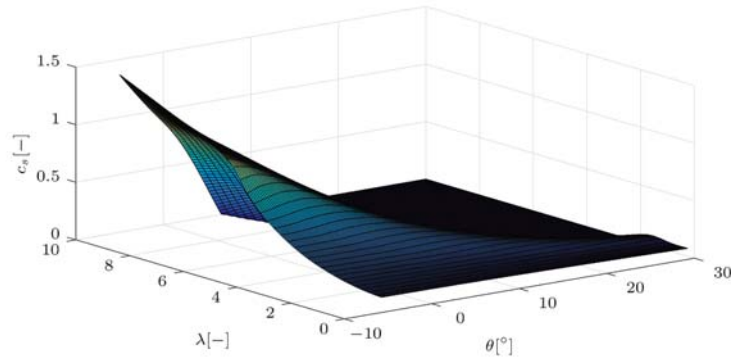


Figure 2 – Aerodynamic thrust coefficient of the scaled rotor used in SLOW.

The hydrodynamic model uses constant hydrodynamic coefficients for the added mass and damping.

$$(\mathbf{M} + \mathbf{A}(\omega_c))\ddot{\xi} + \mathbf{B}(\omega_c)\dot{\xi} + \mathbf{C}\xi = \mathbf{F}_{exc}(t) \quad (1)$$

Consequently, no radiation memory effects are implemented and the added mass is not frequency-dependent but interpolated at the eigenfrequency of the respective mode. Morison equation is implemented but has not been enabled for the simulations presented here. Linear damping coefficients have been used with values derived from free-decay experiments. The wave excitation force is calculated based on the results of a panel code. The wave excitation force in time-domain results from an inverse Fourier transform of the wave spectrum multiplied with the frequency-dependent wave excitation force vector (force-RAO) of the panel code.

The scaled platform is moored by three catenary lines that are anchored on the seabed. The differential equation for a stationary line is solved analytically. According to (Jonkman, 2007) the resulting nonlinear system of equations for the horizontal displacement x_F and the vertical displacement z_F of the fairleads with the corresponding horizontal force H_F and the vertical force V_F has the form

$$\begin{aligned} x_F &= f(H_F, V_F) \\ z_F &= f(H_F, V_F). \end{aligned} \quad (2)$$

Applying a numerical solver, the forces on the fairleads can be obtained for various displacements x_F and z_F . Eventually, a function interpolates this data and returns the external forces on the platform body during runtime. Figure 3 shows the force-displacement lookup table.

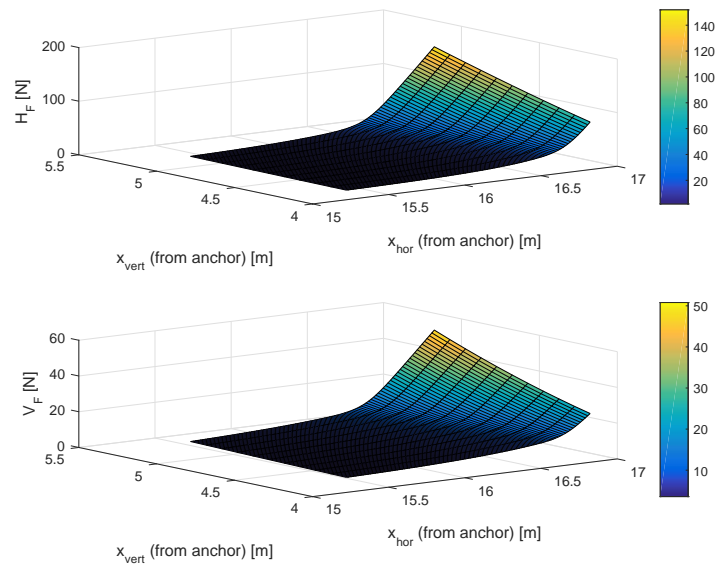


Figure 3 – Quasi-static mooring line forces of the scaled chains used in SLOW.

1.7 Coupled multibody model for floating offshore wind turbines (SIMPACK) [USTUTT-SWE]

The multibody software (MBS) SIMPACK is a commercially available simulation code, developed for general purpose usage in different industry sectors such as automotive, railway, aerospace and energy science. For the simulation of a floating wind turbine system the simulation code can be extended by using different user-specific subroutines for the modeling of the aerodynamics, hydrodynamics and mooring line dynamics. Therefore, various different load case scenarios can be investigated since the code is easy adaptable with these user-specific subroutines.

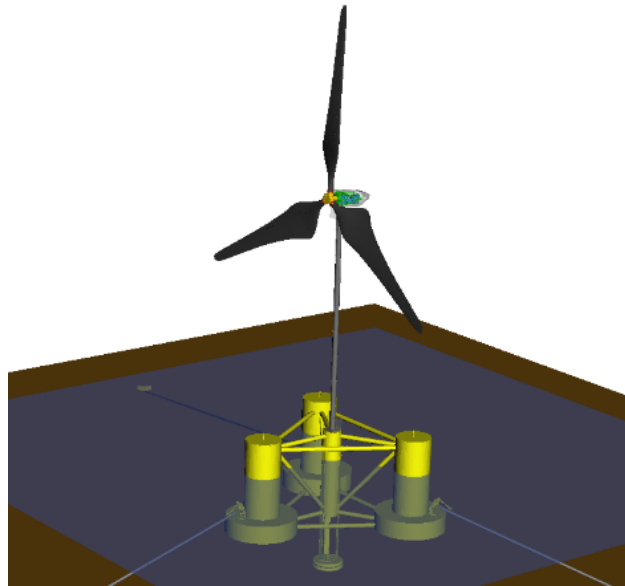


Figure 4 – Topology of the scaled SIMPACK model.

The MBS code permits the usage of a variable number of degrees of freedom (DOFs). Beside the utilization of rigid bodies also flexible bodies can be used. The modeling of the aerodynamics is done by the AeroDyn-Module of NREL, which is based on the blade element momentum theory (BEM), in which different correction factor models as e.g. Prandtl tip/hub loss, dynamic stall models can be implemented. The hydrodynamic forces in the MBS are calculated using the HydroDyn Module of NREL. In a precomputation step the frequency-dependent added mass, damping and the diffraction forces as well as the hydrostatic restoring matrix and the displaced water volume of the overall system has been calculated with the panel code algorithm in ANSYS AQWA. The hydrodynamic coefficients are then used by the HydroDyn module. As an update to the version described in INN WIND.EU D4.24, (Azcona, et al., 2014), the mooring lines are here modelled using the quasi-static mooring line analysis program MAP++, which is also coupled to the MBS and is interfaced with the main code at each time step.

More details on the validation of the model with the experiments presented here can be found in (Koch, Lemmer, Borisade, Matha, & Cheng, 2016) and (Koch, Validation of a reduced-order model of a floating wind turbine with experiments, 2016).

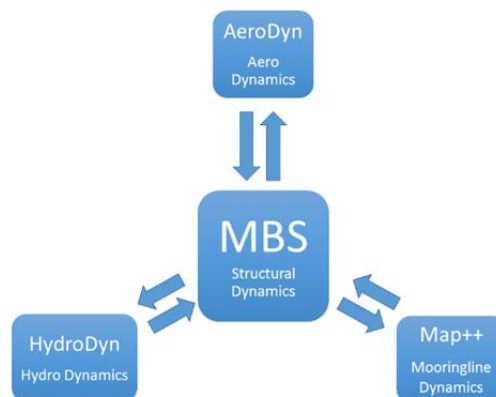


Figure 5 – Submodels of the scaled FOWT of the SIMPACK model.

The different bodies in the MBS are connected using joints of different complexity, which allows utilizing different types of force elements. These force elements can be implemented in such way that they are acting in the inertial system on the bodies (such as e.g. the forces on the rotor due to aerodynamics, forces out of the hydrodynamics on the platform) or between the bodies (e.g. spring damper elements). Different bodies can be connected using joints with different types of force elements acting from the inertial system on the bodies (e.g., aerodynamics on the rotor, hydrodynamics on the support structure) and between bodies (e.g., spring-damper elements).

Beside rigid bodies also flexible bodies can be modelled inside the MBS. Commonly the tower as well as the blades is modelled as flexible bodies. However in this deliverable the blades are considered as rigid bodies. This simplification seems reasonable because of the fact that due the construction for the low Reynolds conditions of the blades these are stiff and therefore relative deflections of the blades are small compared to a rigid body.

For the tower the beam theory is applied, beside Euler-Bernoulli also Timoschenko equation can be used or geometrically nonlinear beams. Here, the tower is discretized with 10 equally spaced nodes of the tower length Timoschenko beam theory.

Blade-element momentum theory (BEM) is used for the scaled SIMPACK model. AeroDyn v13 of NREL, (NREL, NWTC Information Portal (AeroDyn). <https://nwtc.nrel.gov/AeroDyn>. Last modified 27-July-2016 ; Accessed 10-October-2016 , 2016) is officially coupled in the commercial SIMPACK wind program. A difficulty of using the rather simple BEM method for this scaled experiment is that flow separation occurs not only at the hub and the root as for a full-scale turbine but, due to the low Reynolds numbers in the experiment also at other span-wise locations of the blade. Here, polars based on XFOIL (Drela, 2016), calculated by POLIMI, who built the scaled rotor are used. The only activated correction models are Prandtl's hub loss and tip loss models, no dynamic stall model is enabled. The time-step for the aerodynamic calculations is set to 0.01s, according to the SIMPACK time-step. The value for the tolerance of iterations is ATOLER=0.005. The results of the aerodynamic model compare generally well with the measurements but the CFD calculations by USTUTT-IAG presented later show a higher accuracy.

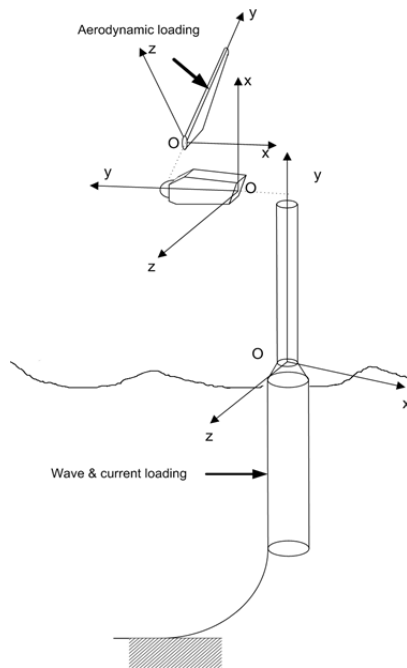
A pre-processing of the hydrodynamic coefficients is done using the panel code ANSYS AQWA (Ansys, 2013). SIMPACK is coupled to the hydrodynamic module HydroDyn of NREL, (NREL, NWTC Information Portal (HydroDyn), 2016). Within the module a frequency-to-time-domain conversion is done in order to use the frequency-domain results of the panel code for the transient time-domain simulation. Cummins equation is used with the convolution integral representing the radiation memory effects.

The MAP++ Module of NREL (NREL, NWTC Information Portal (MAP++). , 2016) is added to the MBS using a new user force. During the simulation in every time step the main code and the MAP++ code are executed to obtain the quasi-static forces of the scaled chains on the fairleads for each line. The MAP++ code has the advantage that the definition of the mooring system is very flexible and, e.g., also connectors can be simulated. Dynamic effects, however, are not included as opposed to the hGAST code by NTUA which is presented next.

1.8 Coupled multibody model for floating offshore wind turbines (hGAST) [NTUA]

NTUA is participating in WP4 with hGAST (Manolas,2015) an in-house developed software designed to perform time domain simulations for the complete wind turbine system. hGAST is modular comprising:

- The 'dynamic module' that defines the dynamics of



the whole system

- The “structural module” that provides the deformed shape and the associated kinematics defined for each separate solid component of the machine
- The “aerodynamic module” that provides the aerodynamic loads along the rotor blades
- The “hydrodynamic module” which provides the wave & current loading on the support structure (monopile, jacket or floater)
- The “mooring module” which provides the geometry of the mooring line as well as the associated loads
- The “servo-module” which defines the torque and the blade pitch angle demands based on the calculated rotational speed and mean pitch angle.

The modular definition in hGAST accommodates various options for the physical modelling associated to a specific module. A brief description of the available options is given next.

The dynamics of the complete system is formulated in the framework of multi-body dynamics including the control equations together with their associated degrees of freedom, in fully coupled mode. At points of connection (junctions), the constraints or connection conditions of the relevant numerical bodies (which correspond to either a physical component of the wind turbine or part of its division in sub-bodies as done for example for the blades) correspond to kinematic and loading matching.

All structural modelling is based on beam theory and the FEM approximation. All components are modelled by one or several beams with appropriate connections.

- Timoshenko beam modelling (for the blades, the drive train, the tower, the members of the support structure either floater or jacket)
- Truss element modelling (for the mooring lines)

Bending in two directions, shear, tension and torsion are included as degrees of freedom.

Note: Large displacements and rotations are taken into account by sub-body partitioning which consists of dividing a component in a number of beam parts non-linearly connected.

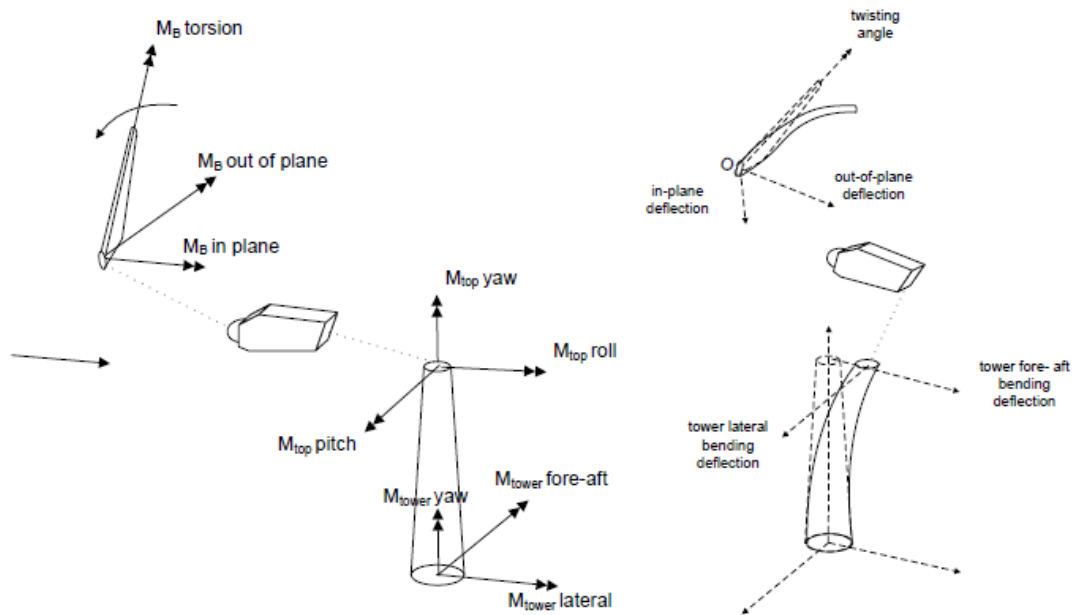


Figure 6: The multi-body definition of a wind turbine and the coupling principle. Each main component is modeled separately. At the connection points (e.g. the tower top, the blade roots) amongst the connected bodies one is defined as the component providing displacements and rotations while all others provide back the loads. The “dynamics” module in hGAST accommodates rigid body motions as well control equations.

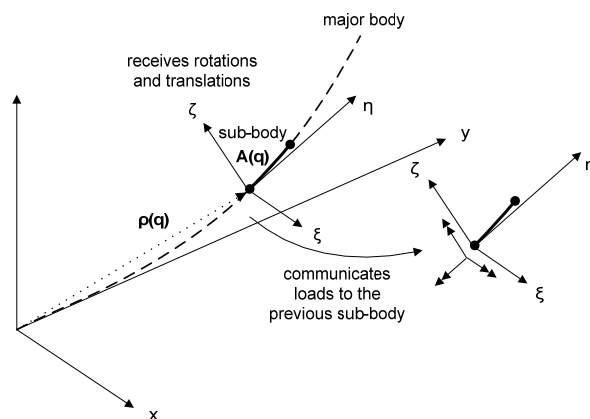


Figure 7: In the sub-body partitioning of a true component (e.g. the blade), every sub-body is introduced within the context of multi-body dynamics. At the connection points between sub-bodies kinematic and dynamic continuity act as boundary conditions. Thus a specific sub-body by cumulatively receiving the deformations of the previous sub-bodies, will have in its dynamic equations the terms that correspond to large displacements and rotations.

Two aerodynamic methods are available in a fully coupled aeroelastic context.

a) A BEM model (RAFT).

RAFT follows the usual guidelines of BEM modelling. It contains: root and/or tip losses correction, 3D correction of the 2D polars (if not included already in the tables), a cylindrical wake model to account for skewed inflow (yaw, inclination), a dynamic inflow model and ONERA model to account for shed vorticity effects and dynamic stall.

b) A free-wake 3D model using vortex particle dynamics (GENUVP).

GENUVP (Voutsinas, 2006) combines a panel representation of the solid surfaces with a vortex particle approximation of the wake. Solid surfaces can take one of the following representations: non-lifting bodies represented by sources (the tower), open lifting surfaces carrying dipoles and shedding vorticity along their edges (blades, tower of downwind machines), closed lifting surfaces carrying sources and dipoles (thick blades). The evolution of the wake is followed in the Lagrangian formulation of the vorticity including convection and deformation.

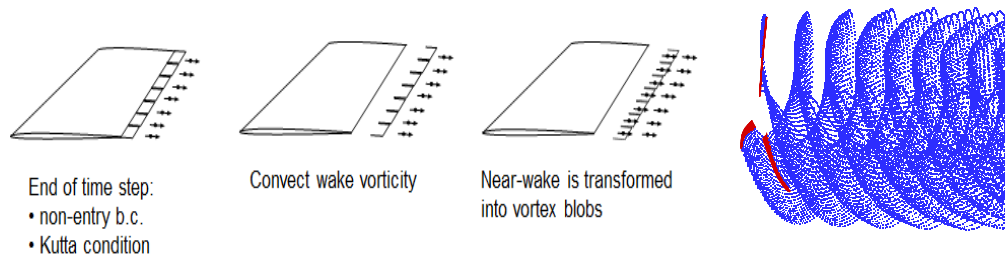


Figure 8: The surface singularity intensities are determined using the non-entry boundary conditions and the pressure Kutta along the emission lines. Upon convection, the surface vorticity of the recently released wake is transformed into vortex particles which are subsequently followed as fluid particles (as shown in the last plot on the right).

Loads are calculating using the pressure distribution obtained directly from the flow solver. An a posteriori viscous correction is applied using 2D tabulated polars. The correction is based on the estimation of an effective angle of attack and an effective relative velocity. The effective angle of attack is obtained from the potential load calculation assuming that the potential force per strip corresponds to lift. The effective relative velocity is taken as the average per strip relative surface velocity.

GENUVP is also using the ONERA model for correcting the potential loads with the following particularity: instead of the so called “attached” part in the ONERA model, the potential loads are retained. So the correction is restricted to the “separated” part which corresponds to the purely viscous contribution.

Special cost reduction techniques such as tree algorithms for the solution of the integral equation associated to the panel part of the model (Figure 9) and multi-block Particle Mesh solution of the Poisson equation associated to the evolution of the wake (Figure 10).

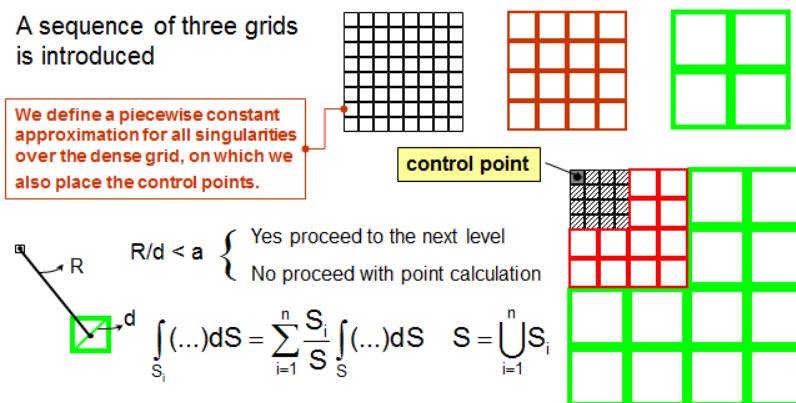


Figure 9: Tree-algorithm is used evaluating panel integrals. To this end a sequence of surface grids are introduced. Each grid level is produced by that of the previous level by regular partitioning. The choice of level is decided based on the ratio of the distance over the panel surface. As the evaluation point approaches the solid surface the tree algorithm moves from coarser to finer grids. The saving achieved decreases the cost from being $\sim N^2$ to $N \cdot \log N$. In this way very large surface grids can be accommodated.

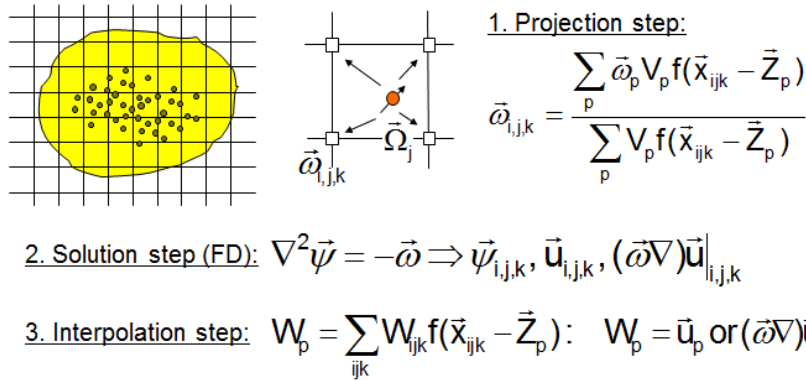


Figure 10: Outline of the PM method. The PM method is used instead of the Biot-Savart law and concerns the particle-to-particle interactions. Using a fast Poisson solver it is possible to obtain the velocity and deformation induced by the wake over the entire flow field. The Poisson equation for the vector potential is solved with exponentially decaying far field conditions. To this end the vorticity carried by the particles is projected on a Cartesian grid. The projection functions are constructed to conserve all moments of vorticity up to a certain order which also defines the accuracy of the approximation. In GENUVP up to 3rd order projection functions are available. The flow information from the grid is back interpolated to the particles using the same functions

In cases of long runs (10min or more), a further reduction is accomplished by the hybrid wake approximation (Figure 11) .

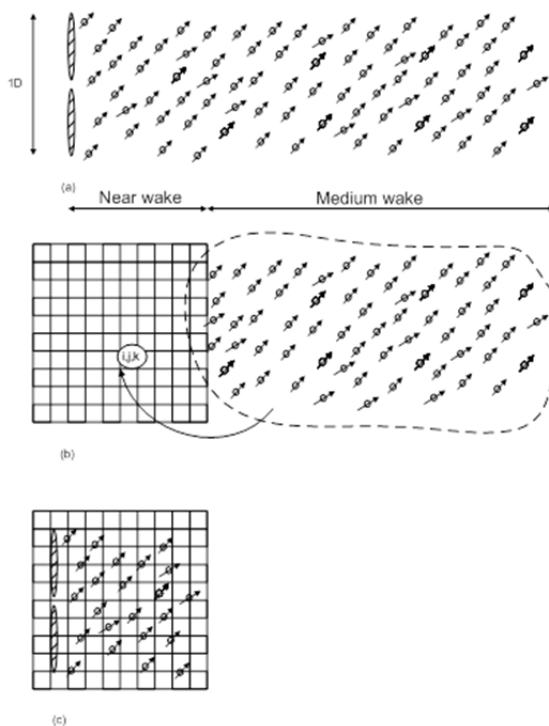


Figure 11: Schematic description of the hybrid wake approximation.

The hybrid wake is suitable when the main interest is in the rotor region. The basic idea is that the medium wake region contains the starting vortex and that its further evolution in time and its effect in the rotor and near wake regions will remain the same and at most periodic. This has been verified with numerical tests. The near wake covers a space of $\sim 2 D$ in length while the medium wake extends another $\sim 2 D$. Once the space specified for the medium wake is covered by the wake, the effect of this part on the PM grid covering the rotor and near wake region is calculated and stored. All subsequent computations are restricted up to the near wake. As the simulation proceeds, the particles that exit the near wake region are discarded. In this way the cost of the wake evolution is kept to a reasonable level. In fact the application of the hybrid wake approximation allows performing long full aeroelastic simulations with turbulent wind inflow as defined in the IEC.

There are two options for calculating the wave and current loading:

a) Potential theory.

The default option in this case is to solve the linear hydrodynamic problem (diffraction/radiation) in the frequency domain and thereby obtain the hydrodynamic operators (added mass, added damping and excitation) needed in the dynamic equations of the floater rigid body degrees of

freedom. The problem is solved in integral form and uses surface grids on which piecewise constant source distributions are defined. The wave kinematics are defined based on Airy theory,

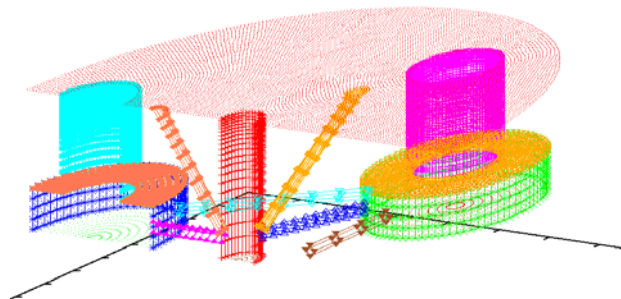


Figure 12: Surface grid for the OC4 semi-submersible floater defined within IEC Annex 30

b) Morison's equation.

Application of Morison's equation provides a fast way to introduce the hydrodynamic loads, also accounting for the viscous drag. It is the default option for bottom based support structures and an alternative option for floaters. The wave kinematics is defined based on Airy theory or stream function theory.

The moorings are modelled by the so called "dynamic mooring line model" defined in the FEM context. The mooring line is modelled as a series of truss elements (elements only transferring axial loads) with the possibility to also accommodate buoys as lumped masses. The interaction with the sea bed is modelled by a series of springs which are activated once the mooring line approaches the sea-bed surface. Gravitational, inertial, hydrostatic and hydrodynamic loading (using Morison's equation) is applied on the elements.

A variable speed/variable pitch controller can be considered either defined by external subroutines or Dynamic Link Library (DLL) files, in most cases corresponding to linear control elements (PID) and additional filters.

Time integration in hGAST is carried out in the so-called incremental context. The equations are linearized with respect to the most current solution and solved for the incremental correction. In each time step an iterative procedure is followed until the incremental correction converges to a predefined error bound.

Linearization is part of the software and besides assisting in time integration, offers the possibility to perform linear stability analysis in combination with Coleman's transformation (Riziotis et al., 2010).

In non-symmetric but still periodic cases, Floquet's theory should be applied. Due to its high computational cost, in this case the analysis is carried out with respect to a reduced order model.

1.9 BLADED aero-hydro-elastic model [GL-RC]

For the simulation of a 1:60 scaled tank test model of the INNWINN.D.EU 10MW floating tension leg platform the simulation code **Bladed for Windows version 4.7** has been applied. Bladed is a widespread, commercial wind turbine simulation code developed by Garrad Hassan. It was originally designed for the simulation of onshore wind turbines using a cantilevered tower base. The code has been further developed during the last years and allows the calculation of offshore bottom fixed as well as floating wind turbine structures in the time domain with its fully coupled aero-hydro-servo-elastic simulation code.

Wind turbine structural model:

Structural dynamics in Bladed are modelled as a non-axisymmetric support structure where the modes are three-dimensional and contain all six degrees of freedom (DOF) at each node.

Since Bladed considers a multi-member tower structure, a local member coordinate systems is introduced at each element of the construction. The x-axis is set along the member, starting at end 1 and pointing towards end 2. The y-axis can have two different orientations, but will always lie in the horizontal plane of the brace. The z-axis is orientated perpendicular to the x-y-plane, spanning a right-handed coordinate system.

Additionally to the multi-member coordinate system, Bladed sets an output convention for loads and deflections. While deflection output is according to the global GL coordinate system in (GL Rules and Guidelines, 2012), loads are output with reference to the local member coordinate system. As the member's x-axis is aligned along the member axis, the z-axis is perpendicular to the x-axis and defined by the cosines of the z-axis in reference to the global coordinate system. These cosines can be checked in the tower section of Bladed.

In Bladed the support structure (as well as the blades) is modelled by single linear flexible components using the modal approach. The deformation is represented by a linear combination of pre-calculated mode shape functions. The modal amplitudes are the scalars of this linear combination representing the generalized strains and therefore the degrees of freedom for the component. The generated mode shape functions are constant over time but vary spatially. The mode shape functions for flexible components are calculated by a fundamental structural model based on standard linear finite element technique. This means, that the actual deformation of the component is considered to be rather small. The underlying finite element model assumes the structure as linear space, see (Garrad Hassan & Partners, Bladed Theory Manual, 2015).

The applied beam element can be considered as an extended version of a Timoshenko beam element (standard three-dimensional beam element) with nodes at each of the two ends of the beam. The element has a total of twelve degrees of freedom: three translational and three rotational DOF, for each of the two nodes. The deflection is calculated at all intermediate points.

Axial, shear, and bending stiffness, as well as torsional rigidity are not necessarily constant over the length of the beam. The dimensions (diameter and wall thickness) of the modelled tube can change along the element. The resulting stiffness matrix is constant over time and calculated by numerical integration. An advantage of this method is, that certain DOF can be constrained (e.g. when elongation can be neglected) by a constant constraint matrix and Lagrange's method).

For the connection of elements, the nodes are subdivided into boundary stations that couple to other components. In order to prevent rigid body displacement modes, the proximal node (node in the centre of the structure, in case of the TLP Bladed model the proximal node is the floater base node at the connection point to the spokes) is completely constrained. Two kinds of modes are generated with this method, attachment modes and normal modes.

- Attachment modes, which may couple to other components, are calculated from the components stiffness matrix by a static equilibrium, where the component is fixed at the proximal node and loads are applied in turn at the distal nodes.
- Normal modes, which may be considered as internal vibration modes, are calculated from the mass and stiffness matrices by a generalized eigenvalue problem, where the element is fixed at all boundary stations.

The modes of tower and blades are calculated internally before each simulation. The number of modes as well as damping factors for each mode can be set beforehand. The modal analysis output consists of the frequencies of the modes as well as generalized mass and stiffness properties. Bladed calculates the generalized mass matrix and generalizes stiffness matrix during the modal analysis, by transforming the mass and stiffness matrices of the component, using the normalized mode shape matrix.

Aerodynamic Model:

When calculating the aerodynamic forces on a rotor, with the blades moving relative to the wind, it is common practice, to divide the blade in a finite number of elements. The aerodynamic forces (contributing to the driving torque of the rotor as well as the thrust on the rotor) are then calculated for each segment and finally summed up. This Blade Element Momentum Theory is applied as the aerodynamic load modelling in Bladed. This commonly used method for rotary-wing systems discretizes the rotor disk into annular regions, solving the momentum balance for each segment and is implemented in Bladed similar to beforehand described simulation codes FLEX5, FAST, SLOW or hGAST, see also (R. Gasch and J. Tvele, Wind Power Plants Fundamentals, 2012).

For steady-state conditions, a dynamic stall model considers the dynamic response of a flexible rotor to an unsteady inflow, e.g. during operational conditions. Dynamic inflow accounts for unsteady flow conditions. In this case Bladed recalculates the inflow factors at given intervals, however not at every instant in time. This option is recommended for the simulation of the parked turbine.

For the wind turbulence Bladed offers the options of modelling the wind field by following options:

- No variation: constant wind speed and direction
- Single point history: setting a time history of wind speed and direction which is coherent over the rotor area
- 3D turbulent wind: setting a wind file with a 3-dimensional turbulent wind field (as shown in Figure 14 the wind “volume” passes through the plane of the turbine in x -direction as time passes)
- Transients: using sinusoidal wind speed and direction as defined by some standards [2] (deterministic wind models)

Hydrodynamic Loads Modelling in Bladed:

When handling with the hydrodynamic loading in Bladed, it is possible to choose from three options. These are calculating the hydrodynamic forces by either Morison’s equation or BEM Hydrodynamics with or without Morison drag.

- Morison’s Equation: Bladed calculates all forces on structural elements using Morison’s equation. Buoyancy and wave dynamic pressure forces are being calculated by integration of pressure forces on each of the members.
- BEM Hydrodynamics: The wave induced forces as well as buoyancy is being set by BEM hydrodynamics definition. It is therefore necessary to provide this BEM definition for all structural members, which face hydrodynamic loading. Bladed calculates the loading from incident waves, diffraction, radiation, and hydrostatics from coefficients that need to be provided and calculated pre-processed by a linear BEM (Garrad Hassan & Partners Ltd, Bladed User Manual, 2015).

It shall be mentioned that the standard for Floating Wind Turbines DNV-OS-J103 allows three options: 1) modelling the floater as a slender structure and calculating the loads by Morison, 2) modelling the structure as a three-dimensional diffraction body (BEM) or 3) using a combination of both. Each of the methods has its disregards. While Morison neglects radiation and diffraction, the potential theory (which BEM is based on) does not account for viscous drag. So either method will not predict the wave loads fully correct, as described in (DNV, Design of Floating Wind Turbine Structures, 2013 and DNVGL, Structural design of TLPs - LRFD method, 2015).

Mooring Lines Model:

In Bladed generally the mooring lines are included through non-linear force-displacement relationships. The resulting forces from the defined relationship are applied to the translational and rotational platforms degree of freedom. Bladed offers three types of mooring to be defined:

- Catenary moorings
- Tension leg moorings
- 2D lookup moorings

Catenary and tension leg moorings are defined similar to bottom fixed foundations by stiffness, damping, and mass matrices. 2D lookup moorings are handled by a force/displacement lookup table which is pre-processed separately and then used as underlying data.

In the case of the TLP model, Bladed allows the assignment of a nominal pre-tension for the tendon line, as well as longitudinal and torsional stiffness and damping values of the tendons. Note that the actual line tension, which emerges when an equilibrium state is set, is still influenced by the submerged volume. The total tendon tension only depends on the difference between buoyancy force and the weight force of the TLP platform (note that a strain of the tendons and the changing buoyancy due to the elongation is neglected). Further details regarding Bladed features and peculiarities for modelling TLP floating wind turbines can be found in (Starr, Structural Analysis of Tension Leg Platforms for Floating Wind Turbines, 2016).

1.10 REFERENCES

- Azcona, J., Bekiropoulos, D., Bredmose, H., Fischer, A., Heilskov, N.F., Krieger, A., Lutz, T., Manjock, A., Manolas, D., Matha, D., Meister, K., Pereira, R., Ronby, J., Sandner F. and Voutsinas, S. D4..21: State-of-the-art and implementation of design tools for floating structures. INNWIND.EU. 2014.
- Azcona, J., Lemmer, F., Matha, D., Amann, F., Bottasso, C. L., Montinari, P., Chassapoyannis, P., Diakakis, K., Voutsinas, S., Pereira, R., Bredmose, H., Mikkelsen, R., Laugesen, R. and Hansen, A. M. D4.2.4: Results of wave tank tests. Description of Floating Wind Model Tests at ECN and DHI. INNWIND.EU. 2016.
- Berberovic E, Van Hinsberg NP, Jakirlić S, Roisman IV, Tropea C. (2009) *Drop impact onto a liquid layer of finite thickness:dynamics of the cavity evolution*. Physical Review E Statistical, Nonlinear, and Soft Matter Physics 79(3):1–15. Art.no: 036 306.
- Heilskov, N.F., Petersen, O.S.: Comparison of Non-linear model of a floating wind turbine against wave tank tests, OMAE 2016.
- Higuera, P., Lara, J.L. and Losada, I.J. (2013). *Realistic wave generation and active wave absorption for Navier–Stokes models*. Application to OpenFOAM. Coastal Engineering
- Jasak, H. (2009) *Dynamic Mesh Handling in OpenFOAM*, 48th AIAA Aerospace Sciences Meeting, Orlando, Florida.
- Jasak, H. and Tukovic, Z. (2010) *Dynamic mesh handling in OpenFOAM applied to fluid-structure interaction simulations V* European Conference on Computational Fluid Dynamics, ECCOMAS CFD, Lisbon, 14-17 June
- Jonkman JM. Dynamics of Offshore Floating Wind Turbines - Model Development and Verification. Wind Energy 2009; **12**:458–492.
- Koch, C., Lemmer, F., Borisade, F., Matha, D., & Cheng, P. W. (2016). Validation of INNWIND.EU Scaled Model Tests of a Semisubmersible Floating Wind Turbine. ISOPE.
- Kroll, N, Rossow, CC, Becker, K and Thiele, F (2000). "The MEGAFLOW project," Aerosp. Sci.Technol. 4(4), 223–237
- Azcona, J., Lemmer, F., Matha, D., Amann, F., Campagnolo, F., Bredmose, H., et al. (2014). *INNWIND.EU D4.24: Floating Wind Model Tests Ecole Centrale de Nantes 2014*. Tech. rep., INNWIND.EU
- Lemmer, F., Raach, S., Schlipf, D., & Cheng, P. W. (2015). Prospects of Linear Model Predictive Control on a 10MW Floating Wind Turbine. *Proceedings of the ASME 34th International Conference on Ocean, Offshore and Arctic Engineering*. St. John's/Canada
- Lutz, T, Arnold, B, Bekiropoulos, D, Illg, J, Krämer, E, Wolf, A, Hann, R and Kamruzzaman, M (2015). „Prediction of Flow-Induced Noise Sources of Wind Turbines,“ accepted for publication in: Special Issue of the International Journal of Aeroacoustics, 2015.
- Matha, D., Sandner, F., & Schlipf, D. (2014). Efficient critical design load case identification for floating offshore wind turbines with a reduced nonlinear model. *Journal of Physics: Conference Series* , 555
- Manolas, D., 2015. "Hydro-aero-elastic analysis of offshore wind turbines," PhD Thesis, NTUA, Athens
- Mayer, B. (2016). *Validation of a reduced-order model of a floating wind turbine with experiments*. University of Stuttgart
- Papadakis, Giorgos. "Development of a hybrid compressible vortex particle method and application to external problems including helicopter flows." NTUA, PhD Thesis, Athens (2014).

Pegalajar-Jurado A, Bredmose H, Borg M. Multi-level hydrodynamic modelling of a scaled 10MW TLP wind turbine. *13th Deep Sea Offshore Wind RD Conference, EERA DeepWind2016*, Elsevier: Trondheim, 2016 (a).

Pegalajar-Jurado A. Numerical reproduction of laboratory experiments for a TLP wind turbine. MSc thesis, DTU Wind Energy. Kgs. Lyngby, Denmark, 2015.

Pegalajar-Jurado A, Hansen AM, Laugesen R, Mikkelsen RF, Borg M, Kim T, Heilskov NF, and Bredmose H. Experimental and numerical study of a 10MW TLP wind turbine in waves and wind. *TORQUE Conference*, Munich, 2016 (b).

Riziotis, V.A., Voutsinas, S.G., Politis, E.S., Chaviaropoulos, P.K., 2010 "Stability analysis of parked wind turbine blades using a vortex model," *Proceedings of the Science of Making Torque from the Wind Conference*, Heraklion, Greece, June 28-30, 2010.

Ramachandran, GKV. A numerical model for a floating TLP wind turbine. PhD thesis, DTU Wind Energy. Kgs. Lyngby, Denmark, 2013.

Sandner, F., Schlipf, D., Matha, D., & Cheng, P. W. (2014). Integrated Optimization Of Floating Wind Turbine Systems. *Proceedings of the ASME 33rd International Conference on Ocean, Offshore and Arctic Engineering*. San.

Sandner, F., Schlipf, D., Matha, D., Seifried, R., & Cheng, P. W. (2012). Reduced Nonlinear Model of a Spar-Mounted Floating Wind Turbine. *Proceedings of the German Wind Energy Conference DEWEK*. Bremen

Schlipf, D., Sandner, F., Raach, S., Matha, D., & Cheng, P. W. (2013). Nonlinear Model Predictive Control of Floating Wind Turbines. *Proceedings of the Twenty-third International Conference on Offshore and Polar Engineering (ISOPE)*, (pp. 440-447).

Voutsinas, SG, 2006. "Vortex Methods in Aeronautics: How to make things work," *International Journal of Computational Fluid Dynamics*, 20 (1), 3-18.

Weihing, P, Meister, K, Schulz, C, & Lutz, T (2014). „CFD simulations on interference effects between offshore wind turbines." *Journal of Physics: Conference Series* (Vol. 524, No. 1, p. 012143). IOP Publishing.

Weller HG, Tabor G, Jasak H and Fureby C (1998) *A tensorial approach to computational continuum mechanics using object oriented techniques*, *Comput. Phys.* 12, 620.

Øye S. FLEX4 simulation of wind turbine dynamics. *Proc.*, 1996.

GL Rules and Guidelines – IV Industrial Services, Part 2 – *Guideline for the Certification of Offshore Wind Turbines*, Edition 2012

Garrad Hassan & Partners Ltd, *Bladed User Manual*, 2015.

Det Norske Veritas AS, "Design of Floating Wind Turbine Structures," DNV-OS-J103, 2013.

R. Gasch and J. Tvele, *Wind Power Plants Fundamentals, Design, Construction and Operation*, Heidelberg Dordrecht London New York: Springer Verlag, 2012.

Garrad Hassan & Partners Ltd., *Bladed Theory Manual Version 4.7*, DNV GL - Energy, Bristol, England, 2015.

DNV GL, *Structural design of TLPs - LRFD method*, DNVGL-OS-C105, 2015.

2 SEMISUBMERSIBLE VALIDATION TEST CASES

2.1 Introduction

The semisubmersible campaign consisted of four testing weeks (divided in two different time slots) at the *LHEEA - Research Laboratory in Hydrodynamics, Energetics and Atmospheric Environment* of the Ecole Centrale de Nantes (ECN) wave tank. The tests at *LHEEA* were performed between September and November 2014. A detailed description of the facility, the model, sensors and test cases can be found in INN WIND.EU D4.24, (Azcona, et al., 2014). The campaign was prepared, organized and conducted by the University of Stuttgart, CENER and Politecnico di Milano.

The scaled model tested in this campaign represents a 10MW semisubmersible floating wind turbine. As the newly developed INN WIND.EU floating platform (Task 4.3) for the 10MW wind turbine was not yet finalized at the time the scaled platform model was designed, a 10MW model was developed based on the upscaling of a 5MW model. Therefore, the campaign will allow accomplishing the objectives of the task based on a large floating wind turbine with an upscaled semi-submersible platform.

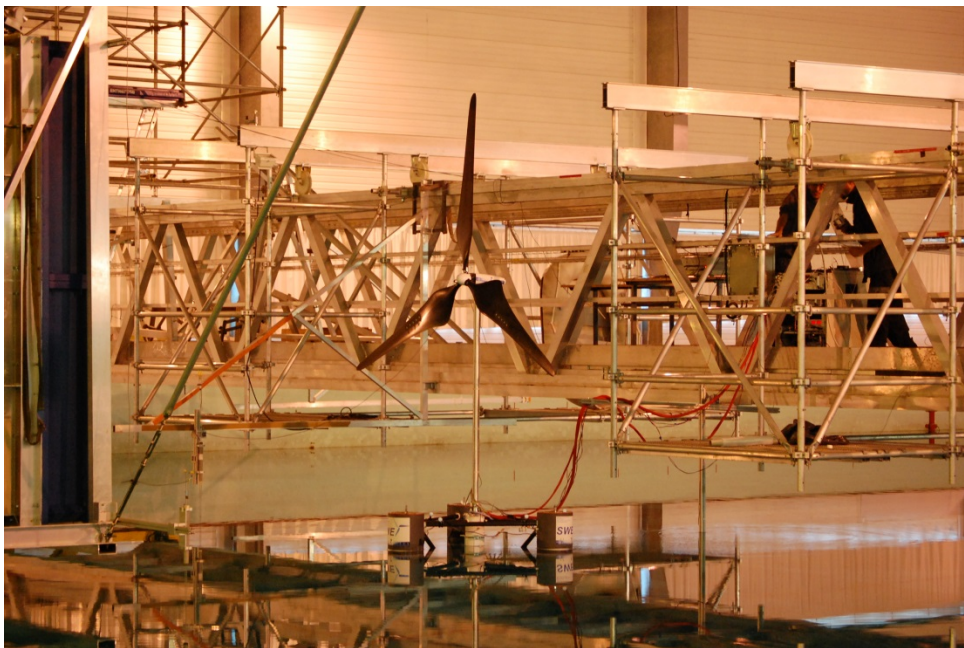


Figure 13: Semi-submersible test [Foto: H. Bredmose, DTU].

The 10MW platform model is based on the OC4-DeepCWind design (Robertson A. , et al., 2014). It is composed of a central column with structural function and three columns located at a certain distance from the platform center, one upwind and two downwind, which provide the stability of the platform. Each of these columns has a heave plate at the bottom to damp the vertical platform motion. Figure 13 shows a photo of the floating offshore substructure and wind turbine. The floating platform model was built at the University of Stuttgart and the Froude-scaled rotor at Politecnico di Milano. Additionally, a ducted fan to be mounted on the nacelle instead of the rotor has been built by CENER as a thrust actuator. The model building process and the test description has been presented in (Sandner, et al., 2015).

In this chapter, the validation of different simulation tools against these experimental data is presented. The chapter is divided into three main sections, where different validation cases and

tools are discussed. In section 2.3, integrated codes are validated with measurements of the scaled model where a Low-Reynolds rotor was used. This corresponds to the testing weeks 1 to 3. In this validation, USTUTT has participated with the SLOW code and also with SIMPACK, and NTUA has validated computations their h_GAST software. In section 2.4 CENER has validated FAST using a quasi-static model for the mooring lines and also FAST coupled with the OPASS code for the dynamic simulation of the moorings. The measurements used by CENER correspond to the scaled semisubmersible model where the SiL methodology was used to include the coupled aerodynamic rotor force, during the week four of the test campaign. Finally, in section 2.5, USTUTT has used the CFD code called FLOWer to evaluate the influence on the floating turbine behaviour of the existing wind generator setup at the ECN (Ecole Centrale de Nantes) facilities in comparison with a totally homogeneous flow.

2.2 Load cases database

The total number of load cases of the database is 110 for week 1/2 and 58 for week 3/4 (http://www.ifb.uni-stuttgart.de/windenergie/download_messdaten.en.html). For the tool validation a selection of the cases useable for system identification has been made. This selection consists of 18 load cases. Out of these the ones with the most significant findings will be presented in the following.

2.3 Validation based on the Froude-Scaled rotor model

In this section, the validation of the tools based on the experiments using the Froude-Scaled rotor model to represent the rotor will be presented.

Scaled model properties

The main scaling parameters of the model with the Froude Scaled rotor can be found in Table 1.

Table 1 – Baseline design, 10MW prototype and scaled model ideal properties

Target Property	Baseline 5MW Prototype	10MW Prototype	Scaled Model	
Overall mass, including ballast	1.41E7	3.34E7	150.39	Kg
Platform mass, including ballast	1.348E7	3.20E7	144.06	Kg
Overall CM location below SWL	9.893	13.19	0.22	m
System roll inertia about overall CM	1.13E10	4.76E10	59.64	kgm ²
System pitch inertia about overall CM	1.13E10	4.76E10	59.64	kgm ²
System yaw inertia about overall CM	1.23E10	5.18E10	64.91	kgm ²

The original OC4-DeepCwind hull shape has been modified for this test in order to account for the additional mass of the nacelle, due to actuators of the rotor. Two additional dumbbell disks were placed underneath the keel in order to achieve the same rotational steady states of the platform as of the OC4-DeepCwind platform. Details can be found in (Azcona, et al., 2014).

The scaled model mass properties were identified through pendulum tests and a detailed CAD model set up of the assembled model for a computation of the inertia tensor, see also (Azcona, et al., 2014).

The scaled rotor is a Froude-scaled applying the principle of “performance scaling”, which means that the blade is not scaled geometrically but newly designed in order to match the Froude-scaled thrust force of the DTU10MW rotor. Especially the low Reynolds number is a problem due to the low wind speeds in the experiment. For details see (Azcona, et al., 2014) and (Müller, Sandner, Bredmose, Azcona, Manjock, & Pereira, 2014).

For an easier understanding and interpretation of the results the eigenfrequency of the scaled model are compiled in Table 2.

Table 2 – Scaled model eigenfrequencies.

Degree of freedom	Eigenfrequency [Hz],
Surge	0.058
Heave	0.39
Pitch	0.23
Tower	2.60

Description of the test cases

In the following the results with the most significant findings will be shown and the differences between the models discussed. More details on the validation task can be found in (Koch, Lemmer, Borisade, Matha, & Cheng, 2016), (Koch, 2016) and (Mayer, 2016).

A subset of load cases has been selected for presentation in this report. Out of the 168 load cases of the campaign 18 cases most suitable for system identification were analysed and a selection will be presented in the following. Starting with decay tests of the floating platform, followed by wind-only and wave-only tests. The load case numbers in the following section headings correlate with the numbering of the test case database.

After the basic system identification tests the platform displacements in surge, heave and pitch direction as well as the tower-base fore-aft moments will be shown in time- and frequency domain.

The color coding in this chapter is such that the measurements are blue, the SIMPACK model (USTUTT) is purple, the hGAST model (NTUA) is green and the simplified SLOW model (USTUTT) is orange. In some cases 2nd-order wave kinematics were used for the damping term of Morison equation within SIMPACK. Here, yellow has been used for the results.

Static mooring displacement (LC96)

In the following the mooring identification cases are shown, where the platform was displaced in the measurements with a string and kept at various surge positions. The static fairlead tensions could then be compared to the simulations in order to identify the uncertainties involved in the mooring system and the fairlead sensors.

Figure 14 through Figure 17 show the three static fairlead tensions for the four different axial displacements for the measurement and the simulations. Up to a displacement of $x_p = 0.33\text{m}$ the agreement with the simulations is good but then it seems that the front load cell was damaged and shows higher tensions. This was also reported in (Azcona, et al., 2014) without however specifying the time when this happened.

Also as part of the system identification tests, the steady state of the system without wind was also compared with a reasonable agreement amongst the codes. The difficulties involved here were mainly due to the unknown mass distribution of the nacelle and the additional mass and stiffness introduced by the power cable, which was suspended from the tower base to the static bridge. A detailed collection of the system properties has been made for this work, based on (Azcona, et al., 2014).

The platform position and velocity in all six degrees of freedom was measured by an optical system (Qualisys). Here, the global reference frame origin was recorded once at the beginning of the campaign based on the position of the cameras installed in the basin. In the course of the campaign, however, the steady state position of the platform without wind or wave excitation changed slightly due to unknown reasons. The results shown here are the measured ones shifted by the offset measured for the steady state in a representative measurement for each week of the campaign.

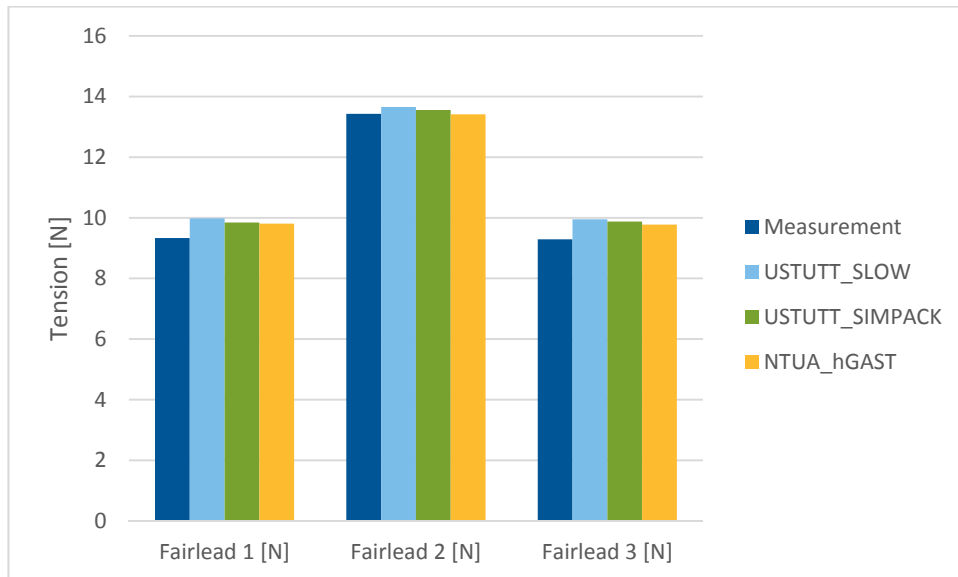


Figure 14: Fairlead tensions @ $x_p = 0.15\text{m}$, LC96

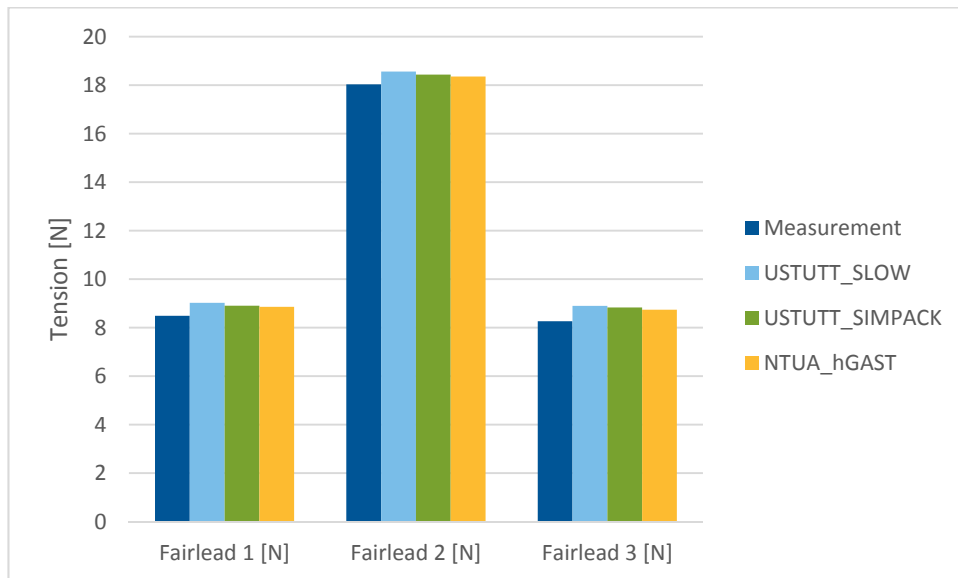


Figure 15: Fairlead tensions @ $x_p = 0.33m$, LC96

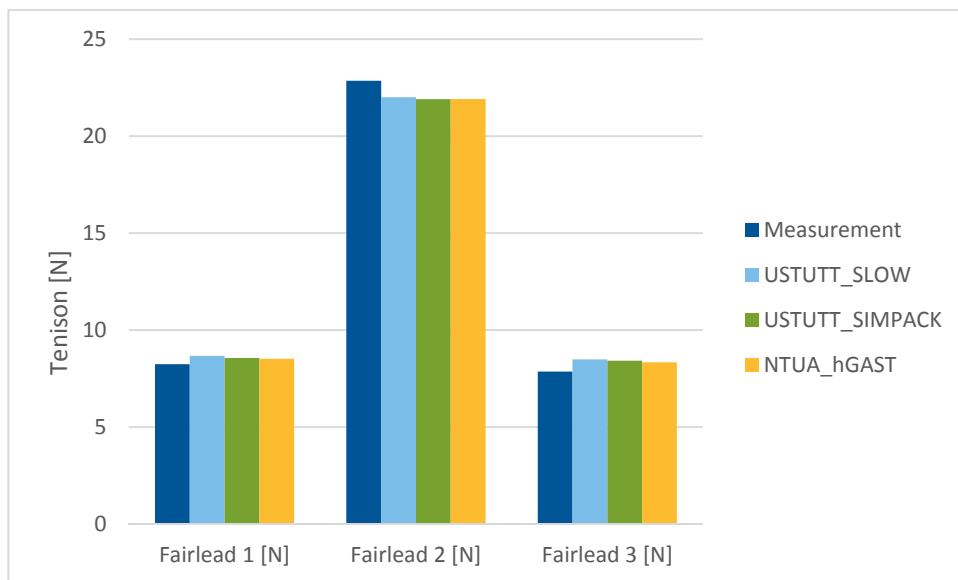


Figure 16: Fairlead tensions @ $x_p = 0.4m$, LC96

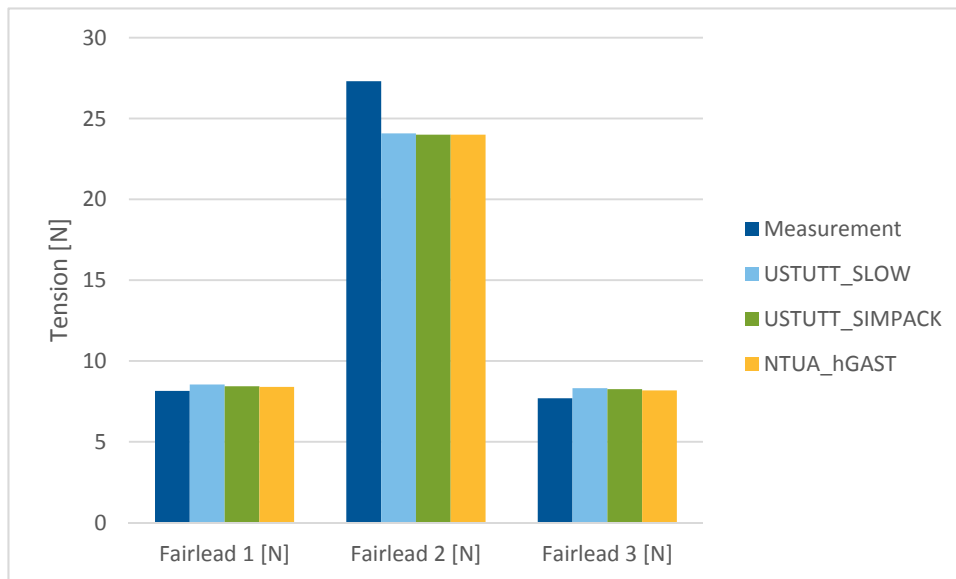


Figure 17: Fairlead tensions @ $x_p = 0.44\text{m}$, LC96

Free Decay (LC32)

Figure 18 shows the platform displacements after an initial displacement of the platform in pitch-direction (LC32). This was done in the experiment by placing a weight on one column and pulling it up to initiate the decaying motion of the model. In the simulation codes the full 6-DOF initial position was imposed in order to compare well with the measurements. One can see that the predicted pitch signals agree very well with the measurements and the pitch-contribution to the surge signal agrees also well. In surge the $\sim 15\text{s}$ -period has a slightly larger amplitude in the experiments. This might be due to an inaccurate damping model or reflection of the waves in the basin. The heave signals are very small, showing that the pitch decay was not coupled with a heaving motion.

The tower base moment signals in Figure 19 are not available from the measurements. Nonetheless, they have been compared amongst the simulation tools to check them for consistency. The SLOW model does not feature any lateral motion. hGAST shows a slightly smaller amplitude in fore-aft direction. As will be seen more clearly later the reason for this might be the mooring system, which is a dynamic model in the case of hGAST compared to quasi-steady model MAP++ of SIMPACK.

The fairlead tensions of Figure 20 show the platform pitch frequency but more important here are the absolute mean values of the tensions. It has to be mentioned that the correct placement of the anchors at 4m water depth and at a distance of about 17m from the model is not an easy task and includes quite some uncertainty. Considering this, it is quite remarkable that the mean absolute values compare well in simulations and measurements. SLOW shows generally higher values, which might be due to an interpolation function involved. The mooring line dynamics can be seen in the hGAST results.

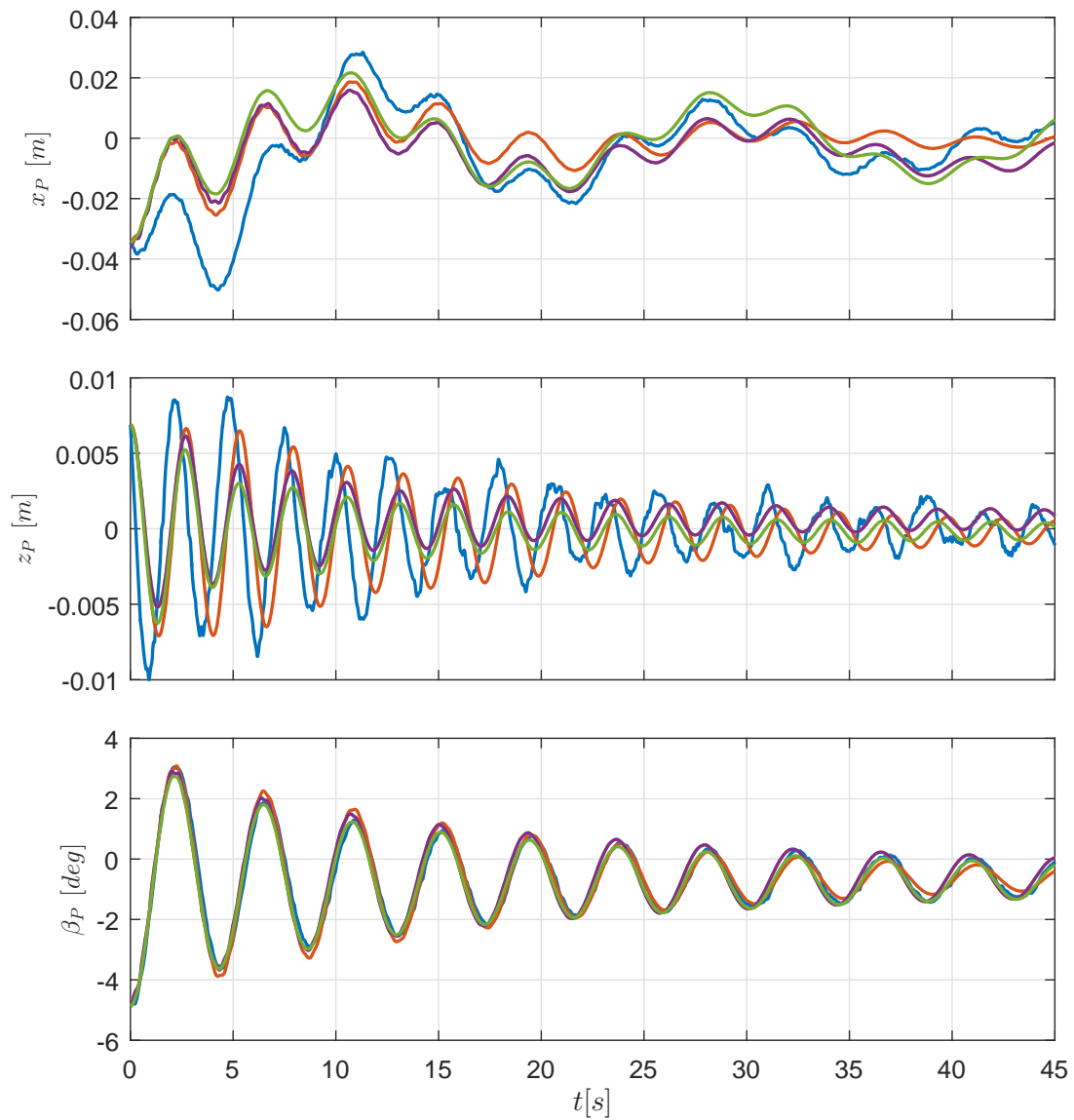


Figure 18: Pitch free decay (LC32); Platform displacements in Surge (x_P) Heave (z_P) and Pitch (β_P); blue: Measurement, orange: USTUTT (SLOW), purple: USTUTT (SIMPACK) green: NTUA (hGAST)

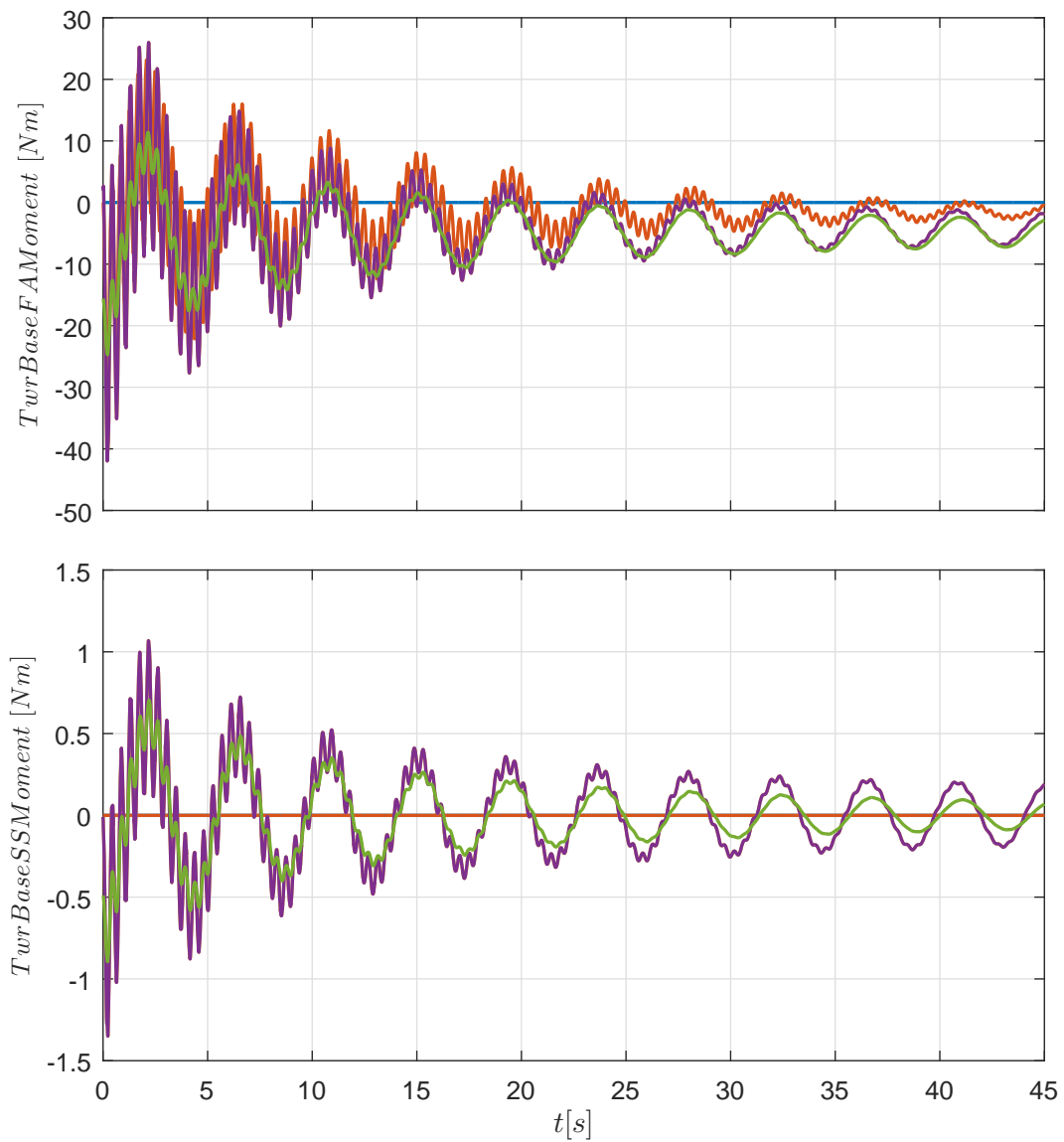


Figure 19: Pitch free decay (LC32); Tower base bending moments in Fore-aft (FA) and Side-Side (SS) direction; blue: Measurement, orange: USTUTT (SLOW), purple: USTUTT (SIMPACK), green: NTUA (hGAST)

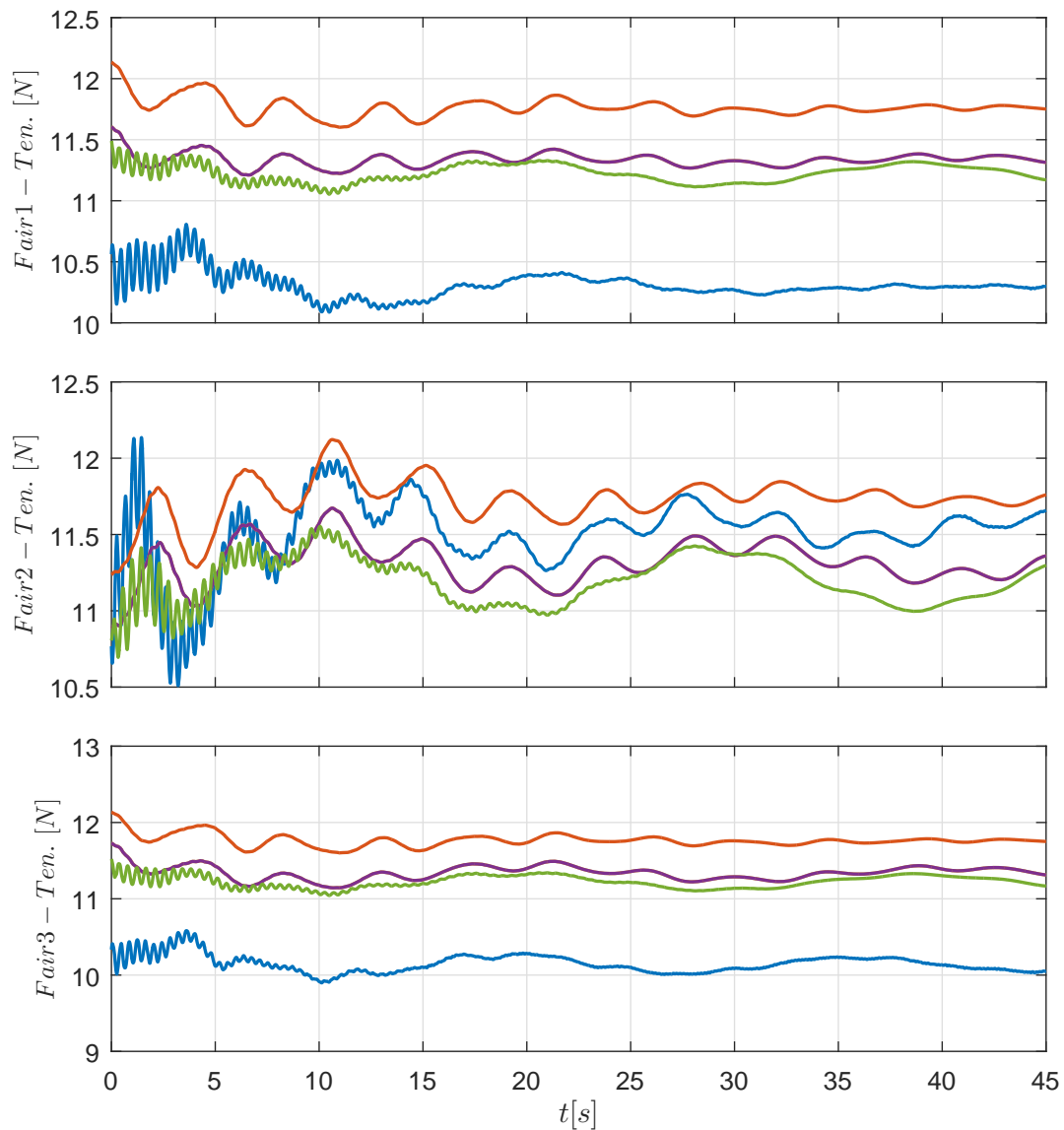


Figure 20: Pitch free decay (LC32); Fairlead Tensions ; blue: Measurement, orange: USTUTT (SLOW), purple: USTUTT (SIMPACK), green: NTUA (hGAST)

Regular wave only (LC52)

In the present load case a regular wave with height $H=0.3\text{m}$ and period $T=2.23\text{sec}$ is considered, while the wind speed is zero and the wind turbine is parked (no rotation). In Figure 21 the wave elevation and the 3 most excited motions of the floater: the surge, the heave and the pitch, are compared as time series. All the numerical models can sufficiently predict the dynamic behaviour of the floater since the agreement with the experimental results is good. The signal with the highest uncertainty is the surge motion where differences are depicted with respect to the mean value, while the amplitude, the period and the phase of the motion are well compared to the experiment.

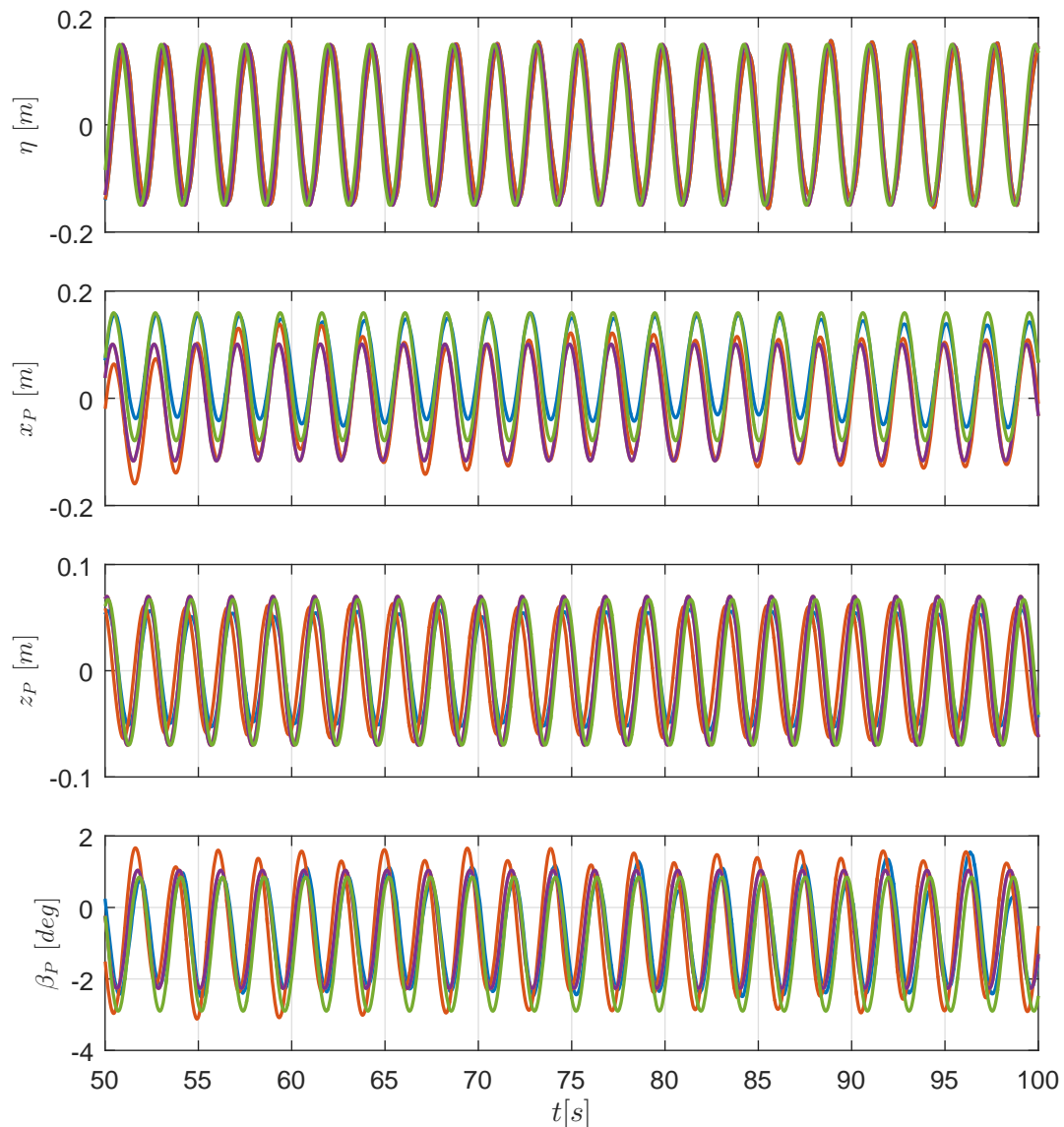


Figure 21: Regular Wave Only Load Cases LC52; From top: Wave Elevation(η), Surge (x_p), Heave (z_p), Pitch (β_P) motions; blue: Measurement, orange: USTUTT (SLOW), yellow: USTUTT (SIMPACK 1order), purple: USTUTT (SIMPACK 1order+ 2 order contributions), green: NTUA (hGAST)

In Figure 22 time series of the 3 mooring lines tension at fairleads are presented. Prediction by hGAST (green line) which adopts a dynamic mooring line model is in quite good agreement with the experiment (blue line) – the agreement with the 2nd mooring line is especially good – , while prediction by SIMPACK (purple line) and SLOW (orange line) which both adopt a quasi-static mooring line model is fair. Differences between the 2 modeling options mainly concern the amplitude of the tension and a small phase shift due to the inertia of the mooring lines that is only taken into account by the dynamic mooring line model. All codes predict a slightly higher mean value of the mooring lines tension at fairleads 1 and 3, while at fairlead 2 the agreement in the mean values is almost perfect.

It is noted that as it is already concluded in (Robertson A. , et al., 2014) and also derived from Figure 21, differences on the mooring line model do not affect the dynamic behaviour of the coupled system and could only be important for the design/certification of the mooring lines.

Generally, better agreement was found in the cases with higher wave heights (regular & irregular) between simulations and test. This difference in terms of wave height may be attributed to measurement noise and waves in the basin, which do not originate directly from the wave maker, such as reflected waves.

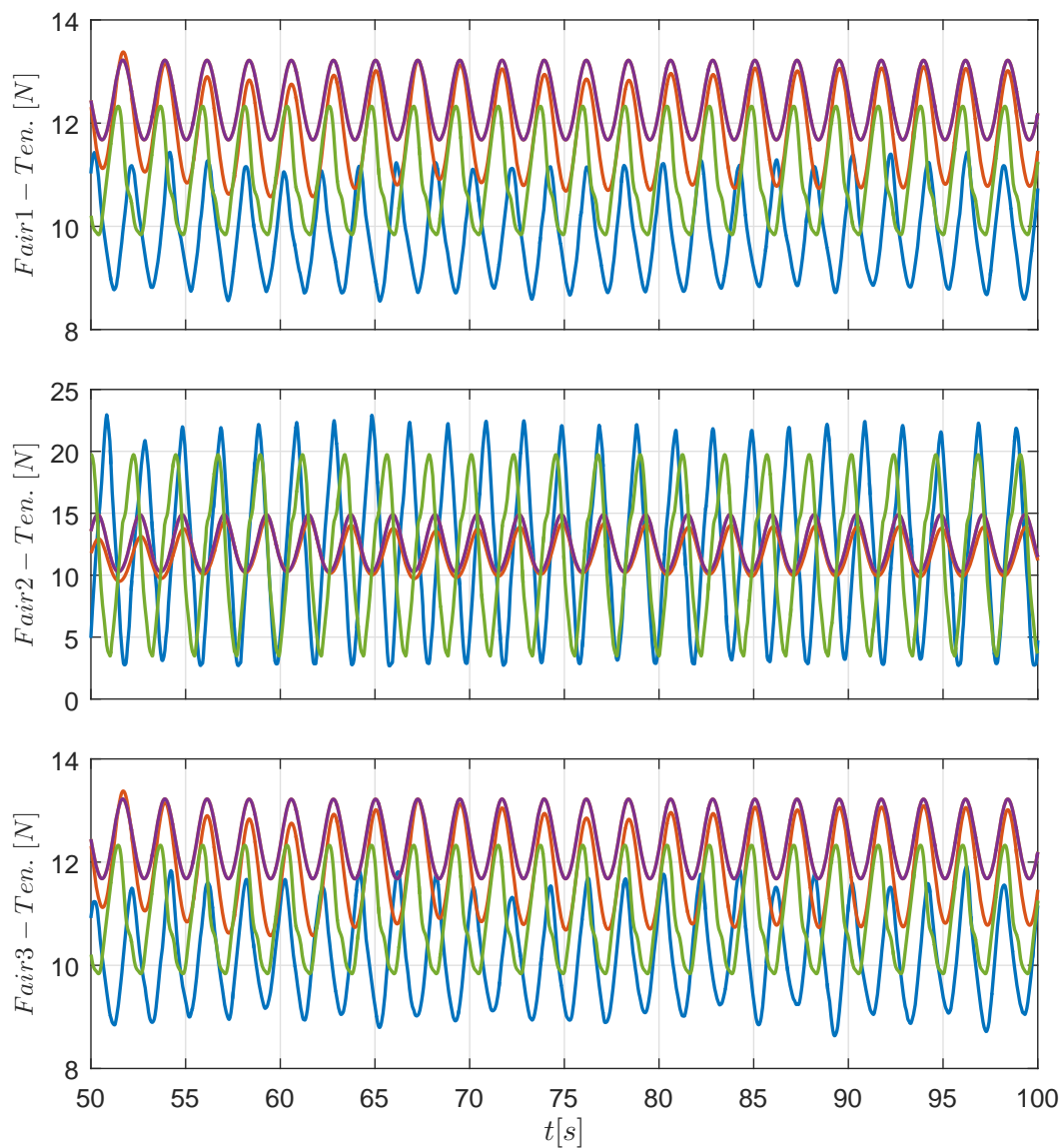


Figure 22: Regular Wave Only Load Cases LC52; From top: Fairlead tensions 1-3; blue: Measurement, orange: USTUTT (SLOW), yellow: USTUTT (SIMPACK 1order), purple: USTUTT (SIMPACK 1order+ 2 order contributions), green: NTUA (hGAST)

Figure 23 presents 50sec time series of the tower base bending moment in the fore-aft direction. The higher fidelity hydro-servo-aero-elastic tools hGAST and SIMPACK predictions are in excellent

agreement while the simplified tool SLOW gives similar results but with significantly lower amplitudes and reduced mean values. Unfortunately there are no experimental data for this specific load case for the considered sensor.

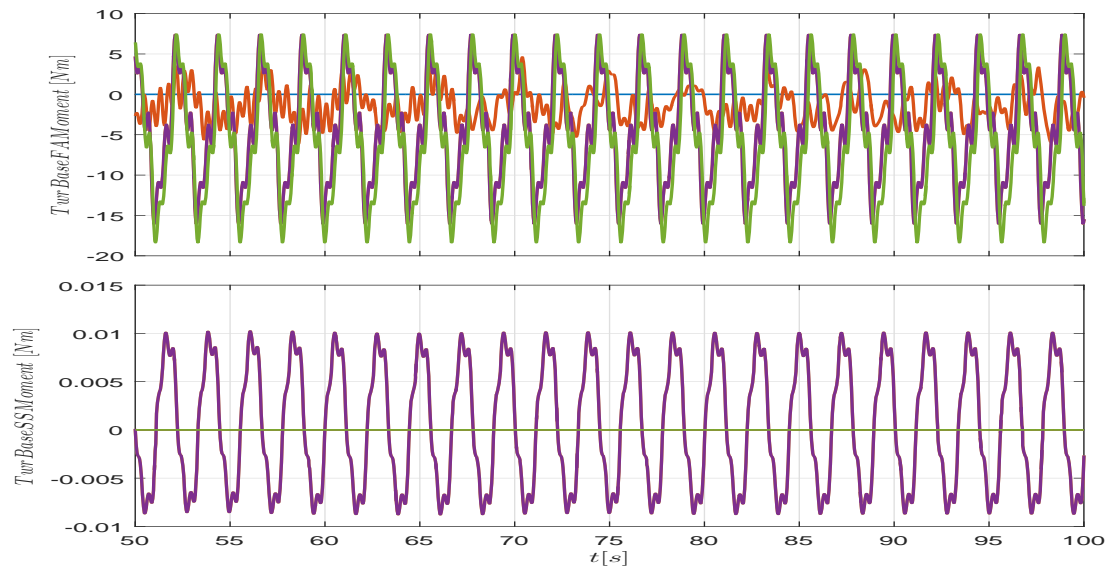


Figure 23: Regular Wave Only Load Cases LC52; 50sec time series of the Tower Base Bending Moments in fore-aft (FA); blue: Measurement, orange: USTUTT (SLOW), yellow: USTUTT (SIMPACK 1order), purple: USTUTT (SIMPACK 1order+ 2 order contributions), green: NTUA (hGAST)

Irregular wave only (LC12)

In the present load case an irregular wave is considered, defined by the Jonswap spectrum with significant wave height $H_s = 0.13$ m peak period $T_p = 1.29$ s corresponding to a peak frequency $f_p = 0.775$ Hz and peak shape parameter $\gamma = 2.87$, while the wind speed is zero and the wind turbine is parked (no rotation). In Figure 24 the wave elevation and the surge and heave motions of the floater are compared in terms of power spectral densities (PSD).

In general the agreement is good since all the numerical models capture the energy distribution in the wave frequency range from ~ 0.4 Hz and above in both motions. Moreover the surge natural frequency at about 0.06Hz is well captured. Differences in the low frequency range are mainly due to the different way hydrodynamics is modelled. In SLOW (orange line) the measured wave elevation profile is fed into the code and so the agreement of the surface elevation PSD is perfect. The difference concerns the excitation in the low frequency range, which in turn influences the response of the system to this frequency range. It is more pronounced in the heave direction because the wave excitation load in this direction (F_z) is non-zero for frequencies close to zero, while the surge exciting force is almost zero for low frequencies and so the excitation in the surge direction is mainly due to couplings.

The second order model of SIMPACK (purple) includes a calculation of 2nd order wave kinematics, which is used for the calculation of the Morison drag term. The wave height spectrum shows here a better agreement with the measurements for very low frequencies.

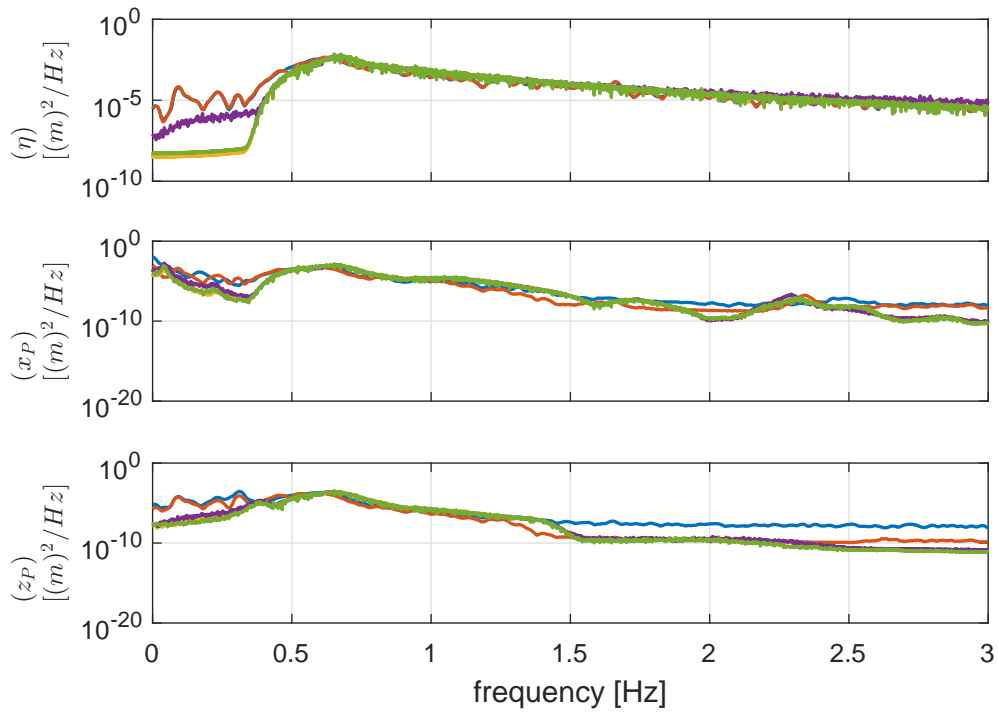


Figure 24: Irregular Wave Only Load Cases LC12 PSD; From top: Wave Elevation (η), Surge (x_p), Heave (z_p); blue: Measurement, orange: USTUTT (SLOW), yellow: USTUTT (SIMPACK 1order), purple: USTUTT (SIMPACK 1order+ 2 order contributions), green: NTUA (hGAST)

In Figure 25 PSDs of the floater pitch angle and the tower base fore-aft bending moment are presented. Again the numerical models compare well in the wave frequency range, but underpredict the excitation in the pitch natural frequency at about 0.2 to 0.25Hz. All numerical models agree well and predict a slightly increased pitch natural frequency compared to the experiment.

For the tower base moment no experimental data are available for this load case. The agreement between the numerical models is very good, especially between the higher fidelity tools hGAST and SIMPACK.

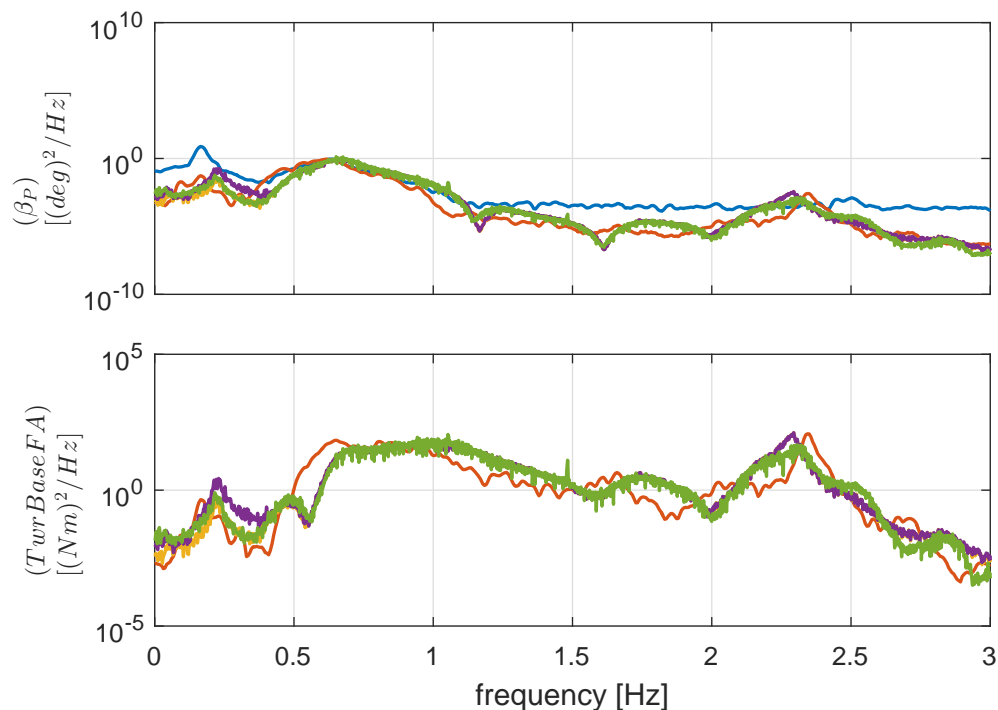


Figure 25: Irregular Wave Only Load Cases LC52 PSD; From top: Pitch (β), Tower Base Bending in fore-aft (FA); blue: Measurement, orange: USTUTT (SLOW), yellow: USTUTT (SIMPACK 1order), purple: USTUTT (SIMPACK 1order+ 2 order contributions), green: NTUA (hGAST)

Wind only cases (LC142-145)

The present load cases consider steady inflow conditions, produced by an array of fans forming a square section 3x3m, located 4m upstream of the rotor. The centre of the wind generator is at $z=2\text{m}$. No wave excitation is considered, so only the hydrostatic loads are acting on the floater. Four different wind speed cases are presented at 0.9m/s, 1.48m/s, 2.3m/s and 2.63m/s corresponding to LC142 to 145. Constant blade pitch angle and rotational speed are assumed for the simulations. At 0.9m/s the blade pitch is 1deg and the rotational speed is 46.69rpm, at 1.48m/s the pitch angle is -2.2deg and the rotational speed is 71,24rpm, at 2.3m/s the pitch angle is 13deg and the rotational speed is 75,26rpm and at 2.63m/s the pitch angle is 16deg and the rotational speed is 75,27rpm. Results are presented in terms of steady state values due to the absence of the wave loading.

As already stated in (Lemmer, et al., 2014) two points concerning the aerodynamics are uncertain.

The first concerns the estimation of the C_L , C_D , C_M data at a significantly low Re number (~ 60000), which is input to the BEM aerodynamic models. The provided “default” data which is used in the

numerical models has been calculated using XFOIL. Also a set of C_L , C_D , C_M data calculated using MaPFlow CFD code assuming fully turbulent conditions is available.

The second concerns the jet flow provided by the fan system that can have significant effects on the behavior of the wind turbine. The fact that outside the jet stream there is no air flow, renders the inflow conditions different from the full scale “infinite” conditions. The rotor acts as a resistance to the flow and will force the jet to expand and therefore reduce the mass flow through the rotor disk. Unfortunately BEM models can not model this effect.

Figure 26-Figure 28 present the mean floater surge motion, the mean floater pitch motion and the mean tower base fore-aft bending moment for the four considered wind speeds. SLOW and SIMPACK codes adopt the BEM method for the estimation of the aerodynamic loading, while in hGAST both aerodynamic options (BEM and free wake vortex method) have been used. Simulations by SLOW and SIMPACK have been performed using the XFOIL polars, simulations by hGAST BEM with both the XFOIL and the CFD polars, while those by hGAST Vortex with CFD polars.

In general the agreement between the measurements and the numerical predictions in the wind only cases is fair, in contrast to the wave only cases where the agreement was good. This is attributed, as already mentioned, to the sectional aerodynamic properties of the Froude scale blade and the jet flow produced by the wind generator system. All numerical models predict 25-90% higher surge motion at all wind speeds compared to the measured data most probably due to the jet effect which reduces the inflow velocity on the rotor during the experiment. The differences are smaller at higher wind speeds. The vortex code predicts slightly lower surge motions compared to the BEM model with the CFD polars.

Predictions in pitch motion are close to the experiment and not in line with those for the surge motion. Since both signals are driven by the thrust it is expected that the pitch predictions should be higher than the measured ones. In most cases this is not true, probably due to uncertainties with respect to the modeling of the added stiffness coupling term in surge-pitch motion contributed by the power cables. Also the tower base fore-aft moment agrees with the experimental data, but with opposite trend in wind speeds 0.9m/s and 2.63m/s. For these wind speeds the experimental pitch angle is slightly higher compared to the simulations, while the opposite is observed for the tower moment. It is noted that for these specific cases the absolute values are small. At 1.48m/s wind speed where the thrust is higher and in turn all the signals get higher, the comparisons are more consistent, although again the predicted surge motion is higher than the measured one.

The selection of the C_L , C_D , C_M data, although in general is important, in the present case does not seem crucial. For the lower wind speeds (0.9m/s, 1.48m/s) both predictions by hGAST BEM using the different polars are very similar. For the higher wind speeds (2.3m/s, 2.63m/s) the results using the polars produced with CFD are closer to the experiment, but similar to those provided by SLOW and SIMPACK that use the XFOIL data. It is noted that at the higher wind speeds the rotor operates at lower TSR and therefore inappropriate blade pitch setting may result differences.

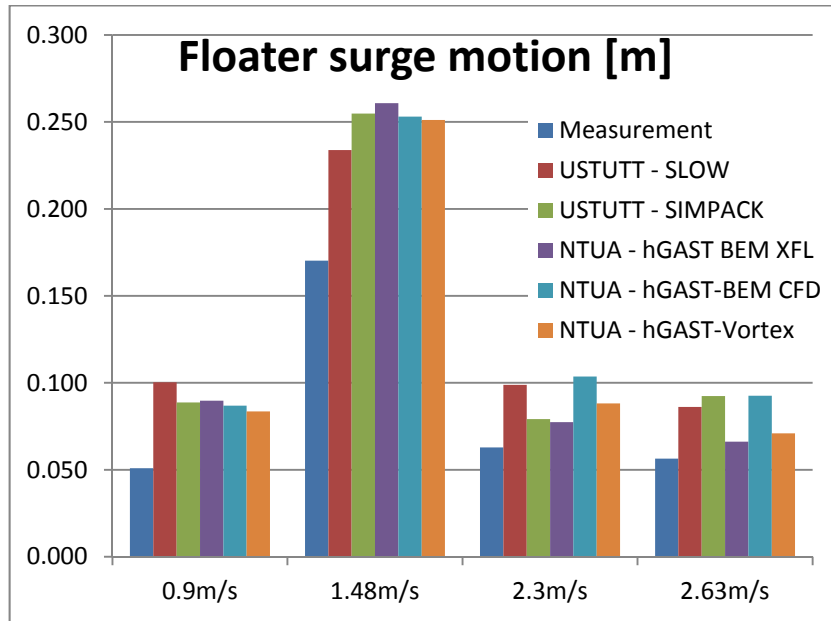


Figure 26: Wind only cases LC142-145; Mean floater surge motion [m]; blue: Measurement, dark red: USTUTT (SLOW), green: USTUTT (SIMPACK), purple: NTUA (hGAST BEM XFL polars), cyan: NTUA (hGAST BEM CFD polars), orange: NTUA (hGAST Vortex)

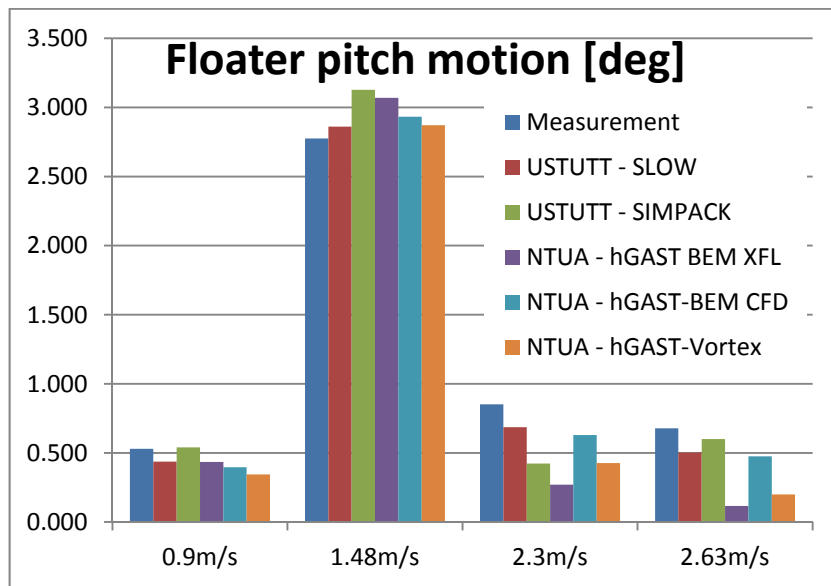


Figure 27: Wind only cases LC142-145; Mean floater pitch motion [deg]; blue: Measurement, dark red: USTUTT (SLOW), green: USTUTT (SIMPACK), purple: NTUA (hGAST BEM XFL polars), cyan: NTUA (hGAST BEM CFD polars), orange: NTUA (hGAST Vortex)

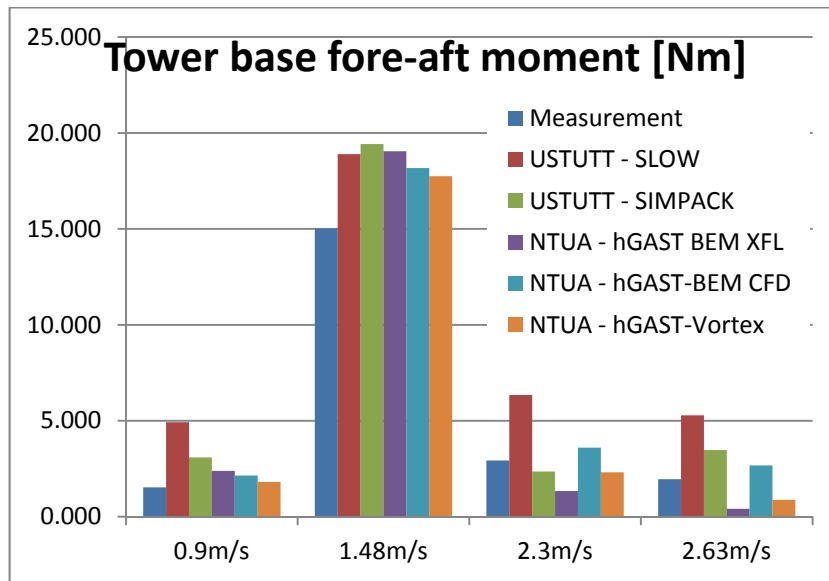


Figure 28: Wind only cases LC142-145; Mean tower base fore-aft moment [Nm]; blue: Measurement, dark red: USTUTT (SLOW), green: USTUTT (SIMPACK), purple: NTUA (hGAST BEM Xfoil polars), cyan: NTUA (hGAST BEM CFD polars), orange: NTUA (hGAST Vortex)

Wind and Regular Wave (LC65)

The present load case is a combination of the “Regular wave only case” and the “Wind only case”, considering steady inflow conditions at 2.68m/s and a regular wave with wave height $H=0.137\text{m}$ and period $T=1.33\text{sec}$. The fixed blade pitch angle is 15.5deg and the rotational speed is 81.6rpm .

In Figure 29 the wave elevation and the 3 most excited motions of the floater the surge, the heave and the pitch are compared in the time domain. As already concluded for the wave only case (see Figure 21) all the numerical models can sufficiently predict the dynamic behaviour of the floater due to the wave excitation. This is also true for the present case regarding the amplitude of the motions that are imposed by the waves. Differences in the mean values are mainly due to aerodynamics as stated in the previous section and mainly concern the surge and the pitch motions.

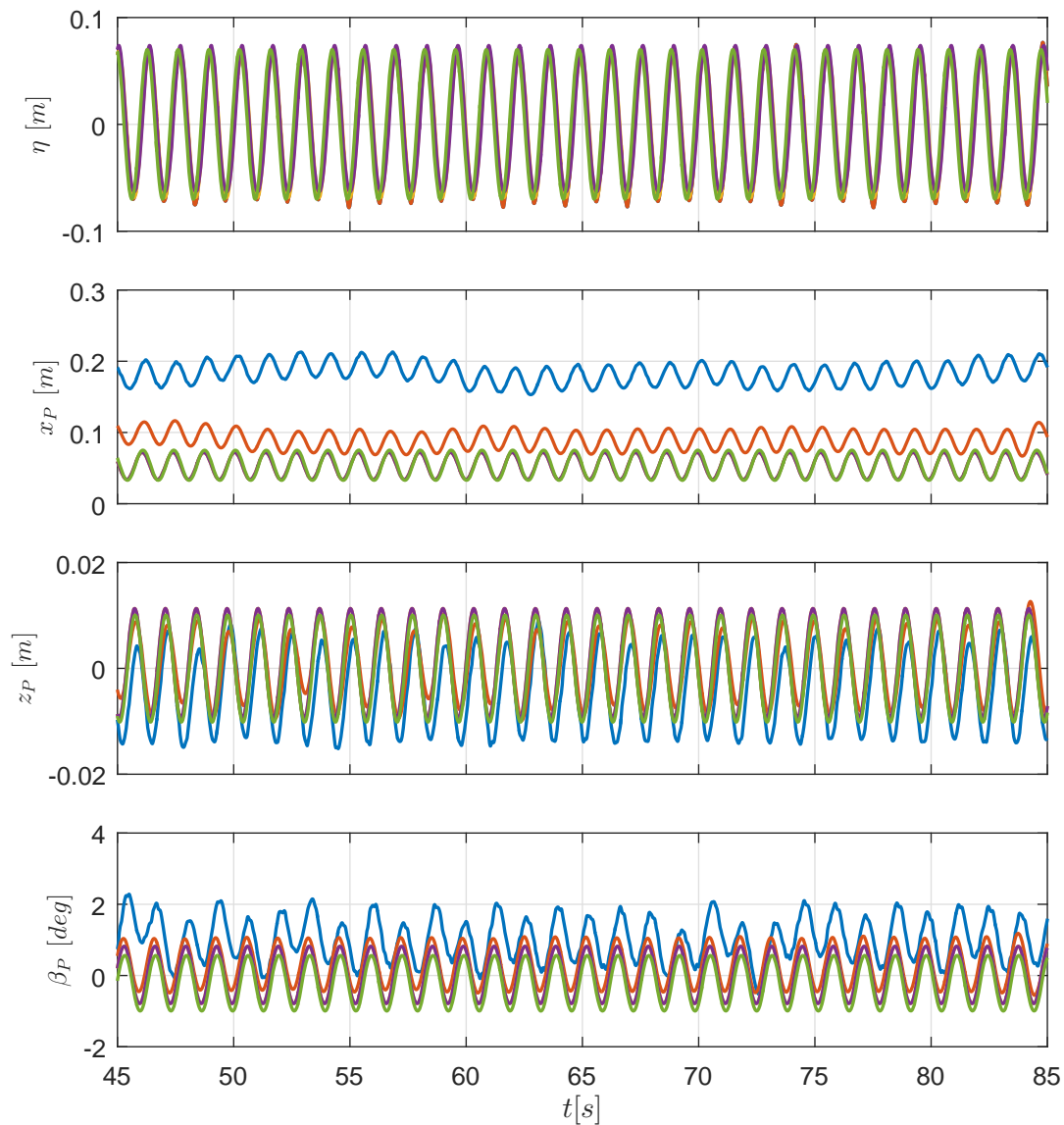


Figure 29: Combined Regular Wave and Wind Load Case LC65; From top: Wave Elevation (η), Surge (x_p), Heave (z_p), Pitch (β) motions; blue: Measurement, orange: USTUTT (SLOW), yellow: USTUTT (SIMPACK 1order), purple: USTUTT (SIMPACK 1order+ 2 order contributions), green: NTUA (hGAST)

In Figure 30 time series of the 3 mooring lines tension at fairleads are presented. Similar to the wave only case (see Figure 22) predictions by hGAST (green line) which adopts a dynamic mooring line model are in quite good agreement with the experiment (blue line) but only with respect to the shape of the signal (amplitude and phase). All numerical models predict different mean values of the mooring lines tensions due to the different surge mean position, which again is caused by the aerodynamics.

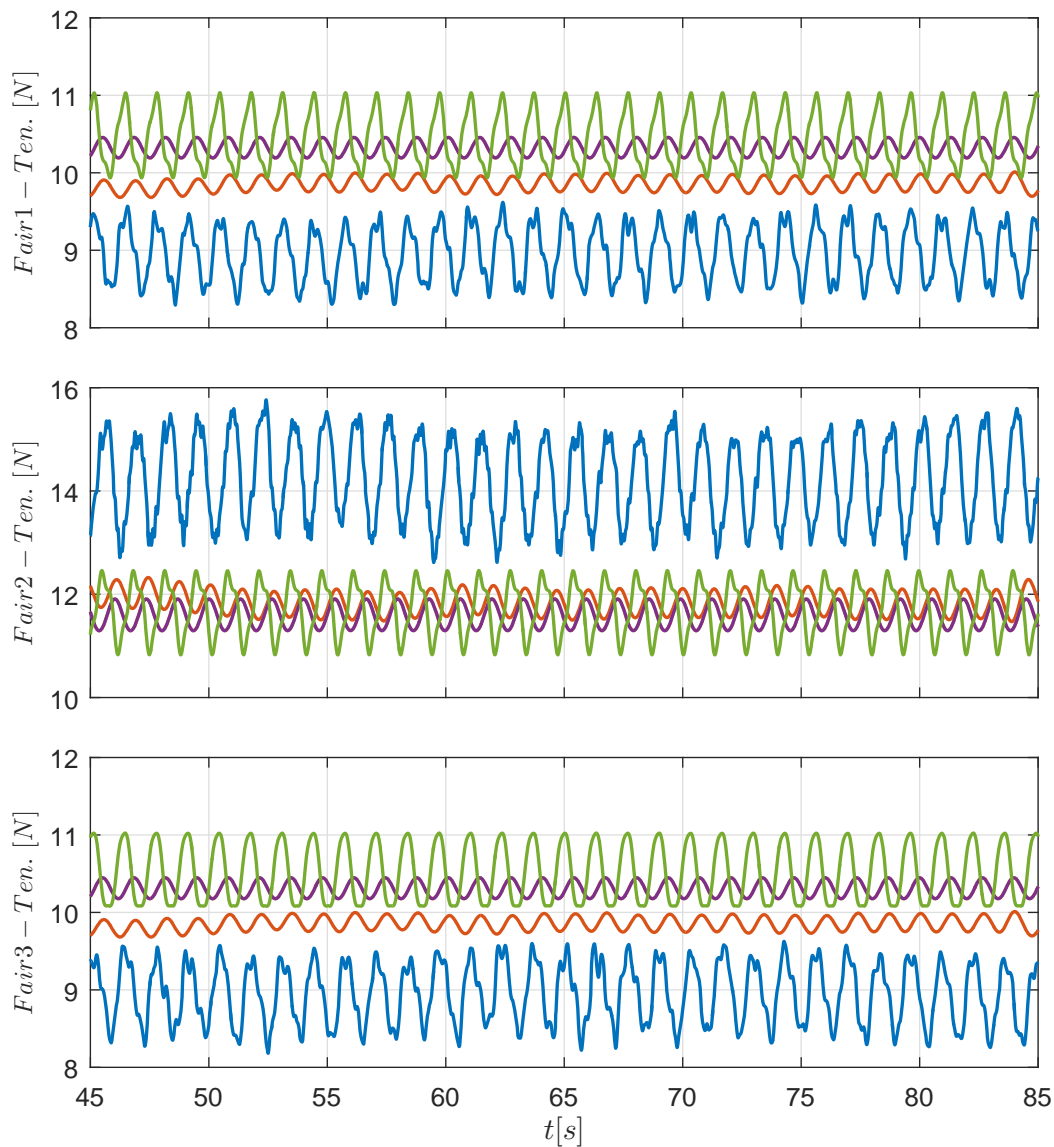


Figure 30. Fairlead tension for Load Case LC03, from top: Fairlead tensions 1-3, blue: measurement, orange: USTUTT (SLOW), yellow: USTUTT (SIMPACK 1order), purple: USTUTT (SIMPACK 1order+ 2 order contributions), green: NTUA (hGAST)

Figure 31 presents time series of the tower base bending moment in the fore-aft and the side-to-side directions. The agreement of the predictions in the fore-aft moment is good; small differences in the mean values are observed that are consistent with the pitch motion. The side-to-side moment exhibits high frequency oscillations well captured by hGAST and SIMPACK. Unfortunately there are no experimental data for this specific load case and for the considered sensor.

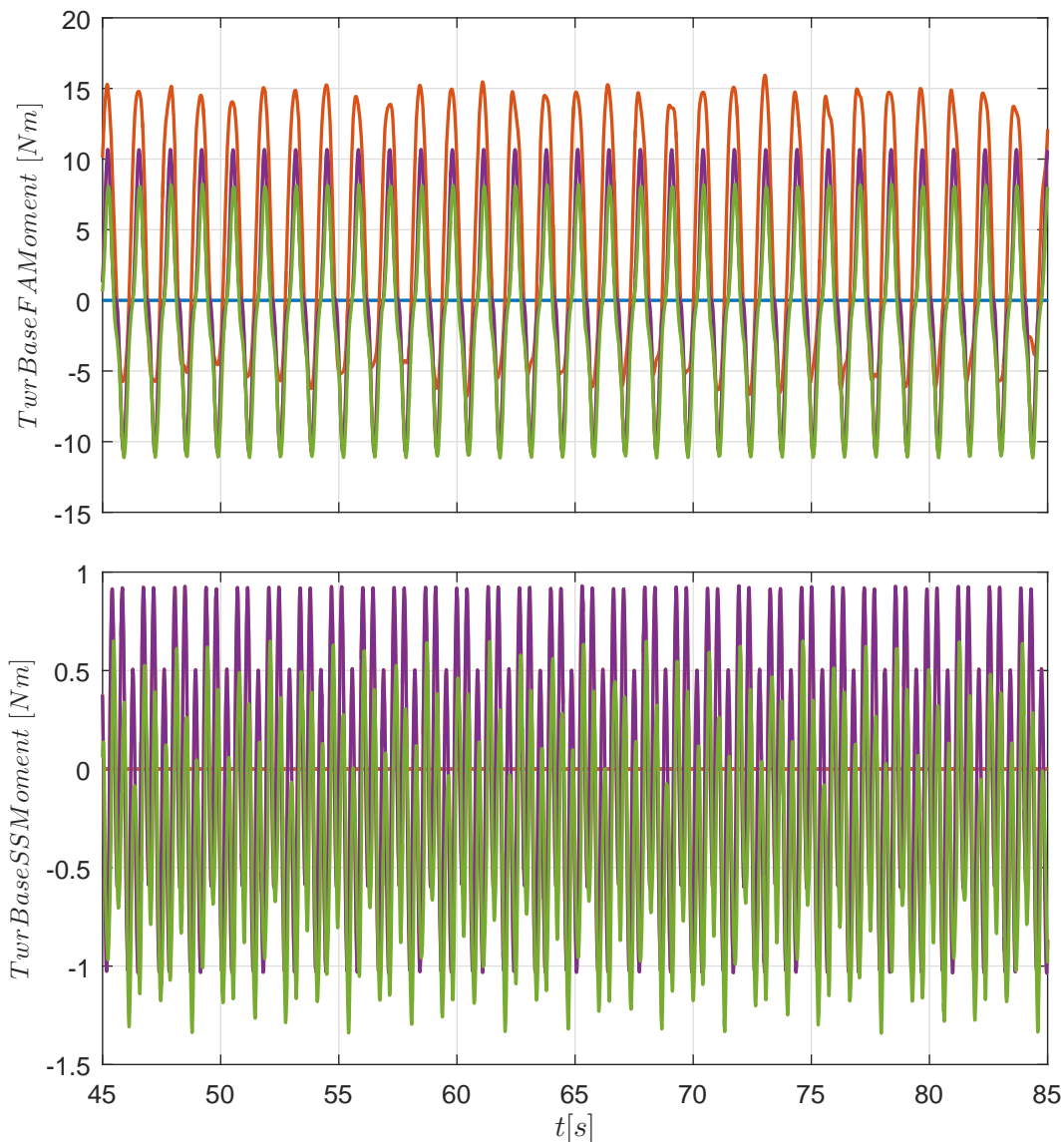


Figure 31: Tower Base Bending Moments for LC65; From top: Tower Base Bending Moments in fore-aft (FA) and side-side (SS); blue: Measurement, orange: USTUTT (SLOW), yellow: USTUTT (SIMPACK 1order), purple: USTUTT (SIMPACK 1order+ 2 order contributions), green: NTUA (hGAST)

Wind and Irregular Wave (LC 166)

Figure 32 shows the power spectral density of the wave elevation, surge and heave signals of an irregular wave and wind load case. The platform pitch and tower-base fore-aft moment signals can be found in Figure 33. Again, the most severe environmental conditions are shown with a significant wave height of 0.13m, a wind speed of 2.63m/s and a peak spectral period of 1.29s (≈ 0.8 Hz).

For frequencies below the wave frequency, the codes using only first order wave models show little components of the wave height spectrum (SIMPACK & hGAST). As SLOW reads in the measured wave height in order to calculate the complex spectrum for the computation of the wave forces, the spectra are identical. The modelled response of surge and heave agrees well with the

measurements in the wave frequency range. For higher frequencies the higher response of the measurements is most likely due to noise.

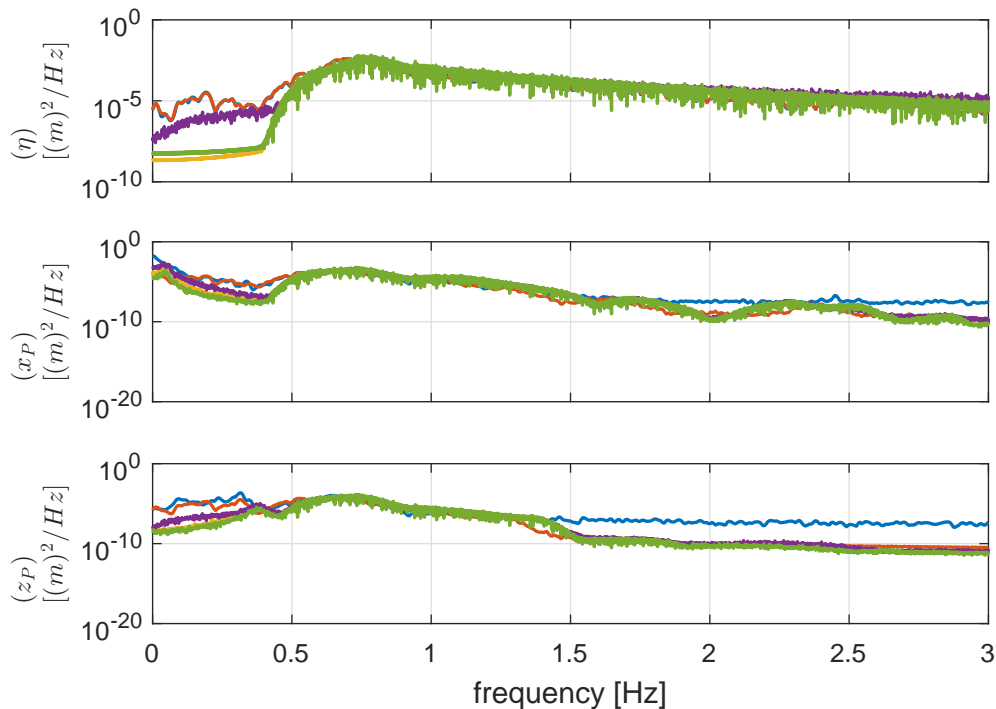


Figure 32: Irregular Wave and Steady Wind LC166 PSD; From top: Wave Elevation (η), Surge (x_p), Heave (z_p); blue: Measurement, orange: USTUTT (SLOW), yellow: USTUTT (SIMPACK 1order), purple: USTUTT (SIMPACK 1order+ 2 order contributions), green: NTUA (hGAST)

The platform pitch signals of Figure 33 agree well for the wave frequencies. Here SLOW shows better agrees with the experimental data for the platform pitch and for the tower-base moment. Since the pitch free-decay test showed that there is no difference in the modeling of the pitch-dynamics, see Figure 18, this difference is likely due to the different modeling of the waves. This would mean that the measured waves have a slightly smaller peak frequency than expected.

The same difference around the wave frequency is visible for the tower-base fore-aft moments. The tower-base bending moment measurements show the tower eigenfrequency at 2.5 Hz, whereas the simulations show a wider peak at about 2.25Hz. Unfortunately, there are no measurements available for the tower-base sensor for the cases with irregular waves and without wind.

The measured power spectral density of the platform pitch and tower-base fore-aft signals shows clearly higher magnitudes around the surge and pitch eigenfrequencies as the simulations. This indicates higher-order wave excitations at frequencies lower than the first-order waves. Except for the wave kinematics and the Morison damping term higher-order wave force models have not been included in the simulation models that are shown.

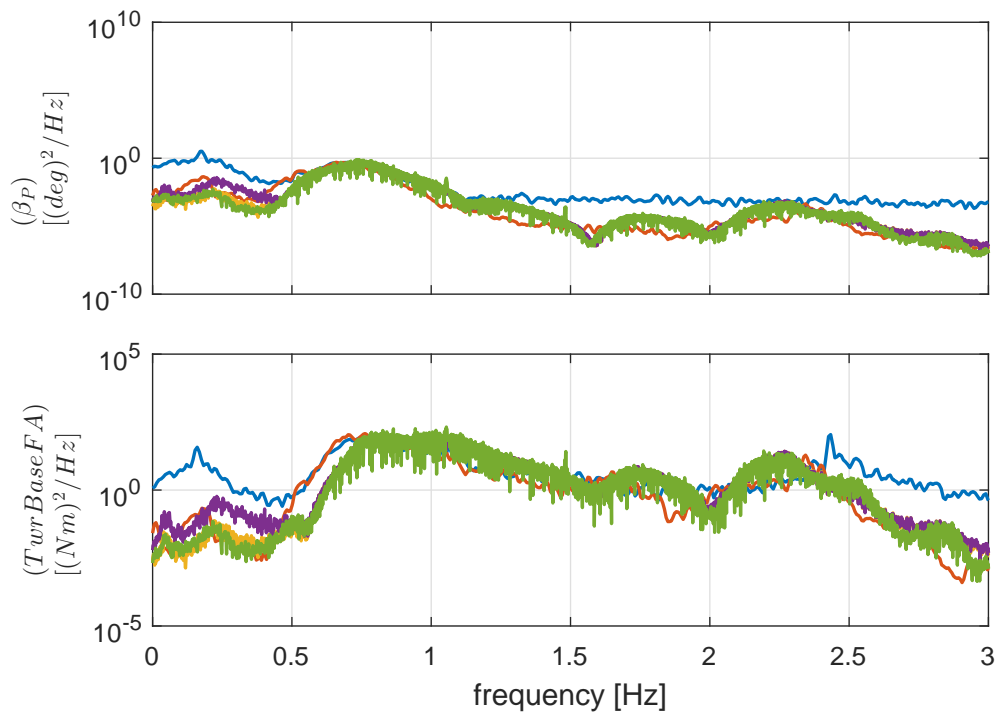


Figure 33: Irregular Wave and Steady Wind LC166 PSD; From top: Pitch (β), Tower Base Bending in fore-aft (FA); blue: Measurement, yellow: USTUTT (SIMPACK 1order), purple: USTUTT (SIMPACK 1order+ 2 order contributions), green: NTUA (hGAST)

Survival Load Case (LC162)

In this case shut-down conditions are modelled with a standstill rotor, high wind speeds of 4m/s, a significant wave height of 0.23m and a peak spectral period of 2s (0.5Hz). Figure 34 shows the wave height, surge and heave signals, which show the same frequencies as the previous case at operating conditions.

The tower-base fore-aft moment of Figure 35 shows the wave peak frequency, which is now lower as in the operational case and more narrow-banded. The difference of the tower eigenfrequency is the same as the one in Figure 33.

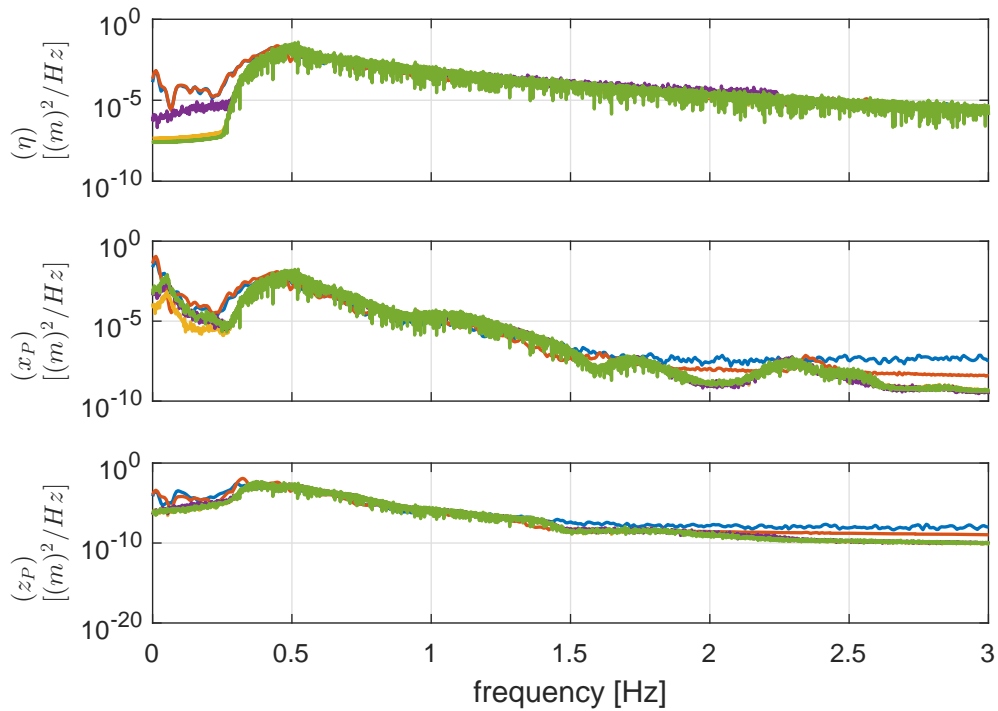


Figure 34: Survival Test Load Case LC162 PSD; From top: Wave Elevation (η), Surge (x_p), Heave (z_p); blue: Measurement, orange: USTUTT (SLOW), yellow: USTUTT (SIMPACK 1order), purple: USTUTT (SIMPACK 1order+ 2 order contributions), green: NTUA (hGAST)

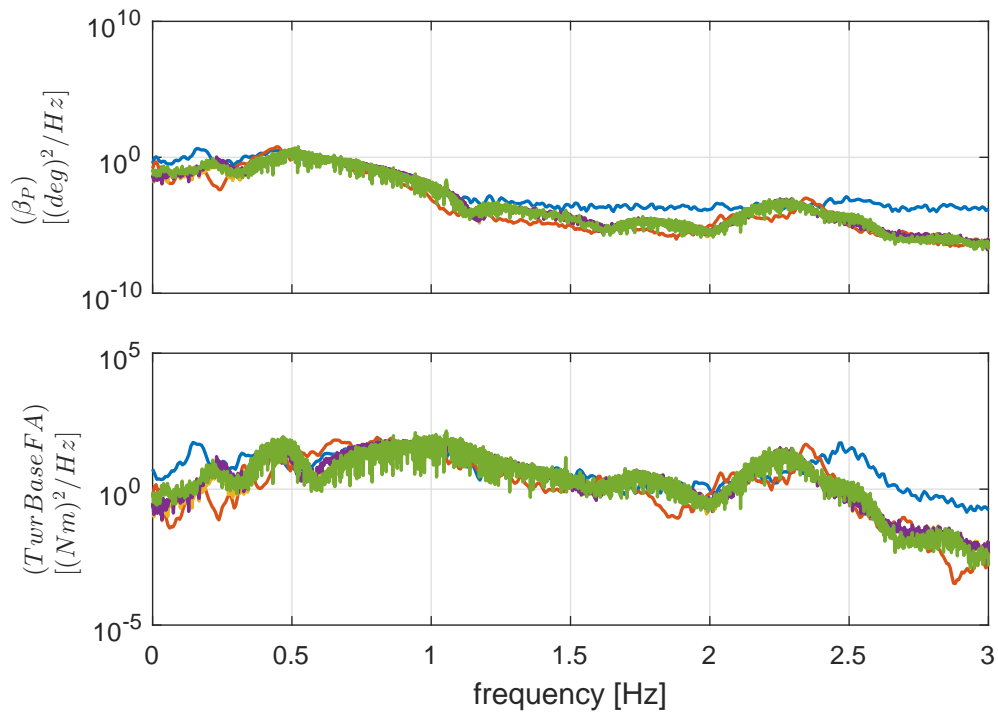


Figure 35: Irregular Wave and Steady Wind LC162 PSD; From top: Pitch (β), Tower Base Bending in fore-aft (FA); blue: Measurement, yellow: USTUTT (SIMPACK 1order), purple: USTUTT (SIMPACK 1order+ 2 order contributions), green: NTUA (hGAST)

Conclusions of the validation based on the model with Froude-Scaled rotor

The validation of three software codes using measurement data from the four-week campaign at EHEEA Nantes/France in 2014 has been shown. The validation task has been structured such that first, the steady states of the platform were compared and verified within the simulation models. In a next step the static mooring forces were compared for a validation of the static properties of the mooring models as well as the experimental mooring system and force sensors. Free-decay experiments were used to verify the mass and inertia properties of the models. Here, the mass distribution is of special importance since it is not known exactly for all parts. The hydrodynamic damping was identified through the free-decay tests and equally defined as a linear coefficient in the models.

In a next step the wind-only tests were used to verify the aerodynamic models. Due to the fact that the wind field was measured without the operating turbine there is some uncertainty about the rotor-effective inflow wind speed due to blocking effects of the open jet. Therefore, the models based on Blade-Element Momentum Theory (BEM) and using the XFOIL polars, provided the platform pitch and tower-base fore-aft moments for a range of wind speeds resulting in a sensitivity analysis about the rotor-effective wind speed. It turned out that, based on the BEM results the rotor-effective wind speed was likely to be 10% smaller than the commanded one. With this chain of identification studies the three different simulation models were set-up and combined wind-and-wave experiments were conducted with a range of environmental conditions for operation and standstill of the turbine. Generally, larger wave heights showed a better agreement with the models due to the large portion of noise and reflection of waves for small wave heights.

The study shows that with a Froude-scaled platform and mooring system and a performance-scaled rotor it is possible to obtain valid measurements, which are predicted well by the state-of-the-art simulation models. This proves that this kind of tests can be used to study the complex effects in off-shore floating conditions. It is challenging to model at reasonable computational cost, effects like large, nonlinear and coupled responses, wind/wave misalignment, higher-order waves and others. Due to the inhomogeneity of the wind field and the limited number of wind measurements, however, it is difficult to validate, e.g., sectional blade loads, especially if flexible blades are tested. Active blade-pitch control is a next step for floating wind model tests.

Recommendations for future tests are to perform a detailed identification of the subsystems mooring lines, inertial and elastic properties of the structure, the aerodynamic rotor coefficients, the wave maker and the wind field. Also, an uncertainty analysis of the sensors should be performed and a calibration on site.

2.4 Ducted Fan Tests

This section is dedicated to the validation of the FAST code based in those measurements of the semisubmersible campaign that used a fan and a Software in the Loop (SiL) approach to introduce the scaled aerodynamic rotor forces. Therefore, these results pretend to validate the simulation tools, but also will show the performance of the SiL and its ability to include the rotor aerodynamics during combined wind and wave tests.

The experimental results are compared with two sets of computations. The first one corresponds to the FAST V6 code using the quasi-static mooring model. The other one is also the FAST code, but coupled with CENER's dynamic mooring lines code called OPASS. This method allows showing the influence of the mooring dynamics in the results of the simulations. Version 8 of the FAST code has been recently released including non-linear hydrodynamics, but our code OPASS has not been coupled with this last version yet.

An experimental validation of the OPASS code as a stand-alone tool was also performed against tension and motion measurements of a chain submerged in a water tank and are presented in Chapter 4. The validation in the present chapter refers to FAST version 6 coupled with OPASS and also with its quasi-static mooring line model for comparison.

Description of the numerical models

The FAST code (Jonkman, 2007) is an integrated tool developed by NREL that allows the simulation of floating wind turbines. The code is a multibody model for the structural dynamics coupled with an aerodynamic model and a hydrodynamic model for the calculation of the external loads. The aerodynamics is based on the Blade Element Model (BEM) including several corrections for the tip and hub losses, for the skewed flow, etc. and using a Leishman–Beddoes model for the unsteady aerodynamics. The hydrodynamics are based on potential flow, which neglects the viscous damping. CENER has also implemented a model to include the viscous damping in the slender elements based on Morison equation. For the moorings, the two approaches considered are the quasi-static and CENER's dynamic model OPASS. The quasi-static model, represented in Figure 36, consists on the resolution of the static catenary equation at every time step of the simulation. This means that only static effects such as gravity, buoyancy, seabed-line contact, longitudinal seabed-line friction and axial stiffness are considered. In contrast, the dynamic mooring model OPASS takes into account the line inertia, the hydrodynamic tangential and normal drag, the added mass, the structural damping and the seabed-line friction in the longitudinal and normal directions, as it is represented in Figure 37.

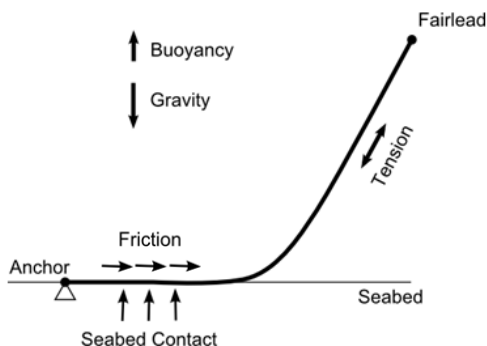


Figure 36 – Quasi-static model

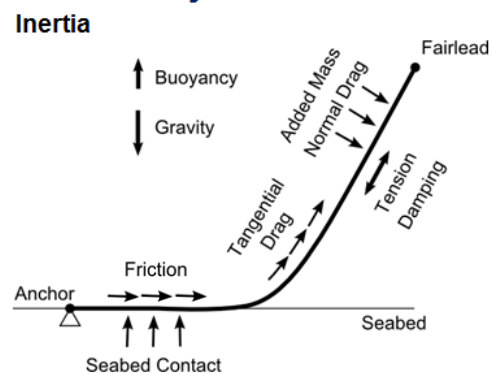


Figure 37 – Dynamic model

The OPASS code has been described in detail in the INN WIND.EU deliverable 4.21 (Azcona, et al., 2014). Since the publication of this deliverable, some improvements have been introduced in the OPASS code. The code is now able to model lines composed of different segments with different materials and can also include buoys at a certain position. Nevertheless none of these improvements were applicable to the test data from this campaign.

Scaled floating wind turbine model

The scaled model used in this validation corresponds to the model described in the INN WIND.EU deliverable 4.2.4 (Azcona, et al., D4.2.4: Results of wave tank tests. Description of Floating Wind Model Tests at ECN and DHI, 2015) for the week 4 of the semisubmersible testing campaign that took place at ECN (Ecole Centrale de Nantes). The main difference with the model used in the weeks 1-3 is that the low Reynolds rotor was removed and, instead, a ducted fan was installed at the hub height to include the aerodynamic loading using the Software in the Loop approach.

Integration of aerodynamic thrust using SiL

As has been mentioned, in contrast with the other 3 weeks of testing, the results during this week 4 were generated using the SiL approach to include the scaled rotor force. The basic concept of the method consists of substituting the rotor by a fan driven by an electric motor. The fan thrust is controlled by the fan rotational speed set by the controller, which again depends on the real time simulation of the full scale rotor in a turbulent wind field, with the platform motions measured in real time in the wave tank test. A detailed description of this method can be found in (Azcona, et al., 2014). A picture of the ducted fan at the tower top is shown in Figure 38.



Figure 38 – Ducted fan (week 4)

The fan and its real-time controller are lighter than the scaled mass and thus, ballast has been added to the scaled model tower top to match the full scale configuration. The fan is mounted on the same tower as the Froude-scaled rotor.

The model of ducted fan selected to generate the force representing the aerodynamic thrust during the tests is the DS-30-AXI HDS, manufactured by the German company Schübeler. As shown in Figure 39, the fan is powered by a brushless motor HET 2W20 that is controlled by an Electronic Speed Controller (ESC) YGE 90 HV, and works with an industrial AC/DC power supply. This system configuration produces an approximate force range of 0-18N. The rpm of the motor (and therefore the force produced by the fan) is controlled by a Pulse Width Modulation (PWM) signal that is generated with the LabVIEW control software, using servo libraries for Arduino. The

demanded force for the fan is provided by the full scale simulation of the rotor's aerodynamic thrust.

The software used to compute the aerodynamic loads in real time during the tests is the version v6.02c-jmj of the FAST code, with AeroDyn 12.58. These codes have been by CENER to be used in real time and coupled with the test. The software has been compiled in Linux and during the test campaign it was ran in a computer with a 2.54GHz Intel Core Duo CPU and 2GB of RAM.

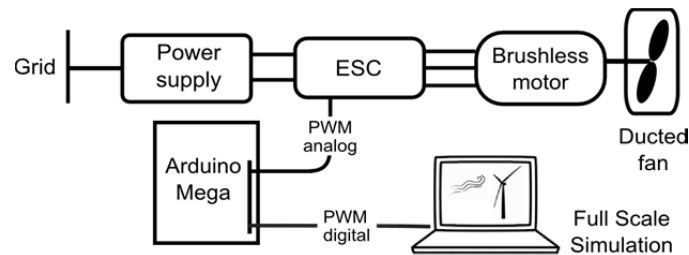


Figure 39 – Fan Control System Lay Out

Main characteristics of the scaled model

The geometry and mass of the model was designed based on a upscaling of the OC4-DeepCwind semi-submersible design. Additional mass was added at the tower top to match the RNA mass and the inertia in roll and pitch motions. Table 3 presents the main characteristics of the scaled model. As the weight of the fan is relatively low, ballast was added at the tower top matching the target weight that represents the full scale RNA mass. For this reason, the additional shifted ballast below the platform keel, used to match the overall centre of gravity weeks 1-3, was removed.

Table 3 – Main properties of the scaled model

	Prototype	Scaled model
Platform mass including ballast [kg]	1.38E+07	151.29
Platform CM location from SWL [m]	12	0.27
Platform inertia in pitch [kg m ²]	1.13E+10	61.16
Platform inertia in roll [kg m ²]	1.13E+10	61.16
Platform inertia in yaw [kg m ²]	1.19E+10	64.24
Platform displaced volume [m ³]	14245	0.16

The coefficient for compensation the water densities (ρ_{salt}/ρ_{sweet}) was not applied, because the sweet water density was given as input for the simulations.

Mooring line properties

The geometric properties of the scaled mooring system as they were installed at the wave tank are presented **Error! Reference source not found.**:

Table 4 – Mooring system scaled properties

	Anchor radial distance from platform center line [m]	Anchor angular position [deg]	Anchor depth location [m]	Radial fairlead location [m]	Fairlead angular position [deg]	Fairlead draft from SWL [m]	Unstretched line length [m]
L1	17.110	60	4.958	0.928	60	0.334	17.273
L2 "upwind"	17.110	180	4.958	0.928	180	0.334	17.272
L3	17.110	300	4.958	0.928	300	0.334	17.270

In the week 4 of the tests, a reduction in the water depth was detected. This is the reason why **Error! Reference source not found.** presents the anchor depth location at 4.958 m instead of the original objective of 5 m.

The chain density for the computational model was assumed 7850 kg/m³ based on steel and the line axial stiffness was based on the OC4 model resulting in 1.67E+07 N for the scaled model.

The quasi-static model requires an equivalent hydrodynamic diameter to calculate the buoyancy force on the line. The volume of water displaced by the chain was measured and the resulting diameter was 0.00318 m.

The OPASS code takes into consideration the hydrodynamic drag forces. A representative reference diameter together with the tangential and normal drag coefficients have to be defined. For the OPASS computational model a reference diameter of 0.002 m was defined per each line with a $C_{Dn}=2.4$ a $C_{Dt}=1.1$, according to DNV-OS-E301 (Bureau Veritas, 2002). The added mass coefficient was set to 1.0 according to (Det Norske Veritas, 2010).

Viscous damping on the platform members

A viscous damping model based in the Morison equation has been applied in the computational model to the slender members of the platform such as columns, braces and pontoons. Table 5 shows the coefficients values that were taken from OC4 DeepCwind semisubmersible.

Table 5 – Drag coefficients applied to the slender member of the platform in the computational model

Floater tubular member	CD
Central column	0.56
Upper external columns	0.61
Base external columns	0.68
Pontoons and cross members	0.63

Description of the test cases

Table 6 presents the tests used for the validation in this chapter. All the wind loading in these cases was included using the SiL method. The table shows a step by step strategy, beginning with simple cases and continuing with increasing complexity.

First, a free decay test (LC182) is performed to adjust the damping of the platform.

The tests 169, 170 and 171 are cases with constant wind and no waves. They allow checking the platform displacements generated by a constant wind force. Three different wind velocities (below rated wind speed and over rated wind speed) were tested.

The aerodynamic damping is verified in cases 179, 180 and 181. In these cases, once the wind turbine under constant wind has reached its steady state, a pitch displacement is introduced. The pitch motion of the platform is damped by the aerodynamic force at the rotor. The control of the wind turbine is included in these simulations. The same three wind velocities are used in these test cases.

The cases 174, 175 and 177 consist of three constant wind speeds combined with regular waves. The periodic response of the platform for three different wave amplitudes is evaluated in these cases. The cases 186, 187 and 188 are similar, but waves are irregular instead of regular waves. Finally, turbulent wind and irregular wave are combined in experiments 183, 184 and 185.

All the results are presented at wave tank scale to give a better idea of the physics of the experiment.

Table 6 – Summary of test cases

LC	Test run identifier	Wind speed [m/s]	H [m]	T [s]	Comment
182	S1P7	0.00	0.0	0.0	Free decay test
169	S1O2	1.267	0.0	0.0	Constant wind
170	S1O3	1.699	0.0	0.0	
171	S1O4	2.683	0.0	0.0	
179	S1P4	1.267	0.0	0.0	Aerodynamic damping test
180	S1P5	1.699	0.0	0.0	
181	S1P6	2.683	0.0	0.0	
174	S1Q2	1.267	0.07	0.969	Regular wave, constant wind
175	S1Q3	1.699	0.09	1.088	
177	S1Q4	2.683	0.11	1.327	
LC	Test run identifier	Wind speed [m/s]	Hs [m]	Tp [s]	Comment
186	S1R2	1.267	0.07	0.969	Irregular waves, constant wind $\gamma=3.3$
187	S1R3	1.699	0.09	1.088	
188	S1R4	2.683	0.11	1.327	
183	S1T2	1.267	0.07	0.969	Irregular waves, turbulent winds $\gamma=3.3$
184	S1T3	1.699	0.09	1.088	
185	S1T4	2.683	0.11	1.327	

Free decay test

Figure 40 shows the surge displacement of the platform in a free decay test case. Together with the experimental results (in blue) the FAST and the FAST-OPASS simulations have been plotted. This test case has been used to adjust the damping of the FAST model. Potential hydrodynamics under-estimates the total damping of the system and additional linear and quadratic damping has been added.

In addition, certain stiffness in the surge degree of freedom was also required to match the natural period of the platform. This additional stiffness takes into account the effect of the cables between the crane and the platform, which are required to power the fan and to acquire the signals from the sensors.

The adjusted coefficients for linear and quadratic damping and also for the stiffness are collected in Table 7.

Once the model was adjusted, the results in Figure 40 show a good agreement in the surge displacement between the measurements and the results provided by FAST with the two different mooring system approaches: the quasi-static and OPASS. These additional damping and stiffness are kept for all the remaining simulations.

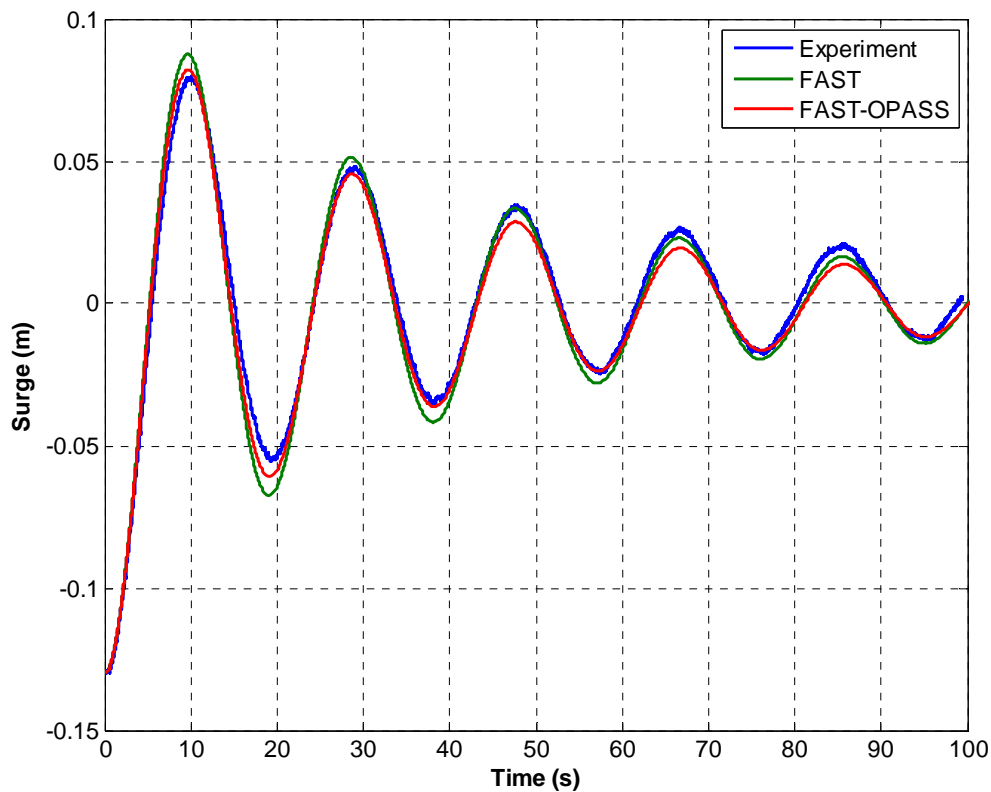


Figure 40: Free decay test on platform surge. Test case LC182

Table 7 – Additional damping and stiffness

Degree of freedom	B [Ns/m]/ [Nms/rad]	Q [Ns ² /m ²]	C _{Quasi-Static} [N/m]	C _{OPASS} [N/m]
-------------------	---------------------	--------------------------------------	---------------------------------	--------------------------

Surge	$50 \cdot 10^3$	$400 \cdot 10^3$	$5 \cdot 10^3$	$5,5 \cdot 10^3$
Pitch	$80 \cdot 10^6$	0	0	0

Constant wind and no waves

In these cases a constant wind with three different wind speeds at 1.267 m/s, 1.699 m/s and 2.683 m/s (below rated, rated and over rated wind speed) has been applied in the absence of waves. Figure 41 compares the platform surge displacement once the transients have disappeared and the steady position of the platform is reached.

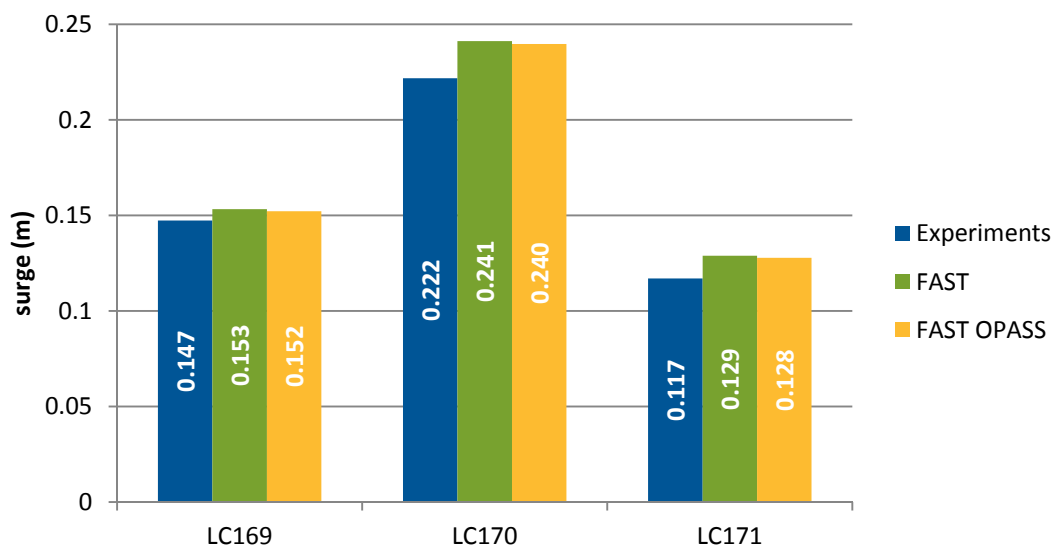


Figure 41: Steady surge position of the platform

The larger surge displacement occurs for the rated wind speed (LC170) that produces the highest thrust at the rotor. The numerical solutions result in slightly larger displacements than experimental results, in particular for the rated and above rated wind speeds, with differences under 10%.

Figure 42 reveals that the inclination of the structure produced by the rotor thrust is well captured by the numeric models. The highest discrepancy, around 5% appears for the below rated wind speed.

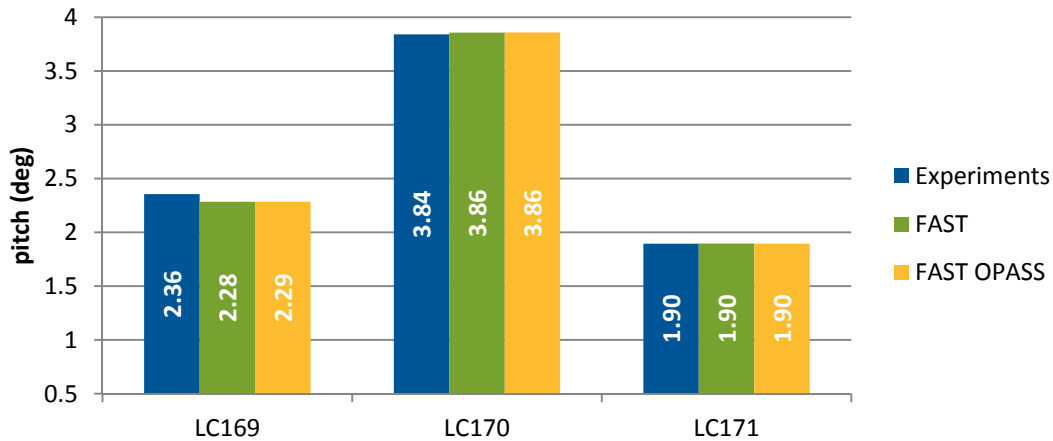


Figure 42: Steady pitch position of the platform

Finally, Figure 43 presents the steady tension at the upwind line “L2”. Tension on LC169 was not recorded during the test case. Apparently, the mooring line models tend to over predict the tension, with maximum differences up to 7%.

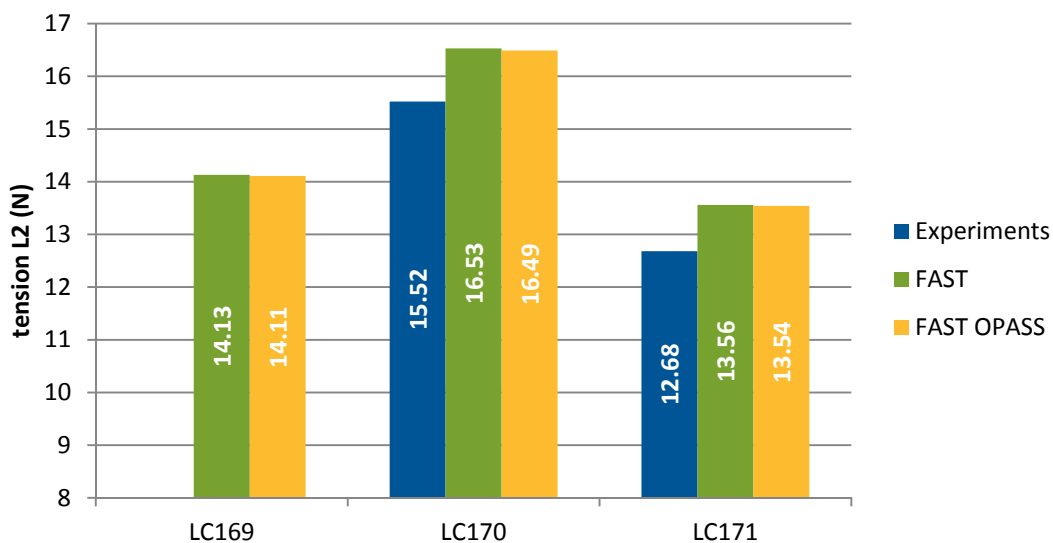


Figure 43: steady tension at fairlead "L2" (up-wind)

Constant wind and regular waves

In these cases, together with three constant wind speeds at 1.267 m/s, 1.699 m/s and 2.683 m/s (below rated, rated and over rated wind speed), regular waves are included with heights 0.07 m, 0.09 m and 0.11 m and period 0.969 s, 1.088 s and 1.327 s, respectively. The wind speeds are the same as in the previous section and the wave period and wave height are consistent with them as it was summarized in Table 6. Figure 44 shows the mean displacement in surge for each of the three cases, including the experimental results and the computations using FAST with the quasi-static mooring model and FAST with OPASS.

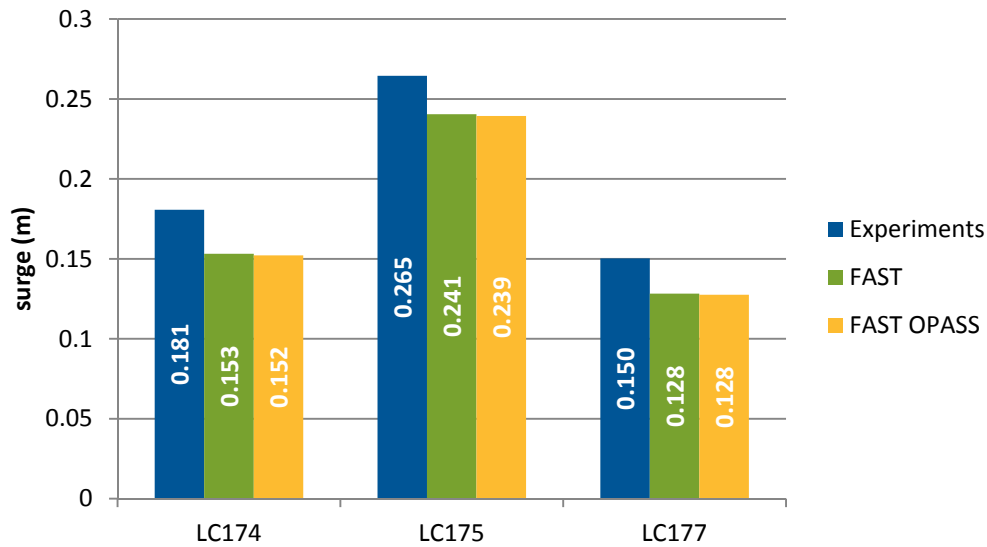


Figure 44: Mean position for the surge motion

It has to be noticed that the mean positions provided by the computational models are coincident with the displacements in the cases with only wind (Figure 41). The FAST simulations do not include second order effects in the hydrodynamics, and the regular waves provoke an oscillation of the platform around the mean displacement caused by the aerodynamic thrust. The experimental results present some differences with these computations: the mean surge displacement is higher for the three cases. The reason for this deviation is probably caused by the effect of mean wave drift forces. This is a second order effect that is neglected in the computations.

The mean wave drift effect can be estimated using the first order wave potential (Faltinsen, 1999). The mean wave drift force is related with the capacity of generating waves of the platform, this is modelled through linear potential theory and specifically considers the reflected wave caused by the platform as showed in the following equation where "R" is the wave reflection coefficient, ρ water density, $D_{Upper\ Column}$ is diameter of the column at the SWL and ζ_{wave} is the incident wave amplitude

$$F_{MDF}^{Pot} = \frac{1}{2} \rho g D_{Upper\ Column} (R \cdot \zeta_{wave})^2$$

Viscous effects on the platform splash zone also contribute to the mean wave drift force that is proportional to the relative vertical motion between the waves and the floater as can be seen on the equation, here C_D is the drag coefficient for the column, u_x is the horizontal wave velocity at SWL, \dot{x} surge velocity of the floater and z is the heave motion of the platform center of mass:

$$F_{MDF}^{Vis} = \frac{1}{2} \rho C_D D_{Upper\ Column} (u_x - \dot{x}) |u_x - \dot{x}| (\zeta_{wave} - z)$$

Figure 45 shows a comparison between responses of the system for all loads cases adding the viscous and potential term on surge balance of equation with first order wave potential theory.

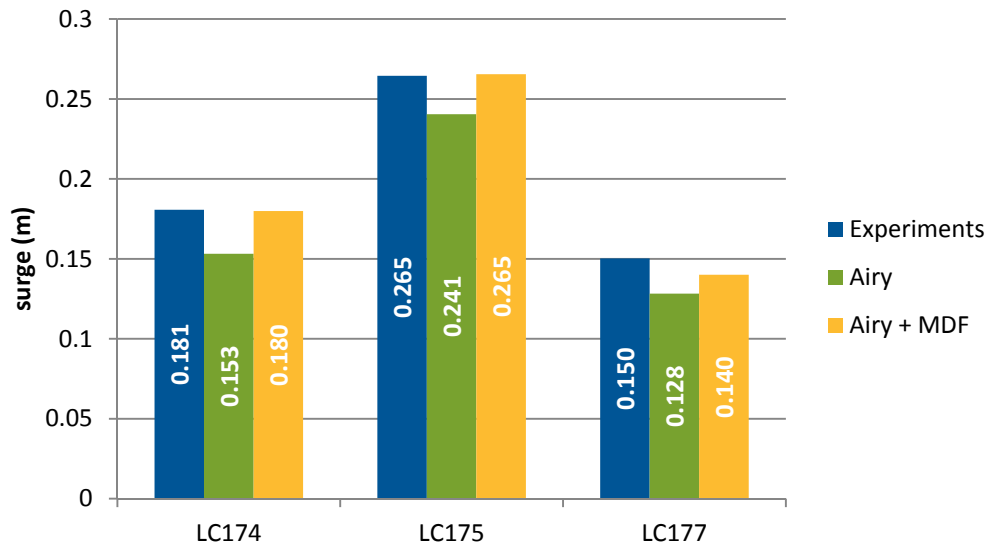


Figure 45: Effect of mean wave drift force on surge

In order to approach the FAST results to the experimental mean a reflection coefficient was assumed for the potential term of the mean drift force. The values applied were $R=8\%$ for the LC174, $R=4\%$ for the LC175 and $R=2\%$ for the LC177. The reduction in magnitude of the reflection is related with the increase in height of the incident wave. As the wave height increase respect the structure it tends to goes moving the floater without generates any wave reflection instead of hit and diffracts around the columns.

Even that was not possible to obtain a wave measurement of the reflection coefficient during the experiments, the coefficients values could be assumed based on the load case videos where clearly is identifiable a wave scatter pattern moving away from the structure.

This also means that for large wave heights the MDF it's going to be purely by the viscous term as there is not going to be wave reflection.

However, in order to totally match the results it is required to develop a more complete and detailed second order wave model that takes into account the complete kinematic of the structure and the high order wave potential, because according to Faltinsen (1999) the mean drift force could result into a direction opposite to the wave direction as a result of the interaction between the incident wave length, phase and the floater length.

Figure 46 presents the amplitude of the surge motion once the steady state has been reached. The amplitude of the motion depends on the wave amplitude. The case LC174, with an incident wave height of 0.07m, presents the smallest surge amplitude and the case LC177, with a wave height of 0.108m, presents the highest.

The amplitude of the surge motion is small, and although differences between experiments and computations are in the range of millimeters, the relative differences can be important. These discrepancies could be produced by disagreements between the specified wave height and the resultant wave height at the tank, small differences in the computational parameters and the real setup of the experiment (for example in the mooring lines) and also the influence of the mean drift forces that are neglected in the computations.

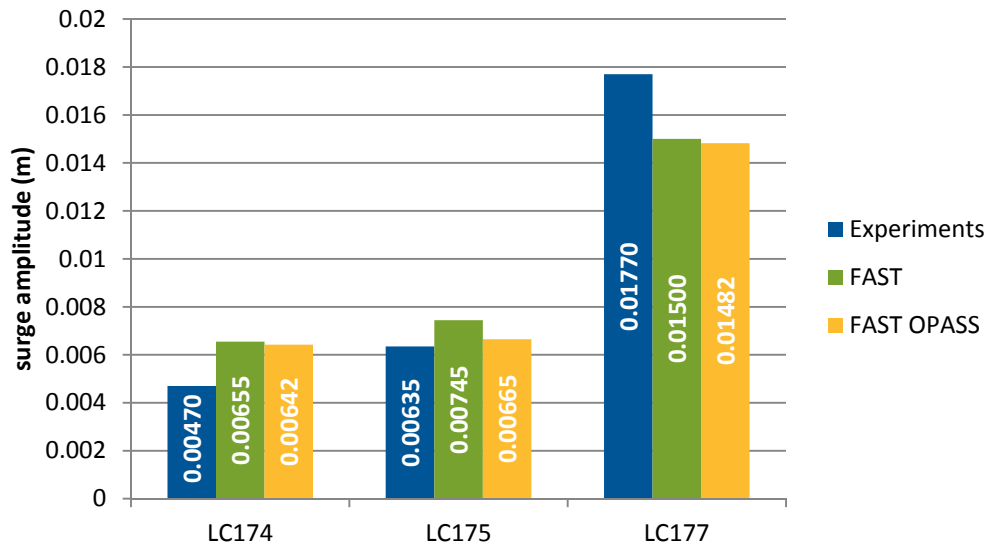


Figure 46: Amplitude for the surge motion

Figure 47 shows that the mean pitch from computations agrees very well with the experimental response for all wind speeds and waves. The mean pitch displacement is determined by the aerodynamic loading, more than by the waves, and results are very similar to the value of the steady pitch in the cases with only wind (Figure 42).

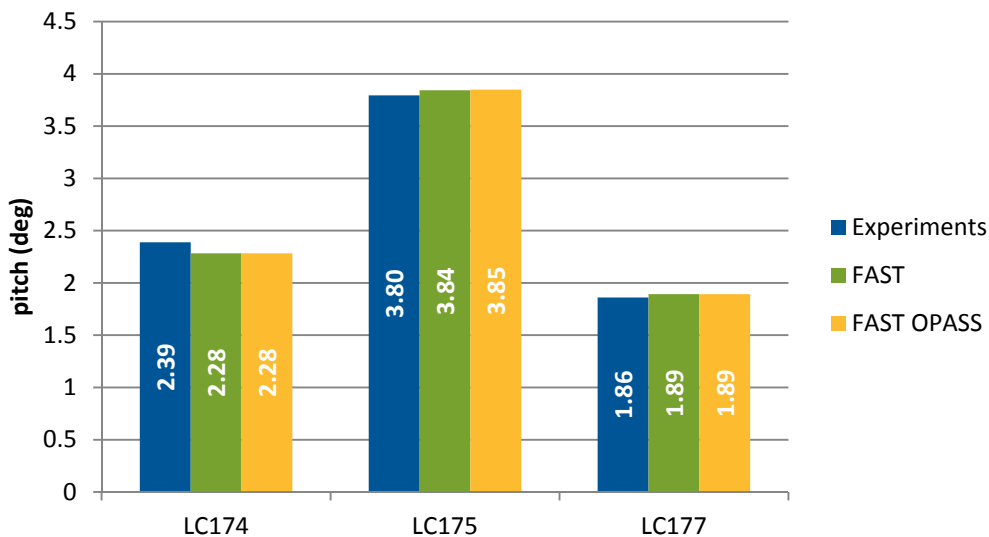


Figure 47: Mean position for the pitch motion

The amplitude of the pitch motion is showed in Figure 48. This amplitude is small (less than 0.9 deg for all the cases), because the pitch motion is only slightly affected by the waves. There are some discrepancies in the amplitudes between the experiments and the computations, which can be produced by small differences between the parameters of the computational model and the experimental scaled model (for example in the inertia of the system) or due to the discrepancies in the damping level.

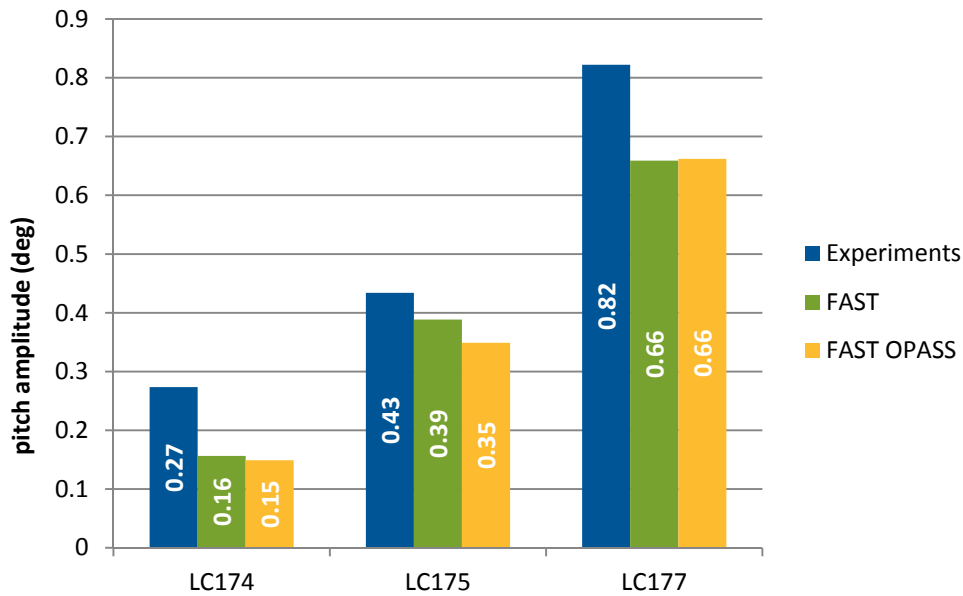


Figure 48: Amplitude of the pitch motion

Finally, the mean tension on the fairlead “L2” is presented in Figure 49, both for the experiments and the simulations. The agreement between the mean tension value from experiments and computations is good, with discrepancies in the range of 3-4% for all the cases. Again, the computational mean value is consistent with the results provided by the cases with only constant wind (Figure 43).

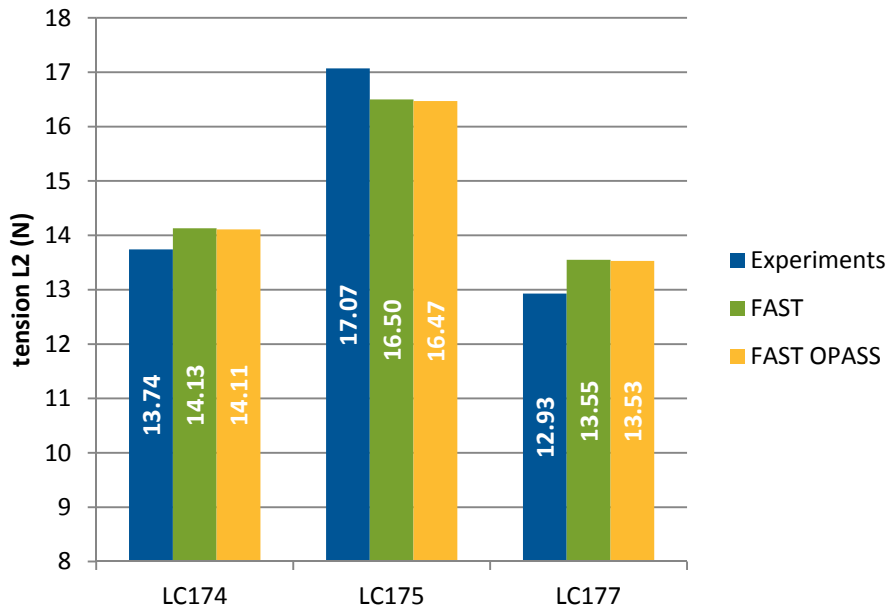


Figure 49: Mean tension at fairlead for line 2

Figure 50 shows the amplitude of the tension in the line 2 for the three cases considered. There is a clear disagreement between the experimental results and the predictions using the quasi-static mooring lines model and the dynamic model OPASS. Simulations using both the quasi-static

model provide much lower tensions at the line. This is what can be expected, because this model neglects important dynamic effects that have influence on the lines tension, such as the inertia or the hydrodynamic drag. In contrast, the simulations using OPASS provide significantly higher tensions, because they include the hydrodynamic loads and the inertia in the computation of the tension. Nevertheless the resulting tensions are higher than experiments. This indicates that drag coefficients, taken from guidelines for the full scale moorings, may be not correctly tuned for the scaled model.

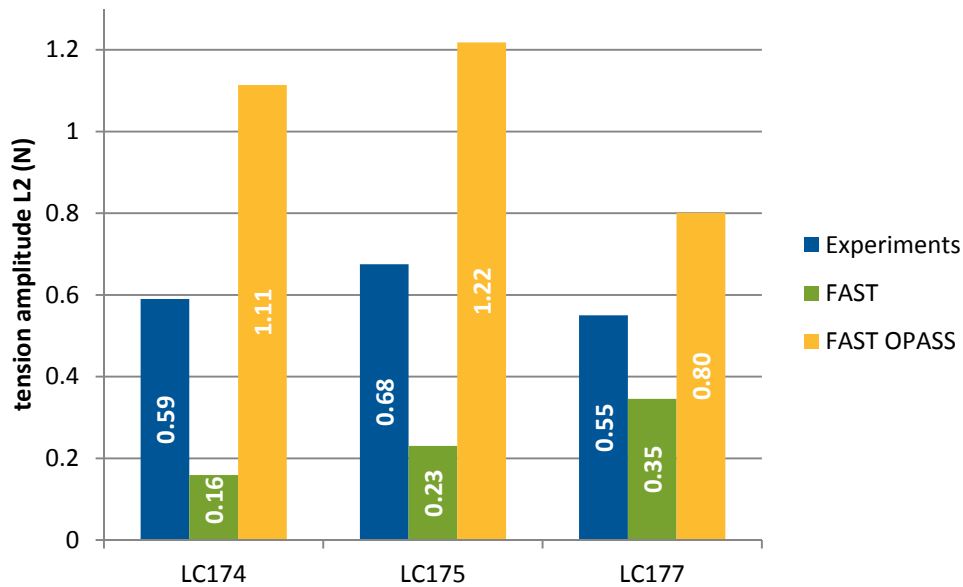


Figure 50: Amplitude of the fairlead tension for line 2

Free decay tests under constant wind

In these cases, once the platform has reached the steady position under the constant wind, a displacement is applied in pitch and then, the platform is released. The platform pitches until the steady position is reached again. In the experiments, the ducted fan reacts and varies the applied thrust to take into account the change in the aerodynamic force due to the relative velocity of the rotor in the constant wind field. This effect damps the platform response in pitch, and is called aerodynamic damping. Figure 51 presents the free decay pitch response with no wind loading and also with the loading corresponding to three constant wind speeds (1.27, 1.7 and 2.68 m/s respectively).

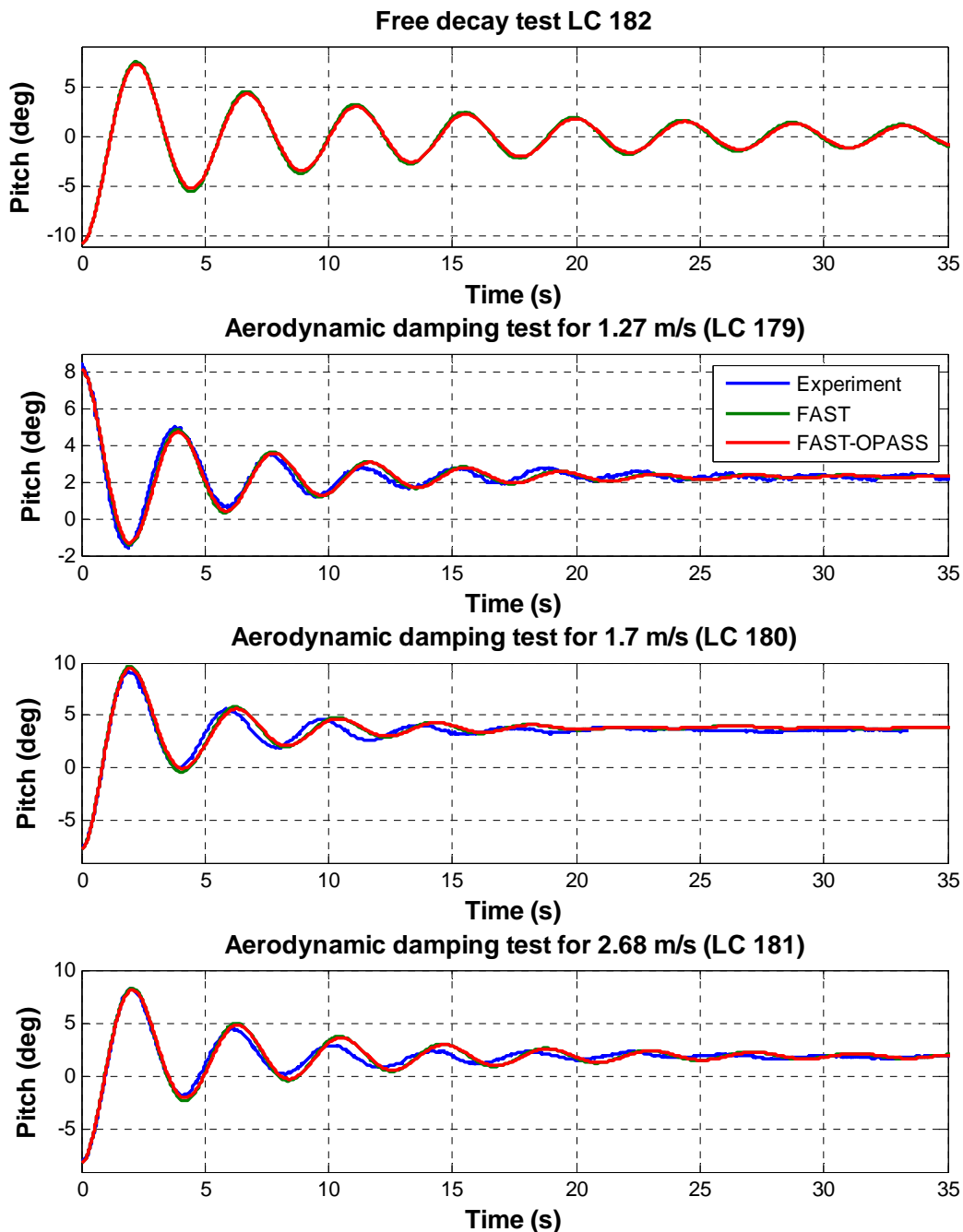


Figure 51: Pitch perturbation after the platform reaches it steady state for different wind speed

It can be observed how the pitch response of the platform damps faster under wind loading in comparison with the free decay with no wind, LC182.

Computations and experimental results show a good agreement for the three wind speeds. The level of damping due to aerodynamics is very similar in experiments and computations, in particular for the larger oscillations at the beginning of the case. Some slight differences in the amplitude arise as the response damps, in particular for the case with wind speed over rated. For the below rate case, this differences are the smallest. There is also a slight difference in the frequency of oscillation between computations and experiments for the three cases, probably due to a small error in the position of the global center of gravity that can affect the pitch natural

frequency. The mooring model does not affect too much the platform motion in pitch, and both simulations (quasi-static and dynamic mooring models) are very similar.

Constant wind and irregular waves

In these cases, different irregular sea states defined by a peak period T_p and significant wave height H_s according to the JONSWAP spectrum are combined with different constant wind velocities as it was described in Table 6.

Test case LC186

In this case, a scaled irregular sea state $H_s = 0.07\text{m}$ and $T_p=0.969\text{s}$ was combined with a wind velocity of 1.267 m/s .

Figure 52 compares the Power Spectral Density (PSD) of the wave height in case LC186 for the experiments and the FAST simulation. There is a good agreement in the frequency range between 0.6 and 2.5 Hz. Below that range, the experimental wave spectrum presents more energy.

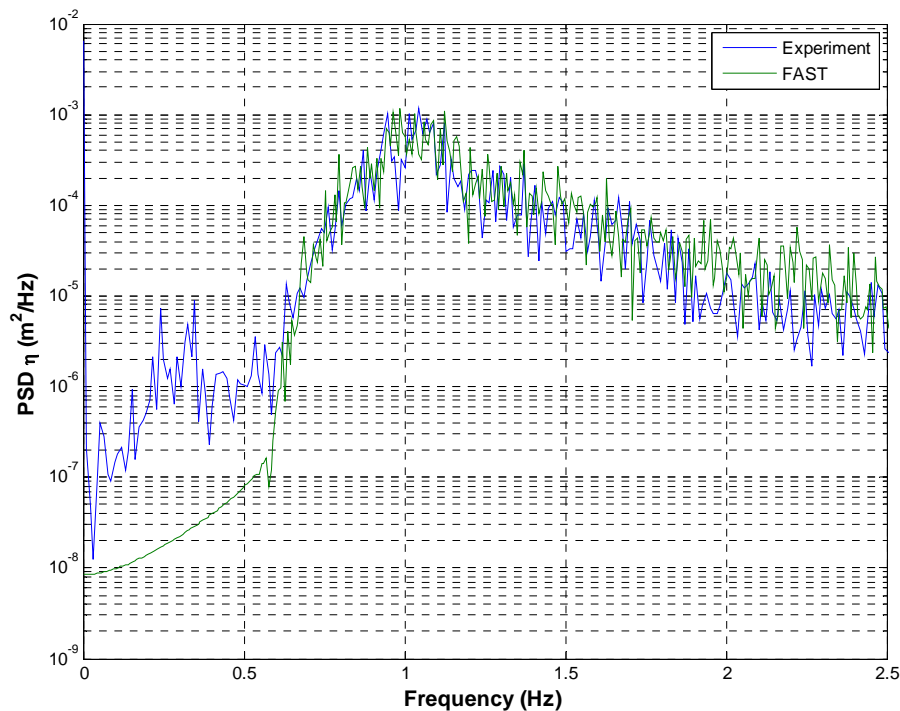


Figure 52: Wave height PSD comparison for test LC186

Figure 53 presents the PSD for the pitch and surge motions and also for the fairlead tension of line 2. Three different series of data are plotted in each of the graphs in the figure. One of the series is measurements from the tests and two are computations with FAST: one with the quasi-static mooring model and the other one with the dynamic mooring model OPASS.

The figure shows that the PSD's around the wave peak period for the surge and pitch motions agree well between experiments and the computations with both mooring line approaches. In contrast, for the low frequencies, there is a disagreement between the measurements and the computations both for the pitch and the surge motions. The natural frequencies of these degrees of freedom are located in this low frequency region: 0.054 Hz for surge and 0.25 Hz for pitch. The experimental measurements show higher excitation of these natural frequencies than the computations. The computational model does not include second order hydrodynamics, which could be relevant for the platform dynamics. This non-linear effect is probably the cause for the

higher energy in the experimental data for the lower frequency region of the spectrum, when compared with the computations, where linear hydrodynamics have been used.

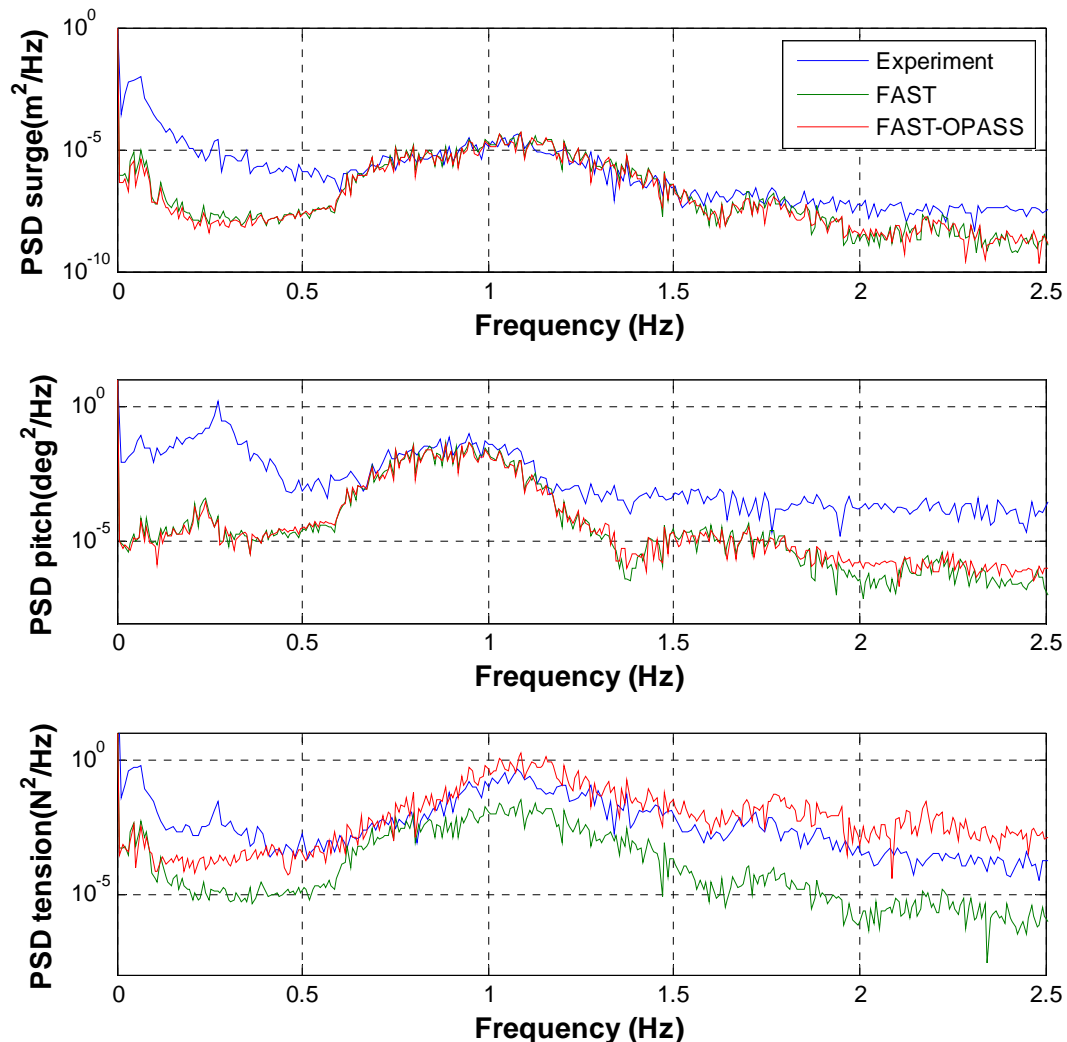


Figure 53: PSD for surge, pitch and mooring tension for test LC186

A similar effect caused by second order effects was reported in the DeepCwind semisubmersible test campaign. Figure 54 shows the surge power spectrum for a case with irregular waves from the DeepCwind semisubmersible test campaign from (Robertson A. , et al., 2013) compared with simulations. These simulations include linear potential theory, 2nd order potential theory and an additional simulation where second order effects are included based on Newman’s approximation. It can be observed that at low frequencies the linear potential computation underestimates the response of the platform. Once second order effects are included, the agreement of the computations with the measurements is much better.

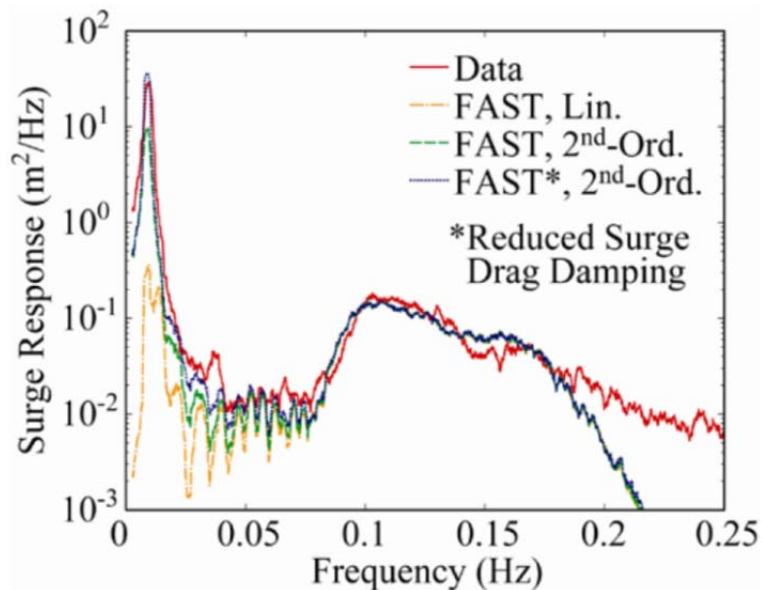


Figure 54: Comparison of simulated to experimental surge response of a semi for an irregular wave-only test ($T_p=7.5$ s) (Robertson A., et al., 2013)

The PSD of the tension, in Figure 53, shows that the quasi-static approach is underestimating the tension in all the frequency range, in comparison with the experiments. This is what can be expected, because the quasi-static model is not considering dynamic effects that influence the line tension as inertia or hydrodynamic drag. The computations using OPASS show a better agreement with measurements around the wave peak spectrum, although it is slightly higher than the experimental data. This is consistent with Figure 50 and suggests that drag coefficients could be better tuned in the dynamic mooring line models. At low frequencies, the tension is underestimated with respect to the experiments. Once more, the lack of second order effects in the computations could be the cause for this lower response in the tension at low frequencies.

Test case LC187

In this case the irregular sea state is defined by $H_s = 0.09$ m and $T_p=1.088$ s. The constant wind velocity is 1.699 m/s. Figure 55 presents the PSD of the platform surge and pitch motions in comparison with the computations. Similar comments to the previous case can be made for this Figure. Surge and pitch motions present a good agreement with the experiments around the peak spectrum frequency. At low frequencies, the lack of second order effects in the simulations introduces differences with the measurements. Figure 55 also shows the PSD for the tension. It can be observed that the dynamic mooring model provides higher level of tension and a better agreement with the experimental data than the simulation using quasi-static mooring model.

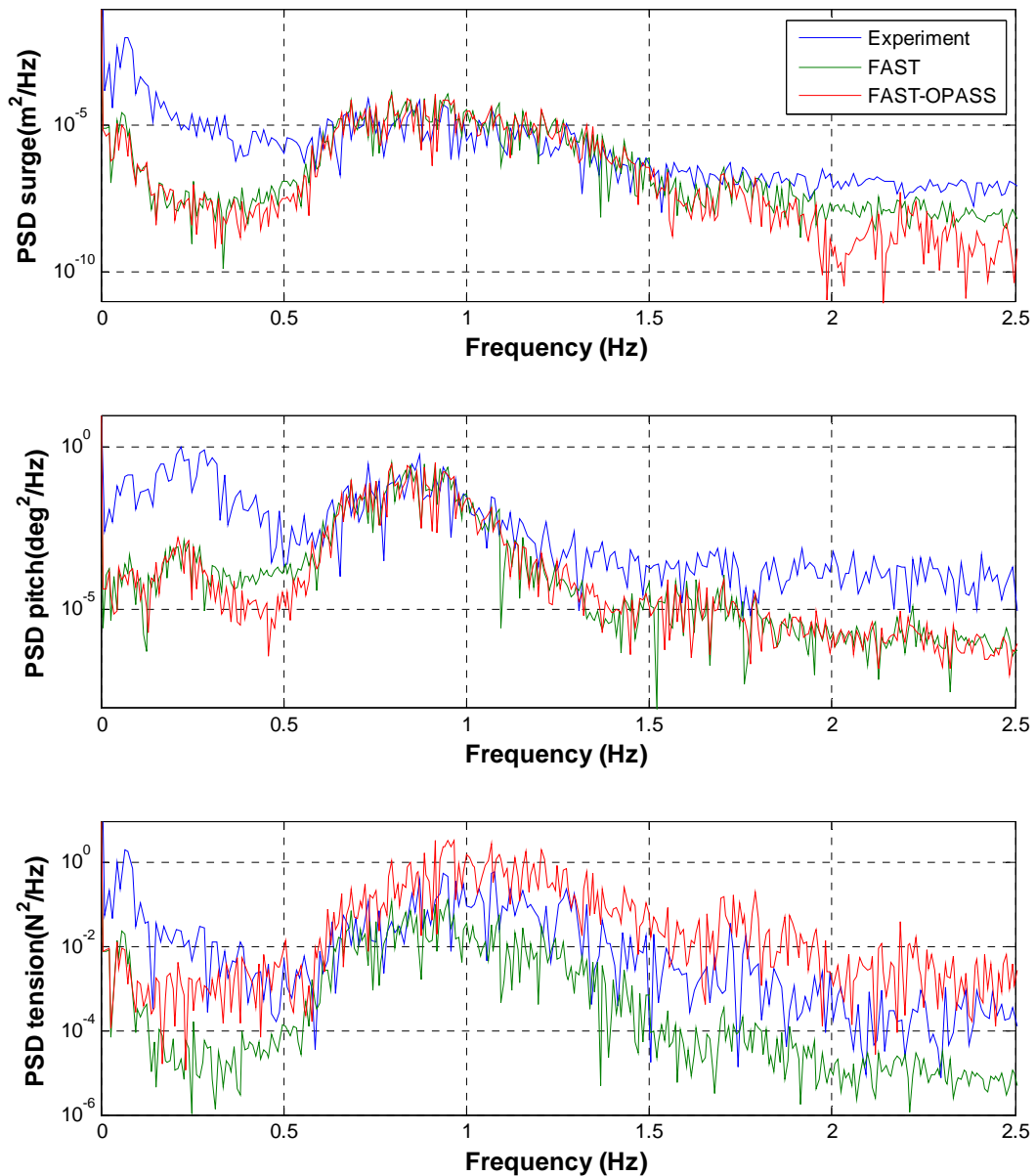


Figure 55: PSD for surge, pitch and mooring tension for test LC187

Test case LC188

Finally, the last case with constant wind and irregular waves is defined by a significant wave height $H_s = 0.11$ m, a peak period $T_p = 1.327$ s and a wind velocity of 2.683 m/s. Figure 56 presents the PSD of the platform surge and pitch motions in comparison with the computations. The conclusions are similar than in the previous cases. The platform motions agree well around the peak spectrum frequency, although neglecting second order effects in the simulations causes differences with the measurements at low frequencies. Figure 56 also shows the PSD for the tension. Simulation with the dynamic mooring model gives a better agreement with the experimental data than the simulation using quasi-static mooring model.

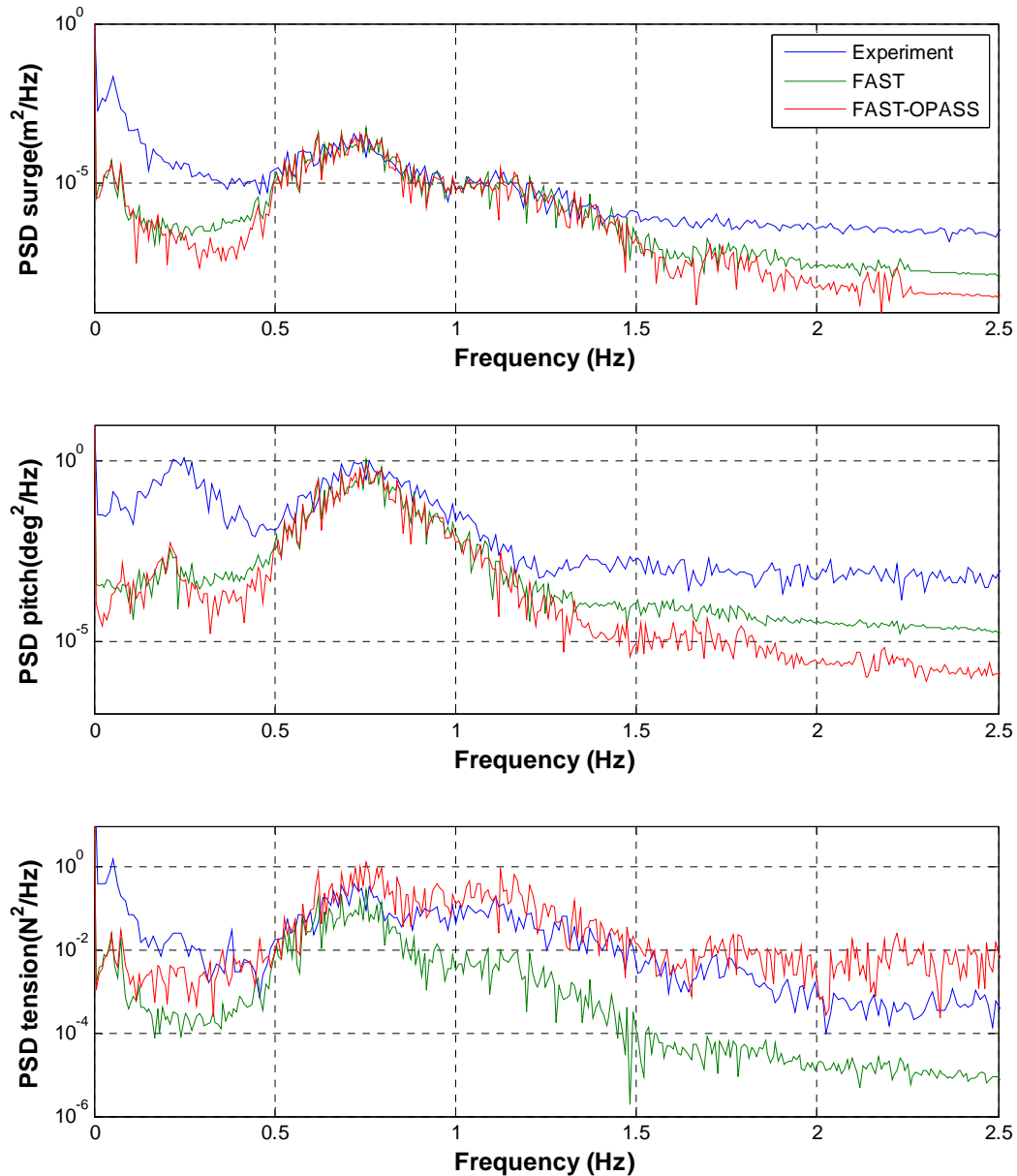


Figure 56: PSD for surge, pitch and mooring tension for test LC188

Turbulent wind and irregular waves

In this last set of comparisons between experiments and simulations, cases including combined turbulent wind and irregular waves are discussed.

Test case LC183

In the test case LC183 a scaled irregular sea state with $H_s = 0.07m$ and $T_p = 0.969s$ was combined with a turbulent wind with a mean velocity of $1.267 m/s$, that corresponds to the below rated region. The PSD for the platform surge and pitch can be seen in Figure 57. The agreement between the surge and pitch measurements with the computations is very good in all the range of frequencies. It has to be noted here, that in the results presented in the previous section, where the irregular waves were combined with a constant wind instead of a turbulent wind, there was an

under-prediction of the motion. This variance was located at the low frequency region, where the surge and pitch natural frequencies are located. As it was discussed, this was probably caused by the hydrodynamic second order effects that are not taken into account in the computations. In the cases of this section, where the turbulent wind is included, it is very noticeable that the agreement between simulations and measurements is very good also at low frequencies. The wind is a low frequency excitation force and it dominates the platform motion at low frequencies, masking the differences between experiments and computations due to second order effects. The agreement around the surge and pitch natural frequencies (0.05 Hz and 0.24Hz, respectively) is also good, although for the pitch the experimental natural frequency seems to be slightly higher than the computed one. It has to be remarked that these results show the very good performance of the SiL when introducing aerodynamic loading in tests.

The PSD of the line tension is also shown at the lower part of Figure 57. The introduction of turbulent wind results on a good agreement at low frequencies between measured tensions and computations, hiding differences due to second order hydrodynamics. Around the wave peak frequency (1Hz, approximately), the agreement of the simulation using a dynamic mooring line is better than the one using the quasi-static approach. Nevertheless, the tension predicted by the dynamic code OPASS is slightly higher than the measurements, indicating that drag coefficients may have to be tuned for the scaled tests conditions. The surge and pitch natural frequencies are visible at the spectrum, as peaks of tension, indicating the influence of these motions over the line dynamics.

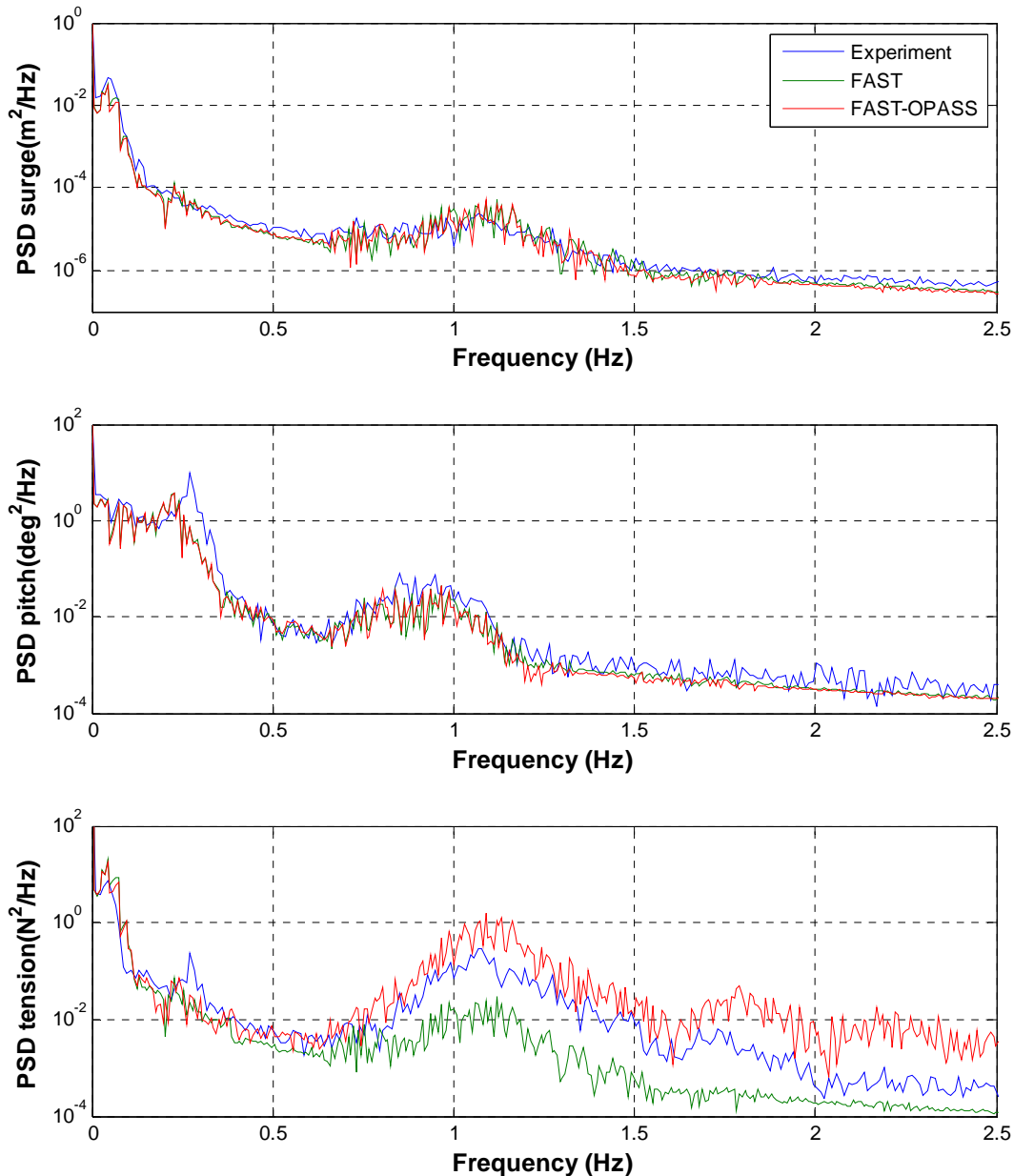


Figure 57: PSD for surge, pitch and mooring tension for test LC183

Test case LC184

In this case LC184 the irregular sea state is defined by a significant wave height of $H_s = 0.09\text{m}$ and a wave peak period $T_p = 1.088\text{ s}$. The mean speed of the turbulent wind is 1.699 m/s . The wind speed corresponds to the rated wind and thus, the rotor thrust is around the maximum value. Similarly to the previous case, Figure 58 shows that the agreement between the computed and the experimental platform motions is very good in all the range of frequencies. For the line tension, there is also a good agreement, in particular for the computations using the dynamic model, although the tension is overestimated around the wave peak period. This could indicate the need of a slight decrement of the drag coefficients.

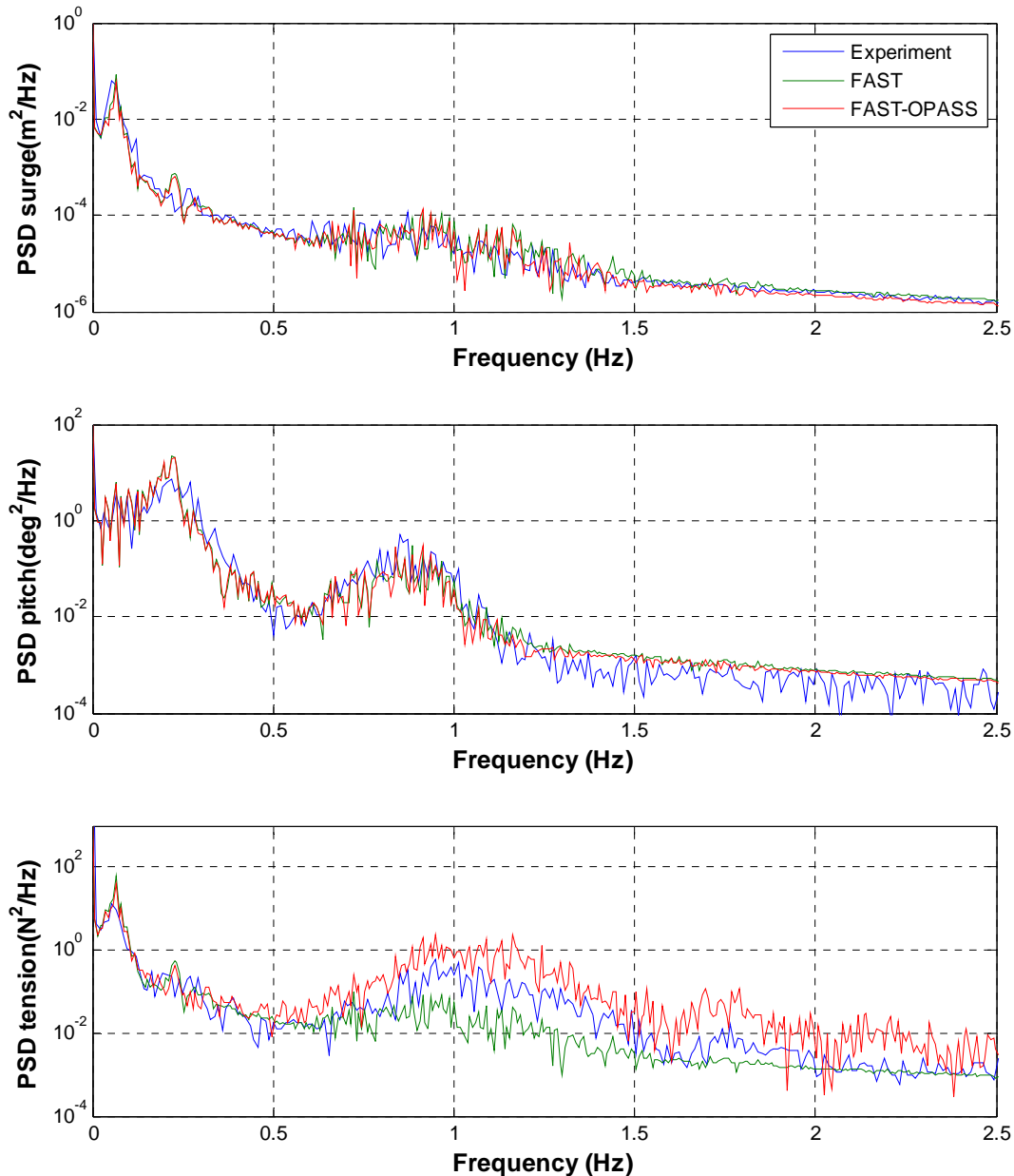


Figure 58: PSD for surge, pitch and mooring tension for test LC184

Test case LC185

Finally, the case LC185 corresponds to an irregular sea state with $H_s = 0.11\text{m}$ and $T_p = 1.327\text{ s}$. The mean speed of the turbulent wind is 2.683 m/s , which correspond to the pitch controlled region. In this region, the aerodynamic rotor thrust is lower than around the rated wind speed area. In these conditions, Figure 59 shows that a slight disagreement in the surge and pitch motions arise at low frequencies, indicating that, as the rotor thrust decreases, the second order hydrodynamic effect may become more important and has an impact on the platform dynamics. Figure 59 also presents a comparison of the tension PSD for the experimental and the computational results. Again, the computations using the dynamic mooring line model approaches better the measurements than those using the quasi-static, although in this case, the tension tends to be lower. At low frequencies, the tension provided by both mooring models is below the

experiments. In this region, second order hydrodynamics may become again important due to the decrease of the rotor thrust at over rated wind speeds.

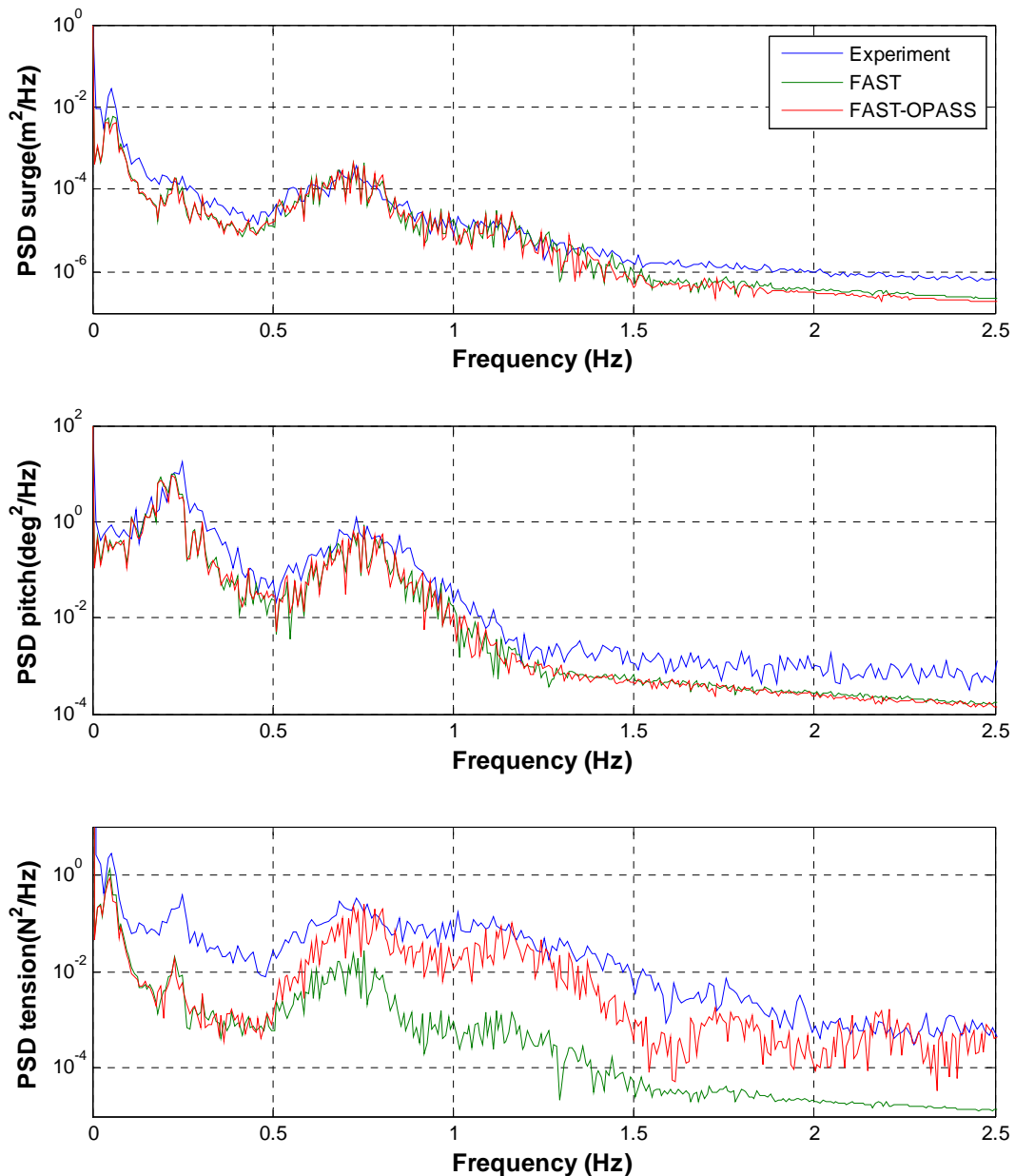


Figure 59: PSD for surge, pitch and mooring tension for test LC185

Software in the Loop (SiL) performance

In this section we want to make a few comments on the performance of the SiL methodology that was used for the inclusion of the scaled aerodynamic thrust in the considered test cases.

To illustrate the SiL's performance, we have introduced Figure 60 and Figure 61, showing the PSD of the surge motion for two cases. These cases have the same irregular wave ($H_s = 0.09\text{m}$, $T_p = 1.088\text{ s}$) but one of them has a constant wind speed of 1.699 m/s (Figure 60) and the other one a turbulent wind speed with mean wind speed of 1.699 m/s (Figure 61). Similarly, Figure 62

and Figure 63 show the PSD of the platform pitch motion for the same cases with constant and turbulent wind. It has to be mentioned that the same turbulent wind file was used in the SiL computations for the experiments and in the simulations using FAST-OPASS.

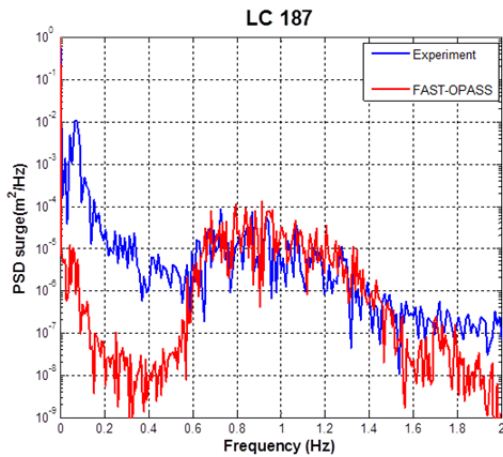


Figure 60 – PSD of the surge motion with irregular waves and constant wind

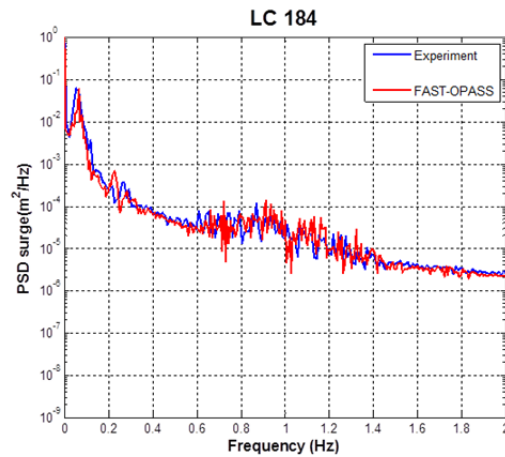


Figure 61 – PSD of the surge motion with irregular waves and turbulent wind

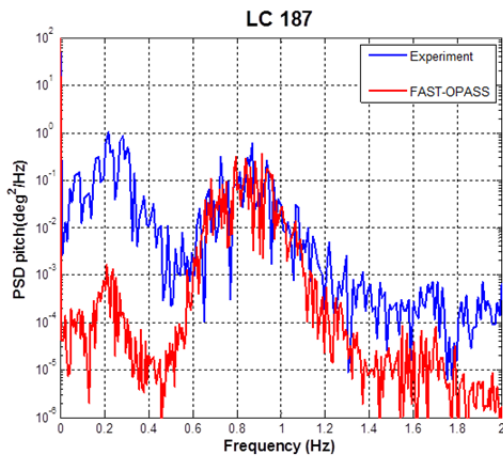


Figure 62 – PSD of the pitch motion with irregular waves and constant wind

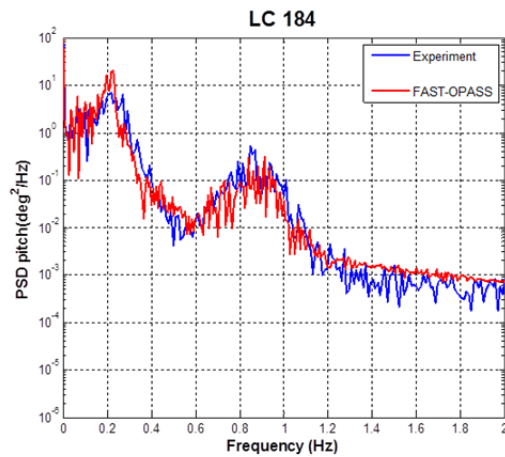


Figure 63 – PSD of the pitch motion with irregular waves and turbulent wind

These comparisons show that the SiL is able to capture the influence of the turbulent wind on the motions of the platform. The wind is a low frequency loading, and therefore its effect is clearly observed below 0.6 Hz.

In the case LC187, where the wind is constant, the differences at low frequencies between experiments and computations are clear (Figure 60 and Figure 62). In this case, hydrodynamics govern the platform motion in all the frequencies, and the lack of non-linear hydrodynamics in the computations introduces differences with measurements for the low frequency region. When turbulent wind is included, the motion of the platform at low frequencies is governed by this loading. This can be clearly observed when Figure 60 and Figure 61 are compared for the surge

motion and also when Figure 62 and Figure 63 are compared for the pitch motion. As can be observed, the match between the aerodynamic loadings introduced using the SiL method in the experiments and the computation is very good. This shows the good performance of the system during the test campaign and its capability to mimic aerodynamics.

Conclusions of the validation based in the model with SiL and a ducted fan force actuator

A ducted fan and the software-in-the-loop (SiL) methodology was applied to the semisubmersible scaled model to integrate the rotor aerodynamic thrust in the tests.

The experimental data was compared with computations of FAST and a quasi-static mooring model and also with computations of FAST coupled with the OPASS dynamic mooring line simulator.

The free decay tests were used to tune the computational models. The results showed that the scaled experimental model and the computational model in FAST have equivalent natural periods, hydrostatic stiffness and mooring stiffness. The pitch free decay tests with constant wind showed a similar level of aerodynamic damping in the experiments using SiL and the computations.

The steady wind test with no waves showed that simulations and experiments were responding with the same constant pitch. For the surge motion, the differences were higher, but below 10%. Floating platforms present lower stiffness in surge than in pitch, making displacement more sensitive to differences in the forces. The computed and measured tension agreed well, with differences below 7%.

In the cases with constant wind and regular waves, the experimental surge displacement are higher, probably due to mean drift forces that are not captured by the simulation code. In addition, although the mean value of the tension is well predicted, the amplitude predicted both, by the quasi-static and also the dynamic approaches are different. In particular, the dynamic computations overestimate this tension. This could indicate that the drag coefficients, taken from the guidelines, may not be representative of the scaled testing conditions.

The cases with irregular waves and constant wind were analysed using PSD. The main differences in the measured and computed platform motions arise at low frequencies. These differences are caused by the lack of second order effects in the FAST version used, which produced an underestimation of the platform motion at low frequencies. As expected, the tensions computed with the dynamic code matches better the experiments than the quasi-static.

The importance of second order effects suggests the convenience of measuring the wave height in front of the platform to characterize the wave refraction and thus, estimate the importance of second order hydrodynamics.

In the cases combining irregular waves and turbulent wind, the platform motions at low frequencies are dominated by the aerodynamic thrust, masking the differences due to second order hydrodynamics. In these cases the agreement between computations and experiments is very good in all the range of frequencies. This fact also demonstrates the good performance of the SiL approach to include the aerodynamics on the experiments, including the effect of the control strategy and the turbulent winds.

2.5 Aerodynamic High-Fidelity Simulations

The CFD solver FLOWer was used to simulate the model offshore wind turbine. It was planned to validate the numerical results with the experimental results. Due to a lack of measurement data regarding the wind conditions (jet flow) and the forces and moments on the rotor a validation of the simulations was not possible.

To evaluate the influence of the influence of grid resolution on the CFD results, a grid convergence study has been performed at rated tip speed ratio using a 1/3 model of the turbine. Additionally, the turbine has been simulated at different pitch angles and the aerodynamic behavior has been analyzed.

Instead of validating the code with the measurement data, CFD simulations have been applied to quantify the influence of the jet flow on the aerodynamic forces on the turbine. Therefore, the turbine has been simulated in uniform inflow as well as in the jet flow. As detailed measurement data of the jet flow is only available for significantly higher wind speeds, a velocity distribution at the wind generator outlet has been assumed and prescribed in the simulation.

From two test cases the turbine motion has been extracted and analyzed. A short sequence including high amplitudes has been extracted and prescribed in the CFD simulation and the resulting aerodynamic forces have been analyzed.

The Reynolds number based on rotational velocity ranges around 45000 for most of the blade. At this low Reynolds numbers laminar separation very likely occurs on the blade. As there is no transition measurement data available from the experiment, computed transition cannot be validated in this experiment. Moreover inflow turbulence has an influence on the transition point. Because of this reasons it has been decided not to consider transition at all and to perform fully turbulent simulations.

Blade surface smoothing and 1/3 model simulations

The quality of CFD simulations is depended of the quality of the CFD surface. The provided CFD blade surface had a remarkable dent close to the position of maximum chord length. This directly influenced the CFD results as it could be seen in the spanwise load distribution. As the dent in the blade surface was not present in the blades manufactured at POLIMI, but just in the CAD geometry, it was removed in the CAD. Figure 64 shows the original blade geometry as well as the modified blade geometry.

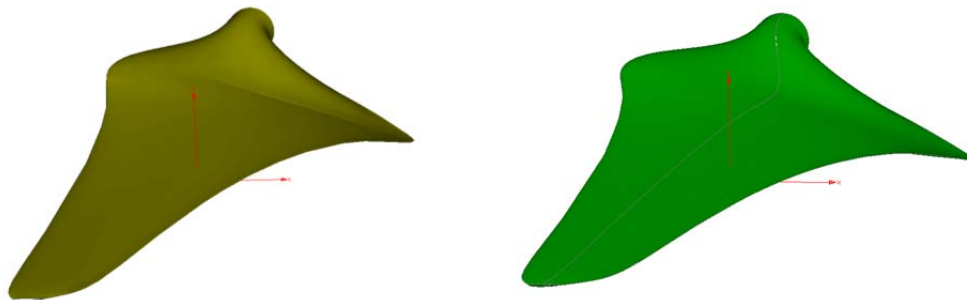


Figure 64 – Original blade surface with dent (left) and smoothed blade surface (right)

The influence on the spanwise load distribution is presented in Figure 65 and Figure 66. In the area of the dent, the curves are not smooth. By removing the dent, the fluctuations could be reduced significantly. It has to be mentioned, that there is almost no influence on the total loads.

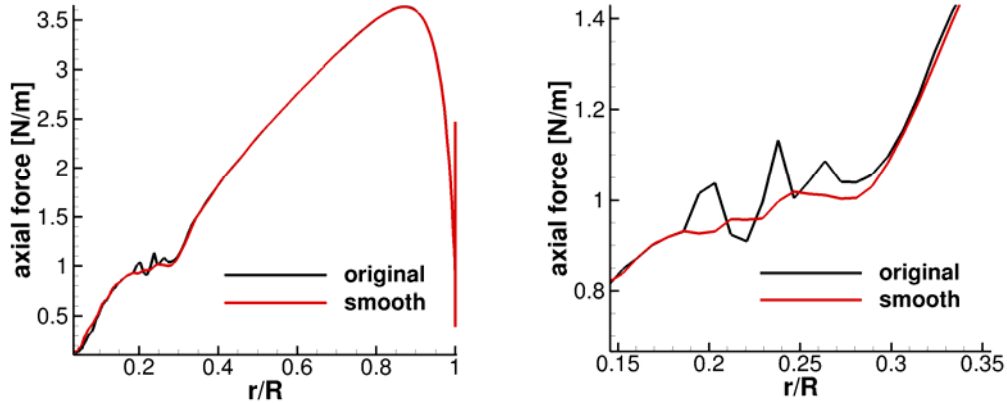


Figure 65 – spanwise axial force distribution: total (left), detail (right)

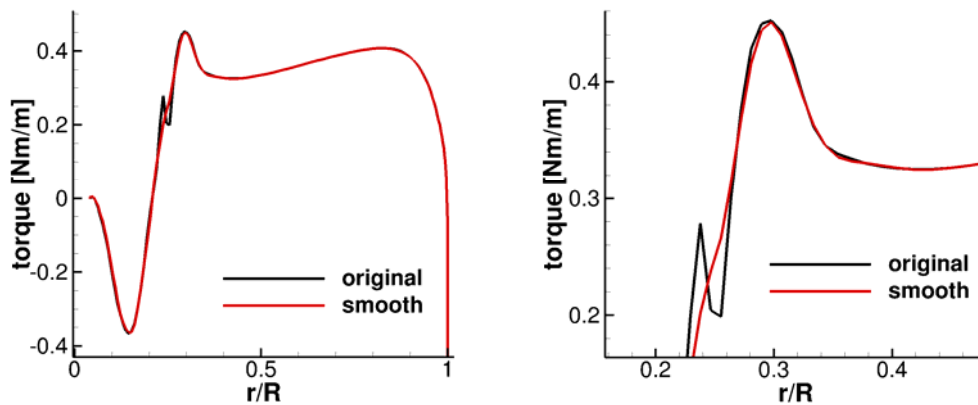


Figure 66 – spanwise torque distribution: total (left), detail (right)

This simulations have been conducted on a one third model of the turbine. By applying periodic boundary conditions, the turbine can be simulated using only one blade, this saves computational costs. Consequently, the computational domain has the shape of one third of a cylinder. This has been done on the one hand to evaluate the grid uncertainty and on the other hand to analyze the behavior of the rotor under rated tip speed ratio (TSR=7).

Figure 67 shows the background grid and the blade grid for the one third model simulation. The blade grid is meshed using a c-grid topology with fully resolved boundary layer.



Figure 67 – Background (left) and blade (right) grid of the one third model in FLOWer

To evaluate the grid uncertainty according to (Celik, 2008) three blade grids of increasing resolution have been compared. All three setups have been simulated unsteady as restart from a steady solution and the last three revolutions of 13 have been evaluated. The results have been

averaged to reduce the influence of unsteady effects on the results of the grid convergence study. Details on the number of cells in the investigated blade grids can be found in Table 8.

Table 8: Number of cells in the blade mesh for the grid convergence study

	Cells			
	Spanwise	Chordwise	Radial	total
Coarse	88	152	80	2,326,976
Medium	120	200	108	5,660,840
Fine	160	264	144	13,352,832

First, the grid dependency has been evaluated using the integral values. The result can be found in Table 9. For most of the loads the grid convergence index (GCI) is very low, but for thrust (Fx) and blade root bending moment (My) it is quite high. This is because there is no real trend in the results of the different grid resolutions. As My is directly dependent of Fx, it is clear, that both show the same behavior. A look into the spanwise distribution of the loads shows a little bit different result.

Table 9: Results of the grid convergence study, integral values of forces and moments.

	Fx [N]	Fy [N]	Fz [N]	Mx [Nm]	My [Nm]	Mz [Nm]
Coarse	2,84846	-0.41676	0.64553	0.31116	2.61802	0.02122
Medium	2.82556	-0.42238	0.64346	0.31071	2.59726	0.02132
Fine	2.79965	-0.42309	0.64010	0.30932	2.57467	0.02071
GCI _{fine}	11.59%	0.22%	0.74%	0.09%	21.53%	0.12%

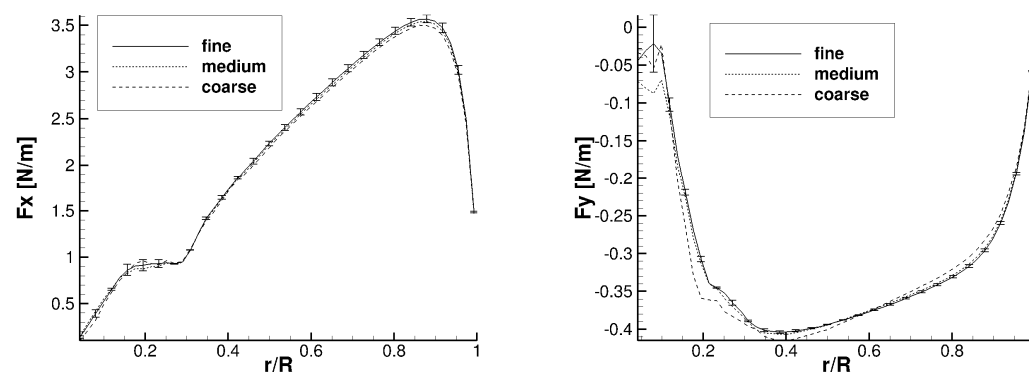


Figure 68 – Results of the grid convergence study, spanwise load distribution. GCI plotted as error bar for the finest grid level. Sectional load in axial direction (left) and tangential direction (right) of the rotor.

Figure 68 shows the average sectional axial force (Fx) as well as the average sectional tangential force (Fy) with respect to the radius as results of the grid convergence study. Besides the curves for three grid resolutions the grid convergence index is plotted in the form of error bars for the fine grid solution. For Fx, the average GCI is 2.28%, which is much lower than the GCI for the integral forces, but in the outer region of the blade where the highest forces occur, the GCI ranges between 1% and 1.5%. For Fy the result is even better, as it could be expected from the integral results. Medium and fine grid solution lie very close together, while the coarse grid solution deviates clearly from the other solutions. From this results, the medium grid has been chosen as

appropriate for the following studies. This means a save of more than 50% of the cells in the blade grid compared to the fine grid.

In a next step steady state simulations have been performed at different pitch angles to investigate the influence on thrust and power coefficient at wind speed 1.7 m/s and TSR 7. The resulting thrust and power coefficient over the pitch angle for the one third model simulations are presented in Figure 69.

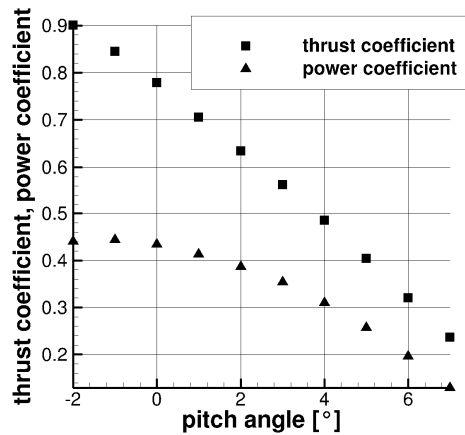


Figure 69 – Thrust and power coefficient from the steady one third model FLOWer simulation

pitch	C_T	C_P
-2°	0.901	0.441
-1°	0.845	0.444
0°	0.779	0.434
1°	0.705	0.413
2°	0.634	0.387
3°	0.563	0.354
4°	0.485	0.31
5°	0.404	0.257
6°	0.32	0.195
7°	0.236	0.129

Table 10: Thrust and power coefficient from the steady one third model FLOWer simulation

While the thrust coefficient curve is almost linear, the power coefficient has its maximum of 0.44 at -1° pitch. It corresponds to a thrust coefficient of 0.85.

The results have been compared to the DTU 10 MW turbine (Bak et al., 2016) and the results presented D4.2.4 in Figure 37. The DTU 10MW results have been obtained from BEM and CFD and for D4.2.4 the model turbine has been simulated with BEM using free transition XFOIL polars. For 0° pitch and TSR 7 a thrust coefficient of 0.825 and a power coefficient of 0.42 were obtained. These comparisons can be found in Table 11.

Table 11: Maximum thrust and power coefficients for model turbine simulated with FLOWer, BEM (Xfoil-polars) and the full scale turbine.

	Model turbine FLOWer	Model turbine BEM(Xfoil)	Full scale turbine
Pitchangle	-1°	0°	
C_T	0.85	0.825	0.84
C_P	0.44	0.42	0.495

In comparison to the other results the one third model FLOWer results of the model turbine appear reasonable. The thrust coefficient is in the same order and the power coefficient is considerably lower than in full scale. Compared to the BEM results of the model turbine the CFD thrust coefficient is a bit lower and the power coefficient a bit higher. The higher power coefficient can be explained by CFD approach that uses a fully turbulent boundary layer. For these low Reynolds conditions, this results in higher tangential force, as no laminar separation occurs and the flow stays longer attached. Figure 70 shows the spanwise load distribution with respect to the pitch angle of the blade.

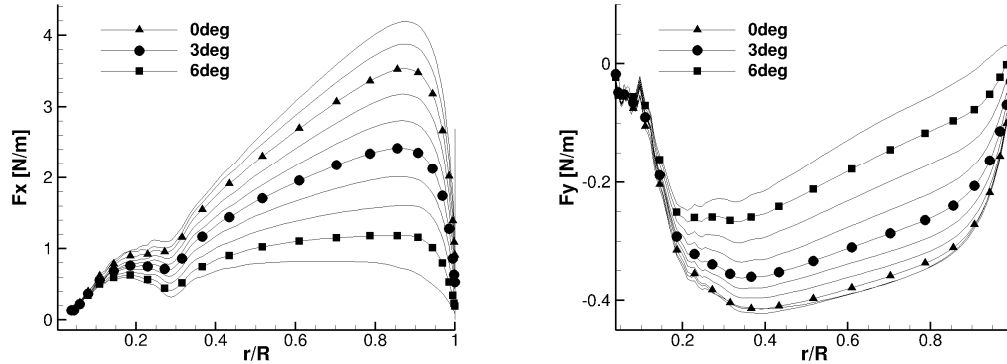


Figure 70 – Spanwise load distribution for various pitch angles from steady one third model simulations. Sectional axial force (Fx) (left) and sectional tangential force (Fy) (right).

Sectional Fx and Fy for the different pitch angles are shown in Figure 70. To compare the aerodynamic performance of the airfoils with the 2D airfoil polars used for the BEM simulations, the aerodynamic coefficients have been extracted from the FLOWer simulations. Therefore, the annular average sectional velocity in the rotor plane has been extracted from the CFD results using the method presented in (Johansen & Sørensen, 2014). From the local velocity the axial and tangential induction, as well as the angle of attack and lift and drag coefficients can be computed. Figure 71 shows the axial induction in dependency of the blade pitch angle, while in Figure 72 the local angle of attack, calculated under consideration of axial and tangential induction is displayed.

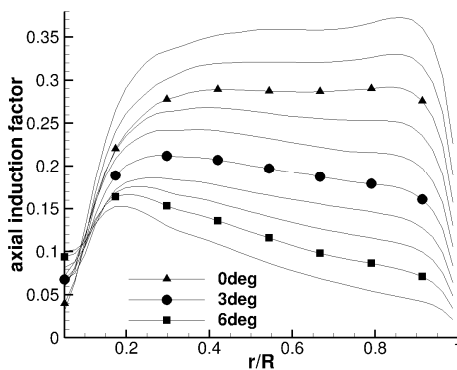


Figure 71 – Spanwise distribution of the axial induction factor obtained from CFD simulation

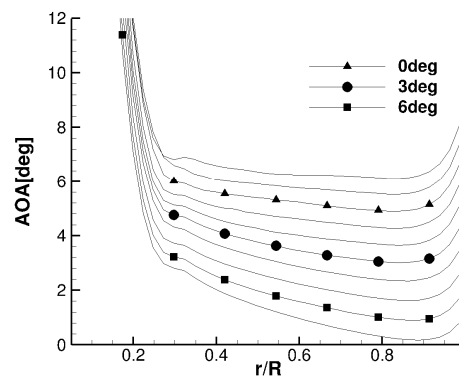


Figure 72 – Spanwise distribution of the angle of attack obtained from CFD simulation

Using the local velocity in the rotating frame of reference, the local c_l and c_d coefficient can be calculated. As they are calculated from 3D rotor results, they are influenced by 3D effects like tip loss. The results can be found in Figure 73 and Figure 74. Both, c_l and c_d show a linear behavior over a big spanwise range. In the tip region lift decreases and drag increases due to the tip loss. This looks quite reasonable. In the inner region, the uncertainty of the results increases. The used method calculates a negative drag in the region of $r/R = 0.3$. This is at least questionable, but the drop could be a result of 3 dimensional effect. It has to be mentioned that the calculation of the drag coefficient is very sensitive to changes in the calculated angle of attack. Additionally, the chord length is very high in this part of the blade, covering a much big part of the rotor area, compared to the outer region of the blade. Therefore, at least the extracted c_d values in the inner blade region should be handled with care.

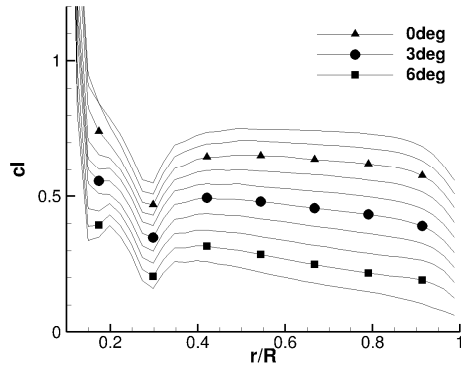


Figure 73 – Spanwise distribution of the lift coefficient obtained from CFD simulation

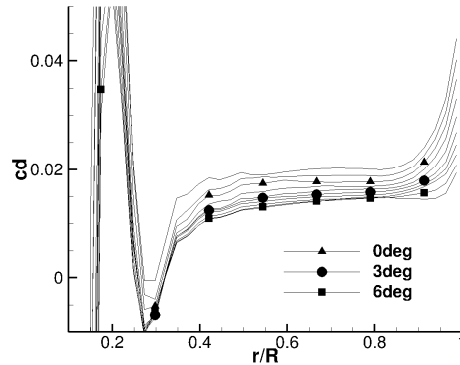


Figure 74 – Spanwise distribution of the drag coefficient obtained from CFD simulation

Because of this, in Figure 75 and Figure 76, only results from radial positions between 45% and 85% are shown. All this sections use the same airfoil, that's why they have the same airfoil data in the BEM simulation. In the figures the aerodynamic coefficients are plotted together with this airfoil polar. For c_l , the extracted points from the CFD simulations show a very linear behavior. For lower radial positions, the points lay a little bit lower, than for higher radial positions. The airfoil polar is lower below 2.5° AOA and higher above 2.5° AOA. For c_d a higher dependency on the radial position can be seen. Extracted drag coefficients are lower for inner radial positions. In most of the shown table, the drag coefficient of the Airfoil data is higher than the extracted drag coefficients. While CFD results show an increasing drag with the radius, drag decreases between 2° and 4° AOA in the polar.

The main reason for the general differences is the fully turbulent boundary layer in the CFD simulations. This leads to a better attached flow compared to free transition, which was used to create the airfoil data. Also 3D effects can change the behavior of the airfoil.

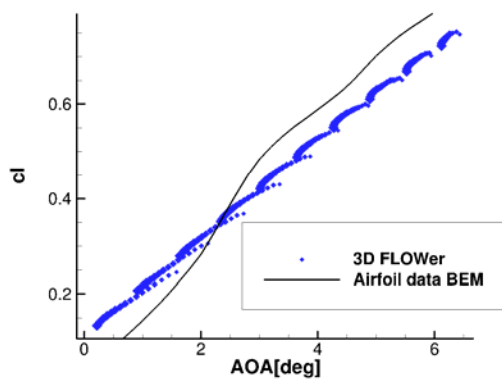


Figure 75 – Lift coefficient obtained from CFD simulation for radial positions between 45% and 85% and corresponding c_l curve from airfoil table. Size of symbols indicate radial position, size increasing with the radius.

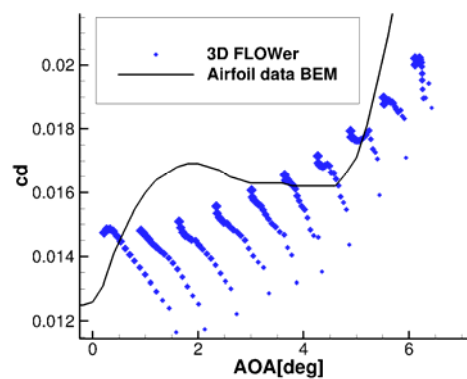


Figure 76 – Drag coefficient obtained from CFD simulation for radial positions between 45% and 85% and corresponding c_l curve from airfoil table. Size of symbols indicate radial position, size increasing with the radius.

Modelling of the jet flow

Consideration of the jet flow is not possible with most model based aerodynamic codes that are used in the integrated tools. In BEM approaches there is normally no way to define a jet as inflow condition for wind turbine simulations. Additionally, these tools would not be able to calculate the influence of the turbine on the jet flow and the resulting induction at the turbine would not be correct. Therefore, in BEM simulations uniform flow has to be applied as inflow condition when simulating the model wind turbine in this experiment.

CFD simulation allows a consideration of the jet flow and a comparison to uniform inflow conditions. The wind generator itself has not been modelled within this project, but it has been modelled by applying a prescribed velocity at the wind generator outlet. Unfortunately no measurement data was available at this position for low wind velocities. Because of this, flat plate boundary layer assumption has been used to take the velocity deficit at the wall into account. At the corners, the influence of both walls has been considered. Outside this boundary layer, a constant velocity, according to the specific loadcase, has been prescribed. The velocity has been prescribed without turbulence. The velocity distribution is plotted in Figure 77 and Figure 78.

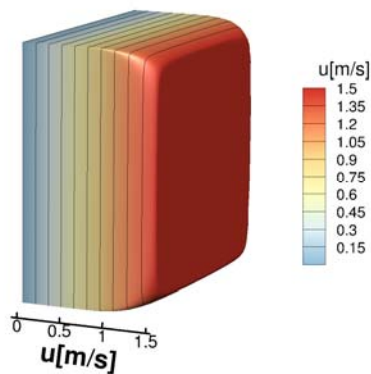


Figure 77 – Prescribed velocity distribution at the wind generator outlet, reference velocity = 1.48m/s

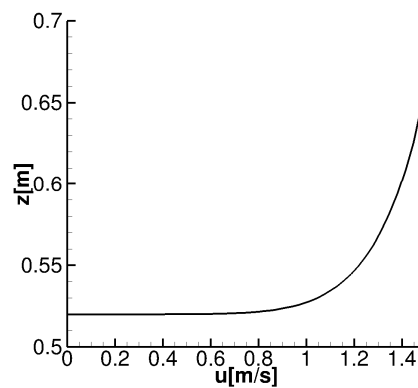


Figure 78 – Prescribed boundary layer profile in the middle of the wind generator outlet, reference velocity = 1.48m/s

Also, the inner of the wind generator has not been simulated, the outer shape has been considered in the CFD simulation. It has been set into the computational domain, using the chimera technique (Benek, 1983). In the area of interest, the background grid has been refined using a hanging grid node approach. The result is presented in Figure 79 where a detail of a cut through the computational domain is shown. In later simulations, the turbine will be placed 4m downstream of the wind generator according to the experiment. The mesh has been refined in the shear layer area of the jet and around the turbine. Additionally, a ground boundary layer mesh has been implemented in the area of interest. In total 14.8 million cells have been used.

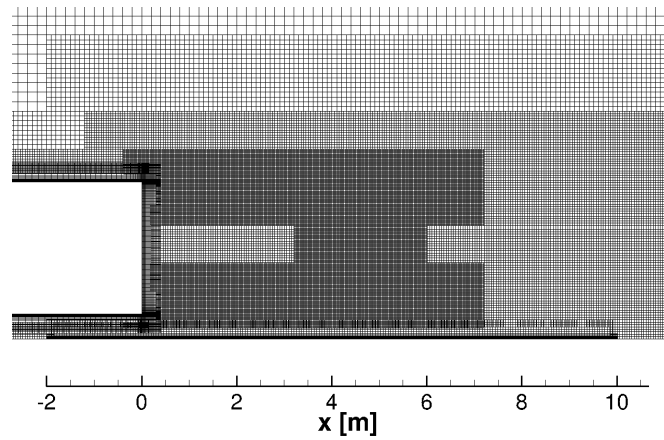


Figure 79 – Detail of the computational grid of the jet only simulation.

Simulations of the jet flow only have been performed first to evaluate how long it takes until the jet flow at the turbine position is converged to a steady solution. The field is initialized with zero velocity, which means, the jet flow also starts from zero. To avoid pressure surge and unrealistic flow conditions at the beginning of the simulation, the flow at the wind generator outlet is accelerated linear to the reference velocity over a time of 1 s. For a reference velocity of 1.48m/s this is shown in Figure 80. The dotted and dashed lines show the velocity profile at the turbine position in the middle of the jet at different times. The continuous lines show intermediate states. After 16.925s the jet has almost reached its final shape at the turbine position and there are only small differences visible compared to the later times. Figure 81 shows the velocity contour at the turbine position in the converged state. The shape of the square outlet is still clearly visible and it can be seen, that the blade tips are temporary located in shear layer of the undisturbed jet. In the center of the jet, the velocity did not change compared to the inflow, only the shear layer was extended and even a small area with increased velocity can be found.

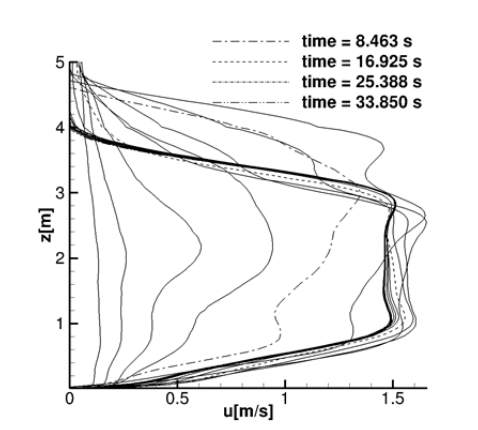


Figure 80 – Velocity profile at the turbine position at different times, reference velocity = 1.48m/s

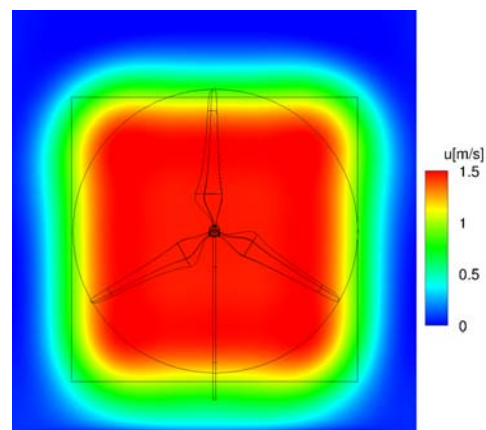


Figure 81 – Velocity contour of the converged jet flow at the turbine position, reference velocity = 1.48m/s. Turbine and wind generator outlet are indicated with thin lines.

Simulation of the full turbine in uniform inflow and test environment

To simulate the turbine in uniform inflow and in the jet flow, the whole turbine has been meshed. Therefore, all relevant components, including blades, hub, nacelle and tower have been considered and placed in the specific background mesh using the chimera technique. The blade grid from the one third model simulations has also been used for the full model simulations and all turbine components have been meshed with fully resolved boundary layer. The floating platform has not been considered and a gap between tower and ground has been left. This allows a prescribed motion of the turbine, without complicated mesh overlapping at the tower bottom. Details of the mesh are shown in Figure 82 to Figure 85.

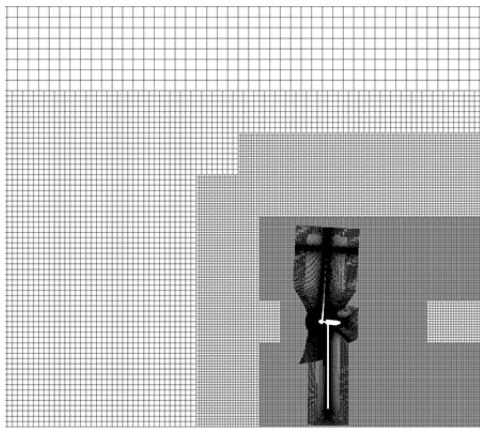


Figure 82 – Cut through the computational domain for the uniform inflow simulation, only part of the grid shown.

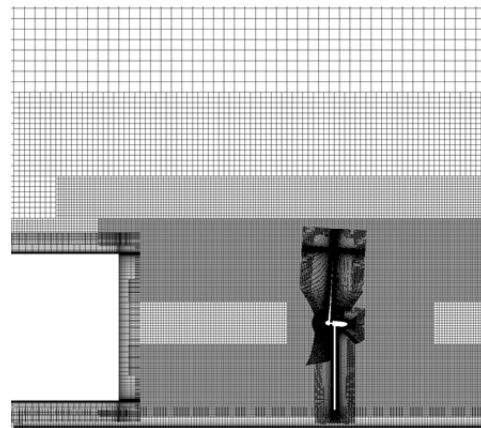


Figure 83 – Cut through the computational domain for the wind generator simulation, only part of the grid shown.

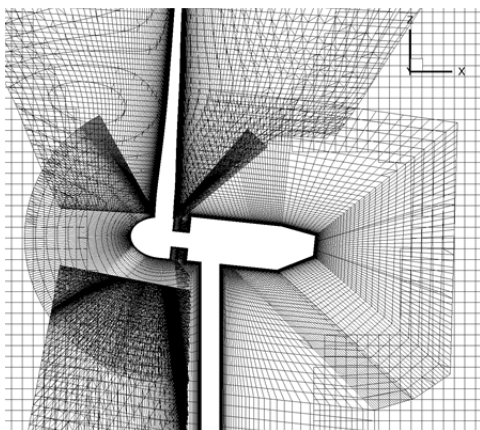


Figure 84 – Cut through the computational domain. Detailed view of overlapping area with tower, nacelle, hub and blade meshes.

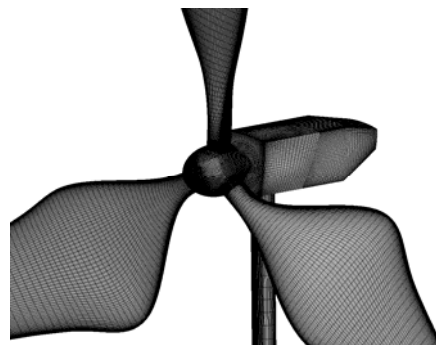


Figure 85 – Detailed view of turbine surface mesh.

Details on the number of cells in the CFD meshes can be found in

Table 12.

Table 12: CFD mesh details, number of cells

	Uniform inflow case	Wind generator case
Blade	5.7 million	
Hub	1.41 million	
Nacelle and tower	1.67 million	
Hub – nacelle connection	0.072 million	
Background	9.09 million	12.53 million
Wind generator	-	1.45 million
Ground boundary layer mesh	-	0.8 million
Total	29.34 million	35.03 million

Before applying the prescribed motion extracted from the experiments, the turbine has been simulated at fixed conditions to investigate and evaluate the influence of the jet flow on the behavior of the turbine. This study has been conducted at the conditions that can be found in Table 13. All parameters have been adjusted to match the experimental conditions as good as possible.

Table 13: Parameters used for the study on jet flow influence (LC147).

Parameter	Exact value
Inflow velocity	1.48 m/s
Temperature	15 °C (288.15K)
Density	1.225 kg/m ³
TSR	7.023
RPM	70.9 1/s
Pitch angle	0°
Cone angle	2.5°
Tilt angle	6°
Hub height	2 m
Distance downstream of wind generator outlet	4 m

Both simulations, uniform inflow and jet flow have been simulated until convergence of the loads. In both cases, for the last revolutions, the time step has been reduced to $1.763 \cdot 10^{-3}$ s to improve the convergence. The thrust and power coefficient curve for both cases is presented in Figure 86 and Figure 87. The uniform inflow case takes much longer to converge, but in the wind generator case low frequency oscillations can be seen, that are induced by fluctuations of the jet flow. Also, the step to the smaller time step can be clearly visible, as the fluctuations are massively reduced. Averaging the load coefficients of the last revolution shows very similar results in both cases (Table 14).

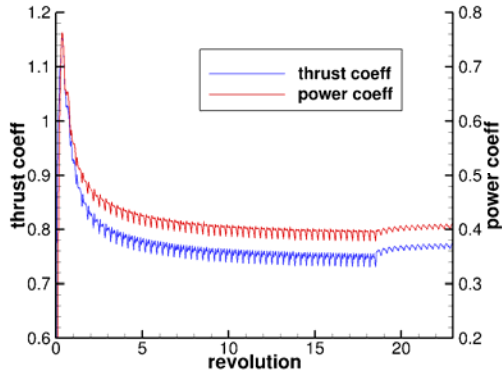


Figure 86 – Thrust and power coefficient over 23 revolutions in the uniform inflow case.

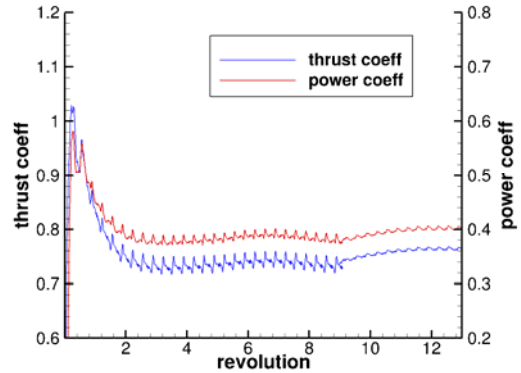


Figure 87 – Thrust and power coefficient over 13 revolutions in the wind generator case.

Table 14: Averaged thrust and power coefficient of the last revolution.

	Uniform inflow case	Wind generator case
C_T	0.77	0.764
C_P	0.406	0.402

The main difference between the cases can be found in the azimuthal and spanwise distribution of the loads. In Figure 88 the thrust slopes of the rotor for one revolution are displayed. In comparison to this, Figure 89 shows the thrust slope of one blade for one revolution of the rotor. While the rotor thrust slope has generally the same shape in both cases, the blade thrust looks totally different. Four distinctive maxima and four minima can be found for the jet flow case (case B). A FFT analyses shows that the main differences occur in low frequencies (Figure 90 and Figure 91).

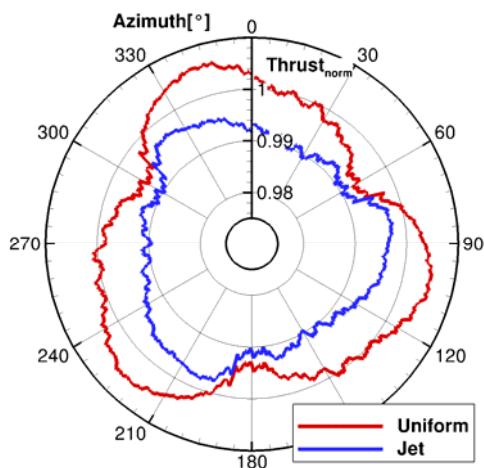


Figure 88 – Comparison of the thrust of the rotor.

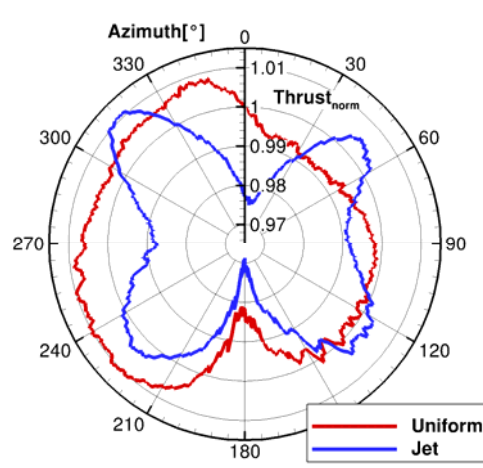


Figure 89 – Comparison of the thrust of one blade.

For the thrust of the rotor in the wind generator case, the 3P amplitude is reduced by approximately 30% and the 6P amplitude by approximately 50%. Analyzing the thrust of one blade, it can be found that for most frequencies below 20Hz the amplitude is amplified in the wind generator case. As expected from the time series, the 4P amplitude is dominant and almost four times higher compared to the uniform inflow case.

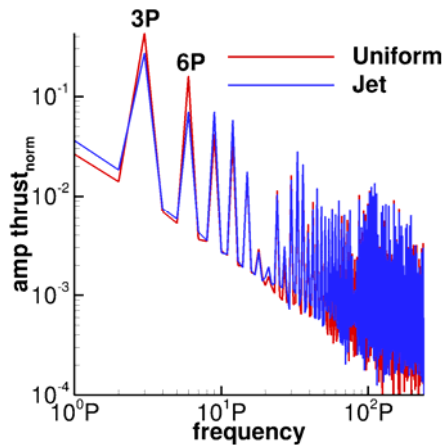


Figure 90 – Result of the FFT analysis of the thrust of the rotor.

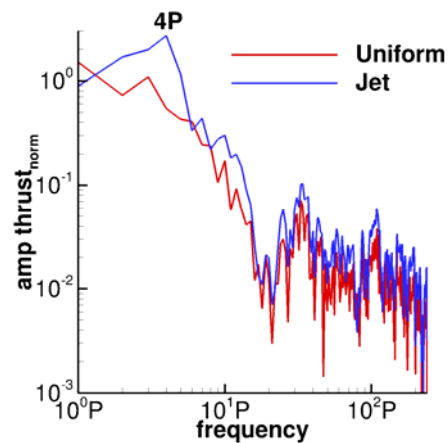


Figure 91 – Result of the FFT analysis of the thrust of one blade.

To understand these differences, the local velocity in the rotor plane has been analyzed. For this purpose, the velocity in two planes close to the rotor, one upstream and one downstream, has been averaged over one revolution. This results in a mean velocity distribution in the rotor plane. Figure 92 shows this plane for the wind generator case. To evaluate the difference of the two cases, the mean velocity distribution of the wind generator case has been set relative to the uniform inflow case. This result is shown in Figure 93. Higher velocities in the wind generator case are indicated as positive, lower velocities as negative. There are four maxima and four minima. Higher inflow velocity results in higher angle of attack and therefore higher loads. Comparing this result to the blade thrust slopes in Figure 89 shows that the maxima and minima correspond very well. A detailed view into the sectional thrust at different spanwise positions is given in Figure 94. It corresponds very well to the observations made in the rotor plane. The areas of higher inflow velocity can be seen clearly in the load distribution. The biggest differences occur at 90% radius, as the blade tip passes through the biggest maxima and minima in inflow velocity.

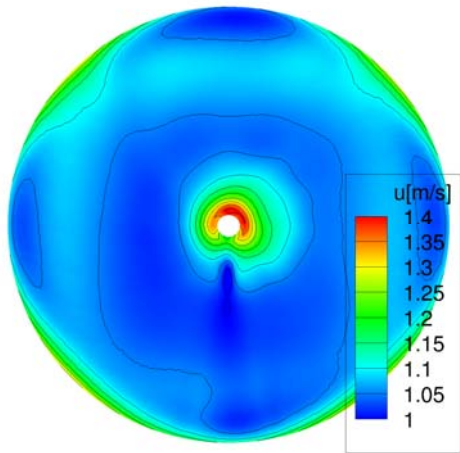


Figure 92 – Mean wind speed in downstream direction in the rotor plane for the wind generator case.

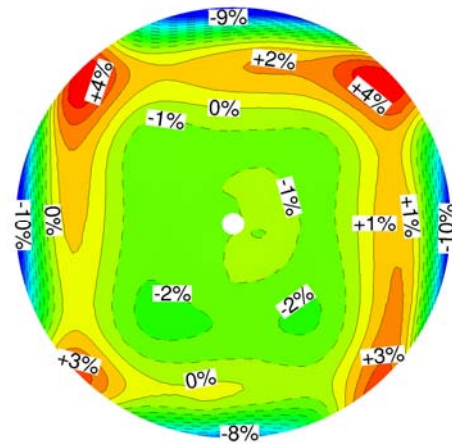


Figure 93 – Velocity difference in the rotor plane, wind generator case relative to uniform inflow case

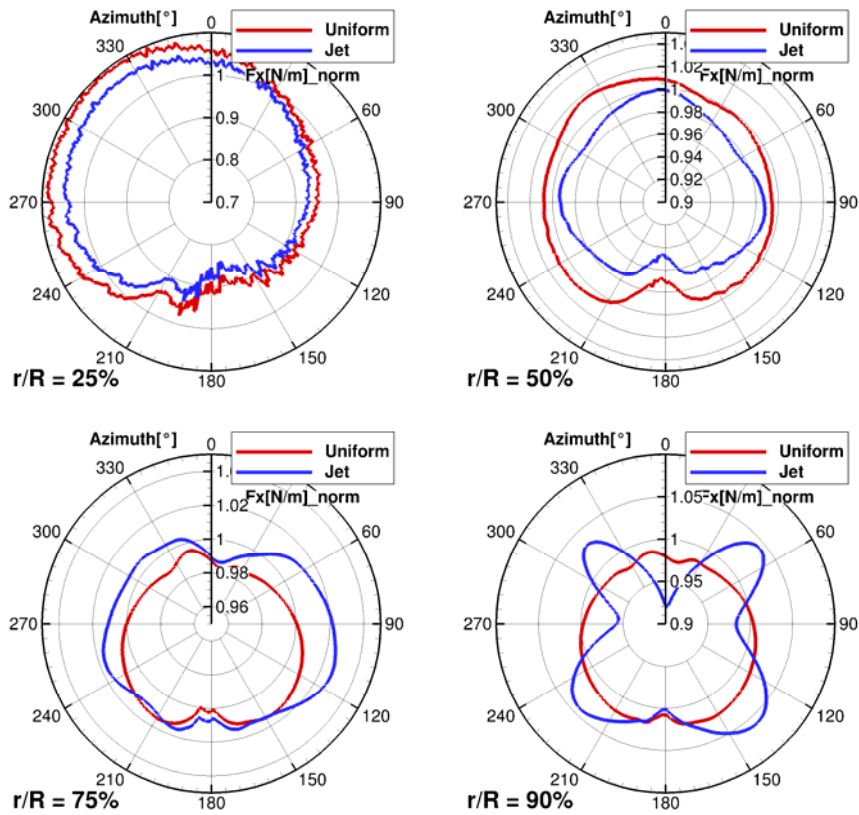


Figure 94 – Sectional thrust at four spanwise positions. Thrust is normalized using the average sectional thrust in the uniform inflow case at this position.

Simulation of the turbine with prescribed motion

To simulate the floating model wind turbine, the motion from experiment has been prescribed. As only very short time series can be simulated in CFD, a sequence ranging over approximately 4.5 revolutions has been selected. Table 15 shows the single steps applied for this simulations. They are the same for both cases, the uniform inflow case and the jet flow case. The simulations have been started from converged results of the fixed turbine. To avoid unphysical behavior jump in the positions and velocity have been avoided by using Fourier series to prescribe the motions. To match the state of the experiment, thrust has been adjusted in the deflected position of the turbine. The change in blade pitch has been calculated from the results of Figure 69 assuming a linear relation of blade pitch and thrust.

Table 15: Approach for the CFD simulation with prescribed motion of the turbine.

	Event	Number of revolutions
1.	Motion of the turbine to the averaged deflected position during (calculated from the entire time series of the selected load case)	1
2.	Fixed simulation with averaged deflection for convergence of loads	1
3.	Change of blade pitch to match thrust of experiment	0.5
4.	Fixed simulation with averaged deflection and new blade pitch for convergence of loads	1-2
5.	Motion of the turbine into the starting position of the selected prescribed sequence. Match of position and velocity of motion in all 6 DOFs	1
6.	Prescribed motion of the turbine according to the selected sequence in the experiment	4.5

Two load cases have been selected for the simulation, LC147 and LC166, detail on both can be found in Table 16. For LC166 only uniform inflow simulations worked, as wind generator simulations did not converge. Figure 94 shows pitch motion of the turbine for the prescribed motion in the LC147 simulation. Figure 95 is a detail of Figure 94 and shows the approximation of the extracted motion by Fourier series. One can see, that the general slope matches very well and noise is filtered out, as only 10 coefficients have been used for the Fourier series.

Table 16: Description of the applied load cases.

	LC147	LC166
Wind speed	1.48 m/s	2.63 m/s
Blade pitch	0°	16°
Adjusted blade pitch	-1.48°	15.38°
Data points extracted from experiment	11319 to 11649	24576 to 24976

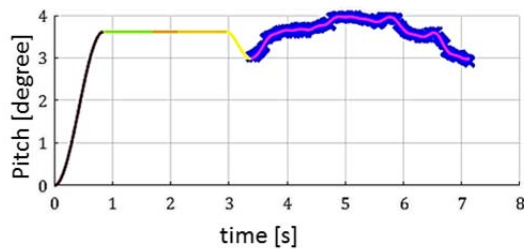


Figure 95 – Definition of the applied turbine pitch motion (LC147).

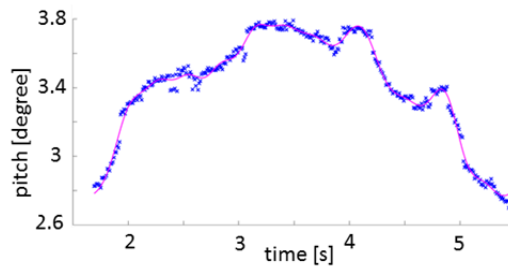


Figure 96 – Turbine pitch motion sequence from experiment and approximation by Fourier series for CFD simulation (LC147).

The resulting thrust and power coefficients of the turbine under prescribed motion for LC147 is shown in Figure 97 and Figure 98. The comparison of uniform inflow and jet flow show, that the behavior under motion is very similar. A small deviation can be found, starting after the pitch adjustment. Also the change in blade pitch is the same for both cases, the differences are higher now compared to the fixed turbine case presented in Table 14. Table 17 shows the load coefficients after 4 revolutions of the LC147 simulation. This phenomena could be explained by the increased distance to the wind generator outlet although differences decrease a little bit to the end of the simulation.

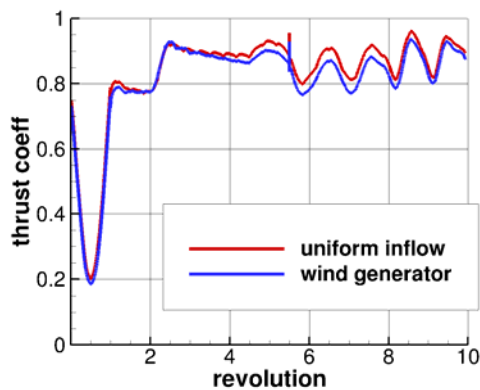


Figure 97 – Results of LC147 CFD simulation, thrust coefficient.

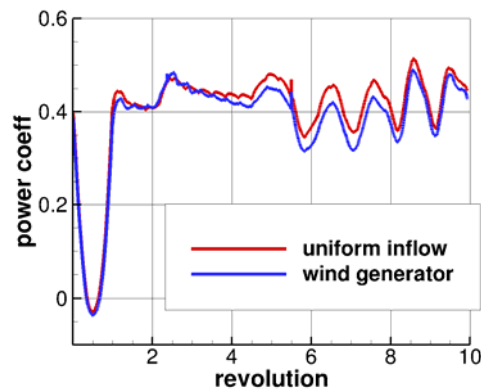


Figure 98 – Results of LC147 CFD simulation, power coefficient.

Table 17: Thrust and power coefficient in LC147 CFD simulations after 4 revolutions (pitch adjusted).

	Uniform inflow case	Wind generator case
C_T	0.891	0.872
C_P	0.437	0.419

As the change of thrust is mainly dependent of the motion of the rotor in x-direction, the x-position of the hub and the corresponding u-velocity resulting of the 6 DOF motion have been calculated (Figure 99). Negative velocity means advancing and positive motion means retreating blade. Figure 100 shows the thrust coefficient together with the hub velocity are plotted. It can be seen that there is a small phase shift between the hub velocity and the thrust slopes with hub velocity advancing.

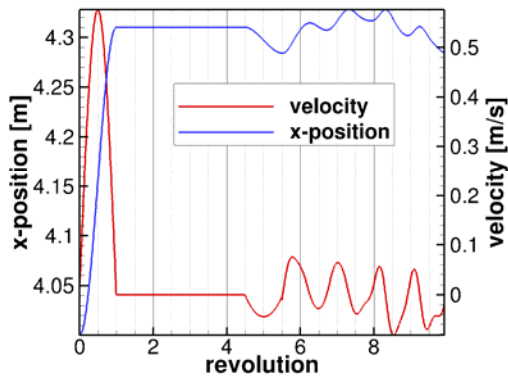


Figure 99 – Results of LC147 CFD simulation, hub position and velocity.

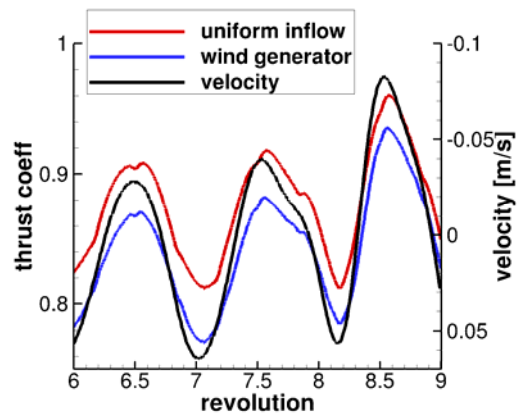


Figure 100 –Results of LC147 CFD simulation, thrust coefficient and hub velocity.

Figure 101 shows the result of the LC166 simulation under uniform inflow conditions. In this case, the motion of the turbine is stronger and this directly corresponds to higher fluctuation in thrust and power of the turbine. The turbine even goes into negative aerodynamic power for a short instant during the selected sequence while thrust coefficient ranges between 0.024 and 0.126. It has to be mentioned that the target thrust coefficient of the experiment of 1.1 has not been matched in the simulation.

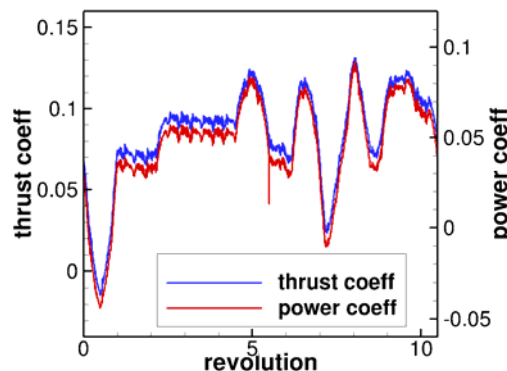


Figure 101 – Results of LC166 CFD simulation, thrust and power coefficient of uniform inflow case.

Conclusion of the aerodynamic high-fidelity model validation

Using fully turbulent CFD simulations the influence on the jet flow as well as the influence of the turbine motion on the aerodynamic loads has been investigated. The jet has been created using assumptions, as to little measurement data was available to rebuild the original jet flow. Grid dependency has been investigated before simulating the full turbine.

The CFD results show that the jet flow has only a small influence on the aerodynamic loads of the rotor. Thrust and power coefficient are similar to uniform inflow conditions when the turbine is fixed at 4 m downstream position. Looking at the spanwise distribution of the loads a clear difference can be found. As the blade tip is operating in or close to the shear layer of the jet, the 4P frequency is strongly amplified compared to the uniform inflow case. At the deflected position of LC147 the load coefficients of the wind generator case are a little lower compared to the uniform inflow case at same blade pitch. When the turbine is moving, no influence of the jet flow

on the rotor loads could be found. Assuming that the real jet is close to the numerical one, it can be concluded that the turbine in the jet of the wind generator behaves similar to uniform inflow conditions.

2.6 Conclusions on the semisubmersible test campaign

A complete validation of different software has been presented using measurement data of the four-week campaign at EHEEA Nantes/France in 2014. The tunnel campaign included: tests with a Froude scale, low Re rotor as well as a ducted fan in connection to a SiL approach.

A stepwise validation has been assumed with test cases of increasing complexity. The simulations have shown good agreement with experiments in free decay cases and in cases with constant wind. These cases have been used to verify mooring stiffness, inertias, masses, aerodynamics, etc. and also to adjust the hydrodynamic damping of the simulation models.

In cases with regular waves the agreement between predictions and test results was good. Also in the cases with irregular waves was good except at low frequencies. This disagreement demonstrates the importance of modelling non-linear waves and second order hydrodynamics.

It has been demonstrated that using a Froude-scaled platform and mooring system in combination with a performance-scaled rotor, valid measurements can be obtained, which are predicted well by the state-of-the-art simulation models.

In the cases using a ducted fan and a SiL predictions have shown a very good agreement with experiments also at low frequencies, demonstrating the capability of this approach to include realistic rotor thrust that is representative of a turbulent wind.

Finally, fully turbulent CFD simulations have been used in order to assess the influence on the jet flow as well as the influence of the turbine motion on the aerodynamic loads. Results showed that the jet flow has only a small influence on the aerodynamic loads of the rotor. Relating the blade loads, it can be concluded that the 4P frequency is strongly amplified compared to the uniform inflow case. Nevertheless, when the turbine is moving, no influence of the jet flow on the rotor loads could be found, although this is something that should be taken in consideration when setting up future test campaigns.

For future tests it is recommended to perform a detailed identification of the subsystems mooring lines, inertial and elastic properties of the structure, the aerodynamic rotor coefficients, the wave maker and the wind field. Also, an uncertainty analysis of the sensors should be performed and a calibration on site.

With regard to the validated software, it has been shown that the integrated tools considered are able to capture the semisubmersible dynamics with generally good agreement. The main disagreement concerns the low frequencies. This indicates the need of include non-linear hydrodynamics in future developments of the software. In addition, non-linear wave theories should also be implemented. For the mooring lines, the importance of using dynamic models for the analysis of the lines has been shown, although the impact on the global system motions is not critical. To accurately capture the line tension levels a better characterization of the drag coefficients for a wider range of mooring types and operating conditions is required.

2.7 Acknowledgements

The authors gratefully acknowledge the loyal and professional support and the expertise of Politecnico di Milano, especially Filippo Campagnolo, Pierluigi Montinari and Alessandro Croce. Without them designing and building the rotor and accompanying the testing, this experimental database would not had been what it is.

2.8 REFERENCES

- Kumar, G., & Ramachandran, V. (2013). *A Numerical Model for a Floating TLP Wind Turbine*. PhD Thesis, DTU Wind Energy.
- Ansys. (2013). *Aqwa Theory Manual*. Tech. rep.
- Azcona, J., Bekiropoulos, D., Bredmose, H., Fischer, A., Heilskov, N. F., Krieger, A., et al. (2014). *D4.21: State-of-the-art and implementation of design tools for floating structures*. INNWIND EU.
- Azcona, J., Bouchotrouch, F., González, M., Garcíandía, J., Munduate, X., Kelberlau, F., et al. (2014, #jun#). Aerodynamic Thrust Modelling in Wave Tank Tests of Offshore Floating Wind Turbines Using a Ducted Fan. *Journal of Physics: Conference Series*, 524, 012089.
- Azcona, J., Lemmer, F., Matha, D., Amann, F., Bottasso, C. L., Montinari, P., et al. (2015). *D4.2.4: Results of wave tank tests. Description of Floating Wind Model Tests at ECN and DHI*. INNWIND E.U.
- Azcona, J., Lemmer, F., Matha, D., Amann, F., Campagnolo, F., Bredmose, H., et al. (2014). *INNWIND.EU D4.24: Floating Wind Model Tests Ecole Centrale de Nantes 2014*. Tech. rep., INNWIND.EU.
- Azcona, J., Sander, F., Bredmose, H., Manjock, A., Pereira, R., & Campagnolo, F. (n.d.). *INNWIND.EU D4.2.2: Methods for performing scale-tests for method and model validation*. Tech. rep., INNWIND.EU.
- Bachynski, E. E. (2014). *Design and Dynamic Analysis of Tension Leg Platform Wind Turbines*. PhD thesis, Norwegian University of Science and Technology.
- Bachynski, E. E., & Moan, T. (2012). Design considerations for tension leg platform wind turbines. *Marine Structures*, 29(1), 89 – 114.
- Bredmose, H., Larsen, S. E., Matha, D., Rettenmeier, A., Marino, E., Eichstaedt, R., y otros. (2012). *D2.04: Collation of offshore wind wave dynamics*. Marine Renewables Infrastructure Network.
- Bredmose, H., Mikkelsen, R., Hansen, A. M., Laugesen, R., Heilskov, N., Jensen, B., et al. (2015). Experimental study of the DTU 10 MW wind turbine. *EWEA Offshore 2015*. Copenhagen, Denmark.
- Bureau Veritas. (2002). *NR 493 R02 E. Classification of Mooring Systems for Permanent Offshore Units*.
- Det Norske Veritas. (2010). *Offshore Standard DNV-OS-E301. Position Mooring*. Høvik, Norway.
- Drela, M. (2016, October). Retrieved from XFOIL Web Portal: <http://web.mit.edu/drela/Public/web/xfoil/>
- Faltinsen, O. M. (1999). *Sea Loads on Ship and Offshore Structures*. Cambridge: Cambridge University Press.
- Fraser, Selig, M. S., & Donovan, X. (1986). *Airfoils at low speed*. SoarTech Publications.
- Giguere, P., Ninham, C. P., Guglielmo, J. J., Selig, M. S., & Lyon, C. A. (1995). *Summary of low-speed airfoil data, vol 2*. SoarTech Publications.
- Goupee, A. J., Koo, B., Kimball, R. W., Lambrakos, K. F., & Dagher, H. J. (2012). Experimental comparison of three floating wind turbine concepts. *31st International Conference on Ocean, Offshore and Arctic Engineering*. Rio de Janeiro, Brasil.
- Hansen, A. M., & Laugesen, R. (2012). *Experimental study of the dynamic response of a tlp wind turbine*. BSc thesis, DTU.
- Hansen, A. M., Laugesen, R., Bredmose, H., Mikkelsen, R. F., & Psychogios, N. (2014). Small scale experimental study of the dynamic response of a tension leg platform wind turbine. *Journal of Renewable and Sustainable Energy*, 6(5):053108.
- Hansen, M. O. (2008). *Aerodynamics of wind turbines*. Earthscan.
- Jensen, B. (2015). *Internal DHI documentation*. DHI.
- Johannessen, K., Meling, T. S., & Haver, S. (2001). Joint distribution for wind and waves in the northern north sea. *Eleventh International Offshore and Polar Engineering Conference & Exhibition*. Stavanger, Norway.
- Jonkman, J. (2007). *Dynamics Modeling and Loads Analysis of an Offshore Floating Wind Turbine*. Ph.D. dissertation.

- Koch, C. (2016). *Validation of a reduced-order model of a floating wind turbine with experiments*. University of Stuttgart.
- Koch, C., Lemmer, F., Borisade, F., Matha, D., & Cheng, P. W. (2016). Validation of INNWIND.EU Scaled Model Tests of a Semisubmersible Floating Wind Turbine. *ISOPE*.
- Laugesen, R., Hansen, A. M., Bredmose, H., Mikkelsen, R., & Heilskov, N. (2015). Experimental Study of the Dynamic Response of the DTU 10 MW Wind turbine on a Tension Leg Platform. *MSc Thesis, DTU Wind Energy M-0065*.
- Lemmer, F., Azcona, J., Matha, D., Amann, F., Campagnolo, F., Bredmose, H., et al. (2014). *INNWIND.EU D4.24: Floating Wind Model Tests Ecole Centrale de Nantes 2014*. Tech. rep., INNWIND.EU.
- Lemmer, F., Raach, S., Schlipf, D., & Cheng, P. W. (2015). Prospects of Linear Model Predictive Control on a 10MW Floating Wind Turbine. *Proceedings of the ASME 34th International Conference on Ocean, Offshore and Arctic Engineering*. St. John's/Canada.
- Martin, H. R., Kimball, R. W., Viselli, A. M., & Goupee, A. J. (2012). Methodology for wind/wave basin testing of floating offshore wind turbines. *31st International Conference on Ocean, Offshore and Arctic Engineering*. Rio de Janeiro, Brazil.
- Matha, D., Sandner, F., & Schlipf, D. (2014, dec). Efficient critical design load case identification for floating offshore wind turbines with a reduced nonlinear model. *Journal of Physics: Conference Series*, 555.
- Mayer, B. (2016). *Validation of a reduced-order model of a floating wind turbine with experiments*. University of Stuttgart.
- Mikkelsen, R. F. (s.f.). *The DTU 10mw 1:60 model scale wind turbine blade*. DTU Wind Energy.
- Müller, K., Sandner, F., Bredmose, H., Azcona, J., Manjock, A., & Pereira, R. (2014). Improved Tank Test Procedures For Scaled Floating Offshore Wind Turbines. *International Wind Engineering Conference IWE*. Hannov.
- Myhr, A., Bjerkseter, C., Ågotnes, A., & Nygaard, T. A. (2014). Levelised cost of energy for offshore floating wind turbines in a life cycle perspective. *Renewable Energy*, 66(0), 714 – 728.
- NREL. (2016, October). Retrieved from NWTC Information Portal (HydroDyn): <https://nwtc.nrel.gov/HydroDyn>
- NREL. (2016, October). Retrieved from NWTC Information Portal (MAP++). : <https://nwtc.nrel.gov/MAP>
- NREL. (2016, July). *NWTC Information Portal (AeroDyn)*. <https://nwtc.nrel.gov/AeroDyn>. Last modified 27-July-2016 ; Accessed 10-October-2016 . Retrieved from NWTC Information Portal (AeroDyn): <https://nwtc.nrel.gov/AeroDyn>
- Orcina Ltd. (2014). *OrcaFlex Manual. Version 9.8b*.
- Robertson, A., Jonkman, J., Masciola, M. D., Molta, P., Goupee, A. J., Coulling, A. J., et al. (2013). Summary of Conclusions and Recommendations Drawn from the DeepCWind Scaled Floating Offshore Wind System Test Campaign. *International Conference on Ocean, Offshore and Arctic Engineering*. Nantes: ASME.
- Robertson, A., Jonkman, J., Masciola, M., Song, H., Goupee, A., Coulling, A., et al. (2014). *Definition of the Semisubmersible Floating System for Phase II of OC4*. Tech. rep., NREL, Boulder/USA.
- Sandner, F., Amann, F., Azcona, J., Munduate, X., Bottasso, C., Campagnolo, F., et al. (2015). Model Building and Scaled Testing of 5MW and 10MW Semi-Submersible Floating Wind Turbines. *EERA Deepwind*. Trondheim/NO.
- Sandner, F., Schlipf, D., Matha, D., & Cheng, P. W. (2014). Integrated Optimization Of Floating Wind Turbine Systems. *Proceedings of the ASME 33rd International Conference on Ocean, Offshore and Arctic Engineering*. San.
- Sandner, F., Schlipf, D., Matha, D., Seifried, R., & Cheng, P. W. (2012). Reduced Nonlinear Model of a Spar-Mounted Floating Wind Turbine. *Proceedings of the German Wind Energy Conference DEWEK*. Bremen.
- Schlipf, D., Sandner, F., Raach, S., Matha, D., & Cheng, P. W. (2013). Nonlinear Model Predictive Control of Floating Wind Turbines. *Proceedings of the Twenty-third International Conference on Offshore and Polar Engineering (ISOPE)*, (pp. 440-447).
- Selig, M. S., Guglielmo, J. J., Broeren, A. P., & Giguere, P. (1995). *Summary of low-speed airfoil data Vol1*. SoarTech Publications.



Tomasicchio, G. R., D'Alessandro, F., Musci, E., Fonseca, N., Mavrakos, S. A., Kirkegaard, J., y otros. (2014). Physical model experiments on floating off-shore wind turbines. *HYDRALAB IV Joint User Meeting*. Lisbon, Portugal.

3 TLP VALIDATION TEST CASES

3.1 Introduction

The numerical results and their comparison with prior water tank measurements of a Tension Leg Platform (TLP) concept of a floating wind turbine are presented in this Chapter. In the first part, the model details are given. In the second part, the code-to-code and the code-to-experiment comparisons are presented.

The TLP is a column foundation characterized by achieving stability by virtue of excess buoyancy and tensioned mooring lines, so-called tendons. This means that the foundation is restrained in heave, pitch and roll motion, while it is pliant in surge, sway and yaw. The physical model tests were performed by DTU at the testing facilities of DHI in Denmark with a Froude-scaled rotor model of the DTU 10MW wind turbine mounted on a TLP foundation (Laugesen, Hansen, Bredmose, Mikkelsen & Heilskov, 2015) and is part of INN WIND.EU D4.24 (Azcona, 2015).

Simulations were performed at a model test scale of 1:60. Hereby the mismatch in Reynolds number between prototype scale and model scale is bypassed, since the numerical modelling is carried out directly at lab scale. Four groups of tests have been selected for the validation of the numerical tools, namely system ID tests, Hydrodynamic response tests, Hydro- and aero-dynamic response tests and Focused wave group tests. Conclusions on the validity of the codes are provided at the end of the chapter.

Three types of codes have been applied for the coupled analysis of the TLP floating wind turbine, namely CFD and aero-hydro-elastic modelling. Two different aero-hydro-elastic models have been objects of this study, namely FAST and BLADED with a dynamic mooring model and FLEX5 with a quasi-static mooring model. The aero-hydro-elastic models include simulation of both wind turbine rotor interaction and motion response from waves. For the DHI-CFD model (Heilskov and Petersen, 2016), the validation has focused on accurate prediction of the hydrodynamic motion response, ignoring the effect of wind, but with attention to nonlinear viscous effects. Accurate prediction of the hydrodynamic motion response of a floating offshore wind turbine is key for optimization of performance and energy harvesting. While the motion is dominantly forced by inertial loads, the damping is the governing factor for the resulting magnitude of the floating structure motion response. In some situations, nonlinear viscous effects may play a significant part on the response and stability. This is particularly likely in situations where the wind turbine substructure is excited by large waves or relatively strong ocean currents.

3.2 The test campaign

The TLP test campaign was carried out at DHI Denmark in December 2014 and January 2015. The tests extend the results of the semi-sub campaign described in Chapter 2 by:

- Application and design of another floater type (TLP) with different dynamic properties than the semi-submersible concept
- A re-designed 1:60 Low-Reynolds number rotor based on the DTU/INN WIND.EU 10MW rotor
- Tests with 3 different mooring configurations
- Tests with directionally spread waves
- Tests in mis-aligned wind-wave conditions
- Tests with focused waves, as a model for extreme waves

The test campaign and its results have been presented orally at the EWEA Offshore 2015 conference (Bredmose, et al., 2015), and reported in detail in (Laugesen, Hansen, Bredmose,

Mikkelsen, & Heilskov, 2015) and in the INN WIND.EU deliverable D4.24. The present description is a condensed summary.

Floater concept and rotor

The TLP floater concept is radically different from the semi-submersible floater by its compact volume and the attainment of stability primarily by the mooring system. The mooring configuration is based on a strong excess buoyancy which makes the floater response much stiffer (higher natural frequencies) than the semi-submersible.

The TLP floater for the present experiments was designed specifically for the DTU 10MW turbine. The foundation consists of a cylindrical transition piece, a cylindrical floater and slender spokes, as shown Figure 102. The TLP is sketched with four tendons which is the configuration chosen for the comparison to numerical models in the present report. The floater was designed for a water depth of $h=180$ m, corresponding to a basin water depth of 3.0 m for the 1:60 scale model tests.

Figure 102: TLP wind turbine with coordinate system and photo of assembled turbine and blade. From Laugesen, Hansen, Bredmose, Mikkelsen, & Heilskov (2015) and Pegalajar-Jurado et al. (2016)



The coordinate system applied for the measurements and tests is shown in Figure 1 as well. The global (x, y, z) -coordinate system is located at the position of the unloaded structure, with $z = 0$ in the mean water level (MWL) and the z -axis pointing upwards. The x -axis is coincident with the primary wave direction. Rigid body displacement in the positive directions of the x , y and z -axes, are denoted surge, sway and heave, while rotations about the same axes are denoted roll, pitch and yaw in accordance with general maritime terminology. These motions are denoted $\xi_1, \xi_2, \xi_3, \xi_4, \xi_5$ and ξ_6 .

The test campaign was carried out with Froude scaling of length and time, consistent with the usual scaling method for wave basin tests, where the ratio of any acceleration to the acceleration of gravity must be preserved between full scale and lab scale. The resultant Reynolds number for the rotor, however, becomes very low, which necessitates a re-design of the rotor to achieve the right scaled thrust. The final blade design is shown in Figure 102.

Model specifications

The key specifications for the prototype wind turbine, the ideally Froude scaled model and the actual model TLP wind turbine is provided in (Laugesen, Hansen, Bredmose, Mikkelsen, &

Heilskov, 2015). Froude scaling implies that structural mass must be scaled down by the scale ratio raised to the third power and be further adjusted by the density ratio of fresh to salt water. Hence, for example 1000 kg at full scale is 4.5 g at model scale. This can sometimes be difficult to achieve. By inspection of Table 18 the difference in mass of the nacelle and hub for the Froude model scale and the actual model scale really stands out, with an exceedance in the actual mass of 40%. Moreover the mass of the floater is too large for the actual model scale, especially for the configuration with 4 spokes. Despite the differences in Froude model scale and the actual model scale, the model is still expected to represent the dynamics of the full scale FWT qualitatively. Even if this is not the case, the results are still valuable for validation of the numerical models by the model scale data. The validated model can next be applied for the design and analysis of the full-scale structure.

Table 18: Key specifications of the prototype scale wind turbine, the ideally Froude scaled 1:60 model, and the actual scaled 1:60 model

Dimension	Proto-type scale	Froude Model Scale	Actual Model Scale (including instrumentation)
Foundation			
Floater diameter D_f	18.0m	300mm	300mm
TP diameter D_{TP}	9.0m	150mm	150mm
Floater height h_f	25.0m	417mm	417mm
TP height h_{TP}	32.0m	533mm	533mm
Spoke length L_s	32.1m	535mm	535mm
Submergence h_s	12.0m	200mm	200mm
Freeboard $h_{freeboard}$	20.0m	333mm	333mm
Mass (3 spokes) M_f	2390ton	10.80kg	11.50kg
Mass (4 spokes) M_f	2403ton	10.85kg	12.49kg
Tendons			
Length l_t	142m	2.36m	2.25m
Stiffness EA_t			8 10 ⁴ N
Tower			
Diameter, D_t	7.82m-5.50m	130mm-92mm	80mm
Tower height, h_t	95.6m	1594mm	1682mm
Hub height o. MWL, h_{hub}	119m	1983mm	2070mm
Mass, M_t	469 ton	2.12kg	1.98kg
Nacelle			
Rotor diameter, D_R	178.3m	2972mm	2972mm
Blade Length L_b	86.5m	1440mm	1440mm
Blade mass M_b	41.7 ton	0.188 kg	0.198 kg
Nacelle+hub mass M_n	552 ton	2.49 kg	3.48 kg
Full model			
Mass (3 spokes), M_{total}	3533 ton	15.96 kg	17.55kg
Mass (4 spokes), M_{total}	3546ton	16.02kg	18.54 kg

Vertical COG (3 spokes), z_{COG}	18.2m	310mm	378mm
Vertical COG (4 spokes), z_{COG}	18.4m	306mm	321mm
Mass moment of inertia (3 spokes) I_{yy}	$1.30 \cdot 10^{10} \text{ kgm}^2$	16.3 kgm^2	22.30 kgm^2
Mass moment of inertia (4 spokes) I_{yy}	$1.30 \cdot 10^{10} \text{ kgm}^2$	16.3 kgm^2	22.70 kgm^2

Wave basin and wave generation

The experiments were conducted in the deep water wave basin at DHI Water & Environment in Hørsholm, Denmark. The length of the basin is 20m, the width is 30m and the depth is 3m throughout the entire basin, with the possibility of increasing the depth at the center of the basin to 6 or even 12m. The full experimental setup is shown in Figure 103.

Instrumentation and sensors

Data was logged for the following sensors:

- 11 wave gauges
- 4 tendon force gauges, mounted at the tendon connection to the floater
- A two component strain gauge for the inline and transverse shear force at the tower top
- Accelerometers: Three at the floater top and two (inline, transverse) at the underside of the nacelle
- Qualisys motion tracking system for the six degree of freedom motions of the floater
- 4 TSI 8455 air velocity transducers (AVT), applied for wind field measurements

3.3 Test cases

For the experiments with the TLP floater, ten environmental conditions (EC) were chosen with a combination of H_s , T_p and wind speed at hub height \bar{U}_{hub} . These are given in Table 19 in full scale and model scale respectively. For convenience, the environmental conditions are referred to as EC1, EC2,...,EC10. The peak wave periods and wind speeds for EC1, EC3, EC5, EC6 and EC7 were chosen equal to the peak periods of sea states 1,2,3,4 and 5 in the week 2 tests conducted for the semisub test campaign of Chapter 2. The test programme included the generation of regular waves, irregular sea states, focused waves and white noise sea states.

The TLP test cases chosen for the present comparisons have four spokes, and four vertical tendons. The spokes are oriented such that the wind direction is right between the two upwind tendons.

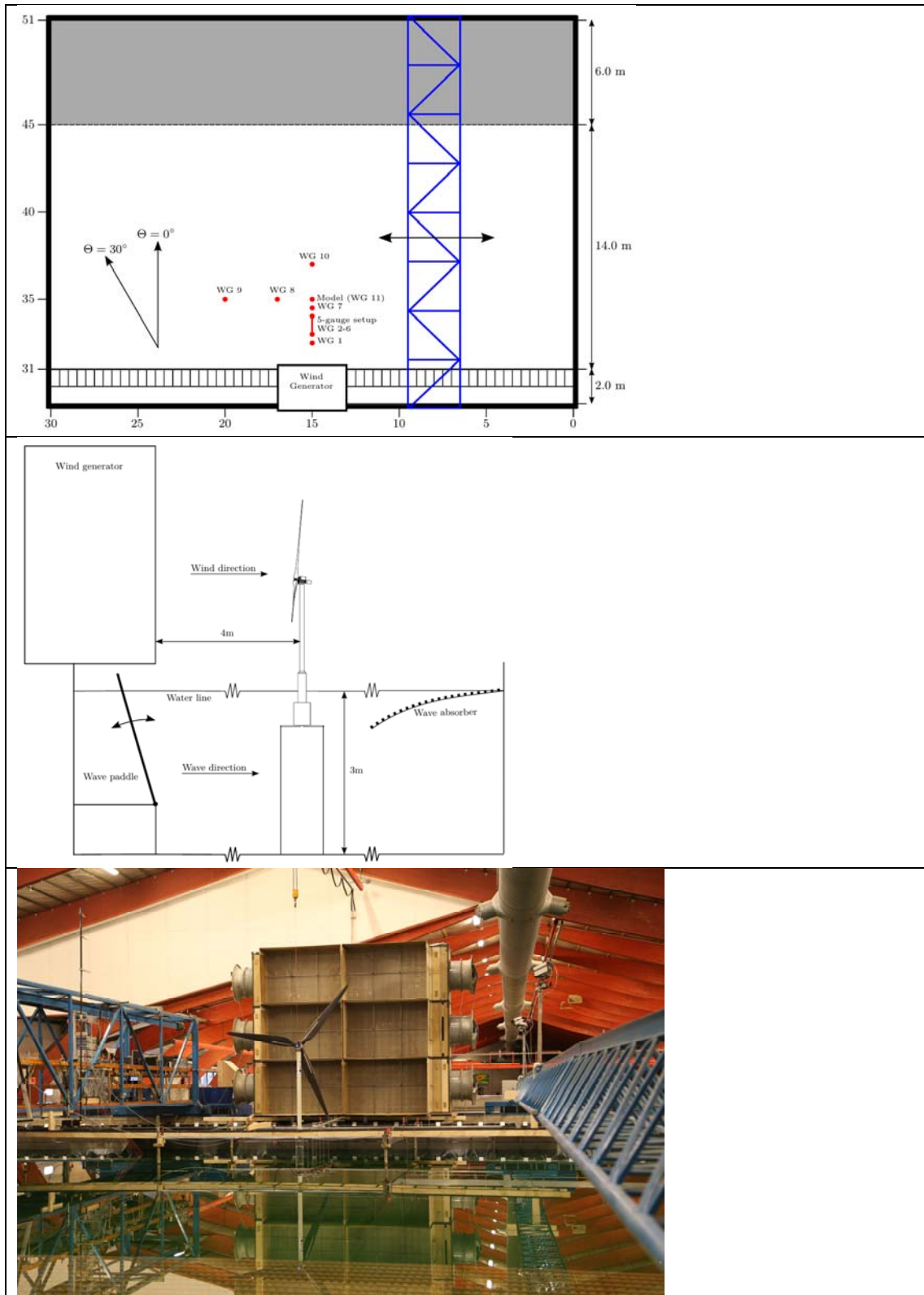


Figure 103: Experimental setup in wave basin at DHI.

Table 19: Environmental conditions described by significant wave height, peak period and hub height wind speed.

Environmental condition		EC1	EC2	EC3	EC4	EC5	EC6	EC7	EC8	EC9	EC10
H_s [m]	full scale	2.36	2.81	3.30	3.72	4.16	6.18	7.80	10.0	12.0	14.3
	model scale	0.039	0.047	0.055	0.062	0.069	0.103	0.130	0.167	0.200	0.239
T_p [s]	full scale	5.50	6.00	6.50	6.90	7.30	8.90	10.0	12.2	13.6	15.4
	model scale	0.71	0.78	0.84	0.89	0.94	1.15	1.29	1.58	1.76	1.99
\bar{U}_{hub} [m/s]	full scale	7.0	7.8	8.5	10.0	11.4	18.0	25	33	40	48
	model scale	0.90	1.0	1.1	1.3	1.5	2.3	3.2	4.3	5.2	6.2

3.4 Analysis specifications and tuning strategy

Four groups of tests have been selected for the calibration of the models, and the validation of the numerical tools, namely system ID tests, Hydrodynamic response tests, Hydro- and aero-dynamic response tests and Focused wave group tests. These are described in the following descriptions.

System ID tests: The intention with these tests is basic checks of the model's ability to reproduce simple test conditions. The tests consist of fixed wind speed tests in wind-only conditions, where the steady thrust of the models for a given wind speed, rotor speed and blade pitch is compared to the measured thrust. Also, decay tests in surge, pitch, and yaw are compared to check the model's representation of natural frequencies and damping. The system ID tests are next used to calibrate the numerical models (not including CFD) such that steady rotor thrust, natural frequencies and damping are matched. The needed calibrations are reported along with the tuned results. This calibration makes a further assessment of the dynamic response predictions of the models possible. Without a calibration of the mentioned system properties, a dynamic response comparison is not meaningful.

Hydrodynamic response: These tests cover regular wave forcing and irregular wave forcing with no wind input. The regular waves are intended for deterministic comparison, where model behaviour and the response of each sensor can be analysed in a well-defined context and where the expectation to the physical behaviour can be checked. Next, for the irregular cases, a broader overview of the match to a stochastic sea state can be checked. This is done in terms of time series, power spectral density and exceedance probability plots for the peaks of the response signal.

Hydro- and aero-dynamic response: These tests contain the same wave conditions as the hydrodynamic response tests, but are carried out with simultaneous wind forcing. Hereby the combined response to waves and wind can be assessed. The tests are complex, both due to the stochastic behaviour of the wind and wave forcing, and to the interaction of the processes – for example through aerodynamic damping of the wave-induced floater motion. The model response is compared to the measured response through power spectral density and exceedance probability plots.

Focused waves: Focused wave groups is a representation of extreme waves. The focused wave group theory, or New Wave Theory, originates from Lindgren (1970), Boccotti (1983) and Tromans et al. (1991) and describes the expected time history of an extreme wave crest for a given wave climate. The theory's central result is that the expected time history of the extreme event is simply

the auto-correlation of the wave spectrum itself, which for a discretized spectrum can be written as:

$$\eta(x, t) = \frac{\alpha}{\sigma^2} \sum_{j=1}^N S_{\eta}(f_j) \cos(\omega_j(t - t_0) - k_j(x - x_0)) \Delta f$$

where S is the wave spectrum, σ the variance of the free surface elevation and α the crest-height of the extreme wave. For the present tests, α was chosen such that the height of the focused wave was 1.86 times the significant wave height of the wave climate, in agreement with a Rayleigh distribution of wave height at the 3-hour probability level.

3.5 Validation and Model Comparison

Table 20 below shows the test cases that were reproduced with each numerical model of the TLP wind turbine.

Table 20: Map of test cases reproduced with the different models

Test	FLEX5 v1	FLEX5 v2 2 nd order	CFD	FAST v1	FAST v2 2 nd order
Steady thrust curve	X			X	
Surge decay	X		X	X	
Heave decay	X			X	
Pitch decay	X		X	X	
Yaw decay	X		X	X	
Regular wave EC5	X			X	
Regular wave EC8	X		X	X	
Regular wave EC10	X		X	X	
Irregular waves EC1-EC8	X			X	X
Irregular waves EC1-EC8 + wind	X			X	
Focused wave EC6	X	X			
Focused wave EC7	X	X			
Focused wave EC8	X	X	X		

Data processing

In order to remove noise and high-frequency content that does not originate from physical phenomena, the experimental data was filtered with a low-pass Butterworth filter of 8 Hz. In addition, the pitch test signal was proven to be amplified by a certain factor, likely due to a calibration error during the campaign. A comparison of line tension during the pitch decay test and the corresponding FLEX5 and FAST results verified the amplification. In order to obtain the amplification factor and correct the test pitch signal, an analysis was carried out on the data from accelerometers at the floater and nacelle. However, since there is no data recorded for tower deflection, a backup pitch signal could not be extracted from the acceleration measurements. The amplification factor was therefore obtained by comparing to the FLEX5 results for regular waves. A factor was selected so that the ratio of surge amplitude and pitch amplitude for FLEX5 was the same as for the tests; this approach intends to make the choice of the factor independent of the added mass coefficient, C_m . However, since the pitch recalibration factor was chosen based on one of the models, the accuracy of the different models in pitch motion is influenced on the choice

of the factor. Therefore, the model accuracy for pitch motion as validated against the re-calibrated experimental pitch signal must be considered indicative rather than rigorous.

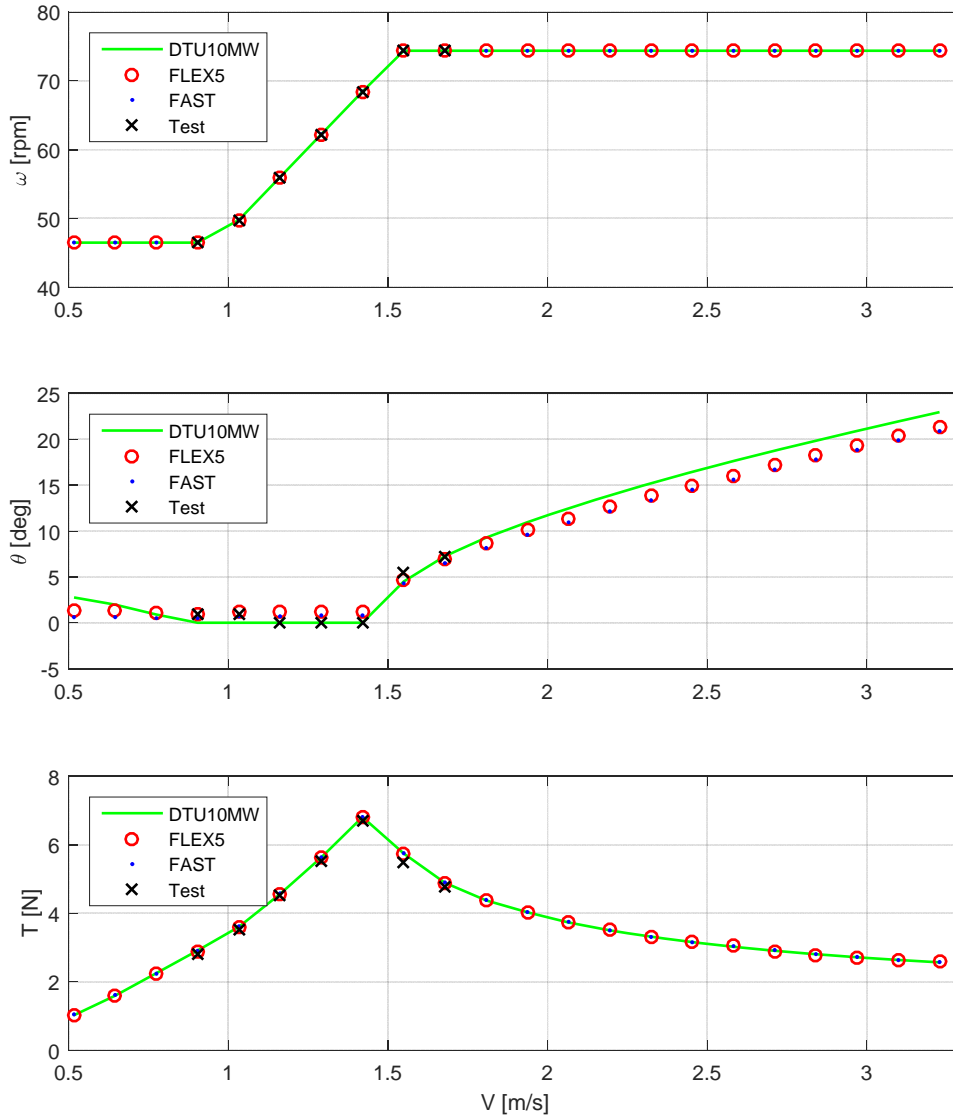


Figure 104: Matching of the steady thrust curve in tests, FLEX5 and FAST

Steady thrust curve

Due to the difference in airfoils between the DTU10MW turbine and the laboratory scale replica, the original blade pitch settings did not produce the right scaled thrust curve. The thrust curve for the numerical models was tuned to the experimental test measurements by modifying the pitch settings, with a maximum deviation from the reference pitch of 2 deg. In the partial load region (below rated wind speed) FLEX5 is run with a blade pitch of about 1 deg, while FAST was calibrated to a slightly lower value. Above rated speed, both FLEX5 and FAST are run with slightly reduced blade pitch relative to the target curve. These differences can be related to the different airfoils, but also to non-uniformities in the experimental wind field. They may also be due to differences between the atmospheric inflow model of FAST and FLEX5 to the labs open-jet wind generation system. It is likely that the induction effects in the lab are different from atmospheric conditions that the numerical models describe. The curves show that it is possible to adjust the steady-wind mean thrust by a calibration of the blade pitch.

Decay tests in water

In this section decay tests are analyzed, which are a general method for hydrodynamic system identification. For a TLP floating wind turbine structure, the motion response of largest interest is surge and pitch, on which we will focus on in the remaining part of the chapter. Decay tests are carried out to determine the natural frequencies and damping for the full system of floater, mooring, tower and nacelle-rotor assembly. CFD simulations of the floating structure have the potential of providing the needed damping calibration for aero-hydro-elastic models – hence replacing possible physical model tests. The system natural frequencies were found to be 0.19 Hz for surge and 1.9 Hz for pitch at model scale.

In surge, the natural frequency at 0.19 Hz is governed by the tendon length, the equilibrium tension, the structural mass and the hydrodynamic added mass. In CFD, the added mass is modelled directly. In FLEX5 and FAST it is included as a constant in the Morison equation. The added mass is the only mass property that cannot be measured a priori to the experiment. It can therefore be calibrated from the decay test.

Surge damping is mainly a result of viscous loads, and is modelled directly in the CFD solver. In FLEX5 and FAST it is modelled through a drag coefficient as part of the Morison equation. The surge decay test can thus be used to calibrate this coefficient.

The comparison (Figure 105) to test in surge decay presents a good match. In the CFD simulation, the natural frequency observed is a fraction higher compared to the physical tests, and the damping estimated slightly lower. In CFD the physical extend of the spokes were not modelled, which would introduce additional viscous damping mainly influencing surge motion response. This lack of additional damping may be the reason for the underestimation of the damping in the surge decay.

In FLEX5 the natural surge frequency of the test was matched by adjustment of the surge added mass coefficient from $C_m=0.770$ to $C_m=0.765$. Further, the damping decay ratio was matched by adjusting the floater drag coefficient from $CD=1.0$ to $CD=1.7$. This compensates for the missing viscous damping from the spokes and mooring lines in FLEX5, as well as for the absence of any linear damping in surge. A similar calibration was made in FAST with resulting values of $C_m=0.74$, and $CD=1$ for the transition piece and $CD=0.6$ for the bottom part of the TLP. Additional linear damping of $B_{11}=2$ N/m/s was introduced in FAST for surge. In FAST, as in FLEX5, the spokes are not modelled. However, since the drag on tendons is modelled, and linear damping in surge is introduced, a lower value of CD is needed for the floater and transition piece, as compared to the FLEX5 value.

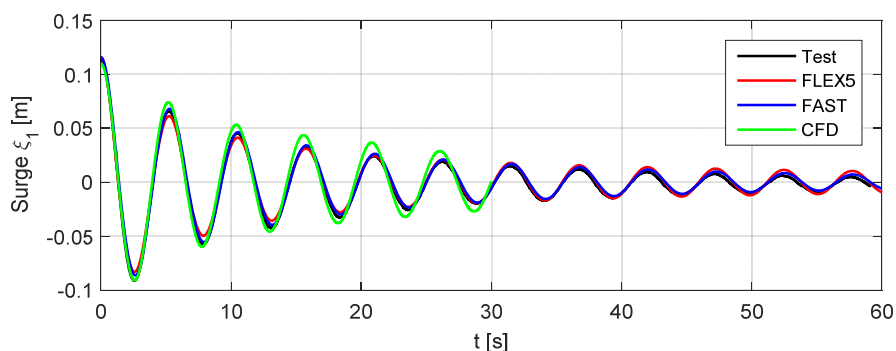


Figure 105: Decay test in surge

In pitch decay, the frequency at 1.9 Hz is governed by hydrodynamic stiffness, mooring stiffness, geometry and the stiffness and mass properties of the full system. Damping is from viscous forces, acting on floater and spokes. Pitch decay information can be used in aero-hydro-elastic models to tune the combined tendon axial stiffness and spoke bending stiffness. The damping decay ratio is a function of the Morison drag coefficient, which was calibrated in surge. The pitch decay signal in the measurement has multiple frequencies present, whereas the simulations are dominated by the pitch natural frequency (see Figure 107). The high-frequency oscillations in the measured signal likely originates from excitation of additional natural modes at higher frequencies than the pitch natural frequency.

FLEX5 and FAST match the pitch natural frequency, once the tendon stiffness was adjusted from EA=80 kN to 90 kN in FLEX5 and to 75 kN in FAST. FLEX5 and FAST match the damping ratio fairly well. The spoke stiffness and damping is not modelled explicitly in any of the models.

The pitch decay test for the CFD model was done with a much larger initial amplitude, due to numerical divergence issues, Figure 106, and can therefore not be compared directly. However, a good match in pitch natural frequency is observed. The damping ratio in the CFD model is lower than in the test, but since the damping ratio is amplitude-dependent, this plot should be merely taken as indicative.

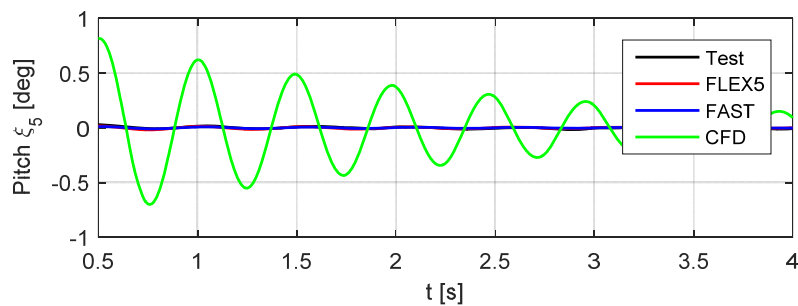


Figure 106: Decay test in pitch - zoomed to CFD signal

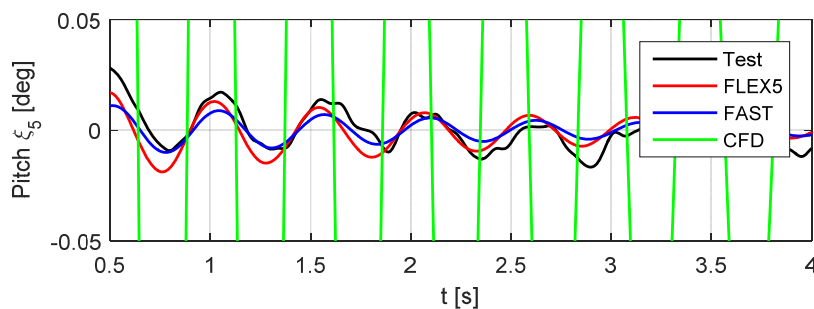


Figure 107: Decay test in pitch - zoomed to test signal

Response to regular waves

Motion response simulations of the TLP floating wind turbine in regular waves have been carried out in CFD (OpenFOAM), FLEX5 and FAST reproducing the physical model test conditions described in Section 3.2. In this Section, focus is on analysis of the hydrodynamic behavior, hence excluding wind. Two tests of regular waves forcing without wind were reproduced, one for EC8 and one for EC10. EC10 represents a more extreme wave condition. Understanding the hydrodynamic

behavior and being able to predict the hydrodynamic motion response accurately, is an important step in the optimization of the floating wind turbine performance for energy harvesting. Comparison of the results between the codes should be viewed while keeping in mind that CFD being a method that is not dependent on prior calibration in view of physics.

In FLEX5 and FAST the wave signal measured in the wave tank tests has been used in the numerical models to compute wave kinematics and wave forcing. In CFD, a regular wave signal has been imposed at the vertical inlet boundary of the rectangular computational domain. In the top of both Figure 108 and Figure 109, the surface elevation of the non-disturbed regular waves is depicted.

Figure 108 shows time series for surge, heave, pitch and nacelle acceleration for regular wave EC8. The right figure shows the corresponding tendon tensions. The periods in the surge and pitch motions correspond to the wave period, which is also observed in the measurements. The wave period is also present in the heave response, however the signal also includes significant motion at half the wave period, which arises from the coupling surge-heave due to the circular trajectory of a TLP in the surge-heave plane (known as set-down effect). No surge wave drift is observed in either the model tests or numerical results. As expected, the surge motion is, together with pitch, the dominant motion response in terms of amplitude. A good match with the measured surge response is obtained with all three codes: CFD, FLEX5 and FAST. In both the measurement and simulations, the TLP moves in surge at the wave period with an amplitude of about 6 cm.

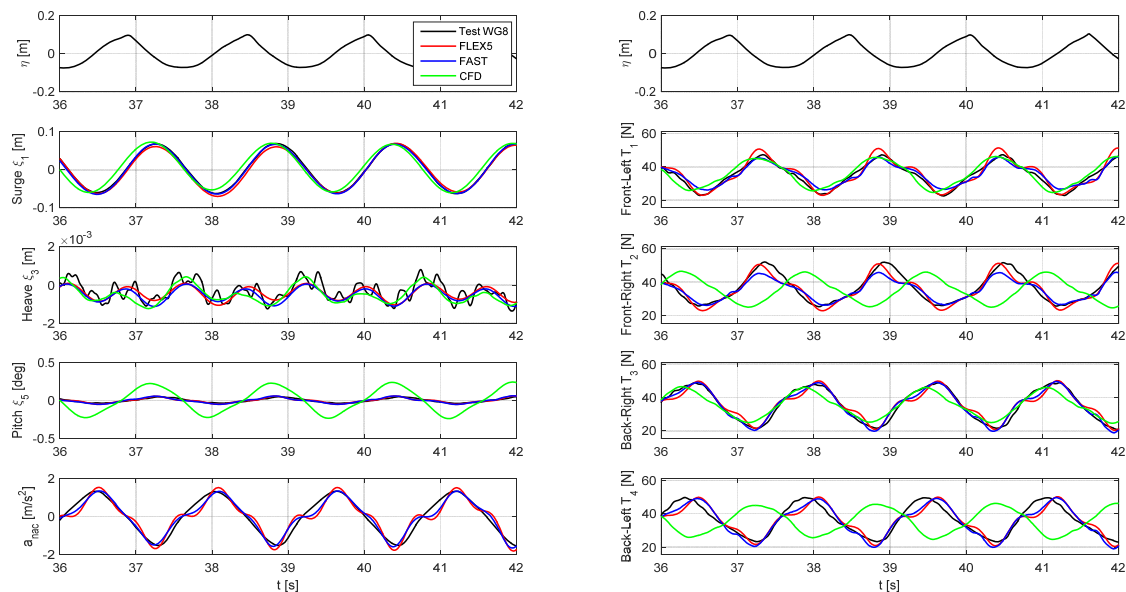


Figure 108: Motion response and corresponding tensions in mooring lines. Regular waves (EC8) with period $T=1.58$ s and wave height $H=0.167$ m (no wind).

While FLEX5 and FAST show good comparison with the measurements for pitch, the CFD model over-estimates the amplitude the amplitude, but has similar shape as in the measurement. As stated in the Data processing section, the calibration error in the measurements implies that a recalibration factor for pitch had to be introduced. Since it was not possible to determine the factor based purely on measurements, the FLEX5 tuning for a specific wave condition was used as basis for computing the amplification factor. Hence the factor used is dependent on the model employed and in this case not a CFD type model but an aero-hydro-elastic model.

Small oscillations overlaying the heave motion response is observed in the measurement, but are absent in the numerical results. The small oscillations overlaying the measured heave motion are most likely due to excitation of the heave natural frequency of 1.9 Hz or/and the spoke bending mode, not included in any of the models. Imperfection in the symmetrical test setup is likely to be present in the physical model test, which may create cross coupling between motions to occur

(e.g. due to motions excited by waves with an oblique incident-wave direction relative to the symmetric system). Numerical models do not suffer from this particular cross coupling effect as they all simulate an ideal symmetric wave-structure interaction situation with no imperfections. Moreover, besides showing a period corresponding to the wave period, the measured heave signal also contains the ‘double hump’ motion of half of the wave period. This is due to the set-down effect, where the mooring lines force a negative heave movement for any surge movement away from the vertical equilibrium point. The simulations all capture the double hump behavior of the heave motion as seen in the measurement signal. Overall, CFD, FLEX5 and FAST compare well with the measurements.

The nacelle acceleration is only modelled in FLEX5 and FAST, and with both codes a good match with the measurements is observed. Looking at the force evolution in the four tendons, it is observed that in the measurement the tensions in front and back are almost 180 degrees out of phase, whereas for CFD the tensions in front and back are in phase. FLEX5 and FAST on the other hand coincide with the phase difference observed in the measurements. This asymmetry in forces in front and back in the measurement is plausible as the combined motion response of pitch and surge will cause a slight reduction in the stretching of the downstream tendons as the wave trough passes (pitch inclination away from the wave maker). A main frequency corresponding to the wave frequency is observed in all of the force signals. Measurement of the force in the two front tension legs shows a double hump similar to the one observed in the heave response, which gives evidence that the heave motion and tension in the two tendons are coupled. The double hump is absent in the CFD results. Furthermore, in CFD a relative good match for the corresponding line tension response can be observed, but in view of the largely over-predicted pitch for the corresponding line tension response, we conclude that the pitch-tension consistency seems not strong. Hence, the phase mismatch between CFD and measurements cannot be attributed to only inaccurate prediction of the pitch motion. For mooring tensions in front tendons, FAST (dynamic mooring model) shows smaller amplitudes than FLEX5 (quasi-static mooring model), and results of both models compare well with measurements. However, the drag coefficient CD for the tendons in FAST may need further tuning.

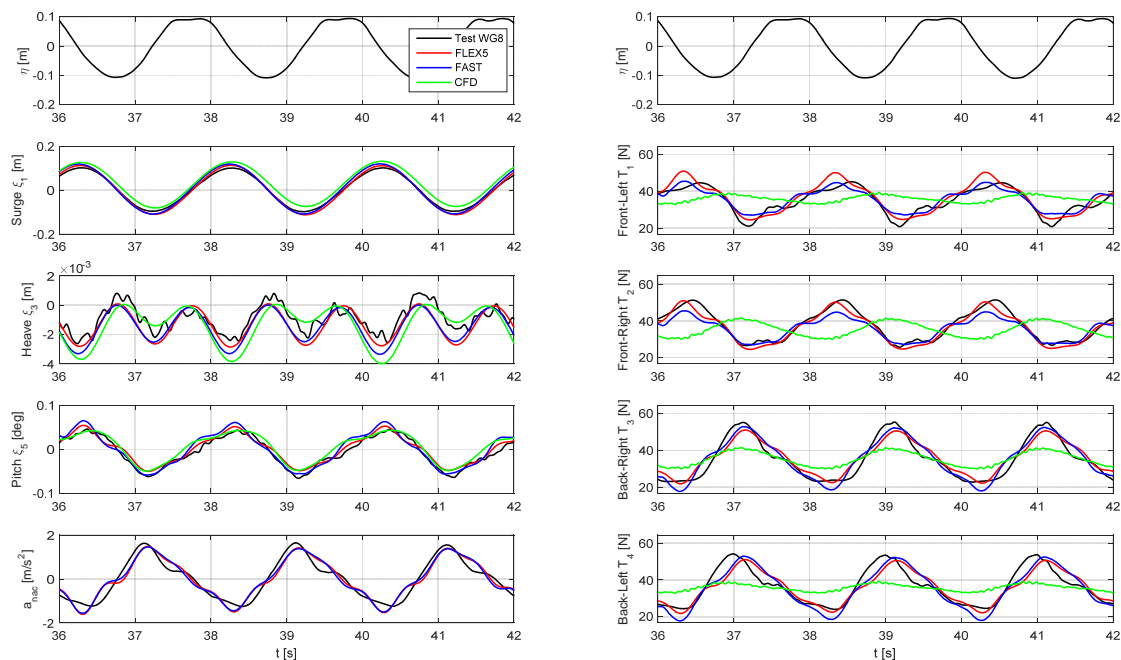


Figure 109: Motion response and corresponding tensions in mooring lines. Regular waves (EC10) with period $T=1.99$ s and wave height $H=0.239$ m (no wind).

Figure 109 shows the results for surge, heave, pitch and nacelle acceleration in terms of time for the regular wave of EC10 characterized by large wave-structure interaction. To the right in the figure the corresponding tendon tensions are shown. The period in surge, pitch motion and nacelle acceleration corresponds to the wave period, which is also observed in the measurements. The wave period is also present in the heave response, however the signal also includes motion at half the wave period. No surge wave drift is observed in either the model tests or numerical results. Similar to EC8, the surge and pitch motion is as expected, the dominant motion response in terms of amplitude. A good match with the measured surge and pitch response is obtained with all three codes: CFD, FLEX5 and FAST. In both the measurement and simulations, the TLP moves with the wave period with an amplitude of about 10 cm in surge.

Small oscillations overlaying the heave and pitch motion response is observed in the measurement, but are absent in the numerical results. The small oscillations overlaying the pitch motion may stem from wave excitation of a higher-frequency structural mode. Even though this study is only focusing on the TLP substructure, the measurements could potentially be influenced by eigenmodes of the non-active wind turbine superstructure mounted on top. However, the small oscillations overlaying the heave motion response in the simulation are most likely the heave natural period of the TLP (mass spring system including added mass \sim buoy analogy). Moreover, besides showing a period corresponding to the wave period, the measured heave signal also contains a short period 'double hump' motion of almost half of the wave period. The three codes all capture the double hump behavior of the heave motion as seen in the measurement signal. Overall, CFD, FLEX5 and FAST compare well with the measurements.

Looking at the force evolution in the four tendons, it is observed that in the measurement the tensions in front and back are almost 180 degrees out of phase. As for EC8 case, the tensions in front and back are in phase in CFD, whereas FLEX5 and FAST match the phase difference observed in the measurements. A main period corresponding to the wave period of 1.99 s is observed in all of the force signals including CFD. No pronounced evidence of motion and tension force coupling like in EC8 is observed. The CFD line tension is largely under-predicted, but in view of the good match for the corresponding pitch response, we conclude that the pitch-tension consistency seems not strong. The same trend in accuracy observed for EC8 is present for mooring tensions results obtained with FAST and FLEX5.

For the larger discrepancy in amplitudes observed in the CFD simulation, a plausible explanation may be found in the moving mesh approach which results in poor mesh quality due to highly distorted computational cells adjacent to the floating structure. The problem becomes more pronounced if motion of the floater is large. Distortion of boundary layer cells obviously has a negative impact on the viscous forces computed which are tightly coupled to the motion response. The flexible mesh method is in particular sensitive to distorted cells that results from angular motion and is further governing the angular motion/impulse that may introduce large errors that may affect e.g. pitch motion. However, this does not explain the large discrepancy observed between good prediction of the dominating motion responses and large under predicted amplitude and phase mismatch in tendon forces. An error in the computation of tension in the mooring line (which in the CFD model is based on motion response input - that is computed with reasonable accuracy) is likely to be the reason.

Response to irregular waves

This section presents results for irregular sea states obtained with FLEX5 and FAST. For all irregular waves, the wave signal measured in the wave tank tests has been used in the numerical models to compute wave kinematics and wave forcing. Figure 110 and Figure 111 below show results for irregular wave 8 using FLEX5 with linear wave kinematics and FAST v1.

Surge matches well in all models. FAST under-predicts the response at surge natural frequency, but the significance is much less than for the wave-excitation region. In heave, only the excitation at low frequency and at twice the wave frequency range is captured by the simulations, while the test also shows energy at the wave frequency and around 3.8 Hz. The origin of this peak is still unknown, but one hypothesis is that it originates from the double-spring system resulting from the

spoke bending flexibility and tendon stiffness. This combined spring system would show two combined frequencies; one higher corresponding to the two springs acting in anti-phase, and one lower for the two springs acting in phase (likely the 3.8 Hz observed). Since the spoke flexibility is not modelled, this peak is not observed in the numerical results. The pitch motion is over-predicted by the two models, especially at the pitch natural frequency (1.9 Hz), and the effect can be also seen in nacelle acceleration and line tension. FAST over-predicts more than FLEX5, but the recalibration factor applied to the measured pitch signal was chosen in favor of FLEX5, so the match in pitch is merely indicative. In addition, since the spokes are not modelled, their damping effect on the pitch motion is missing and therefore a higher level of excitation may be expected at the pitch natural frequency in the models. Except for the over-prediction of energy at the pitch natural frequency, both models predict the nacelle acceleration well. For line tension, the FAST model shows a better match in the frequency domain for the tension at the back tendons, while FLEX5 seems to capture better the energy content in the front tendons.

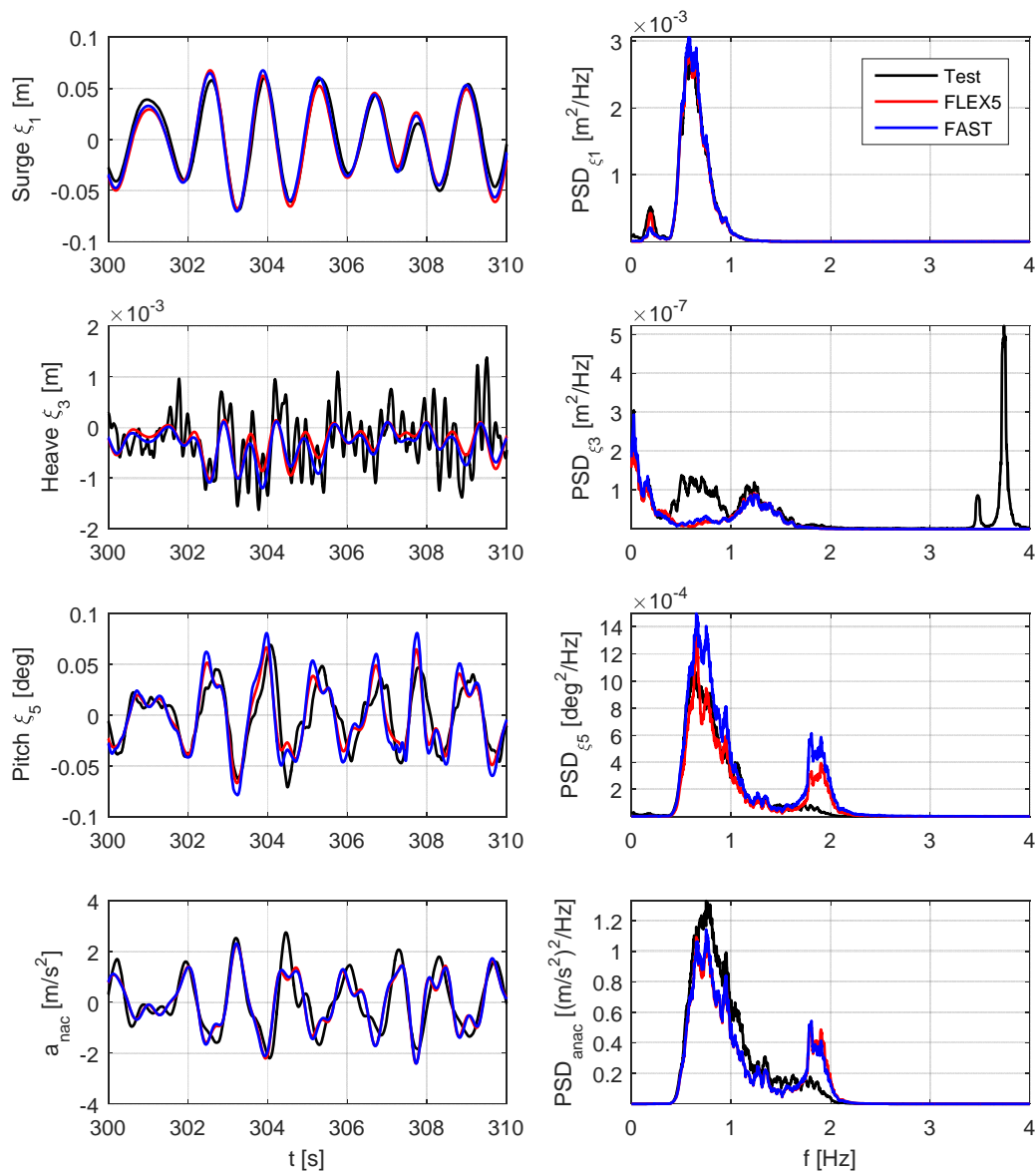


Figure 110: Response for irregular wave EC8, FAST v1

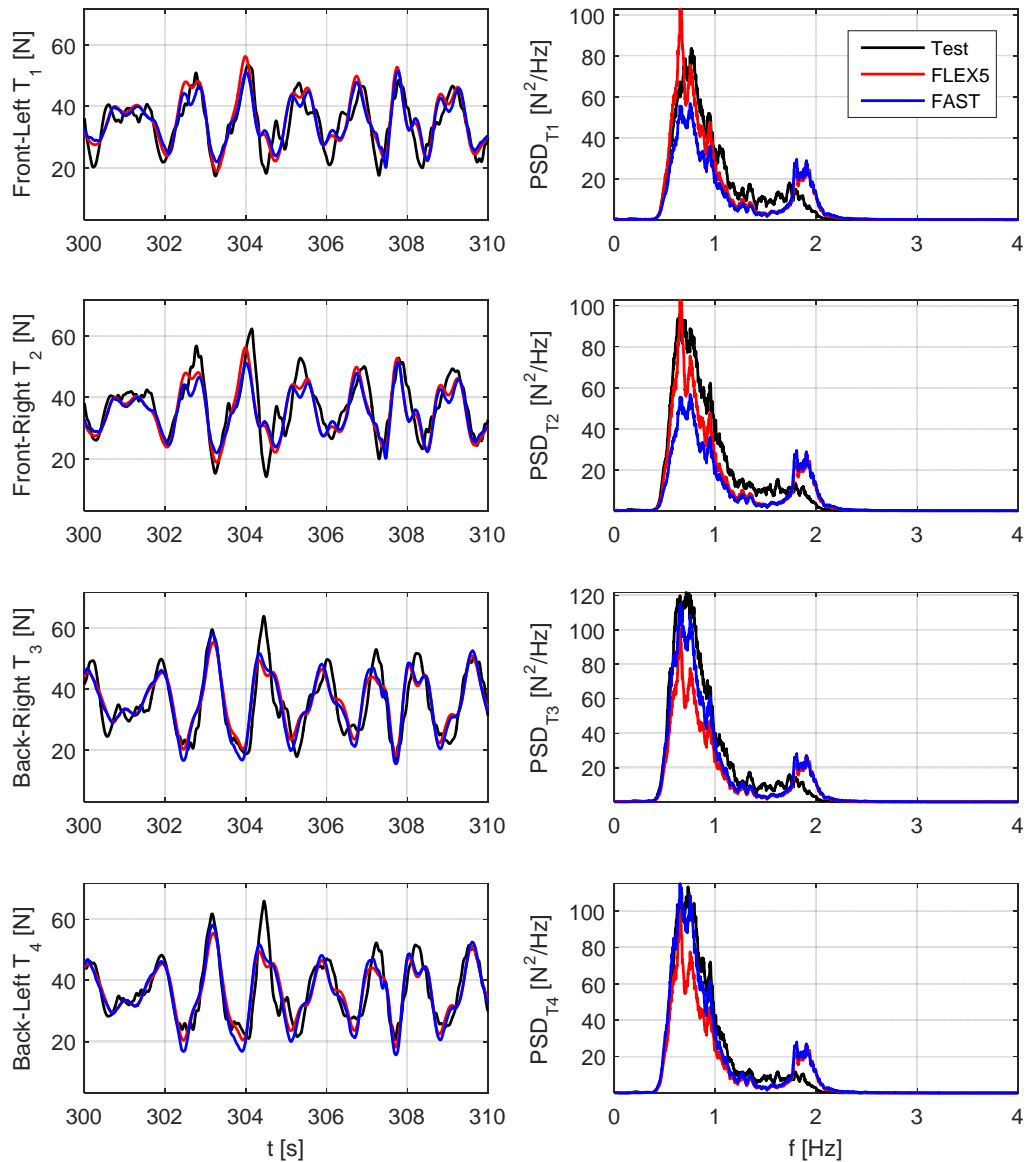


Figure 111: Line tension for irregular wave EC8, FAST v1

Results for the same irregular wave EC8 are shown in Figure 112 and Figure 113, but this time the FAST v2 model is used, which considers second-order wave kinematics. The main difference in results obtained with FAST v1 is in the subharmonic region, especially at the surge natural frequency (0.19 Hz) where the energy predicted by FAST v2 is much higher than in the test, likely due to an insufficient amount of damping in surge at this frequency. Another reason could be related to the need of filtering the measured surface elevation to 1st-order before using it to compute the 2nd-order wave kinematics; for the present simulations the raw measured surface elevation was used as an input for FAST to compute 2nd-order kinematics. The superharmonic wave components do not seem to induce a significant surge response compared to the linearly produced results.. For heave, the subharmonic forcing (meaning by subharmonic the frequency region below the wave peak frequency) improves the results - this is probably through quasi-static heave response to the long second-order variation in the free surf elevation. Pitch, nacelle acceleration and line tension are not too affected by the use of 2nd-order wave kinematics in FAST.

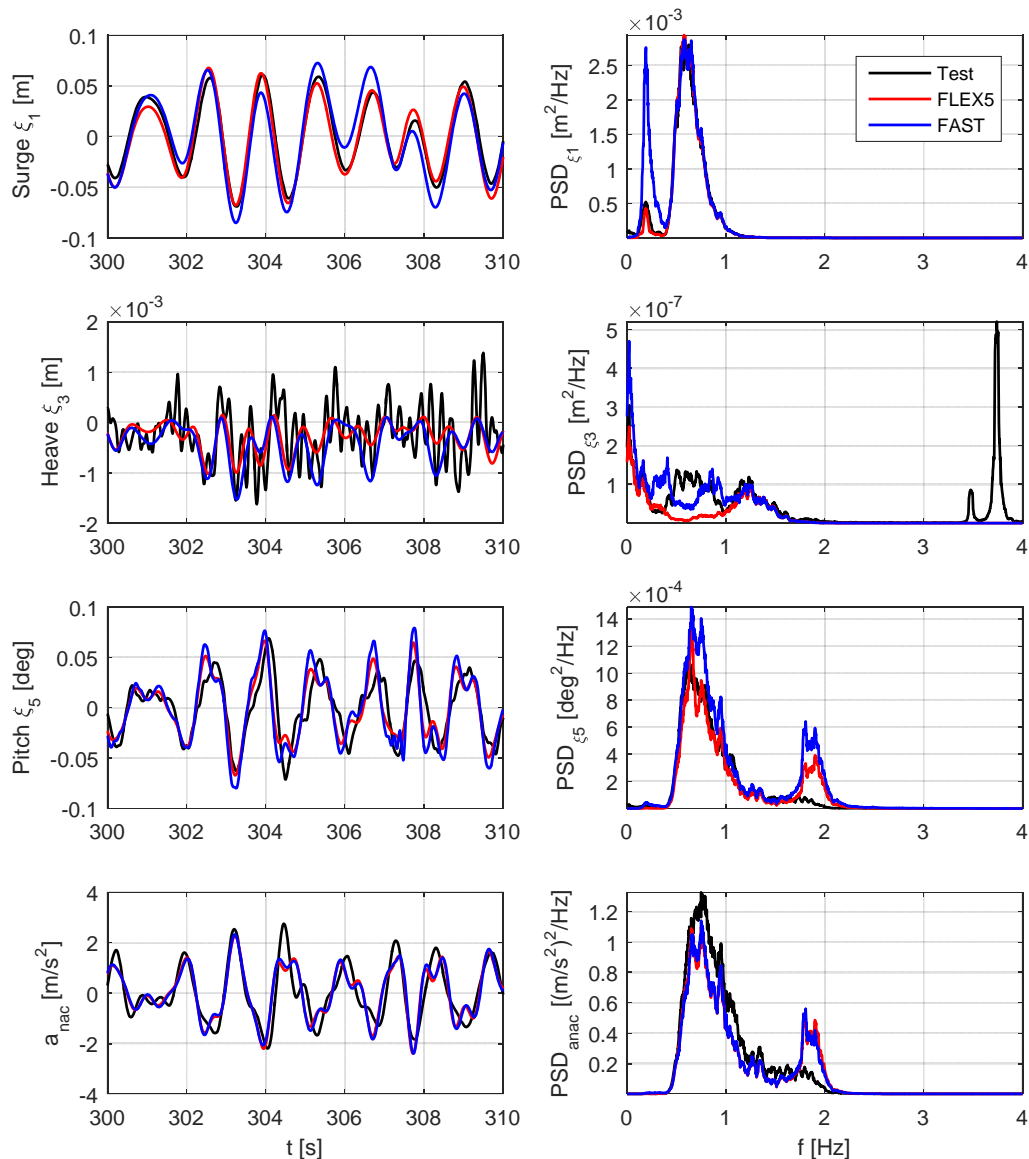


Figure 112: Response for irregular wave EC8, FAST v2

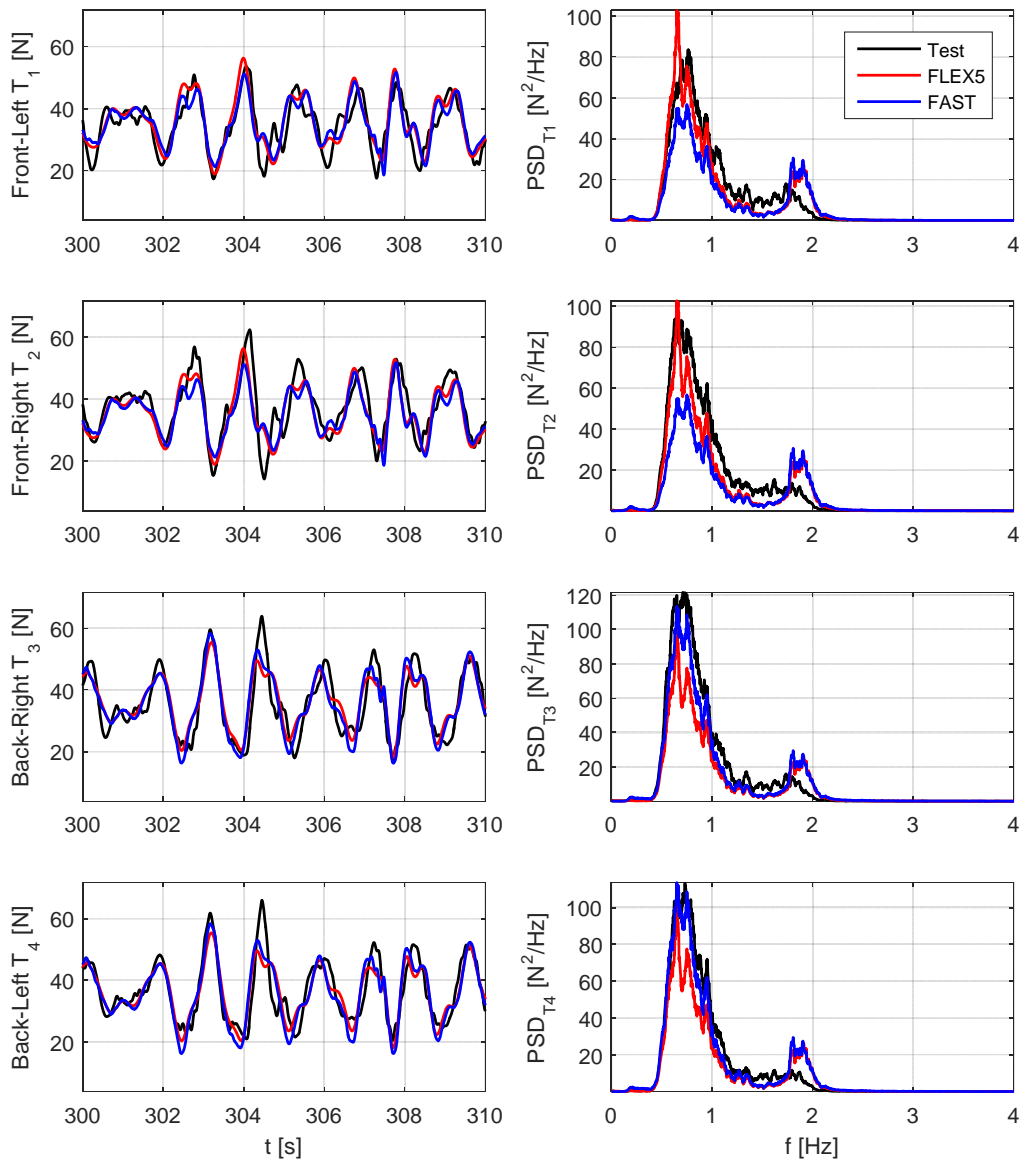


Figure 113: Line tension for irregular wave EC8, FAST v2

Response to irregular waves and wind

The effect of wind on the response is analyzed in this section. Figure 114 and Figure 115 below show exceedance probability plots of motion and line tension for irregular sea state EC5, corresponding to rated wind speed. The FAST model employed here is v1 with linear wave kinematics. There is a good match in surge for FLEX5, and pitch is over-predicted by around 0.05 deg, i.e. 8% for exceedance probabilities below 0.8% while for the largest pitch deflections an overprediction of 16% is seen. Pitch motion is forced by both rotor loads and wave loads and is also damped by both aero- and hydro-dynamic effects. A difference in the results can thus be attributed to differences in the turbulence properties between field and lab and different damping mechanisms. The overall match is satisfactory. For heave, the extreme deflections are matched by FLEX5 while some over-prediction (about 15%) occurs for the main group of peaks. Nacelle acceleration is underpredicted by FLEX5 for all levels of probability. For the extreme values of acceleration the underprediction is 12%.

FAST over-predicts surge, heave and pitch relative to the experiment. A further calibration of the damping in FAST would likely improve the match. However, as stated previously, the recalibration factor applied to the test pitch signal plays an important role on the model accuracy. FAST shows a better match to nacelle accelerations than FLEX5, although some under-prediction is still seen. This difference can be due to different damping modelling of the flexible tower in the two models. In the mooring loads, both FLEX5 and FAST shows an over-prediction in mean tension of 9% for FAST and 14% for FLEX5. FAST generally shows a better match than FLEX5 for the back tendons. This can be explained by the dynamic mooring model of FAST, that takes tendon dynamic effects into account, whereas the mooring model in FLEX5 is quasi-static and therefore expected to be less accurate. For the front tendons, both models show similar accuracy, except for extreme loads in the front-left tendon, where FLEX5 over-predicts more than FAST.

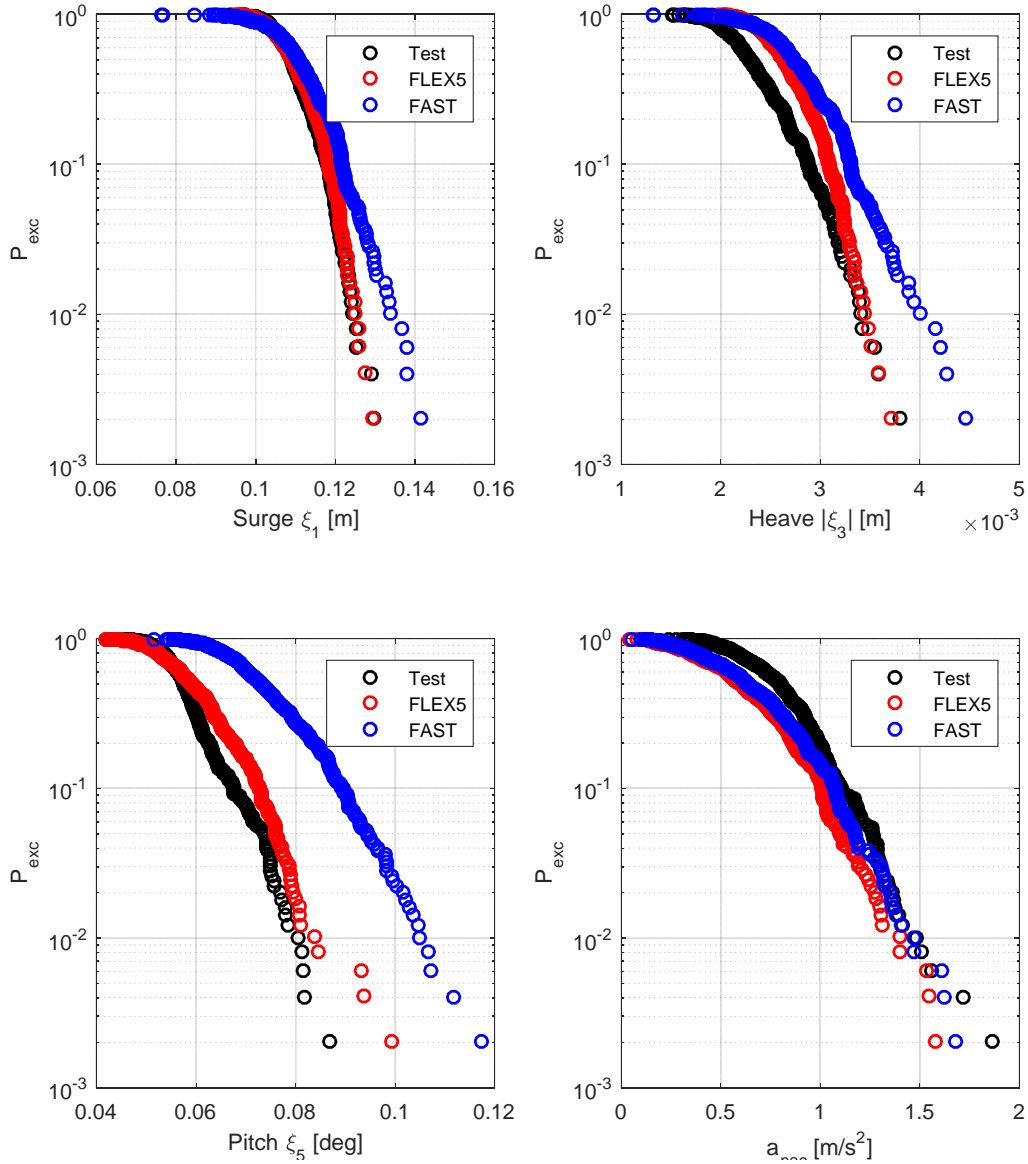


Figure 114: Response for irregular wave EC5 and wind

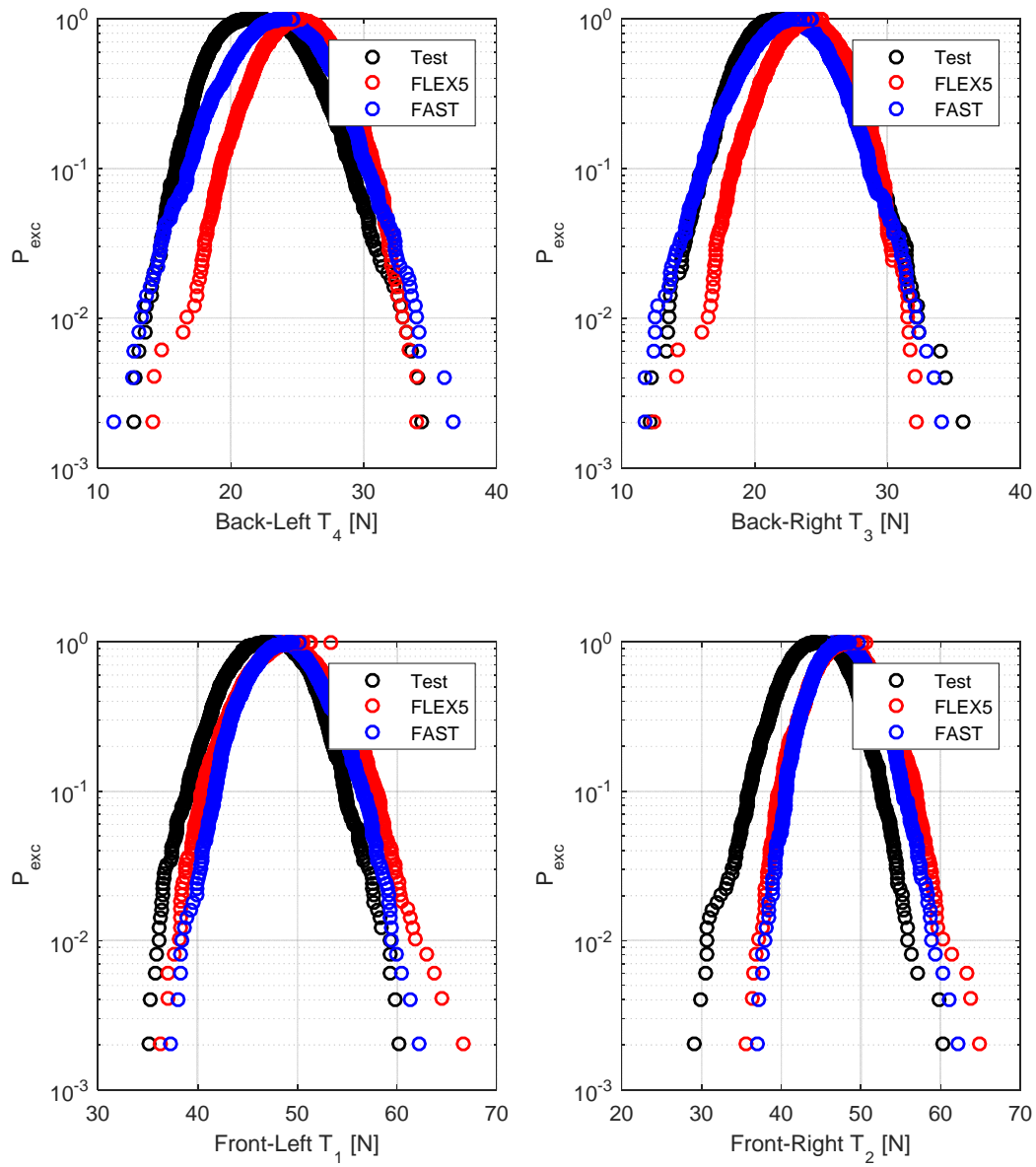


Figure 115: Line tension for irregular wave EC5 and wind

Figure 116 and Figure 117 below show exceedance probability plots for the irregular sea state EC7 and wind, corresponding to the maximum wind speed in the test environment. The match between models is generally closer for this case in surge, heave and pitch. FAST still shows some over-prediction relative to the tests and FLEX5. In nacelle acceleration, the two models agree but both under-predict the measurement. For extreme cases the under-prediction is 16%. In mooring line tension, there is also a difference on the mean values compared to tests. FAST is generally closer to the tests than FLEX5 (e.g. in back tendons), which again can be explained by the dynamic model used for the tendons in FAST. In the front tendons, it may look like FLEX5 is closer to the tests, but the difference in mean tension has to be taken into account.

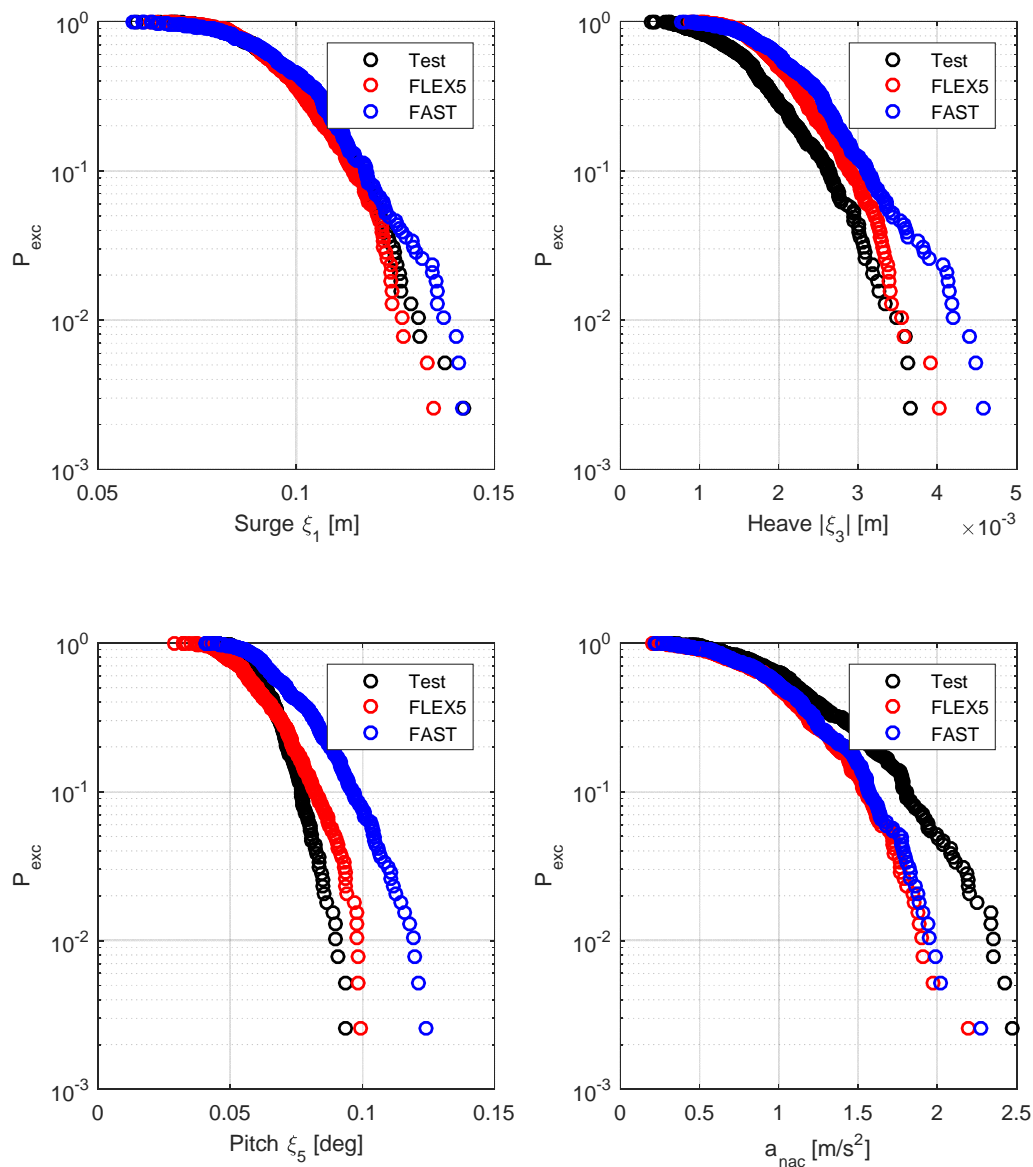


Figure 116: Response for irregular wave EC7 and wind

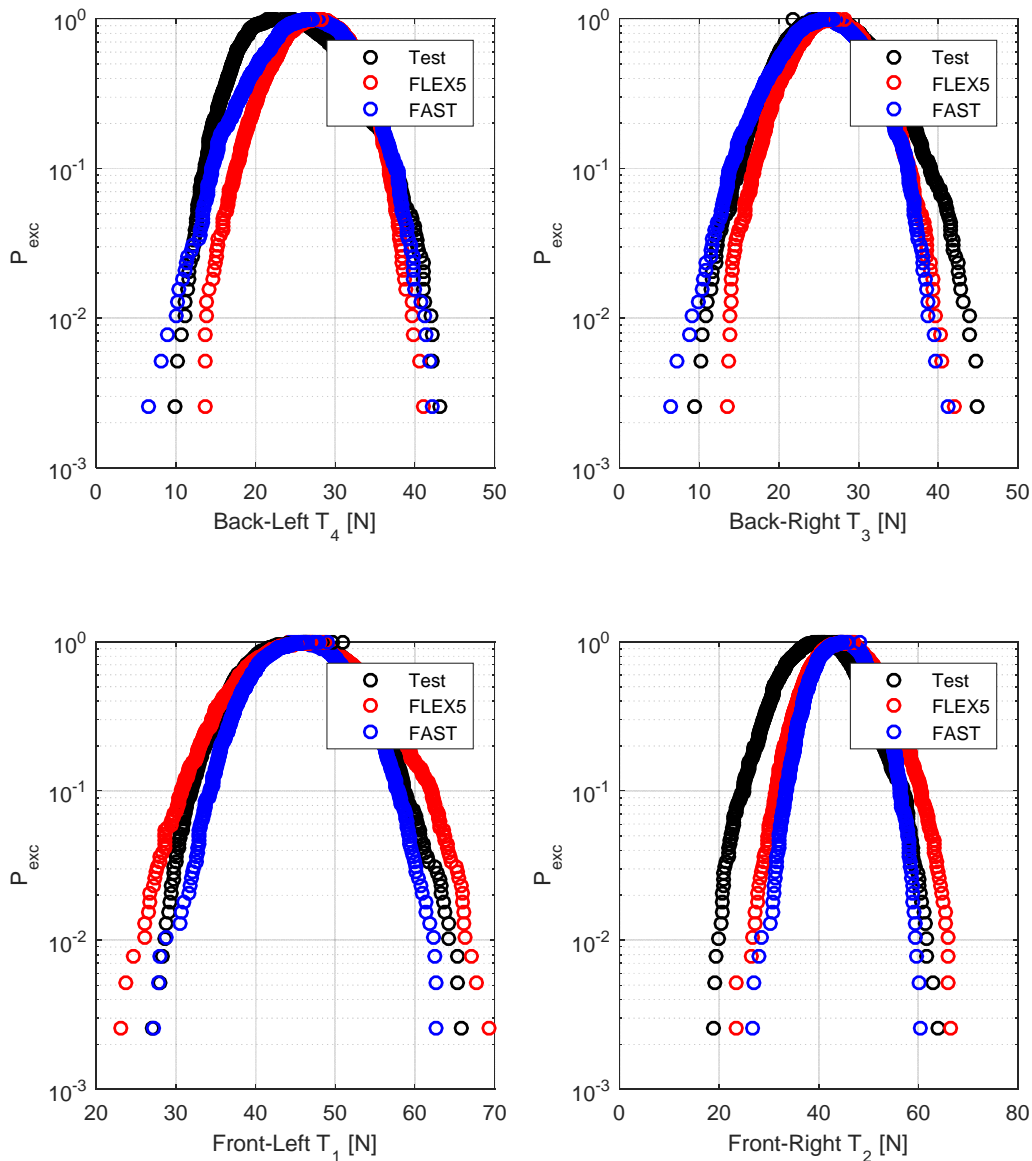


Figure 117: Line tension for irregular wave EC7 and wind

Response to focused waves

Two tests of focused wave group forcing were reproduced: one for EC6 and one for EC8. For EC8, both FLEX5 and the CFD model were run, while for EC6 only FLEX5 was run. We therefore initially discuss the EC8 case.

In FLEX5 the wave signal measured in the wave tank tests has been used in the numerical models to compute wave kinematics and wave forcing. In CFD, the phase focused wave signal used in the wave tank test has been imposed at the vertical inlet boundary of the rectangular computational domain. In top of each of the figures in this section, the surface elevation of non-disturbed wave (WG8) and wave in front (WG6) of the wind turbine is depicted.

Figure 118 shows the results for surge, heave, pitch and nacelle acceleration in terms of time series and power spectral density for the focused wave of EC8. The corresponding tendon tensions are shown in Figure 119.

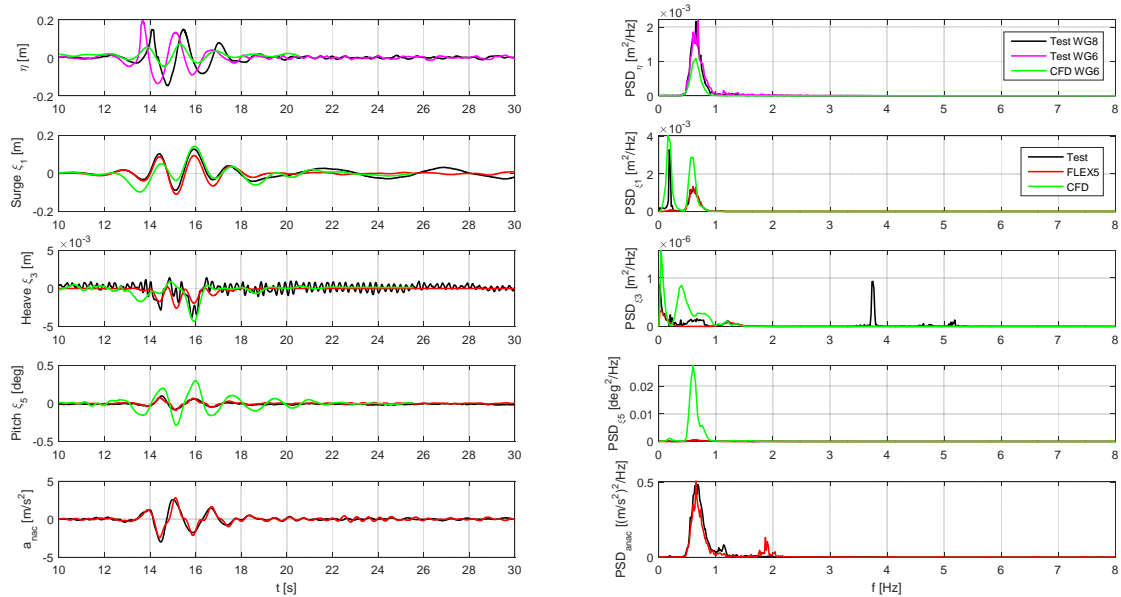


Figure 118: Motion response and associated power spectra for focused wave group test of climate EC8. Linear wave kinematics applied in FLEX5 v1.

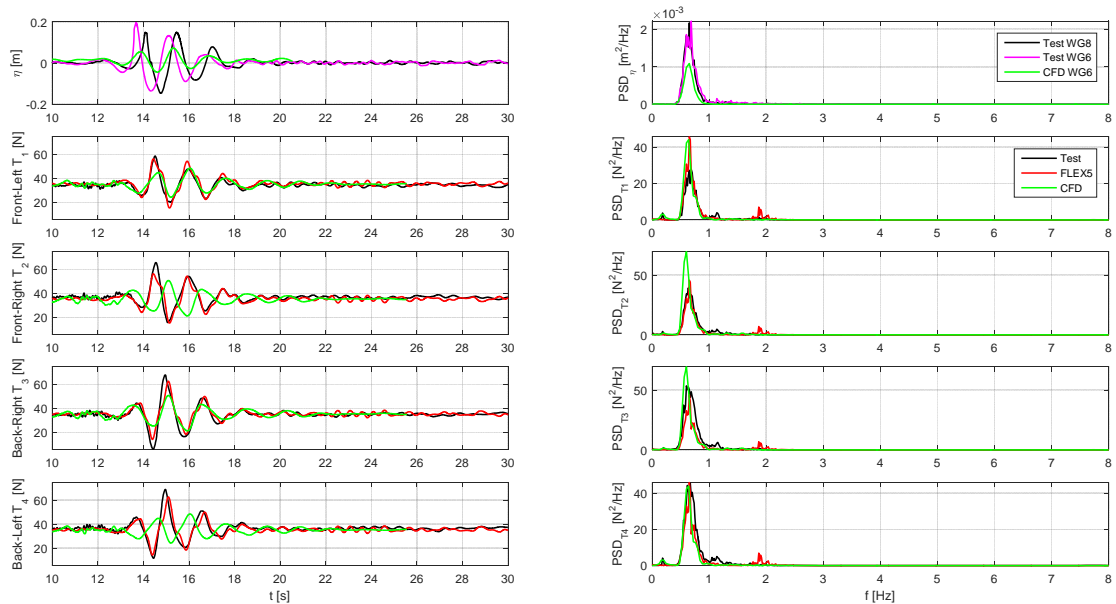


Figure 119: Tendon forces for focused wave, EC8. Linear wave kinematics in FLEX5 v1.

The CFD results show a fair overall match to the surge signal with a very close match of the main surge peak. The subharmonic spectral peak at 0.19 Hz is matched by the CFD model, while the dynamic mooring loads are under-predicted, which is likely due to the computationally propagated

wave signal just in front of the wind turbine having an amplitude half of the one in the measurements. A remedy for this is to calibrate the wave signal in CFD to match the wanted wave height of the wave just before it interacts with the structure. The deviation in wave height is dependent on the numerical convection schemes and turbulence model. On the other hand, the pitch response is over predicted, which implies either lack of stiffness in the tendons or a mismatch between expected and realized force evolution seen in the four tendons. For FLEX5, a good overall match for surge, pitch and nacelle acceleration is seen. The experimental heave signal is quite noisy with heavy excitation at the natural frequency of 3.8 Hz. This may be related to the back-right tendon tension at $t=14.5$ s which almost goes slack (zero tension). As discussed earlier, the heave natural frequency at 3.8 Hz is expected to originate from spoke flexibility, which is not included in the numerical model.

From the spectral density plots, the FLEX5 pitch and nacelle acceleration show some energy at the pitch natural frequency of 1.9 Hz, while the test results do not. This numerical over-prediction can again be linked to missing viscous damping from the spokes in FLEX5.

Figure 120 and Figure 121 shows the same experimental data as before. This time, however, the FLEX5 results are produced with second-order wave kinematics and addition of second-order correction terms in the Morison equation to consistently provide the second-order forcing contribution from the wet area between the mean water level and the instantaneous free surface elevation. The CFD results included in the figures are identical to those already compared to FLEX5 linear wave forcing and tests.

For surge, the inclusion of second-order wave forcing leads to an improvement in the prediction of the oscillatory motion at the natural surge frequency that follows the impact with the wave group. This is also evident from the spectral plot for surge (upper right frame). For pitch and nacelle acceleration both the time series and spectral plot shows increased energy at the pitch natural frequency of 1.9 Hz. This is a natural consequence of super-harmonic second-order wave components, which are created at the pair-wise sum frequencies of the linear wave field. The linear wave fields main frequency peak is around 0.8 Hz and sum-frequency waves are thus able to excite the natural frequency at 1.9 Hz. The measured data, however, do not show a similar excitation. This must be due to (again) a stronger viscous damping of the pitch motion in the lab compared to the numerical model. As stated earlier, the spokes are not modelled explicitly and do therefore not contribute to this damping.

Although the pitch decay test showed a satisfactory damping, the present test situation with ambient wave kinematics changes the nature of the damping from quadratic to linear. This may explain the difference between pitch damping match at the decay test and missing pitch damping in the tests.

The over-prediction of pitch motion at 1.9 Hz carries over to the mooring forces. Although the overall match with the tests is good, the high-frequency oscillations are visible and makes the linear hydrodynamic model results better. The key for improvement of the results will thus be to supplement the second-order hydrodynamic forcing model with appropriate modelling of the spokes and their viscous damping.

One more case of focused waves is presented in Figure 122 (motions) and Figure 123 (tendon tensions). Here the results for EC6 is shown, which is a weaker sea state. The figures show FLEX5 results only, again produced with second-order hydrodynamic forcing.

The results show a very good match for surge, including the excitation of motion at the natural surge frequency after the wave groups passage. The heave signal is mainly noise and has an amplitude of less than 1 mm. Pitch and nacelle accelerations are well matched at the time series level. The spectral plots show an overprediction of motion at the pitch natural frequency of 1.9 Hz, similarly to the EC8 test results. Consistent with the smaller wave amplitude, the excitation is smaller than for the EC8 test and the sum-frequency excitation is also relatively smaller to the motion range at the linear wave frequencies. This confirms that this forcing is a nonlinear effect, included in the second-order model.

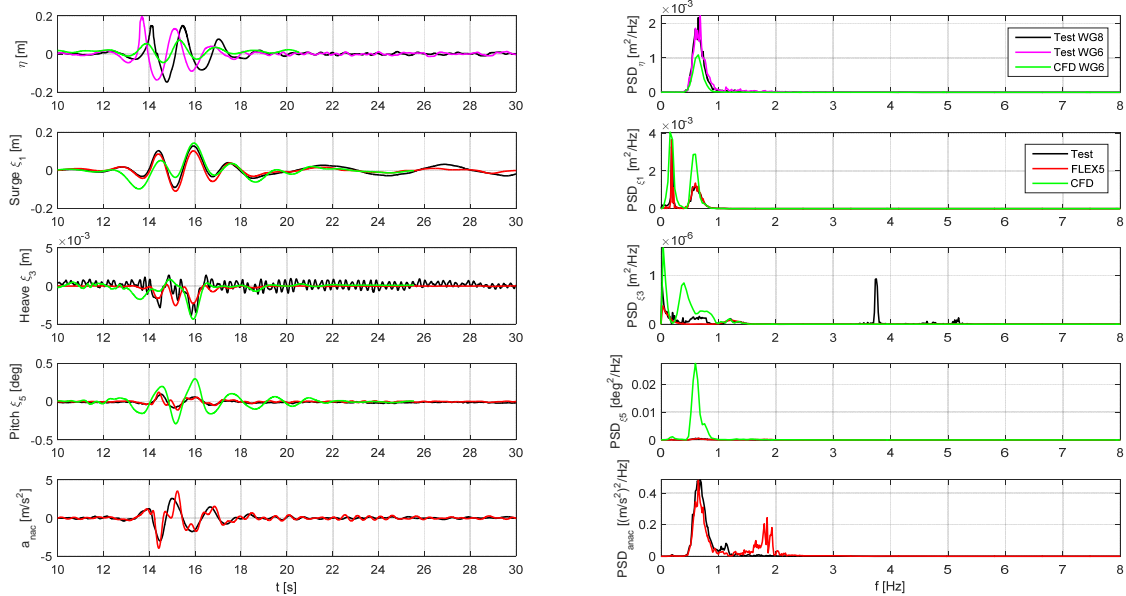


Figure 120: Motion response and associated power spectra for focused wave group test of climate EC8. Second-order wave kinematics applied in FLEX5 v2.

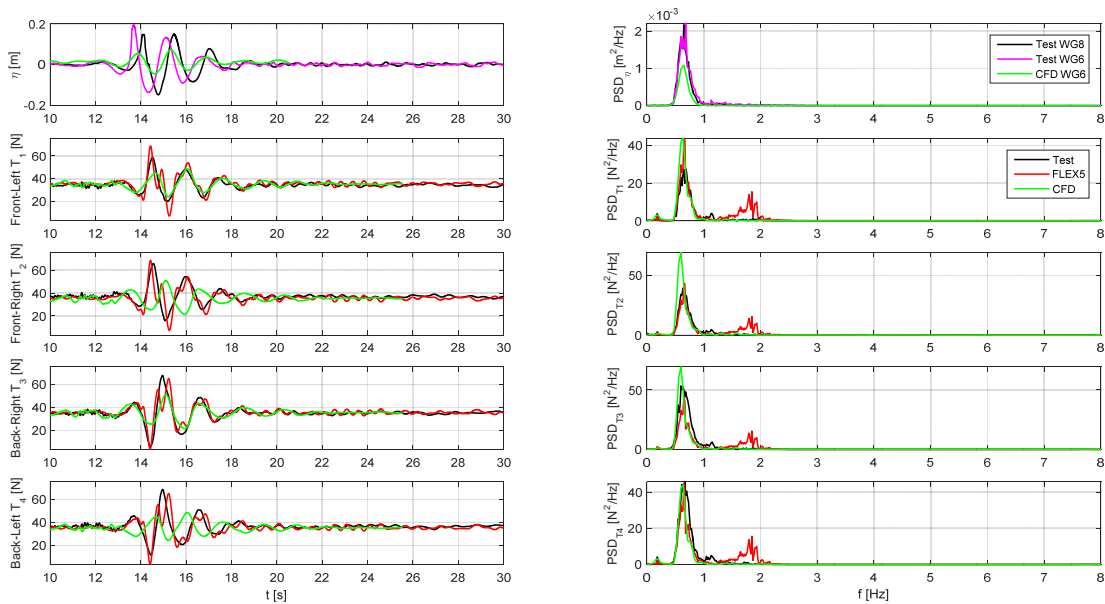


Figure 121: Tendon forces for focused wave, EC8. Second-order wave kinematics in FLEX5 v2.

The mooring forces show a good overall match, still with over-predicted energy at 1.9 Hz arising from the associated overprediction of pitch motion at the same frequency. For this test the measured signals do, however, show excitation at around this frequency in the spectral plots. This can be explained by the smaller peak wave period of EC6, which makes the linear spectral wave peak closer to one-half times the natural pitch frequency. Although smaller in amplitude, the second-order forcing components of the present test are thus closer to the natural frequency.

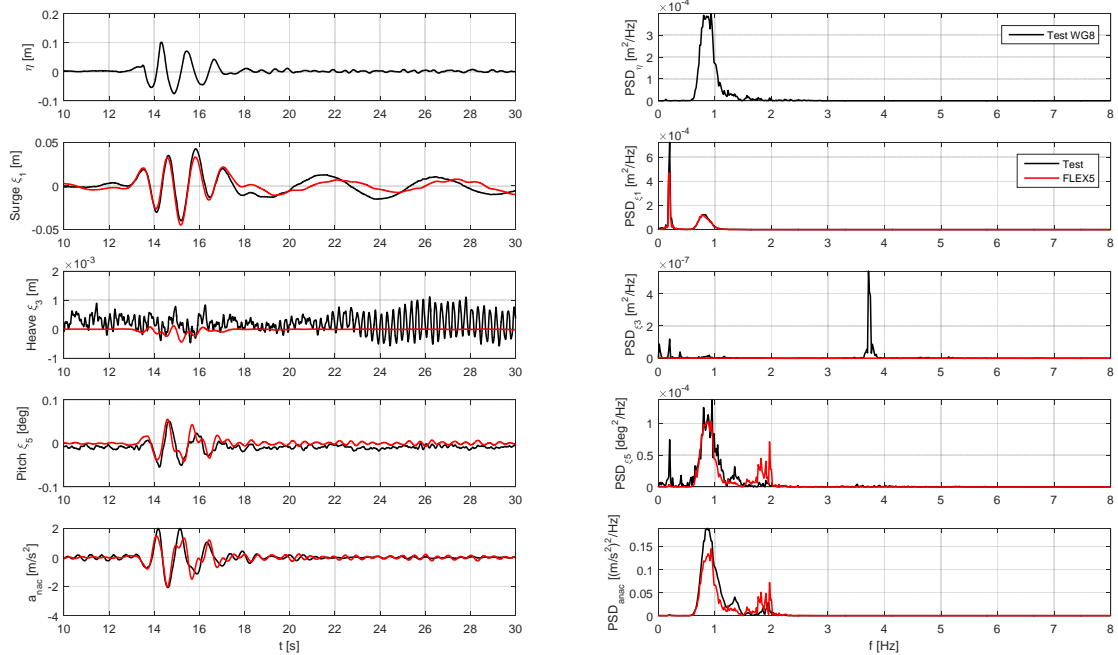


Figure 122: Motion response and associated power spectra for focused wave group test of climate EC6. Second-order wave kinematics applied in FLEX5 v2.

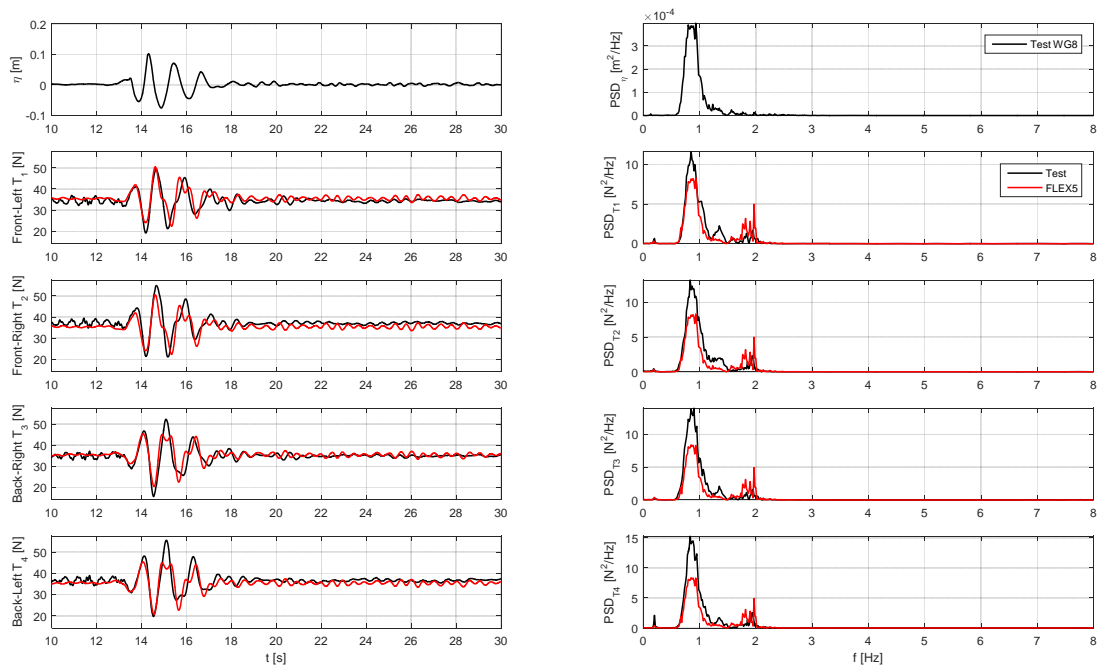


Figure 123: Tendon forces for focused wave, EC6. Second-order wave kinematics in FLEX5 v2.

3.6 Additional simulations with simulation code BLADED

The Bladed simulation code has been applied complementary to the simulation with FLEX5, FAST, and the OpenFOAM® platform (CFD) as shown above, to demonstrate the capability of the Bladed code for predicting floating wind turbine dynamics and loading. The scope of the simulations do not cover the full test case set though the results were not included into the cod-to-code comparison as shown in chapter 3.5. Moreover, focus of the Bladed simulation was put on the interaction between wind and wave dynamics and to the couplings of the different floating deflection due to transient events. Thus primarily the decay tests and the test with rotor thrust participation have been analysed. For consistency also regular and irregular wave conditions have been compared with respective measurement time series.

The model data of the DHI tank test wind turbine in scale 1:60 of a 10MW TLP design have been described already in chapter 3.2. Enclosed essential model data are compiled in figure 23 for the Bladed TLP model. The material properties are shown in table 4. The overall mass of the Bladed model results in 18.43 kg (18.54 kg weighted model mass).

An analysis of the eigenfrequencies of the structural modes showed good agreement.

Table 4: Eigenfrequency comparison of tower modes

Mode	DHI 1:60 model	Bladed 4.7	Deviation
1. mode: Tower fore-aft (global x)	2.0 Hz	2.05 Hz	0.48 %
2. mode: Tower side-side (global y)	2.4 Hz	2.06 Hz	16.5 %

The hydrodynamic coefficients have been established for each member individually according to Keulegan-Carpenter number and present wave condition.

Table 5: Hydrodynamic coefficients for model members

Model scale	0.30 Floater						0.15 Column									
	Wave height Hs	CD			CM	Water depth			Wave height Hs	CD			CM	Water depth		
		-0.20	-0.40	-0.60		-0.20	-0.40	-0.60		0.00	-0.10	-0.20		0.00	-0.10	-0.20
							TP									
	0.04	0.30	0.78	0.60	2.00	1.69	1.20	0.71	0.04	0.46	0.30	0.42	2.00	2.00	1.95	
	0.05	0.30	0.60	0.73	2.00	1.83	1.20	0.78	0.05	0.31	0.30	0.40	2.00	2.00	1.97	
	0.06	0.30	0.52	0.86	2.00	1.88	1.22	0.84	0.06	0.30	0.30	0.40	2.00	2.00	1.97	
	0.06	0.30	0.48	0.93	2.00	1.91	1.49	0.89	0.06	0.30	0.31	0.40	2.00	2.00	1.97	
	0.07	0.30	0.45	0.85	2.00	1.93	1.64	0.94	0.07	0.30	0.32	0.40	2.00	2.00	1.97	
	0.10	0.30	0.40	0.58	2.00	1.97	1.84	1.15	0.10	0.31	0.36	0.42	2.00	2.00	1.96	
	0.13	0.31	0.39	0.53	2.00	1.97	1.88	1.29	0.13	0.34	0.39	0.44	2.00	1.98	1.94	
	0.17	0.32	0.38	0.46	2.00	1.99	1.93	1.58	0.17	0.39	0.43	0.47	1.98	1.95	1.92	
	0.20	0.34	0.39	0.45	2.00	1.98	1.93	1.76	0.20	0.43	0.47	0.51	1.95	1.92	1.89	
	0.24	0.36	0.41	0.46	2.00	1.97	1.93	1.99	0.24	0.48	0.51	0.55	1.91	1.89	1.86	

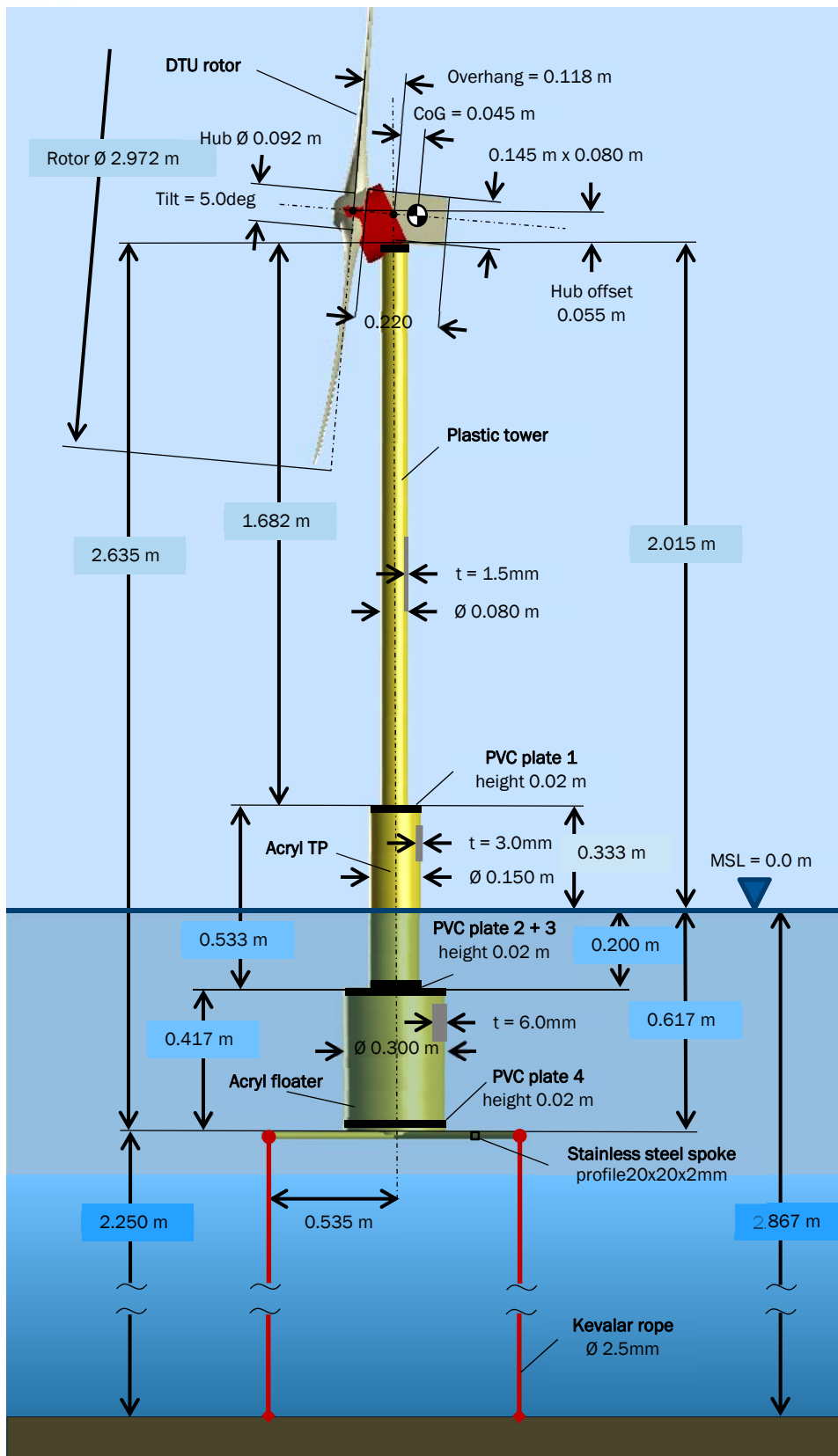


Figure 23: Geometrical model data of the Bladed TLP scale 1:60

The material properties used in the model are given in the tables below.

Table 6: Material properties applied in the Bladed model

Rotor blade	Total mass	Stiffness	Centre of gravity	Imbalance
Unit	kg	Nm ²	m	kgm
	0.198 (one blade)	- (stiff)	0.444	0.005

Hub	Total mass	Inertia about shaft	Inertia perp. to shaft	Imbalance
Unit	kg	kgm ²	kgm ²	kgm
	0.476	6.0E-04	5.5E-04	0

Drive train	Gearbox ratio	HSS stiffness	Generator inertia	Rotation speed (only wind cases)
Unit	-	Nm/rad	kgm ²	rpm
	-	- (stiff)	-	74 (rated)

Nacelle	Total mass	Width x length x height	Centre of gravity behind tower axis	Centre of gravity above tower top
Unit	kg	m ³	m	m
	3.0	0.080 x 0.220 x 0.145	0.045	0.046
Unit	kgm ²	kgm ²	kgm ²	-
	0.007	0.04	0.04	0.6

Support structure	Total mass	Density	Young's modulus	Shear modulus
Unit	kg	k/m ³	N/m ²	N/m ²
Plastic tower	1.343	1,100	2.8E+09	1.7E+09
PVC plates 1	0.393	1,500	3.0E+09	1.7E+09
2	0.351			
3	1.969			
4	2.178			
Acryl transition piece	0.886	1,200	3.0E+09	1.7E+09
Acryl floater	3.0	1,200	3.0E+09	1.7E+09
Stainless steel spoke	2.430 (4 spokes)	7,900	2.0E+11	7.7E+10
Z-gauges / instrumentation	1.0 (4 gauges)	-	-	-

Kevlar tendon	Stiffness	Damping	Torsional stiffness	Torsional damping
Unit	N/m	Ns/m	Nm/rad	Nms/rad
	14,000	500	0	0.25

The intention of the Bladed simulation was to find out the behaviour in coupled conditions with a number of disturbances on several channels. During the decay test not only the excited component have been checked for good matching but also the coupled channels with comparable low signal amplitudes and high noise modulation. The result for the surge decay test case (S1_xi1) shows the relation between coupled sensors.

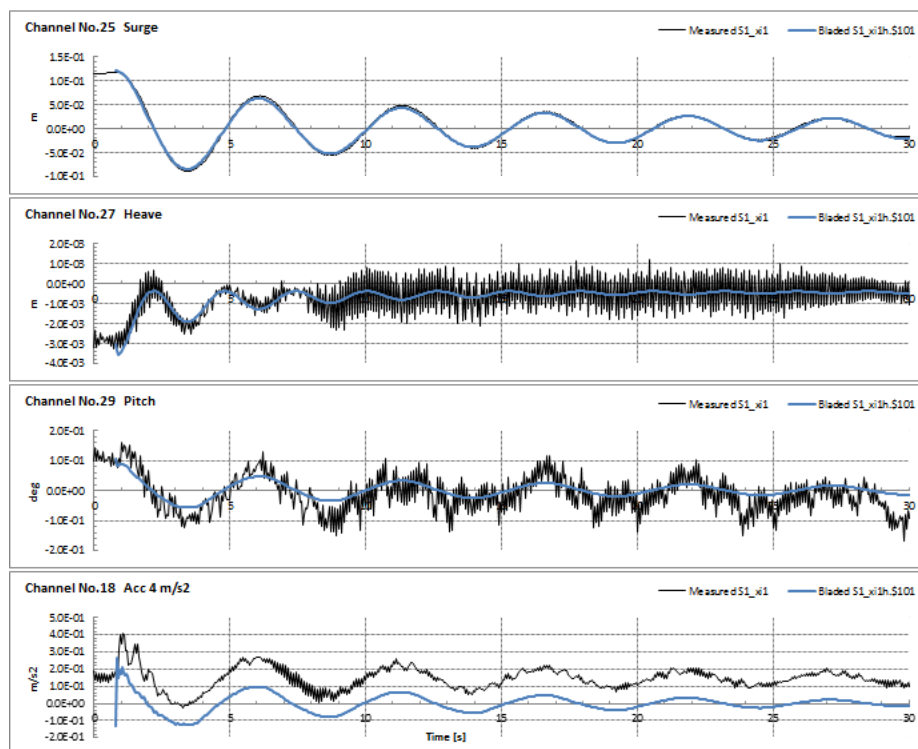


Figure 24: Surge decay test S1_xi1 – deflections and accelerations

This observation includes also the mooring line tension. During the model setup it figured out that stiffness of the Kevlar ropes given in the test specification did not correspond to the dynamic results in Bladed. The original stiffness of EA = 80 kN have been reduced empirical to finally to 36 kN in order to match the tendon frequencies from the measured time series. In some tests it showed up that after an initial excitation the floater remained in an inclined position and did not return to a 0-position. Hence the resulting tendon forces remained asymmetric even after a long fade out period.

The offset in the acceleration signal is probably a calibration inaccuracy since the offset is already present in the stationary decay phase.

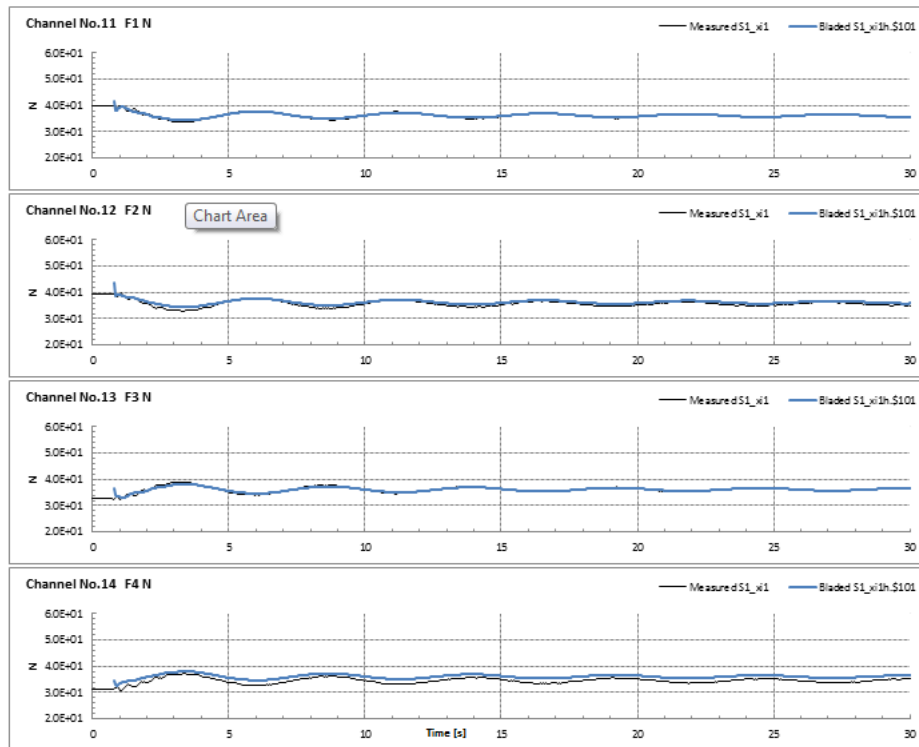


Figure 25: Surge decay test S1_xi1 – tendon tensions

Similar to the code comparison with FLEX5, FAST, CFD the measured pitch behaviour was difficult to match. This is of special interest since the other rotation directions roll and yaw showed very good alignment. In the comparison between measured and computed pitch inclination an obvious offset can be seen. This was visible in later tests as well. Here a calibration displacement of the measurement sensor could be a reason. However, it was decided not to apply correction factors to the simulation results and state the deviations as they occur between measurements.

In the test a strong coupling between pitch inclination and surge deflection occurred. This strong coupling and counter balance behaviour could not be represented in Bladed. Further a phase angle between pitch and surge motion of about 90° seems to be present. This could be a topic for further considerations.

Due to the high stiffness of the tendons and technical complications in exiting the heave mode this decay test has been omitted. But the outer test runs delivered sufficient measurement indication to adjust the tendon structural behaviour in Bladed.

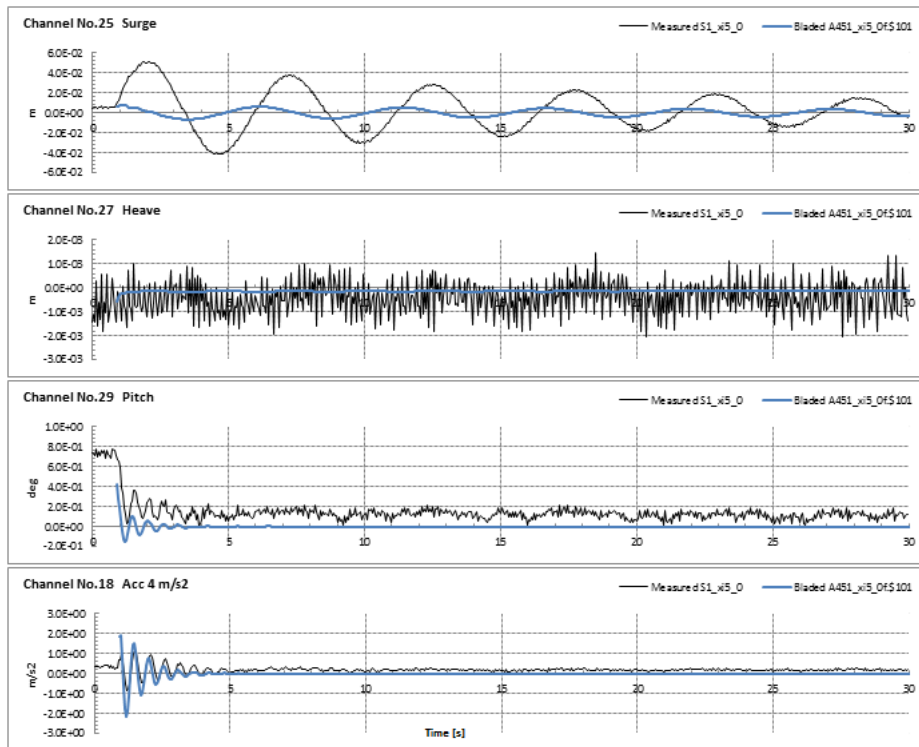


Figure 26: Pitch decay test S1_xi5_0 – deflections and acceleration

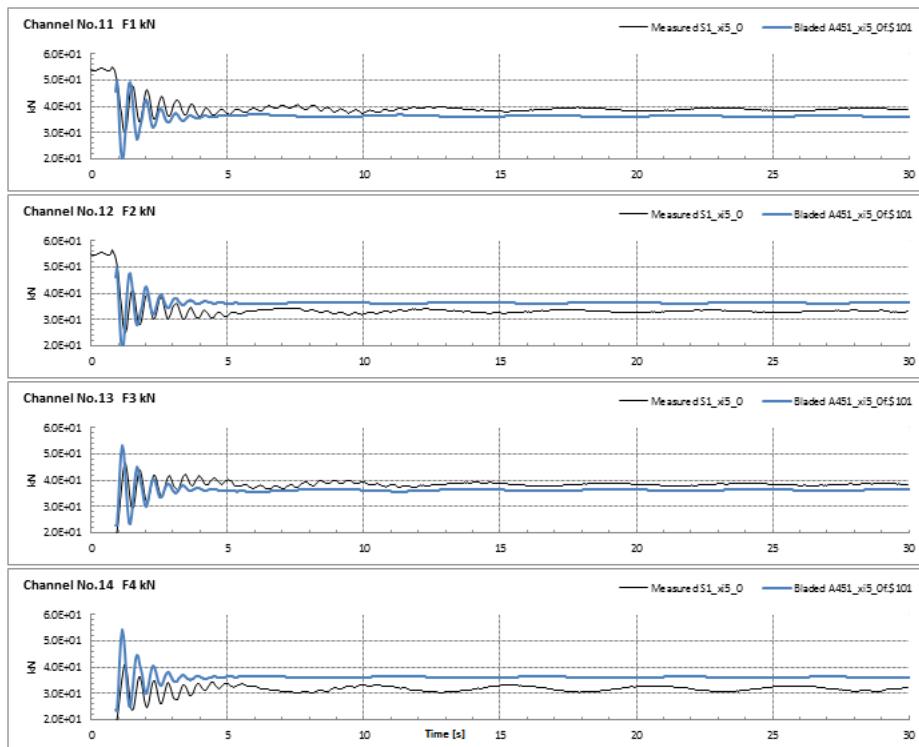


Figure 27: Surge decay test S1_xi5_0 – tendon tensions

A very interesting test case is the combination of decay and thrust generation by wind. Here the case S1W_Xi5 is presented. In Bladed a turbulent wind with 1.4 m/s average wind speed and a turbulence intensity of about 5% has been generated. The wind shear has been configured in a way to match with the test condition at the lab. As described before the open jet of the wind generator did not cover the model turbine's rotor plane sufficiently. By applying the scaled steady thrust curve of the full size 10MW turbine the rotor speed (68 rpm) and the blade pitch angle (0° at 1.4 m/s) could be extracted. This resulted in a tower top thrust force of 6.7 N which has been perfectly appointed by the Bladed simulation. Since during the test the rotation speed has been kept constant these nacelle parameters hub wind speed, rotor speed and blade pitch angle have not been recorded in times series.

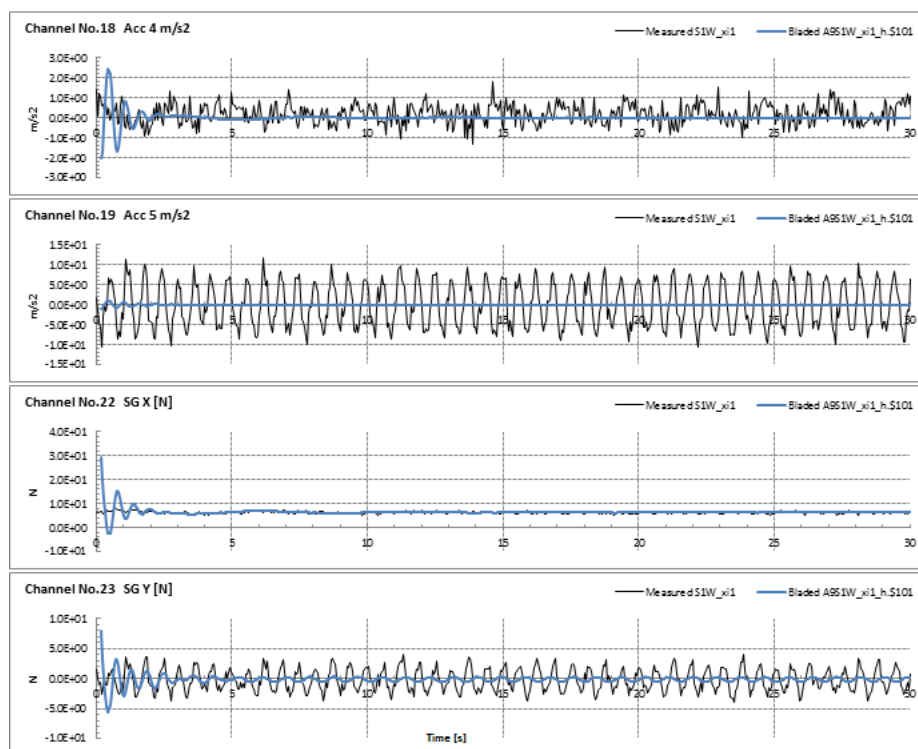


Figure 28: Pitch decay test with wind S1W_xi1 – nacelle accelerations and thrust forces

Another strong deviation which could be observed throughout all the tests is the strong vibration of the coupled roll and sway motion excited by side impacts of other load directions. Here the lack of aerodynamic damping for the side-side motions became apparent in the measurements. Although Bladed considers the different damping regime for side-side and fore-aft deflection it did not conclude with such a difference as shown in the measurements.

Finally the hydrodynamics have been checked by test cases with the presence of regular and irregular waves. As already shown by previous code comparisons with FLEX5, FAST, and CFD the precise wave excitation of the test facility could be represented by the codes in very good agreement.

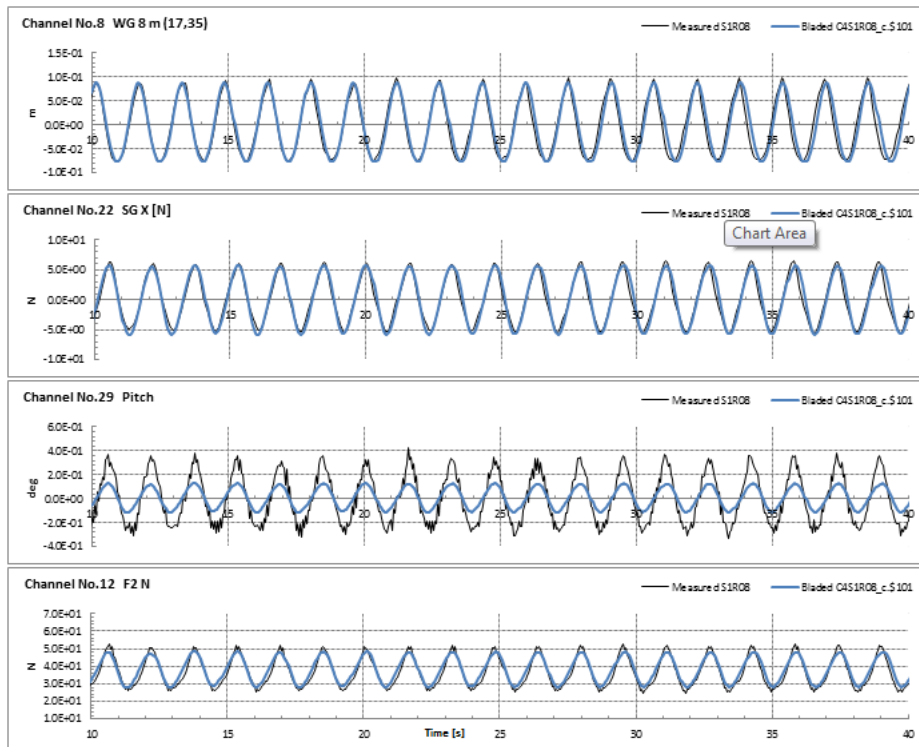


Figure 29: Regular wave case 08 without wind S1R08 – sea state and structure response

Except from the deviation to the pitch sensor which have been already addressed, the example of a sea state of $H_s = 0.167$ m (full scale 10.0 m) and a period of $TP = 1.58$ s (full scale 12.2 s) and the TLP reaction in terms of deflections and forces is met very precisely.

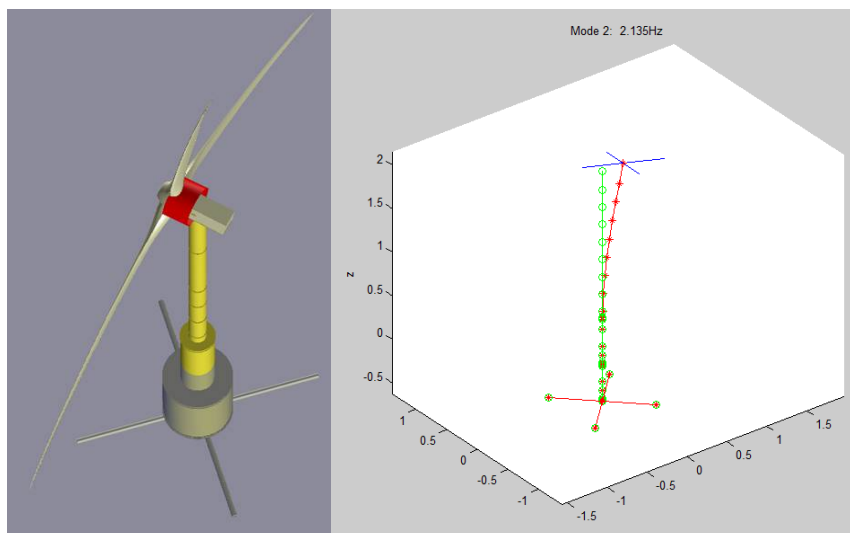


Figure 30: Modal representation of the Bladed TLP 1:60 model

3.7 Conclusions

Two type of codes for performing coupled analysis of a floating wind turbine, namely CFD and aero-hydro-elastic, have been validated against water tank tests of a TLP concept of a floating wind turbine. Two different aero-hydro-elastic models have been objects of this study, namely FAST with a dynamic mooring model and FLEX5 with a quasi-static mooring model. The CFD model is building on the OpenFOAM® platform, with a moving mesh approach. Contrary to the CFD model, both FAST and FLEX5 dependent on prior calibration of added mass and damping. The results from physical model decay test has served as input.

Simulations have been performed at model test scale 1:60 of the prototype floating wind turbine with a TLP foundation in order to avoid scaling inconsistency in the validation. Four types of validation tests have been performed, namely system ID tests, Hydrodynamic response tests, Hydro- and aero-dynamic response tests and focused wave group tests. Together with the phase focused waves, the two regular wave cases have been selected for validation of extreme wave impact interaction. The study focus has been on validation of the governing motion responses of surge and pitch for a TLP column structure and the corresponding forces in the tendons. A general good agreement between measurements and simulations of dominating motion response has been observed.

It has been demonstrated with reasonable results that CFD, FLEX5, BLADED and FAST all are able to capture the transfer of regular wave interaction of large nature on the motion response of TLP. This includes complex interaction between the mooring system and the body. However, CFD fails to simulate the corresponding accuracy in force evolution in the tendons as seen in the motion response signals. This result also applies for focus wave simulation results obtained with CFD compared to measured tension forces. For the larger discrepancy in amplitudes observed in the CFD simulation, a plausible explanation may be found in the flexible mesh approach which results in poor mesh quality due to highly distorted computational cells adjacent to the floating structure. The problem becomes more pronounced if motion of the floater is large. However, this does not explain the large discrepancy observed between good prediction of the dominating motion responses and large under predicted amplitude and phase mismatch in forces.

The validation with irregular waves showed a good agreement, with FLEX5 being slightly more accurate than FAST in surge and pitch. In pitch, both models overpredict the motion due to a larger amount of energy at the pitch natural frequency. However, the necessary recalibration factor applied to the measured pitch signal has to be chosen based on a model, and is hereby selected from FLEX5 simulations; hence, a better agreement with tests in pitch is expected from the FLEX5 model. The nacelle acceleration was well matched by both models. In line tension, FAST generally performs better than FLEX5, which is expected due to the dynamic modelling of tendons in FAST versus the quasi-static approach in FLEX5. When the effect of wind is introduced, the match with tests is generally improved for most of the signals. However, for the maximum wind speed both models slightly underpredict the nacelle acceleration, while the match is quite good for rated wind speed. When assessing model accuracy in cases with wind, the differences in wind field between test facility and numerical models have to be considered (open jet in test versus free atmosphere in models).

The phase focused wave validation provided insight into motion response in case of extreme wave events. The FLEX5 results showed a good match for the surge motion, pitch motion and nacelle acceleration. The tests, however, demonstrates the importance of viscous damping for accurate predictions of the excited high-frequency motion. Hence, the needed calibration of the damping in aero-hydro-elastic codes has a significant impact on prediction accuracy for large wave-structure interaction that excites structural frequencies. Viscous damping in FLEX5 was calibrated for surge decay, however, the present tests includes ambient wave kinematics that changes the damping nature from quadratic to linear. This may explain the good match in decay test but too small damping in focused wave test. However, generally FLEX5 with second-order wave kinematics provides a good prediction of floater motion and nacelle acceleration. The introduction of second-order hydrodynamic forcing improved the subharmonic motion that followed the main group impact for EC8. On the other hand, second-order hydrodynamic forcing enhances super-harmonic forcing of the natural pitch frequency (1.9 Hz), which combined with the insufficient viscous damping in the models, leads to overprediction of the pitch motion. The match in heave is

relatively acceptable, but FLEX5 miss excitation at the range of frequencies corresponding to the wave excitation (this conclusion also applies in cases of irregular waves for both aero-hydro-elastic models). In CFD, the first surge peak is well matched and a fair overall match for surge is obtained. The low-frequency part of the heave signal is also well reproduced by CFD, especially the peaks. However, the line tension is underpredicted by the CFD model for regular waves as well with same explanation as above.

Further research and development

The strength of the CFD model is the accuracy when hydrodynamic viscous effects is key in predicting the hydrodynamic motion response of a floating offshore wind turbine in view optimization of performance and energy harvesting. One of the key challenges in CFD is combining the high fidelity hydrodynamic CFD methodologies with CFD aero-dynamics which rely heavily on advanced turbulence modelling. Some compromises has to be made in term of the hydrodynamics being Froude dominated and the aero-dynamics being Reynolds dominated, which demands a profound research effort in to the core of CFD algorithms and methodologies. The next obvious step for hydrodynamic CFD is to device and implement a simpler aero-dynamic model dependent on wind turbine rotor thrust. After a successful implementation, it would be to combine the aero-dynamic CFD model in Chapter 2 with the hydrodynamic CFD model. Further development is also needed on the moving mesh approach to improve distortion of cells and related accuracy and stability issues. This includes further test and development. Moreover, further work needs to be carried out in relation to the development of active absorption boundary conditions valid for a wide range of conditions, hence improving accuracy for deep water.

For the aero-hydro-elastic models FLEX5, BLADED and FAST, further work to improve the damping is highly beneficial in improvement of accuracy. This will make the improvement of second-order hydrodynamic forcing valuable. The current approach of representing the viscous damping by a bulk calibration of the floater drag coefficient from free decay tests has proven to be insufficient in the cases where high-frequency natural modes were excited. Here, the spokes and their damping needs to be included into the explicit model. Further, a broader approach can be applied where forcing and system response at different frequencies is considered. Furthermore, the flexibility between floater and spokes observed in the test structure (and not modelled in the aero-hydro-elastic codes) would influence the dynamics of the whole system and could potentially add insight into the complex heave motion observed in the experiments.

3.8 REFERENCES

Azcona, J., Lemmer, F., Matha, D., Amann, F., Bottasso, C. L., Montinari, P., Chassapoyannis, P., Diakakis, K., Voutsinas, S., Pereira, R., Bredmose, H., Mikkelsen, R., Laugesen, R. and Hansen, A. M. D4.2.4: Results of wave tank tests. Description of Floating Wind Model Tests at ECN and DHI. INNWIND.EU. 2016.

Bredmose, Henrik ; Mikkelsen, Robert Flemming ; Hansen, Anders Mandrup ; Laugesen, Robert; Heilskov, Nicolai ; Jensen, Bjarne ; Kirkegaard, Jens (2015) "Experimental study of the DTU 10 MW wind turbine on a TLP floater in waves and wind".Presented at: EWEA Offshore 2015 Conference, 2015, Copenhagen.

Boccotti, P.. Some new results on statistical properties of wind waves. Appl Ocean Res 1983;5:134.

Hansen A.M., Laugesen R., Bredmose H., Mikkelsen R. & Heilskov N.F. Experimental study of the DTU 10MW on Tension Leg Platform. DTU Wind Energy. Kgs. Lyngby, Denmark, 2015.

Heilskov, N.F., Petersen, O.S.: Comparison of Non-linear model of a floating wind turbine against wave tank tests, OMAE Conference 2016.

Lindgren, G.. Some properties of a normal process near a local maximum. Ann Math Stat 1970;41:1870.

Pegalajar-Jurado A, Hansen AM, Laugesen R, Mikkelsen RF, Borg M, Kim T, Heilskov NF, and Bredmose H. Experimental and numerical study of a 10MW TLP wind turbine in waves and wind. TORQUE Conference, Munich, 2016 (b).

Tromans, P.S., Anaturk, A., Hagemeyer, P.. A new model for the kinematics of large ocean waves—application as a design wave. In: Proc. 1st Int. Conf. O_sh. Mech. and Polar Engng. (ISOPE); vol. 3. 1991, p. 64–71.

4 VALIDATION OF THE DYNAMIC MOORING LINE CODE OPASS

In this chapter, the OPASS numerical simulation code developed by CENER is experimentally validated against a set of tests performed at the École Centrale de Nantes (ECN) wave tank in France. The tests consist of a suspended chain submerged into a water basin, where the suspension point of the chain is excited with horizontal harmonic motions of different periods in the plane of the catenary. Equivalent simulations of the chain setup are launched to compare against the experimental results. The code is able to predict the tension at the suspension point and the motions at several positions of the line with high accuracy. Even for those cases where the line loses and subsequently recovers tension, the resulting snap load and motions are well captured with a slight overprediction of the maximum tension. The drag coefficients for chains used in the computations have been taken from the DNV guidelines and, in general, predict correctly the hydrodynamic loads though they may require a slight adjustment for the highest frequency test cases. In addition, sensitivity studies and verification against another code show that highly dynamic cases are sensitive to the seabed-cable contact and friction models. The results show the importance of capturing the evolution of the mooring dynamics for the prediction of the line tension, especially for the high frequency motions.

4.1 Description of the numerical model

The code OPASS (Offshore Platform Anchorage System Simulator) is described in detail in the INN WIND.EU deliverable 4.21 [4.1]. The equations of motion of the mooring line are discretized using the finite element method. The mathematical model has been oriented to the achievement of a computationally efficient code. For this reason, it has been selected a lumped mass approach resulting in a global mass matrix composed by 3 x 3 submatrices in the diagonal, that can be inverted with low computational cost. The code can be run as a stand-alone tool or coupled with FAST for the simulation of a complete floating wind turbine. The code takes into account the inertia of the line, the axial stiffness, the structural damping and the gravity and the buoyancy forces. The line-seabed interaction is modelled with a contact model and also a line-seabed friction model. The hydrodynamic forces are also taken into account, considering the tangential and the normal drag and also the added mass using a formulation based in Morison equation.

4.2 Description of the experimental tests

The experiments were performed at the École Centrale de Nantes wave tank whose dimensions are 50m length, 30m width and 5m depth. The experimental setup is described in D4.24 [4.2]. A studless chain was submerged into the water basin, forming a catenary shape with the bottom end anchored to the tank floor. The suspension point was connected through a load cell to a mechanical actuator with the capability of reproducing a prescribed motion that was located at the water free surface. Figure 4.1 shows the configuration of the experiment. The fairlead, located at the water plane, was excited by the mechanical actuator with a sinusoidal prescribed horizontal motion in the plane of the catenary, around a mean position. The distance d is the horizontal distance between the anchor and the mean position of the fairlead during the tests. Two different configurations of the mooring chain corresponding to different values of the parameter d are tested: Configuration 1, where $d = 19.364$ m, and Configuration 2, where $d = 19.870$ m. Figure 4.1 also shows the coordinate system that will be used to present the results.

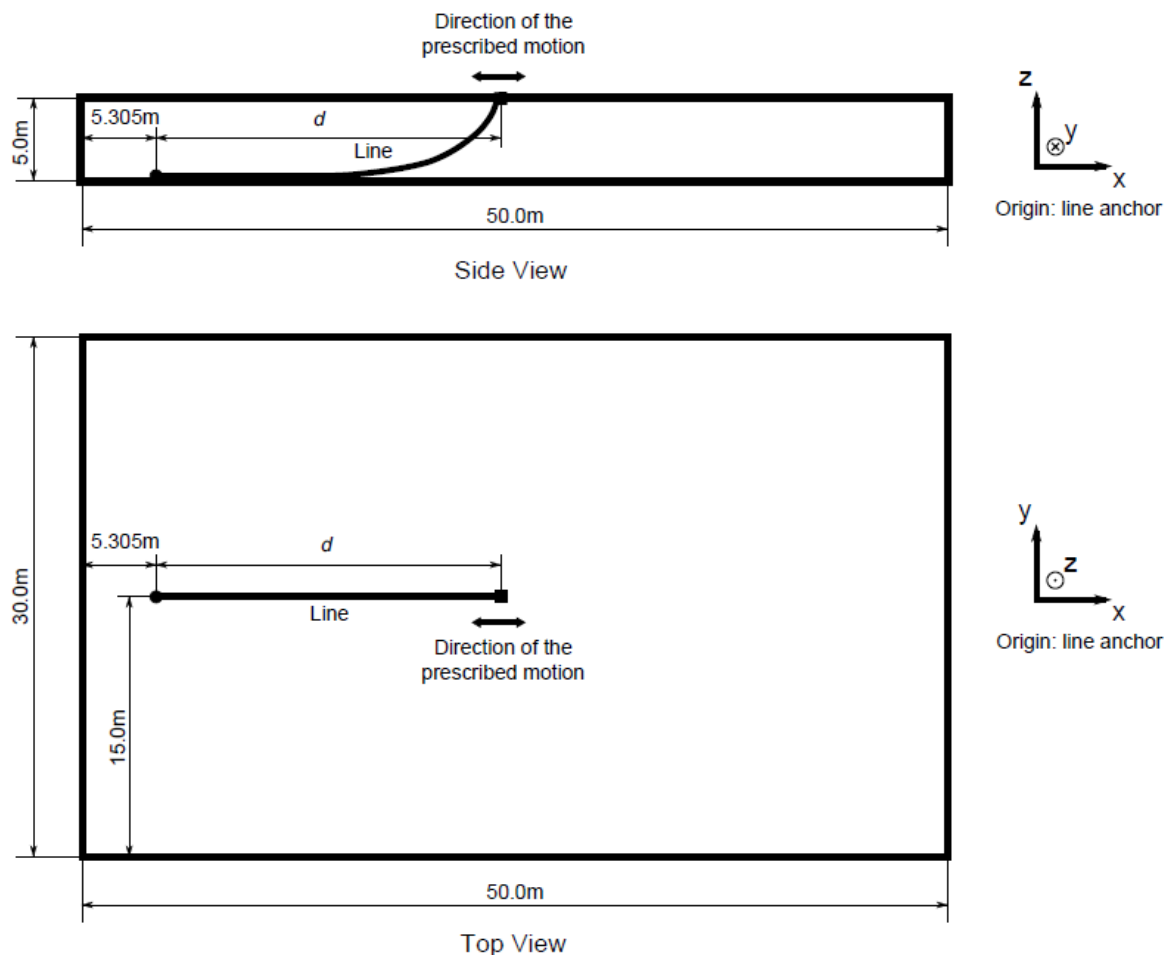


Figure 4.1: Configuration of the experiment

Figure 4.2 shows a photograph of the steel chain selected for the tests. It is a DIN5685A model with a wire link diameter of 2 mm. The mass per unit length was measured and a value of 69 g/m was found, though the original manufacturer specifications was 70 g/m. The length of the chain including the load cell at the fairlead was 21 m. The connection of the cell to the actuator allowed it to freely rotate.



Figure 4.2: DIN5685A chain with wire diameter of 2 mm

Preliminary simulations were performed in order to confirm that the presence of the load cell has not an important impact on the dynamics of the chain. It was confirmed that it has a neglectable impact on the computed tensions.

This chain model was chosen because if a scale factor of 1/40 is considered, the 5 m depth of the basin represents a 200 m depth sea location, and the resulting chain full scale properties are close to the OC4 floating model mooring lines [4.3]. Therefore, this chain represents a typical scaled mooring line used in wave tank tests for floating wind turbines.

First, two static cases with the chain suspension point fixed corresponding to Configuration 1 and Configuration 2 were studied. In addition, 6 dynamic cases were simulated combining the 2 chain

configurations with three different oscillation periods of the motion imposed at the fairlead. Similar criteria based on scale factors used for the chain dimensions were also used in the selection of the excitation periods of 1.58 s, 3.16 s and 4.74 s. These periods correspond to oscillation periods of 10 s, 20 s and 30 s in full scale when a 1/40 scale factor is used. As a matter of fact, a typical surge period of a moored platform is 10 s or higher. The amplitude of the motions was 0.25 m, which corresponds to 10 m if a 1/40 scale factor is assumed and was the maximum amplitude provided by the actuator. The cases considered are described in Table 4.1.

Table 4.1: Description of the test cases

Case ID	Configuration	Anchor Fairlead Mean Distance d (m)	Amplitude (m)	Period (s)
1	1	19.364	Static	
2	2	19.870	Static	
3	1	19.364	0.25	1.58
4	1	19.364	0.25	3.16
5	1	19.364	0.25	4.74
6	2	19.870	0.25	1.58
7	2	19.870	0.25	3.16
8	2	19.870	0.25	4.74

During the dynamic tests, the tension at the fairlead of the chain and the position of 8 reflecting markers located at different chain positions were measured. The load cell used to measure the tension at the fairlead was a submersible DDEN model with a range of 0-500 N and an accuracy of $\pm 0.25\%$. The motion tracking system that captured the motion of the reflecting markers was composed by 6 Qualisys underwater cameras, type Oqus 3+, with 1296x1024 pixels. The lenses had 20 mm and 24 mm of focal length with an averaged residual of 2 mm. This resulted in an uncertainty of the marker position of approximately 2 mm. The distance between two adjacent reflecting markers along the chain is approximately 0.5 m. The exact positions of these markers are provided in Table 4.2.

Table 4.2: Position of the markers

Marker #	Distance along the line from the fairlead (m)
1	0.656
2	1.155
3	1.655
4	2.149
5	2.646
6	3.152
7	3.655
8	4.164

For the static cases (cases 1 and 2), in addition to the markers in Table 4.2, the positions of 4 additional reflecting markers located at the lower part of the chain every 0.5 m were also monitored and the fairlead static tension was measured.

Figure 4.3 shows the load cell connecting the line and the mechanical actuator that excited the line fairlead. The photograph shows the cell before being totally submerged. During the tests the cell was submerged with the upper end connected to the actuator and located at the water level.



Figure 4.3: Load cell for the measurement of the tension

Figure 4.4 shows a portion of the submerged chain with the markers used to capture the motion. The image was taken with a submerged camera and poor light conditions. The structure installed in the basin to hold the mechanical actuator can be seen at the right side of the image.



Figure 4.4: Chain with markers to measure the motions

4.3 Parameters of the computational model

As has been mentioned in Section 4.2, the measured weight per unit length of the chain is 69 g/m and the length is 21 m. As the computational model assumes that the chain is a line with a constant circular section, an equivalent hydrodynamic diameter has to be determined. To do this, the volume of the total length of the chain was measured (Figure 4.5) and the diameter of the circular section that provides that volume for the same length was calculated.



Figure 4.5: Measurement of the displaced volume of the chain

The hydrodynamic coefficients, in particular the drag coefficients, have a great influence on the mooring line dynamics, therefore a realistic selection of the values is critical to obtain accurate simulation results. An added mass coefficient C_{mn} of 1 was chosen according to Bureau Veritas [4.4]. The normal drag coefficient C_{dn} and the tangential drag coefficient C_{dt} were obtained following the indications of DNV [4.5]. For a studless chain, this guideline provides a value for C_{dn} of 2.4 and for C_{dt} of 1.15. These values are referred to the wire diameter of the chain link. For the implementation in the code, the value has to be referred to the equivalent hydrodynamic diameter, resulting in values of 1.4 and 0.67, respectively. The axial stiffness of the chain has been estimated based on the link diameter according to Equation (4.1), see [4.5]:

$$EA=0.854 \cdot 10^8 d_w^2 (kN) \quad (4.1)$$

Where d_w is the wire diameter of the chain link in meters.

The parameters of the chain used in the computational model are summarized in Table 4.3:

Table 4.3: Computational parameters for the chain

	Parameter	Units
Length (L)	21	m
Mass per unit length (γ)	0.069	Kg/m
Density (ρ)	7850	kg/m ³
Axial stiffness (EA)	3.4E5	N
Structural damping as % of critical (ζ)	0.1	%
Equivalent hydrodynamic diameter (D)	0.0034	m
Added mass coefficient (C_{mn})	1.0	-
Normal drag coefficient (C_{dn})	1.4	-
Tangential drag coefficient (C_{dt})	0.67	-

A line-seabed contact model has been defined, including the friction of the chain with the seabed. The parameters related to this model are collected in Table 4.4.

Table 4.4: Parameters of the line-seabed contact and friction models. The stiffness and damping values are per unit length of the line

	Parameter	Units
Vertical seabed stiffness (Ksc)	20	N/m ²
Vertical seabed damping (Dsc)	0.1	Ns/m ²
Tangential friction coefficient (Cft)	0.5	-
Normal friction coefficient (Cfn)	0.5	-

For the computations of the line static shape and the computation of the dynamic cases, 30 elements were used to discretize the chain. A sensitivity analysis was performed running several simulations with 60 elements with no significant changes in the results (the maximum difference in tension was below 0.35%).

4.4 Comparison of computational and experimental results

In this section, a comparison between the experimental results and computations is presented, with the objective of validating the code for the dynamic simulation of mooring lines. First, computed and experimental data of the chain shape and the fairlead tension are presented for the static cases. Afterwards, results comparing measurements and computations of the tension at the suspension point and the positions of different chain points are shown for the dynamic cases. Results in this section are presented according to the reference system in Figure 4.1.

Static cases

These cases were used to adjust the exact horizontal position of the chain anchor that was fixed to the basin bottom by a diver. In contrast to other parameters of the test that can be easily measured or derived, such as the chain length, the weight per unit length, or the equivalent

hydrodynamic diameter; the accurate determination of the anchor position is a difficult step due to the difficulties of measuring and placing it under the water at the exact specified distance of several meters. For this reason, looking at the static shape measured by the underwater cameras, it was concluded that the exact anchor position measured from the basin wall was 5.305m (See Figure 4.1). The results, in particular the dynamic tension, are sensitive to small variations of the anchor position. Assuming this anchor position, the agreement of the computational and the experimental static shape of the chain is excellent in both configurations, with differences below 0.4%, as it is shown in Figure 4.6.

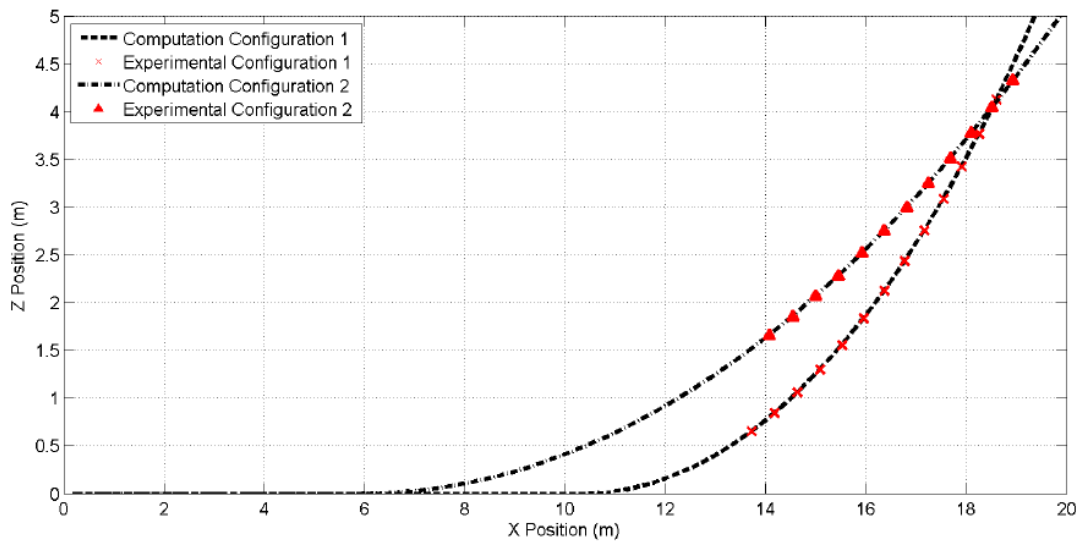


Figure 4.6: Comparison of the computed and experimental static shapes for both line configurations

Table 4.5 shows the difference between the computed tension at the fairlead and the experimental measurement for both configurations. The error in the predicted static tension is below 2%.

Table 4.5: Comparison of static fairlead tension expressed in Newtons

	Configuration 1	Configuration 2
Experimental	8.13	14.48
Computation	8.10	14.70
Difference	0.37 %	1.52 %

Dynamic cases: tension at the fairlead

Figures 4.7 and 4.8 show the comparison between the numerical predictions and the experiments for the different periods of the motion prescribed at the fairlead of the chain for Configuration 1 and Configuration 2, respectively. The plots show the fairlead tension of the chain against the fairlead position. The initial transients have been eliminated and the data are plotted once the stationary state has been reached. The arrows represent the sense of the dynamic loop: higher tensions are achieved when the fairlead of the chain is moving away from the anchor and the lower tensions appear when it is approaching to the anchor.

For the experimental data, the loops have been generated from time series containing several tens of periods of the prescribed motion. As the measured signal presents a certain amount of noise, the direct out-coming data have not been plotted. Instead, the data of the measured time series has been stored into equally distributed bins along the x axis (position of the fairlead) and the mean value and standard deviation calculated for the data of each bin have been represented. The number of bins used is 20 for the two cases with higher excitation period. For the case with the lowest period, 25 bins have been used to obtain a better definition of the curve. The mean value is represented by a circle and the standard deviation by a vertical bar centered at the mean and limited by horizontal lines. The definition of the standard deviation, σ , is given in Equation (4.2):

$$\sigma = \sqrt{\frac{\sum_{i=1}^n (X_i - \bar{X})^2}{n}} \quad (4.2)$$

Where n is the number of elements in the data, \bar{X} is the mean value of the data and X_i is the i^{th} element of the data.

In addition, the plots show the fairlead tension of the chain for the initial static position (red circle) and also the tension provided by FAST's quasi-static model [4.7] for the different positions of the fairlead (gray line).

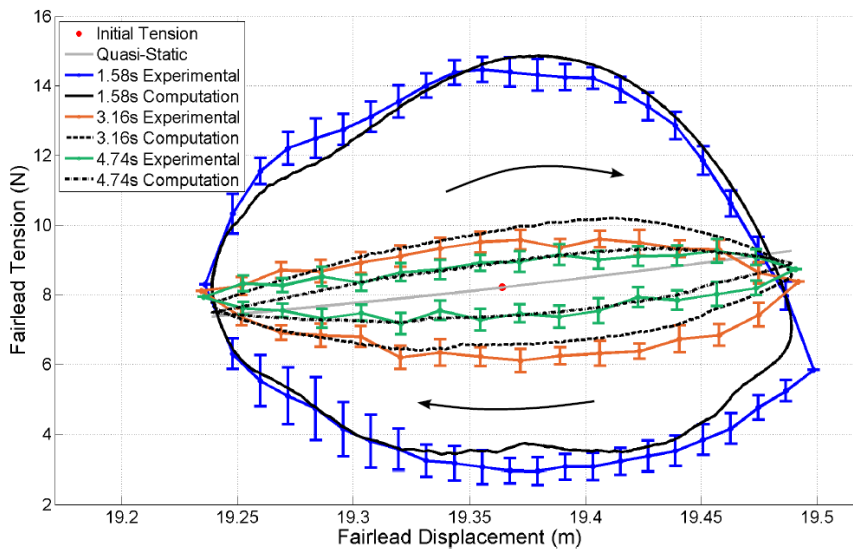


Figure 4.7: Fairlead dynamic tensions for Configuration 1. The initial static tension (red circle) and the quasi-static tension (gray line) are also represented.

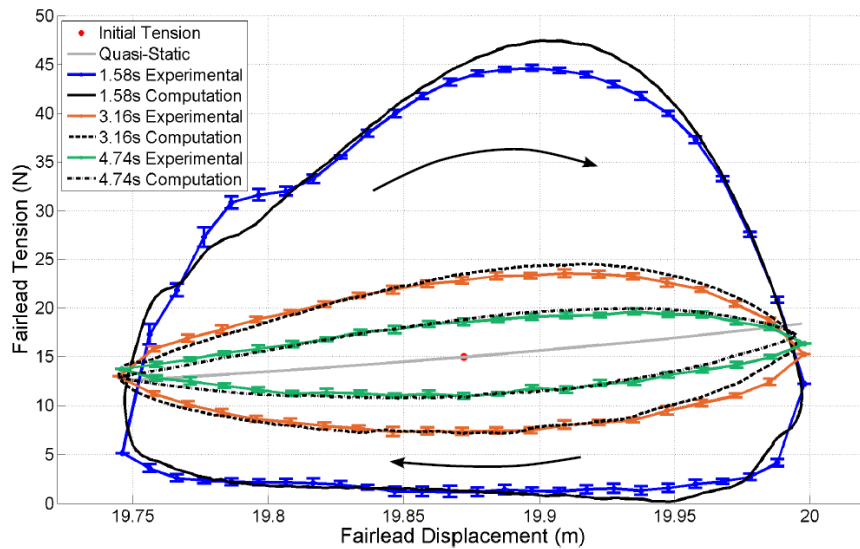


Figure 4.8: Fairlead dynamic tensions for Configuration 2. The initial static tension (red circle) and the quasi-static tension (gray line) are also represented.

As can be observed in Figures 4.7 and 4.8, the tension in the Configuration 1 is lower than in the Configuration 2. In fact, the initial static tension for Configuration 1 is 8 N and for Configuration 2 it is 15 N, and the maximum tension, for the 1.58 s period, in Configuration 2 is three times the value in Configuration 1. As has been mentioned, the tension signal acquired during the tests presents a certain amount of noise. This is the reason why the relative importance of the tension standard deviation in Configuration 1 is higher than in the second one. The figures also illustrate the importance of the dynamic effects, in particular as the excitation frequency increases. The maximum tension for the dynamic computation of the case with 1.58 s of excitation period can be between 2 (Configuration 1) and 3 (Configuration 2) times the value predicted by the quasi-static approach. For fatigue calculations of the fairlead and line, the dynamic effects are even more significant. For Configuration 2 with 1.58 s excitation period, the dynamic tension amplitude is more than ten times times the corresponding quasi-static value.

The agreement between computations and measured tension is, in general, very good for both configurations and all the excitation periods. The two highest excitation periods, 3.16 s and 4.74 s, correspond to the chain's Harmonic Condition described in [4.8], where the measured tension at the fairlead is close to sinusoidal in the time domain. In these cases the agreement is good, in particular for Configuration 2, where the relative importance of the noise, and the standard deviation of the data, is lower.

For the lowest period of excitation, 1.58 s, the dynamics of the chain correspond to the Snap Condition and are more complex. In Configuration 1 the chain partially loses tension, and in Configuration 2 the situation is more extreme and the chain totally loses tension; the measured tension at the fairlead is very close to 0 during almost half of the period. Nevertheless, the agreement with computations is still good: a discrepancy of around 4.5% on the estimation of the maximum tension appears in both configurations. This maximum tension appears approximately when the velocity of the chain's fairlead is maximum. An adjustment of the drag coefficient for the highest excitation frequency may result on a better prediction of the maximum tension for the 1.58 s period case. A sensitivity study of the influence of variations on the drag coefficients on the tension is presented at the end of this section.

Another slight discrepancy appears in both configurations for the period of 1.58 s. When the fairlead moves towards the anchor, the chain loses tension. Then, the fairlead motion reverses, the tension is recovered and the links that are falling freely suddenly are pulled upwards, producing a snap load; a sudden increase of the tension. During this event, the measured tension temporarily reaches a plateau, before again increasing towards the peak value. For the

experimental data this decrease in the slope appears later and it is more pronounced than in the computational results. This effect is even more important in the Configuration 2 case.

The case for Configuration 2 and oscillation period of 1.58 s, where the loss of tension of the line is the most pronounced, is very sensitive to the modelling of the seabed-cable interaction. For this reason, this case was studied more in detail. It has to be noted that the elements maintain axial stiffness when tension is lost, in contrast to a real chain. This fact can affect the behaviour for the part of the chain resting on the seafloor. OPASS takes into account the seafloor with a seabed contact model. The nodes dropping below the defined seafloor, get an applied vertical force that is proportional to the vertical distance to the seafloor. In addition, linear damping is applied to nodes below the seafloor in the vertical direction. This linear damping is scaled with the distance up to the seafloor. Figure 4.9 shows the effect of eliminating the seabed-cable friction on the tension computed with OPASS for the mentioned sensitive case of period 1.58 s and Configuration 2. After a few periods of excitation, an oscillation is generated in the part of the loop where the suspension point moves from the minimum position towards the maximum position and the chain is being lifted quickly off the seafloor. This effect does not arise in any of the other cases studied in this work when the seabed friction model is disabled.

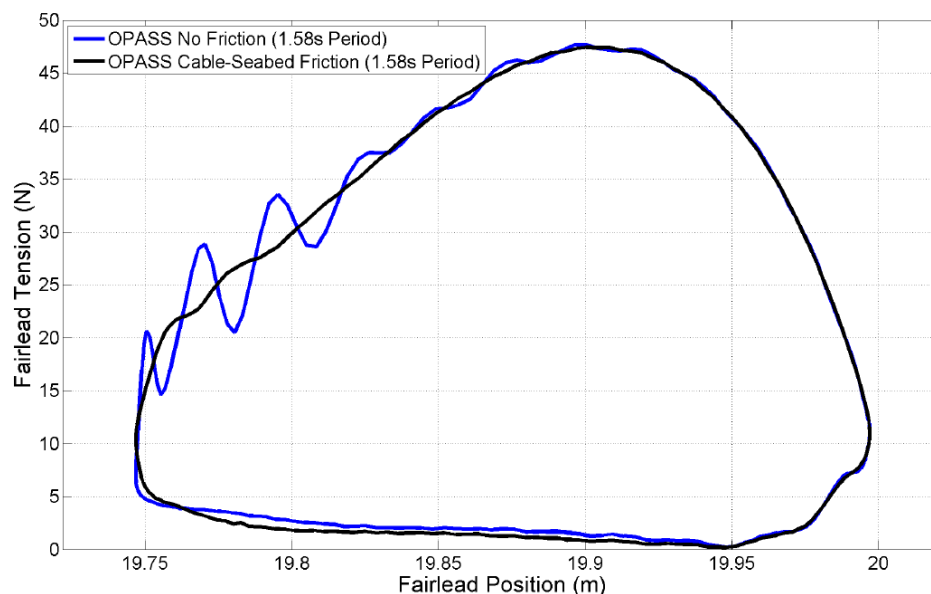


Figure 4.9: Effect of seabed friction on the fairlead tension computed with OPASS for 1.58s period and Configuration 2

Apparently, these dynamics are caused by small motions of the nodes of the line resting on the seabed during the tension-less portion of the dynamic loop. The introduction of seabed friction in the model avoid these small nodal displacements and, consequently, the oscillations are not generated. These dynamics are not present in the experimental results, due to the friction of the chain with the bottom of the basin. This case highlights the importance of a correct modelling of the line-seabed interaction to avoid the generation of instabilities in highly dynamic situations with pronounced loss of tension in the chain.

Finally, a study on the sensitivity of the fairlead tension to the drag coefficients has been performed. Figure 4.11 is similar to Figure 4.8: it shows the comparison of experimental measurements with computations for Configuration 2, but includes additional computations varying the value of the drag coefficients. The lines in black color correspond to the

computations already discussed that used the drag coefficients provided by the guideline (see Table 4.3). The gray lines show the results of the same computations but increasing and decreasing the tangential and normal drag coefficients in 20%, to evaluate the influence of these parameters.

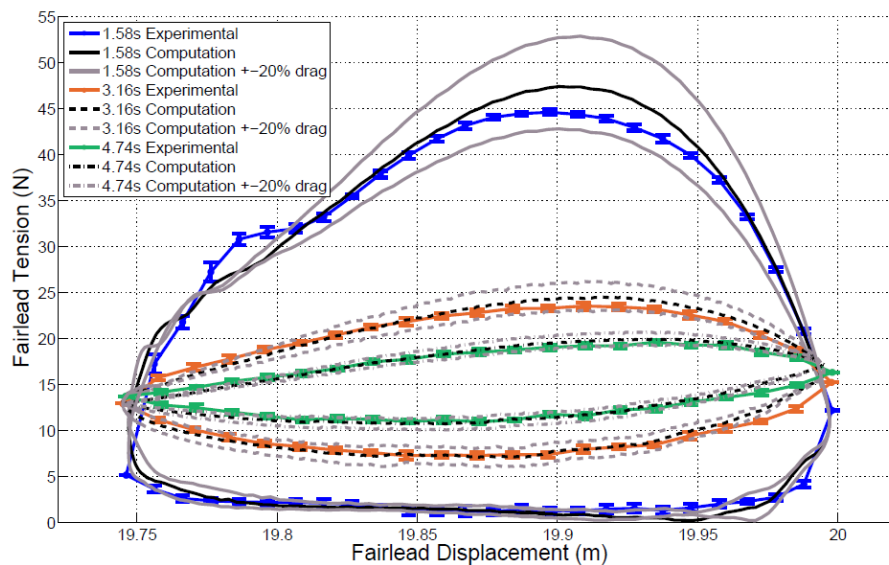


Figure 4.11: Sensitivity of the fairlead tension to changes in the drag coefficients. Computations increasing and decreasing 20% the baseline DNV values for the drag coefficients are shown in gray colour.

The computations using the value of the drag coefficients given by the guidelines provide the best agreement with the experimental data. This is particularly true for the case with the highest excitation period. For the cases with lower excitation periods, specially for the case with a period of 1.58 s, a small decrease of the drag coefficients could improve the agreement between computations and experiments. This suggests that a dependency of the drag coefficients with the frequency of the motion could exist and that the coefficients provided by the guidelines are more adequate for low frequency conditions.

In summary, the computational model is able to predict with good accuracy the tension in all the cases considered. In those cases where chain loses tension and the dynamics are more complex, the computations also predict the tension accurately, though special attention has to be paid to the seabed-cable interaction model. The values for the drag provided by the guidelines give a good agreement with the experimental data, although a slight adjustment for the cases with highest frequencies could improve the comparison.

Dynamic cases: motion of the chain

A comparison between the measured and the computed trajectories of the 8 positions along the chain length specified in Table 4.2 is discussed in this section. Figures 4.12 to 4.27 show the trajectories of the markers for Configuration 1 (C1) and Configuration 2 (C2) and for the different periods of excitation of the chain fairlead. According to the reference system described in Figure 4.1, the x and z coordinates represent the horizontal and vertical positions of the marker respectively.

Similarly to the procedure conducted in Section 4.4.2, the loops of experimental data have been generated based on several tens of periods of the prescribed motion and graphically represented

by the mean value and the standard deviation. The dispersion of data for the motion is lower than in the tension results. For the calculation of the mean value and standard deviation, data have been stored into bins. The classification of data in these bins has been performed in most of cases based on the x axis, but in some particular cases, as for example the motion of markers 5 and 6 for Configuration 2 and period 1.58s (see Figure 4.21 and Figure 4.23), the discretization is based on the z axis, due to the shape of the curve and the requirements of the algorithm used in the data processing. In those cases, the dispersion bars on the plots are shown with their corresponding direction.

As before, the red dot in the plots show the initial static position of the marker before the chain is excited and the gray line represents the displacement of the marker according to the quasi-static model included in the FAST code. The arrows indicate the sense of the dynamic loops.

The scale and length of both the x and z axis is the same in all the plots from Figure 4.12 to Figure 4.27 to keep a constant reference frame for the chain at each marker position.

The loop corresponding to period 1.58 s represented in Figure 4.13 is not complete due to the loss of visibility of the marker by the tracking system during part of the cycle.

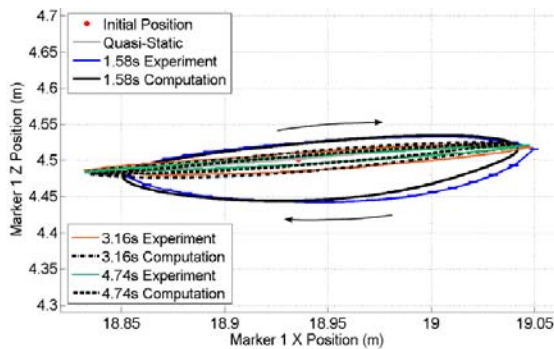


Figure 4.12: Trajectory described by the marker 1 (C1)

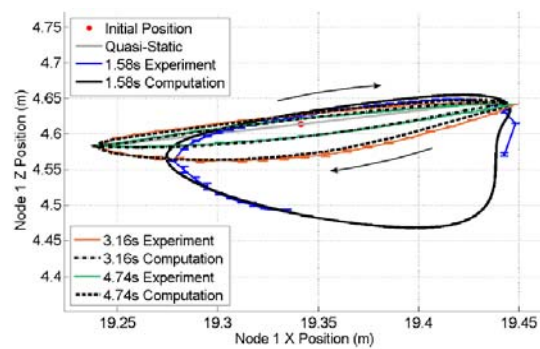


Figure 4.13: Trajectory described by the marker 1 (C2)

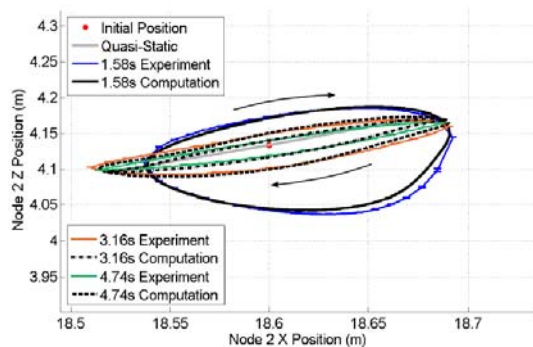


Figure 4.14: Trajectory described by the marker 2 (C1)

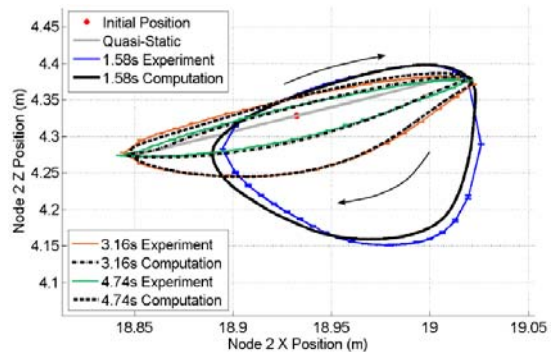


Figure 4.15: Trajectory described by the marker 2 (C2)

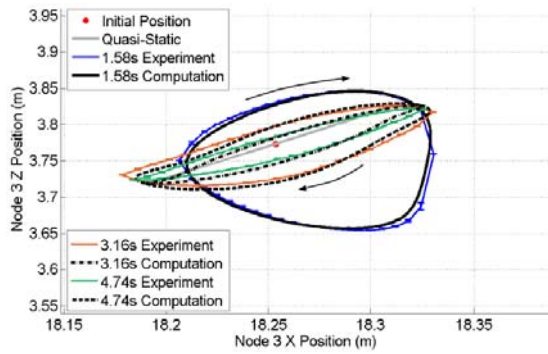


Figure 4.16: Trajectory described by the marker 3 (C1)

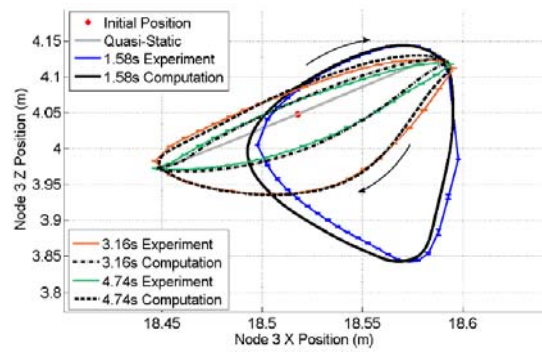


Figure 4.17: Trajectory described by the marker 3 (C2)

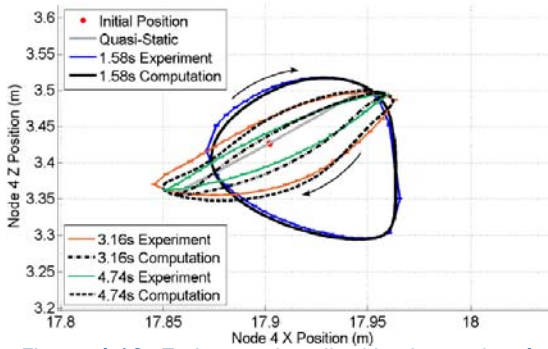


Figure 4.18: Trajectory described by the marker 4 (C1)

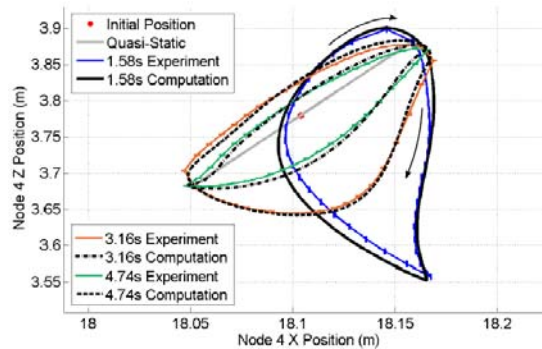


Figure 4.19: Trajectory described by the marker 4 (C2)

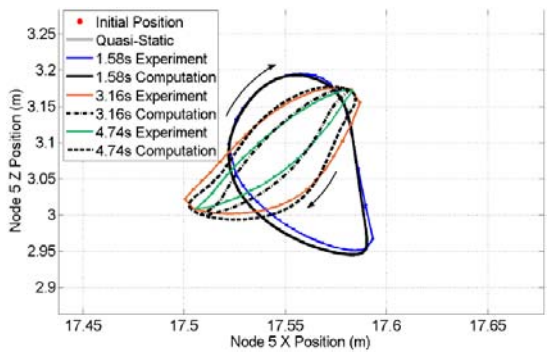


Figure 4.20: Trajectory described by the marker 5 (C1)

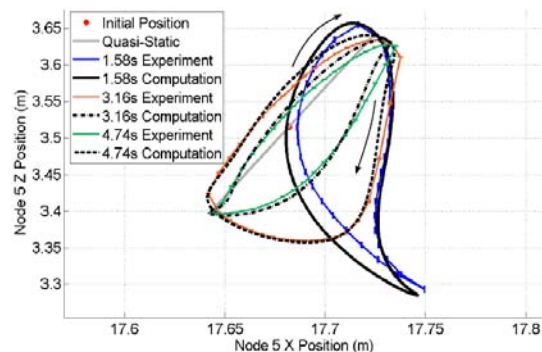


Figure 4.21: Trajectory described by the marker 5 (C2)

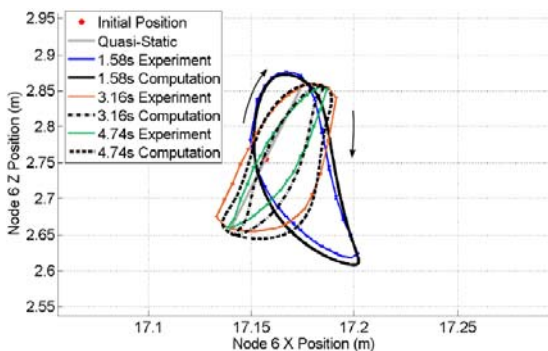


Figure 4.22: Trajectory described by the marker 6 (C1)

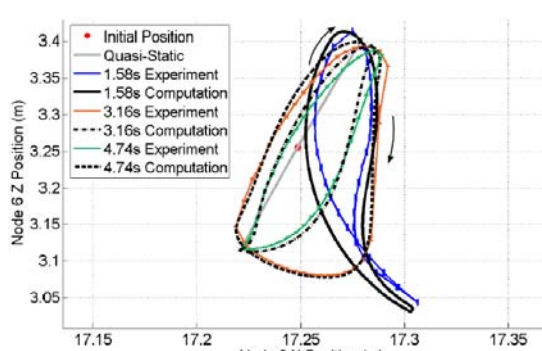


Figure 4.23: Trajectory described by the marker 6 (C2)

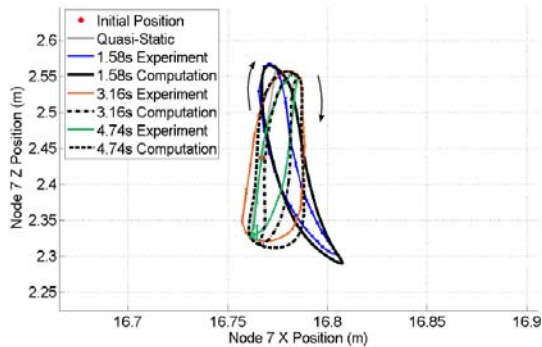


Figure 4.24: Trajectory described by the marker 7 (C1)

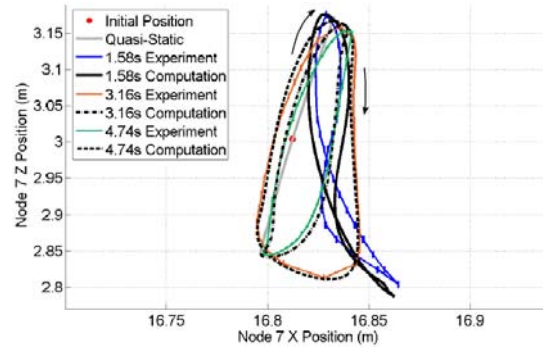


Figure 4.25: Trajectory described by the marker 7 (C2)

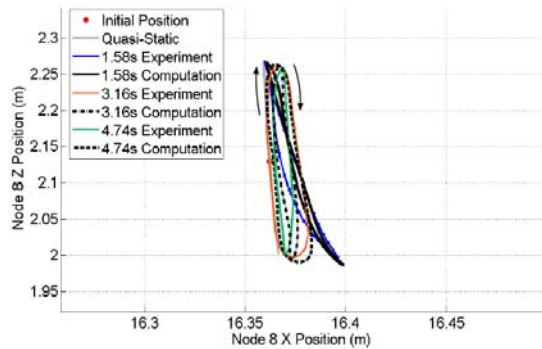


Figure 4.26: Trajectory described by the marker 8 (C1)

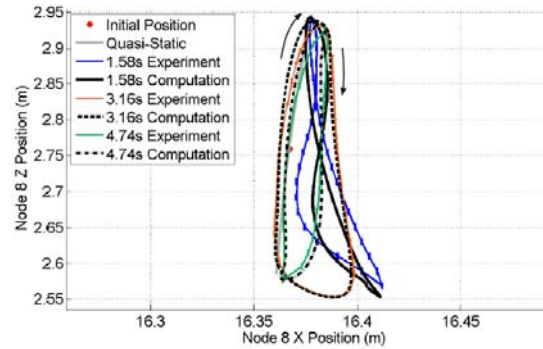


Figure 4.27: Trajectory described by the marker 8 (C2)

In general, the agreement between the measured motions and the simulations is very good for both configurations and all the oscillation periods and positions. The highest disagreement appears for the Configuration 2 at the highest frequency of oscillation (period 1.58 s), where the line totally loses tension. Nevertheless, the agreement is still good.

The motion of the chain markers is predominantly horizontal in the positions closer to the fairlead of the chain, where the horizontal motion was prescribed, but it transforms to a predominantly vertical motion as the distance to the fairlead increases. The reason is that the tension of the chain decreases as we get further from the fairlead. For the markers located deeper, when a low motion period (1.58 s) is imposed, the chain links feel zero load during the portion of the loop where the tension in the chain is lower and consequently fall freely. This corresponds to the right part of the loops, that is almost vertical, especially for the lower excitation periods and markers located far from the fairlead (see for example Figures 4.20 to 4.23). When the tension at the marker position recovers, the predominately vertical motion changes to a negative x-direction and positive z-direction, corresponding approximately to the left part of the loops. The effect of tension loss is even more clear on the short period cases (period 1.58 s), because the decrease in tension along the chain is more pronounced. For the cases with longer periods, the tension remains positive in a longer portion of the chain length, or even all along. In those cases (periods 3.16 s and 4.74 s), the motion of the marker is close to the quasi-static solution.

Figure 4.28 represents the x displacement for the marker 5 in Configuration 2 (motion period of 1.58 s) and the tension at the fairlead of the chain as function of the time. Figure 4.29 represents the z displacement for the same case and marker, also shown with the tension. These Figures illustrate how, as the tension approaches to 0, the marker stops moving in the x direction and freely falls in the negative z direction. During the period when the line remains slack, the marker displacement in x suffers a small oscillation giving a N-shape: the marker is initially moving in the positive x direction, it goes backwards for a while and then continues forwards again. This N-shape effect is responsible for the secondary loops that appear at the deeper markers in the x-z

trajectories of Configuration 2 for period 1.58 s, see Figures 4.25 or 4.27. The N-shape is more pronounced as the distance along the chain to the fairlead increases. For this reason, no secondary loops are present at the markers closer to the fairlead, but they arise and increase their amplitude with the increasing distance to the excitation source. The dynamics of this effect on the loops is well predicted by the code, though it seems to be a complex effect and very sensitive to small variations in parameters. Thus, the trajectories of the markers located lower with the highest oscillation frequency (period 1.58 s) and for Configuration 2 are the ones where the inaccuracy of the computations is higher, in particular for the x coordinate.

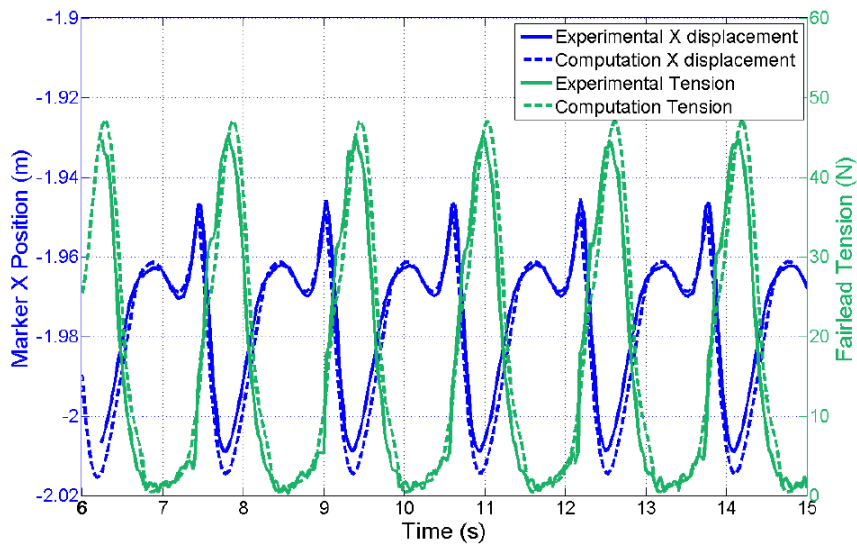


Figure 4.28: X position and tension for marker 5 (Conf. 2, period 1.58s)

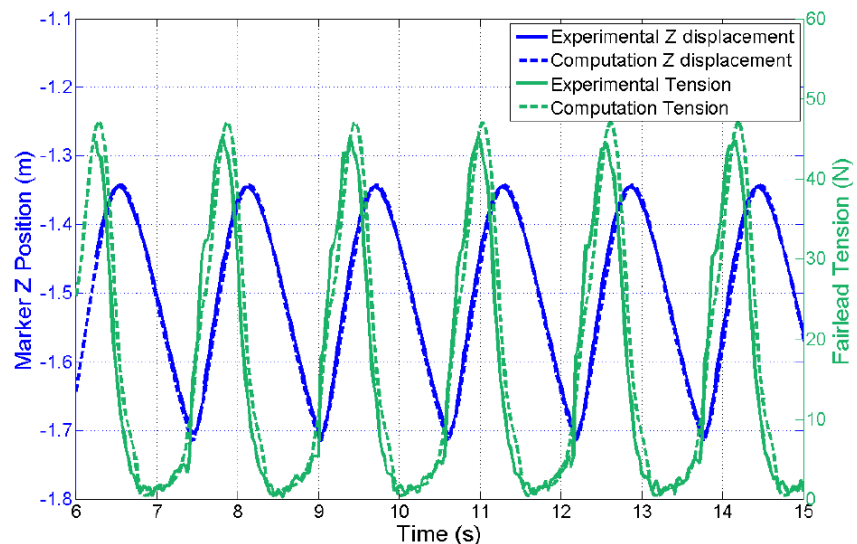


Figure 4.29: Z position and tension for marker 5 (Conf. 2, period 1.58s)

4.5 Conclusions

The OPASS dynamic mooring line code has been successfully validated against experimental data for static and dynamic conditions. Two configurations of the chain have been studied, with

different tension levels. The agreement between computations and experimental results is very good for the chain fairlead tension and also for the motion of the chain at the diverse positions considered.

In the static cases, both the shape of the line and the tension at the suspension point compare very well between the computations and the experiments.

For the dynamic validation, the chain has been excited with a prescribed motion at the fairlead with three oscillation periods, producing different dynamic conditions, including harmonic response, loss of tension and snap loading. The code is able to predict the motion of the chain and the tension with precision in all these conditions.

The added mass and drag coefficients for the chain, that have been chosen from guidelines, in general, represent with accuracy the hydrodynamic loads.

The importance of including dynamic effects on the prediction of the mooring line loads has been shown; the maximum tension can be between 2 and 3 times the value computed by the quasi-static approach when high excitation frequency is imposed. The tension amplitude can be more than ten times times the corresponding quasi-static value.

For the cases with the lowest excitation period, where the line slacks, the computed and measured tension agree well, although a slight difference appears during the snap loads once tension recovers. In these cases, the maximum tension is overpredicted by the code by around 4.5%. These differences could be due to the fact that the drag coefficients could present a dependency with the motion frequency and the values from guidelines could be tuned for the cases with the low excitation frequencies. Regarding the chain motions, those cases where the chain loses tension present the highest inaccuracies in the numerical results, especially in the lowest part of the chain, though the results are still good.

In the cases with higher tension level and higher excitation frequency, the simulation results are particularly sensitive to the cable-seabed interaction model. The computational model is able to predict the tension with accuracy, but the modelling of the seabed friction should not be neglected.

4.6 REFERENCES

- [4.1] Azcona, J., Bekiropoulos, D., Bredmose, H., Fischer, A., Heilskov, N.F., Krieger, A., Lutz, T., Manjock, A., Manolas, D., Matha, D., Meister, K., Pereira, R., Ronby, J., Sandner F. and Voutsinas, S. *D4..21: State-of-the-art and implementation of design tools for floating structures*. INN WIND.EU. 2014.
- [4.2] Azcona, J., Lemmer, F., Matha, D., Amann, F., Bottasso, C. L., Montinari, P., Chassapoyannis, P., Diakakis, K., Voutsinas, S., Pereira, R., Bredmose, H., Mikkelsen, R., Laugesen, R. and Hansen, A. M. *D4.2.4: Results of wave tank tests. Description of Floating Wind Model Tests at ECN and DHI*. INN WIND.EU. 2016.
- [4.3] Robertson, A., Jonkman, J.M, Masciola, M., Song, H., Goupee, A., Coulling, A. and Luan, C. *Definition of the Semisubmersible Floating System for Phase II of OC4*. Technical Report TP-5000-60601. Golden, Colorado, USA: NREL, 2014.
- [4.4] Bureau Veritas. *NR 493 R02 E. Classification of Mooring Systems for Permanent Offshore Units*. 2002.
- [4.5] Det Norske Veritas. *Offshore Standard DNV-OS-E301. Position Mooring*. Høvik, Norway, 2010.
- [4.6] *OrcaFlex Manual. Version 9.8b*. Orcina Ltd. 2014.
- [4.7] Jonkman, J.M. *Dynamics Modeling and Loads Analysis of an Offshore Floating Wind Turbine*. Ph.D. Thesis. University of Colorado, 2007.
- [4.8] Suhara, T., Koterayama, W., Tasai, F., Hiyama, H ., Sao, K. and Watanabe, K. *Dynamic Behaviour and Tension of Oscillating Mooring Chain*. Offshore Technology Conference. OTC-4053. Houston, USA, 1981, pp. 415-424. doi: 10.4043/4053-MS.

5 CONCLUSIONS

A comprehensive validation of different software has been presented using measurement data of the four-week campaign at EHEEA Nantes/France in 2014 on a semi-submersible concept and test campaign carried out at DHI Denmark in December 2014 and January 2015 on a TLP concept. With the two different methodologies for scaled testing of floating wind turbines it could be shown that it is possible to simplify the rotor aerodynamics by using a Software-in-the-loop (SiL) method. It is to be shown if the Froude-scaling of the aerodynamic forces using low-Reynolds rotors gives advantages when including more effects like blade-pitch control or sheared and yawed inflow.

In view of floating wind turbine optimization of performance and energy harvesting, it has been demonstrated that accurate models become particularly important due to the large added complexity of dependence on the hydrodynamic motion response. Accurate prediction of hydrodynamic motion response of floating offshore wind turbine is a key. Two type of codes for performing coupled analysis of a floating wind turbine have been validated, namely aero-hydro-elastic integrated tools and high fidelity aerodynamic and high fidelity hydrodynamic CFD. It is worth noticing that the conclusions on accuracy of the codes, should be viewed in mind that CFD being a code that is not dependent on prior calibration, however, significantly more computational demanding.

A stepwise validation has been conducted, with test cases of increasing complexity. The computations have shown a good agreement with experiments in free decay cases and in cases with constant wind. These cases have been used to verify mooring stiffness, inertias, masses, aerodynamics, etc. and also to adjust the hydrodynamic damping of the computational models. Contrary to the aero-hydro-elastic models, the hydrodynamic CFD model does not dependent on prior calibration of added mass and damping. Thus, the CFD may potentially replace physical model tests for providing the needed calibration data for aero-hydro-elastic models. The general agreement between computations and measurements has been good.

It has been demonstrated that using a Froude-scaled platform and mooring system and a performance-scaled rotor it is possible to obtain valid measurements, which are predicted well by the state-of-the-art simulation models.

Furthermore, a CFD simulations have been used to assess the influence on the jet flow as well as the influence of the turbine motion on the aerodynamic loads. Results showed that the experimental jet inflow only had small influence on the aerodynamic loads of the rotor.

The OPASS dynamic mooring line code has been successfully validated against experimental data for static and dynamic conditions. The agreement between computations and experimental results is very good for the chain fairlead tension and also for the motion of the chain at the diverse positions considered. The importance of including dynamic effects on the prediction of the mooring line loads has been shown.

Recommendations for future tests are to perform a detailed identification of the subsystems mooring lines, inertial and elastic properties of the structure, the aerodynamic rotor coefficients, the wave maker and the wind field. Also, an uncertainty analysis of the sensors should be performed and a calibration on site.

Considering aero-hydro-elastic integrated tools, a good match for the surge motion, pitch motion and nacelle acceleration has generally been achieved. Some disagreement appears at low frequencies, following the focused wave group impacts. This indicates the need of including non-linear wave kinematics and hydrodynamics on future developments of the software. On the other hand, these non-linear effects will increase excitation of the structure in the sub- and super-harmonic regions, hence a more advanced model for the hydrodynamic damping needs to be employed. For the mooring lines, it has been shown the importance of using dynamic models for the analysis of the lines, although the impact on the global system motions is not critical. To accurately capture the line tension levels it is required a better characterization of the drag coefficients for a wider range of mooring types and operating conditions. The effect of wind is generally well captured by the aero-hydro-elastic tools, but wind field discrepancies between tests and numerical models is a gap yet to be bridged.

The strength of the CFD model is the accuracy when hydrodynamic viscous effects is key in predicting the hydrodynamic motion response of a floating offshore wind turbine in view

optimization of performance and energy harvesting. One of the key challenges in CFD is combining the high fidelity hydrodynamic CFD methodologies with CFD aero-dynamics, which rely heavily on advanced turbulence modelling. Some compromises has to be made in term of the hydrodynamics being Froude dominated and the aero-dynamics being Reynolds dominated, which demands a profound research effort in to the core of CFD algorithms and methodologies. Further development is also needed on the moving mesh capabilities.